



Fauré De la Barra, Nicole Eloísa (2016) Understanding immobilised enzymes by NMR spectroscopy. PhD thesis

<http://theses.gla.ac.uk/7319/>

Copyright and moral rights for this thesis are retained by the author

A copy can be downloaded for personal non-commercial research or study, without prior permission or charge

This thesis cannot be reproduced or quoted extensively from without first obtaining permission in writing from the Author

The content must not be changed in any way or sold commercially in any format or medium without the formal permission of the Author

When referring to this work, full bibliographic details including the author, title, awarding institution and date of the thesis must be given.

UNIVERSITY OF GLASGOW

# Understanding Immobilised Enzymes by NMR Spectroscopy

by

Nicole Eloísa Fauré De la Barra

A thesis submitted in fulfilment  
of the requirements for the degree of Doctor of Philosophy

in the  
School of Chemistry  
College of Science and Engineering

May 2016

# Declaration of Authorship

I declare that, except where explicit reference is made to the contribution of others, that this thesis is the result of my own work and has not been submitted for any other degree at the University of Glasgow or any other institution.

Signed: \_\_\_\_\_

Date: \_\_\_\_\_

This thesis was typeset with Microsoft® Word 14.4.8. NMR spectra were processed using Bruker TopSpin 3.2. Figures were created using Stone Create 14.4.1, ChemDoodle 5.1.0 and Wolfram Mathematica 8. References were managed with EndNote X6.0.2.

The follow publication derives from this work:

The work published in Reference [1] appears in Chapter 5.

*A Solid-State NMR Study of the Immobilization of  $\alpha$ -Chymotrypsin on Mesoporous Silica* by N. E. Fauré, P. J. Halling and S. Wimperis [1]

*“You can know the name of that bird in all the languages of the world, but when you’re finished, you’ll know absolutely nothing whatever about the bird. You’ll only know about humans in different places, and what they call the bird. So let’s look at the bird and see what it’s doing – that’s what counts.”*

Richard P. Feynman

# Abstract

Enzyme immobilisation is the conversion of a soluble enzyme molecule into a solid particle form. This allows the recovery of the enzyme catalyst for its re-use and avoids protein contamination of the product streams. A better understanding of immobilised enzymes is necessary for their rational development. A more rational design can help enormously in the applicability of these systems in different areas, from biosensors to chemical industry. Immobilised enzymes are challenging systems to study and very little information is given by conventional biochemical analysis such as catalytic activity and amount of protein. Here, solid-state NMR has been applied as the main technique to study these systems and evaluate them more precisely. Various approaches are presented for a better understanding of immobilised enzymes, which is the aim of this thesis. Firstly, the requirements of a model system of study will be discussed. The selected systems will be comprehensively characterised by a variety of techniques but mainly by solid-state NMR. The chosen system will essentially be the enzyme  $\alpha$ -chymotrypsin covalently immobilised on two functionalised inorganic supports - epoxide silica and epoxide alumina - and an organic support - Eupergit®. The study of interactions of immobilised enzymes with other species is vital for understanding the macromolecular function and for predicting and engineering protein behaviour. The study of water, ions and inhibitors interacting with various immobilised enzyme systems is covered here. The interactions of water and sodium ions were studied by  $^{17}\text{O}$  and  $^{23}\text{Na}$  multiple-quantum techniques, respectively. Various pore sizes of the supports were studied for the immobilised enzyme in the presence of labelled water and sodium cations. Finally, interactions between two fluorinated inhibitors and the active site of the enzyme will be explored using  $^{19}\text{F}$  NMR, offering a unique approach to evaluate catalytic behaviour. These interactions will be explored by solution-state NMR firstly, then by solid-state NMR. NMR has the potential to give information about the state of the protein in the solid support, but the precise molecular interpretation is a difficult task.

# Acknowledgements

I wish to express my sincere thanks to Prof Peter J. Halling, my “protein” supervisor (UoS). I am extremely thankful and indebted to him for sharing his expertise, and for providing me with sincere and valuable guidance. I am also thankful to my “solid-state NMR” supervisor, Prof Stephen Wimperis for his patient help throughout my immersion in the extraordinary world of NMR.

I would especially like to thank Dr John Parkinson for all his time, guidance, expertise and enthusiasm with the solution-state NMR experiments. Further thanks to Prof Colin Gibson (UoS) and his student, James Campbell for the collaboration with the synthesis of one of the inhibitors used in this thesis. I also thank Daniel McSherry for his help in this project as an undergraduate student of UoG. I would also like to thank Dr Rudi Marquez for his support at difficult moments. I would like to take this opportunity to express my gratitude to those cheerful members of the School of Chemistry at UoG for their help and joy (Michael Beglan, Dr Diana Castro, Stuart Mackay and Colin Reilly). Thanks to members of the Wimperis and Ashbrook groups for their invaluable and friendly help and support (Akiko Sasaki, Dr Daniel Dawson, Paula Sanz-Camacho and Scott Sneddon).

I will always be grateful to my family – especially my mother and my grandmother – and friends in Chile for their unceasing encouragement, support and attention despite the distance. I would also like to thank to my friends located nearby in the UK for being there for me and enlightening my pathway when I needed it: Nina Bjornstad, Maria Maciá, Carolina Valenzuela, Marco De Tullio and Smita Odedra. I would also like to thank Mark and Judy Porter for reminding me what it really means kindness.

Finally, I cannot express enough my gratitude to Becas Chile (Conicyt) for the scholarship, which enabled me to undertake my PhD studies.

*to Leo, my life partner.*

*The completion of this thesis would not have been possible without his endless support and love.*

# Abbreviations and acronyms

ADC	analogue to digital converter
AFEB	(R)-1-acetamido-2-(4-fluorophenyl)ethane-1-boronic acid
AM	adsorption method
AS	absorption spectroscopy
ATEE	N-acetyl-L-tyrosine ethyl ester
BET	Brunauer-Emmett-Teller analysis
BPTI	Bovine pancreatic trypsin inhibitor
BSA	bovine serum albumin
CAG	carrier bound group
CD	circular dichroism
CLEA	cross-linked enzyme aggregate
CLEC	cross-linked enzyme crystal
CPMAS	cross-polarisation under MAS
CPMG	Carr-Purcell-Meiboom-Gill
CRAMPS	combined rotation and multiple-pulse spectroscopy
CW	continuous wave
CYCLOPS	cyclically ordered phase sequence
DOSY	diffusion-ordered spectroscopy
DPFGSE	double pulsed field gradient spin echo

DQF	double quantum filter
DSC	differential scanning calorimetry
EASY	elimination of artifacts in NMR spectroscopy
EEW	epoxy equivalent weight
EFG	electric field gradient
EM	electron microscopy
EPR	electron paramagnetic resonance
EXSY	exchange spectroscopy
FAC	frontal affinity chromatography
FEP	Fluorinated ethylene propylene
FID	free induction decay
FM	fluorescence microscopy
FS	fluorescence spectroscopy
FT	Fourier transform
FTIR	Fourier transform infrared spectroscopy
GOPS	3-glycidyloxypropyltrimethoxysilane
HETCOR	heteronuclear correlation
HOESY	heteronuclear Overhauser effect spectroscopy
HSQC	heteronuclear single quantum coherence
IGS	immunogold staining
INPHARMA	interligand NOEs for pharmacophore mapping
ITC	isothermal titration calorimetry
IUPAC	international union of pure and applied chemistry

LBHB	low-barrier H-bond
LDMAS	low decoupling under MAS
MAS	magic angle spinning
MD	molecular dynamics
MIP	mercury intrusion porosimetry
MQ	multiple quantum
MS	mass spectroscopy
NMR	nuclear magnetic resonance
NOE	nuclear Overhauser effect
NOESY	nuclear Overhauser effect spectroscopy
PDB	protein data bank
PFG	pulsed field gradient
PFPTB	potassium 4-fluorophenyl trifluoroborate
PSD	pore-size distribution
PSTMAS	pulse saturation under MAS
PTFE	polytetrafluoroethylene
QCM-D	Quartz crystal microbalance with dissipation monitoring
RAR	reactive amino acid residue
RF	radiofrequency field
ROESY	rotating-frame nuclear Overhauser effect spectroscopy
SALMON	solvent accesibility, ligand binding and mapping of ligand orientation
SAR	structure-activity relationship
SPINAL	small phase incremental alternation

SPR	surface plasmon resonance
STD	saturation-transfer diffusion
TEM	transmission electron microscopy
TGA	thermogravimetric analysis
THF	tetrahydrofuran
TQF	triple quantum filter
TS	thermal shift
WALTZ	wideband alternating-phase low-power technique for zero-residual-splitting
water-LOGSY	water-ligand observed by gradient spectroscopy
WATERGATE	water suppression by gradient-tailored excitation
XRD	X-ray diffraction

# Colour code for chemical structures<sup>1</sup>

Hydrogen	
Boron	
Carbon	
Nitrogen	
Oxygen	
Fluorine	
Aluminium	
Silicon	

---

<sup>1</sup> The colour convention used in this thesis is CPK, named after the CPK molecular models designed by chemists Robert Corey and Linus Pauling [2], and improved by Walter Koltun [3].

# Contents

Declaration of Authorship .....	i
Abstract .....	iv
Acknowledgements.....	v
Abbreviations and acronyms.....	vii
Colour code for chemical structures.....	xi
Contents .....	xii
CHAPTER 1 Introduction .....	1
CHAPTER 2 Theoretical background.....	7
2.1 Methods in structural biology for proteins.....	7
2.2 Nuclear magnetic resonance (NMR).....	9
2.2.1 Fundamentals .....	9
2.2.2 Internal interactions .....	12
2.2.2.1 Chemical shift interaction.....	12
2.2.2.2 The dipolar interaction.....	14
2.2.2.3 J-coupling .....	14
2.2.2.4 The quadrupolar interaction .....	15
2.2.3 Relaxation.....	16
2.2.4 Fourier Transform NMR .....	18
2.2.5 Instrumentation .....	19
2.2.6 Solution-state NMR.....	21
2.2.6.1 The spin echo .....	21
2.2.6.2 Water suppression .....	22
2.2.6.3 Nuclear Overhauser Effect .....	23
2.2.7 Solid-state NMR .....	26

2.2.7.1	Magic-Angle Spinning .....	26
2.2.7.2	Cross-Polarisation .....	27
2.3	Dynamic processes in proteins .....	30
2.3.1	NMR approaches .....	31
2.3.2	Other approaches .....	35
2.4	Analysis of protein-ligand interactions .....	35
2.4.1	Biophysical methods .....	36
2.4.1.1	NMR approaches .....	36
2.4.1.2	Other approaches .....	37
2.5	Immobilisation of enzymes .....	39
2.5.1	Methods of immobilisation .....	40
2.5.1.1	Covalent enzyme immobilisation .....	41
2.5.2	System .....	42
2.5.2.1	Carrier .....	42
2.5.2.2	Reactive enzyme residues .....	45
2.5.3	Evaluation of immobilised enzyme .....	47
2.5.3.1	Immobilisation process .....	47
2.5.3.2	Location of immobilised enzyme .....	48
2.5.3.3	Conformational changes .....	49
2.5.3.4	Enzyme-surface interactions .....	50
2.5.3.5	Enzyme-ligand interactions .....	51
CHAPTER 3	Selection of the system of study .....	53
3.1	Type of Support .....	53
3.1.1	Porous support materials .....	54
3.1.2	Metal-oxide-based supports .....	56
3.1.2.1	Silica .....	56
3.1.2.2	Alumina .....	58
3.1.3	Oxirane functional polymers .....	60
3.1.3.1	Eupergit® .....	60

3.2	Enzyme.....	61
3.2.1	$\alpha$ -Chymotrypsin.....	62
3.2.1.1	General features of structure and action.....	62
3.2.1.2	Conventional mechanism.....	65
3.2.1.3	Catalytic components.....	66
3.2.1.4	NMR observation of active site $^1\text{H}$ signals.....	68
3.2.2	Enzyme interactions.....	71
3.2.2.1	Water.....	71
3.2.2.2	Ions.....	72
3.2.2.3	Inhibitors.....	74
3.3	Method of Immobilisation.....	82
3.3.1	Functionalisation of metal-oxide-based supports.....	82
3.3.1.1	Oxirane functional metal-oxide-based supports.....	84
3.3.2	Mechanism of covalent binding via epoxide groups.....	85
CHAPTER 4 Experimental.....		87
4.1	Quantification of Epoxide Groups.....	87
4.1.1	Preparation of reagents.....	88
4.1.2	Procedure.....	88
4.2	Protein Analysis.....	89
4.2.1	Preparation of reagents.....	90
4.2.2	Procedure.....	90
4.3	Immobilised Protein Determination.....	91
4.4	Enzyme Activity Determination.....	91
4.4.1	Preparation of reagents.....	91
4.4.2	Procedure.....	92
4.5	Immobilisation Procedure.....	92
4.5.1	Activation of Support.....	93
4.5.1.1	Synthesis of epoxide-activated silica.....	93
4.5.1.2	Synthesis of epoxide-activated alumina.....	93

4.5.2	Covalent Binding of the Enzyme .....	94
4.5.2.1	Procedure .....	94
4.6	Sample storing.....	96
4.7	Nuclear Magnetic Resonance.....	96
4.7.1	Solution-State .....	96
4.7.2	Solid-State with Magic Angle Spinning.....	97
CHAPTER 5 Structural Characterisation of the Immobilised Enzyme and its Supports .....		98
5.1	Experimental details.....	98
5.1.1	NMR experiments .....	98
5.1.2	Sample preparation.....	99
5.2	Characterisation of the Supports .....	99
5.2.1	Bare silica .....	99
5.2.2	Bare alumina .....	101
5.3	Characterisation of the Immobilised Enzymes.....	105
5.3.1	Epoxide-silica .....	105
5.3.2	Epoxide-alumina .....	115
5.3.3	Eupergit® .....	123
5.4	Discussion .....	129
5.5	Conclusions .....	131
CHAPTER 6 Quadrupolar Relaxation Studies of Immobilised Enzymes.....		133
6.1	Experimental details.....	135
6.1.1	NMR experiments .....	135
6.1.2	Sample preparation.....	135
6.2	The Triple-Quantum Filter Experiment for $^{23}\text{Na}$ (Spin $I = 3 / 2$ ).....	136
6.2.1	TQF $^{23}\text{Na}$ NMR relaxation study of sodium ions with immobilised chymotrypsin .....	139
6.3	Four-Quantum and Five-Quantum Evolution Experiments for $^{17}\text{O}$ -labelled(Spin $I = 5 / 2$ ).....	144
6.3.1	An $^{17}\text{O}$ multiple-quantum NMR relaxation study of water dynamics and interactions with immobilised chymotrypsin .....	148

6.4	Discussion .....	152
6.5	Conclusions .....	154
CHAPTER 7 Enzyme-Inhibitor Interaction Studies in Solution and in Solid State.....		156
7.1	Experimental details.....	158
7.1.1.1	NMR experiments.....	158
7.1.1.2	Sample preparation.....	159
7.2	Solution-state NMR studies of the free enzyme .....	160
7.3	Interactions with potassium 4-fluorophenyl trifluoroborate .....	162
7.3.1	Solution-state NMR studies of the free enzyme in presence of PFPTB.....	162
7.3.2	Solid-state NMR studies of the the immobilised enzyme in presence of PTPTB .....	169
7.4	Interactions with (R)-1-acetamido-2-(4-fluorophenyl)ethane-1-boronic acid.....	171
7.4.1	Solution-state NMR studies of the free enzyme in presence of AFEB.....	171
7.4.2	Solid-state NMR studies of the immobilised enzyme in presence of AFEB.....	178
7.5	Discussion .....	179
7.6	Conclusions .....	181
CHAPTER 8 Summary .....		183
Bibliography .....		222

## CHAPTER 1

# Introduction

Enzymes, as catalysts, possess the astonishing characteristic of allowing product formation in mild and environmentally friendly conditions with a high specificity. Because of their excellent functional properties (activity, selectivity and specificity) enzymes are capable of catalysing most chemical reactions promptly and in mild conditions [4].

Enzymes have been modified during evolution to optimise their behaviour in living cells. Clearly, the enzymes have not been optimised through evolution to be used as catalysts in industry, therefore many of their properties are not best suited for this purpose. They are soluble, unstable at conditions which differ from physiological ones, are frequently inhibited by substrates and products, and have narrowed substrate specificity.

In most cases it is possible to improve their properties for use as industrial biocatalysts through the engineering of enzymes involving different techniques such as the screening of new enzymes, molecular biology, immobilisation and post-immobilisation, and improvement via reaction and reactor engineering.

For technical and economic reasons, many chemical processes catalysed by enzymes require continuous use or reuse of biocatalysts for a very long time [5-7]. In this context, the immobilisation of enzymes proves to be a strong technique to promote the reuse or continuous use in industrial biocatalysis and therefore improves cost-effectiveness, as well as providing a powerful approach to stabilisation [8].

Since the advent of immobilisation of single enzymes in the 1940s, innumerable methods have been developed. Despite extensive study on different systems there is no clear approach for a given process and enzyme. One reason for this is that little is known about the state of protein molecules in the preparation except, of course, what is deduced from its catalytic activity.

Enzymes, being proteins, possess an inherent flexibility in different environmental conditions. The structure and flexibility of enzymes affects their functionality due to proteins not occupying one structure, rather they are more accurately described by an equilibrating set of time-dependent structures [8].

Figure 1.1 shows a general scheme highlighting the complexity of an immobilised enzyme system. However, much of the detail of the state of the enzyme molecules is speculative, though the use of high resolution techniques should help confirm the detail in the future.

With the purpose of evaluating the dynamic aspects of the protein, structural biology has become a powerful tool for visualising biological processes in space and time at atomic resolution. This tool gathers a group of techniques including X-ray crystallography, electron microscopy and solution-state nuclear magnetic resonance (NMR). Recently, other techniques have been incorporated, all seeking to investigate biological material in its non-crystalline native state, such as small-angle X-ray scattering, electron tomography, femtosecond X-ray and solid-state magic angle spinning nuclear magnetic resonance (solid-state MAS NMR) [9].

The great utility of NMR lies in its unique selectivity where different sites are clearly identified by distinct chemical shifts. Also it is an excellent source of information describing connectivity between different nuclei via scalar and dipolar coupling. NMR is nowadays an established tool in the field of structural biology, and provides insight into molecular interactions and macromolecular structure that is barely attainable by other techniques such as crystallography. The application of NMR to

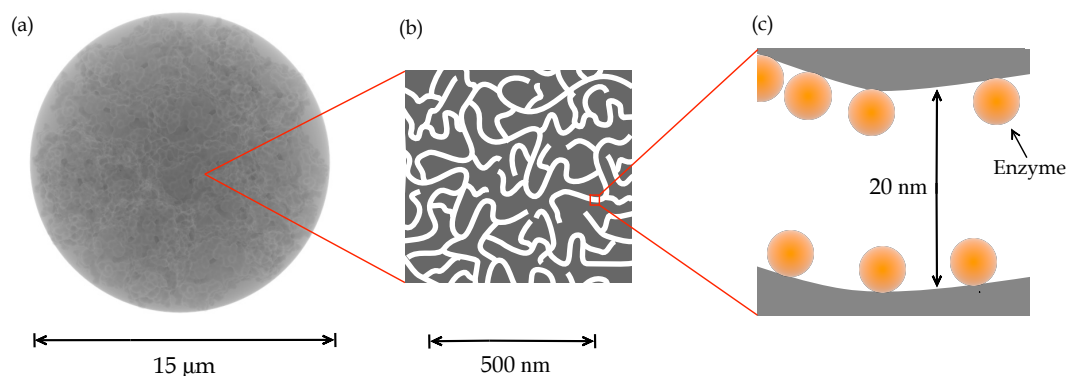


**Figure 1.1. Diagram of immobilised enzyme on a porous support. (a) Single particle of porous support, (b) magnified interior slice of porous support particle and (c) magnified pore region. The diagram shows a support particle of 15 μm of diameter (Figure 1.1a) and a pore size of 20 nm (Figure 1.1b). The diameter of the enzyme molecule in Figure 1.1c is around 5 nm.**

materials in solid form developed at a slower rate than its counterpart for the solution state. This situation arises principally because of an overload of information from dipolar and quadrupolar interactions that generally are negligible in solution state but can diminish the resolution of distinct sites in the solid state. On the other hand, these interactions contain valuable structural and dynamic information. The nature of the sample and the multiple anisotropic NMR interactions are some of the reasons that solid-state NMR is a relatively challenging technique to master. One of the crucial steps in the use of this technique is finding the right approach to refine the information content [10]. However, the work of several research groups in the field of solid-state NMR over the last 15 years has clearly proved its capabilities in the study of biological systems not accessible by either X-ray crystallography or solution-state NMR – for example, insoluble heterogeneous biological systems such as membrane proteins [11].

As mentioned previously, little is known about the protein state in the preparation, and owing to this lack of knowledge it is not possible to achieve the immobilisation of enzymes in a more rational way. Consequently the study of heterogeneous

enzyme systems via solid-state MAS NMR becomes an appropriate approach and an entirely novel one with the aim of studying the protein state.

This thesis has the general objective to achieve a better understanding of the behaviour of immobilised enzymes by solid-state MAS NMR. Our general aim is to establish if solid-state NMR can help to characterise these systems. A particular focus is to see if it is at all possible to use NMR techniques (both solid-state and solution-state methods adapted to hybrid solid-liquid samples) to obtain information about the interaction of the protein molecules with ions, water molecules and inhibitors.

Although widely used in both solution- and solid-state NMR studies of protein structure, the use of isotopically-labelled enzymes (e.g., with enrichment of  $^{13}\text{C}$  or  $^{15}\text{N}$ ) is not envisaged in this work, though such enrichment would make acquisition of the NMR data easier. Potentially, the methods proposed here can be applied diagnostically to immobilised enzymes developed by others, both in industry and academia. These will of course not be isotopically labelled and these potential users will have little interest in our methods if they first have to manufacture labelled proteins, then repeat the immobilisation. In many industrial cases our methods might be considered for application to immobilised derivatives made on a large scale (even tons), where a repeat with labelled material would be inconceivable.

Because of the multidisciplinary nature of this thesis some background topics have not been covered in detail. It is assumed that the reader is familiar with some basic NMR knowledge that can be found in Reference [12].

Chapter 2 introduces the NMR phenomenon and the theoretical framework upon which the experiments described in the later chapters are based. Solution- and solid-state NMR concepts, applied in this thesis, are treated separately in this chapter. A separate section of this chapter is dedicated to introduce the immobilisation of enzymes, describing the elements involved in the process.

In Chapter 3, the systems of study are introduced, discussed and defined. The supports and enzyme are reviewed. A detailed consideration of the enzyme selected for the present study -  $\alpha$ -chymotrypsin - is included here. This is followed by a review of some interesting interactions between this enzyme and ligands.

Chapter 4 introduces the experimental protocols for the evaluation of the systems of study. Biochemical protocols for the quantification of functional groups involved in the immobilisation, immobilised protein and enzymatic activity are described. The procedure of immobilisation on different supports is included here. Finally, a section describing the experimental NMR details is presented.

Chapter 5 presents the characterisation of the covalent immobilisation of  $\alpha$ -chymotrypsin on functionalised silica and alumina particles (glycidoxypropyltrimethoxysilane, GOPS, grafted onto the surface) and Eupergit® (rigid methacrylic cross-linked polymer bearing pendant epoxide groups) by  $^1\text{H}$ ,  $^{13}\text{C}$  and  $^{29}\text{Si}$  magic angle spinning (MAS) NMR. Also relevant results from analytical techniques unrelated with NMR are included in this chapter.

In Chapter 6, multiple-quantum  $^{23}\text{Na}$  ( $I=3/2$ ) and  $^{17}\text{O}$  ( $I=5/2$ ) MAS NMR experiments are used to measure transverse relaxation for quadrupolar nuclei in immobilised enzymes systems. A brief description of the theoretical and experimental principles behind multiple-quantum experiments with the purpose of measuring relaxation is introduced. These studies focus in examining the behaviour of sodium ions ( $^{23}\text{Na}$ ) and isotopically enriched water ( $\text{H}_2^{17}\text{O}$ ) associated with immobilised enzymes.

Chapter 7 presents an experimental  $^1\text{H}$  and  $^{19}\text{F}$  NMR investigation of two fluorinated inhibitors interacting with  $\alpha$ -chymotrypsin. These two inhibitors are potassium 4-fluorophenyl trifluoroborate (PFPTB) and (R)-1-acetamido-2-(4-fluorophenyl)ethane-1-boronic acid (AFEB). Both

enzyme-inhibitor complexes were firstly analysed by solution-state NMR (using free enzyme) and then by solid-state NMR for the immobilised enzyme.

Finally, although Chapter 5 to Chapter 7 each has a Discussion and Conclusions Section where the limitations of the approaches used and future work are identified, Chapter 8 summarises and discusses the most important findings in the thesis and makes recommendations for future research directions.

## CHAPTER 2

# Theoretical background

### 2.1 Methods in structural biology for proteins

Crystallisation of biological macromolecules and their subsequent structure determination by X-ray scattering techniques remain the foundation for much of structural biology. This is reflected in the Protein Data Bank, which holds over 100000 structures of proteins, nucleic acids and their complexes, with around 90% of these having been obtained by X-ray crystallography and the rest by NMR spectroscopy. Very few structures have been obtained by other methods, such as electron microscopy.

However, there are limitations to using X-ray crystallography. These include difficulties in protein crystallisation owing to limited solubility and unresolved protein dynamics [13]. Solubility is a key bottleneck in macromolecular X-ray crystallography because many systems are anchored to the cell membrane or/and insoluble.

Recent advancements in cryo-electron microscopy (cryo-EM), which allow structure determination with near-atomic resolution (higher than 3.5 Å) [14], provide an alternative approach for determining macromolecular structure without crystallisation and, although still requiring sample homogeneity, are less dependent

on issues of solubility [15]. Solid-state NMR methods for biological macromolecules provide another approach for determination of insoluble protein structures [16].

As the majority of X-ray crystal structures of proteins are modelled as single conformation in crystalline environments, the dynamical information is limited. Dynamics are often indirectly addressed by X-ray crystallography by theoretical estimates of uncertainty in atomic positions using B-factors that measure primarily molecular disorder in the crystal in addition to thermal motion [17, 18]. NMR is able to provide detailed information about the dynamics of the molecules studied. The use of NMR data for evaluating conformational dynamics, especially around substrate binding sites, is of particular interest for examining protein interactions [19].

Over the last few years, the application of solid-state NMR to heterogeneous protein systems has made tremendous progress, showing the capability of the method for determining structures and studying ligand binding and insoluble protein dynamics over a variety of time scales at atomic resolution [16]. Electron paramagnetic resonance (EPR) also provides additional information about different conformation states on insoluble protein systems [20].

Immobilised enzymes are composite materials, with a biological and an inorganic (or organic polymer) component. They are inherently non-crystalline and so lack long-range order. Hence they cannot be very usefully studied by diffraction based methods. Solid-state NMR can be applied to these systems as the method does not require long-range order in the sample. However, the intention of this thesis is not trying to determine the three-dimensional structure of the protein immobilised. Protein structure determination is a long-term aim of the project.

## 2.2 Nuclear magnetic resonance (NMR)

Matter is made of atoms. Atoms are made up of electrons and nuclei. Some important physical properties of the atomic nucleus are mass, electric charge, magnetism and spin. Nuclear magnetism and nuclear spin have almost no effect on the normal chemical and physical behaviour of substances. Nevertheless, these two properties provide scientists with a wonderful tool for “spying on” the microscopic and internal structures of objects without disturbing them [21].

In a general sense nuclear magnetic resonance exploits the magnetic interaction of atomic nuclei nuclei with an external magnetic field. This phenomenon was first reported in 1946 [22, 23].

### 2.2.1 Fundamentals

Any nucleus that has a magnetic moment can interact with a magnetic field therefore can be studied by NMR. Nuclei with spin angular momentum quantum number  $I \geq 0$  can be found in  $2I+1$  spin states and possess a nuclear magnetic dipole moment,  $\mu$  of magnitude

$$|\mu| = \gamma \hbar [I(I+1)]^{1/2} \quad 2.1$$

where  $\gamma$  is the gyromagnetic ratio of the nucleus,  $\hbar$  is the Planck constant and  $I$  is the spin quantum number. The spin quantum number  $I$  of a nucleus may have one of following values:

$$I = 0, \frac{1}{2}, 1, \frac{3}{2}, 2, \dots, \quad 2.2$$

The degeneracy of the spin states may be lifted through the Zeeman interaction with an external magnetic field. The energy of a state is then given by

$$E_{m_I} = -\gamma m_I \hbar B_0 \quad 2.3$$

where  $B_0$  is the magnetic field and  $m_I$  is the spin orientation quantum number and has  $2I+1$  values in integral steps between  $+I$  and  $-I$ :

$$m_I = I, I-1, I-2, \dots, -I+1, -I \quad 2.4$$

The spin magnetisation may exist in two types of states depending on the value of  $\Delta m_I$ , which is known as the coherence order and denoted by the symbol  $p$ . States with  $p=0$  are populations of energy levels, while coherent superpositions between the energy levels, termed coherences, are characterised by  $p>0$ . Depending on the number of energy levels between which the state of coherence occurs, coherences are known as single-quantum coherences ( $p=\pm 1$ ), double quantum coherences ( $p=\pm 2$ ) and so on.

Observable transitions between spin states are given by the selection rule  $\Delta m_I = \pm 1$ , resulting in resonance frequencies and energies of

$$\omega_0 = \frac{\Delta E}{\hbar} = -\gamma B_0 \quad 2.5$$

where  $\omega_0$  is called the Larmor frequency (written here in units of  $\text{rad s}^{-1}$ ) and  $\Delta E$  the energy gap.

A selection of some nuclides is given in Table 2.1, where  $\nu_0$ , defined as the frequency of the nucleus in Hz,

$$\nu_0 = \omega_0 / 2\pi \quad 2.6$$

has been calculated for a 9.4 T field using Equation 2.5.

When  $B_0$  is applied, various populations of magnetic nuclei are found in the  $2I+1$  states according to the Boltzmann distribution,

**Table 2.1. Properties of some important nuclides at 9.395 T.**

Nuclides	$I$	$\gamma / 10^7 \text{ T}^{-1} \text{ s}^{-1}$	$\nu_0 / \text{MHz}$	Natural abundance (%)
$^1\text{H}$	1/2	26.75	400	99.985
$^2\text{H}$	1	4.11	61.4	0.015
$^{10}\text{B}$	3	2.87	42.9	19.9
$^{11}\text{B}$	3/2	8.58	12.8	80.1
$^{12}\text{C}$	0	-	-	98.9
$^{13}\text{C}$	1/2	6.73	100.6	1.108
$^{14}\text{N}$	1	1.93	28.9	99.63
$^{15}\text{N}$	1/2	-2.71	40.5	0.37
$^{16}\text{O}$	0	-	-	99.762
$^{17}\text{O}$	5/2	-3.63	54.3	0.037
$^{19}\text{F}$	1/2	25.18	376.5	100
$^{23}\text{Na}$	3/2	7.08	105.84	100
$^{29}\text{Si}$	1/2	-5.32	79.6	4.7
$^{31}\text{P}$	1/2	10.84	162.1	100

$$\frac{N_{\text{upper}}}{N_{\text{lower}}} = e^{\frac{-\Delta E}{kT}} \quad 2.7$$

where  $N$  represents the population of either of two non-degenerate levels (upper and lower states),  $k$  is the Boltzmann constant and  $T$  is temperature.

The fundamental principle governing the NMR technique centres on the induction of transitions between different energy states or Zeeman levels of a particular nucleus. In NMR spectroscopy, an electromagnetic field excites nuclei from a lower energy level to upper energy level (and vice versa). To cause these transitions, a variable radiofrequency field (RF), referred to as  $B_1$ , acts perpendicular to the applied magnetic field ( $B_0$ ). When the frequency of the applied RF is close to the precessional

frequency ( $\omega_0$ ) of the nuclei observed, transitions between nuclear spin states occurs. Upward and downward transitions occur with the same probability and so the net signal strength is proportional to the population difference between the two levels involved. This means that the NMR technique generally only detects one nucleus in every  $10^4$ - $10^6$ . The use of strong magnetic fields helps to increase signal strength by increasing the energy gap ( $\Delta E$ ) and thus increasing the population difference between states at equilibrium. Similarly, nuclei with large  $\gamma$  and a high abundance in nature will yield greater signals (see Table 2.1) [12].

### 2.2.2 Internal interactions

The Zeeman effect (see Section 2.2.1), responsible for lifting the degeneracy of the energy levels of the nucleus, is usually by far the largest contribution to the energy terms arising from the interaction of the spins in the magnetic field. Also, as discussed above, the fluctuating magnetic fields arising from RF radiation give rise to small perturbations in the energy and so cause transitions. The remaining interactions, which are all intrinsic to the sample and are orientation dependent, contribute with important chemical information about the system. In this section, four of these interactions will be briefly discussed.

#### 2.2.2.1 Chemical shift interaction

When a molecule is placed in a magnetic field, the nuclei are magnetically shielded by the presence of electrons, resulting in a shielding field. The circulation of electrons in their atomic or molecular orbits produces an induced magnetic field  $B_{\text{in}}$  that may either augment or oppose the external field. The effective field  $B$  at the nucleus is then

$$B = B_0 - B_{\text{in}} = B_0(1 - \sigma) \quad 2.8$$

where  $\sigma$  is the shielding constant, modifying the Larmor frequency defined in Equation 2.5 to

$$\omega = |\gamma B_0| (1 - \sigma) \quad 2.9$$

Shielding leads to the well known phenomenon of chemical shift. The shielding constant,  $\sigma$ , is an inconvenient measure of the chemical shift. Therefore, it is a common practice to define the chemical shift in terms of the difference in resonance frequencies between the nucleus of interest  $\nu$  and a reference nucleus  $\nu_{\text{ref}}$  to give

$$\delta = 10^6 \frac{(\nu - \nu_{\text{ref}})}{\nu_{\text{ref}}} \quad 2.10$$

where  $\delta$  is a dimensionless parameter that represents the chemical shift.

The chemical shift has been one of the most important sources of information in NMR, allowing chemical structures to be determined.

The fact that the electrons are not spherically distributed around the nucleus gives to the shielding field an anisotropic character. The observed chemical shift in an NMR spectrum,  $\delta$ , is the sum of the isotropic and anisotropic components:

$$\delta = \delta_{\text{iso}} + \frac{1}{2} \Delta_{\text{CS}} (3 \cos^2 \vartheta - 1 + \eta_{\text{CS}} \sin^2 \vartheta \cos 2\phi) \quad 2.11$$

where  $\delta_{\text{iso}}$  is the isotropic chemical shift,  $\Delta_{\text{CS}}$  the chemical shift anisotropy,  $\eta_{\text{CS}}$  is the chemical shift asymmetry, and  $\vartheta$  and  $\phi$  are angles that define the orientation of the  $B_0$  field with respect to the main principal axis of the chemical shielding tensor (further details about the shielding tensor can be found in reference [10]).

The rapid tumbling motion of molecules in the solution state is responsible for averaging out the anisotropic contribution of the chemical shift to zero. In solids, the

anisotropic chemical shift often plays a large part in determining the characteristic width and shape of the NMR spectrum.

### 2.2.2.2 The dipolar interaction

Since each nuclear spin is magnetic, it generates a magnetic field, looping around in the surrounding space. A second nuclear spin can interact with this magnetic field, while the first nuclear spin also experiences the field generated by the second nuclear spin. This interaction is called direct dipole-dipole coupling. Dipolar coupling is a through-space interaction that provides an important route to understanding correlations between spins. This interaction may be either intramolecular or intermolecular.

In solids the dipolar interaction is a significant broadening mechanism. A pair of dipolar-coupled spins will yield a distinctive “Pake doublet” lineshape. As the interaction is anisotropic, the splitting between lines will vary according to crystallite orientation. A typical powder sample will contain many randomly-orientated crystallites: each of these will give rise to a different splitting and the overall spectrum will consist of all these contributions. For this reason, coupled with the fact that usually more than two spins will be coupled to each other, the solid-state spectrum will have a broad lineshape.

Unlike the chemical shift interaction, the dipolar coupling interaction is averaged to zero by rapid tumbling of molecules in solution. However, it contributes to relaxation processes (see Section 2.2.3) and is important in experiments involving the nuclear Overhauser effect (NOE) (see Section 2.2.6.3).

### 2.2.2.3 J-coupling

J-coupling, also known as scalar coupling, is a through-bond interaction between two nuclei. Electrons perturbing the nuclear spins mediate this interaction. The effect of

this perturbation is observed in NMR spectra as splitting patterns (e.g., if two non-equivalent spins  $I=1/2$  are scalar coupled, the spectrum of each will present a doublet and the separation between the two components will represent the characteristic coupling constant). These patterns can assist in determining molecular structure in solution state. In solids, the J-coupling is usually much smaller than other interactions; consequently resolved J-coupled multiplets are not a common feature of spectra.

### 2.2.2.4 The quadrupolar interaction

Nuclei with  $I \geq 1$  have an electric quadrupole moment,  $eQ$ , that interacts strongly with the electric field gradient (EFG) generated by the surrounding electron density. This effect arises from the non-spherical distribution of the charge in the nucleus, where this distribution can be described as a series of multipoles. In contrast, a spin  $I=1/2$  nucleus only has electric monopole and magnetic dipole components and thus would not have any orientation dependence in the same field gradient.

The magnitude of the interaction between the nuclear quadrupole moment and the EFG is expressed as  $C_Q$

$$C_Q = \frac{e^2 q Q}{\hbar} \quad 2.12$$

where  $q$ , the magnitude of the EFG is given by

$$q = \frac{V_{ZZ}}{e} \quad 2.13$$

where  $V_{ZZ}$  is the strongest principal component of the EFG and  $e$  is the electric charge.

Quadrupolar coupling produces splittings in NMR spectra of single crystals and gives rise to broad lines for powders and disordered solids. This anisotropic interaction also causes spin relaxation when modulated by molecular tumbling.

### 2.2.3 Relaxation

According to Bloch, a macroscopic sample containing many identical-non-interacting spins can be considered classically in terms of a bulk magnetisation vector in three dimensional space, providing a simple geometrical insight into the NMR experiment. In an ensemble of spin  $I = 1/2$  nuclei at thermal equilibrium in a magnetic field, there is a population difference between the spin states according to the Boltzmann distribution given by Equation 2.7. This gives rise to a stationary net magnetisation where the vector aligns with the magnetic field  $B_0$  along the z axis, with no xy component at equilibrium.

During the NMR experiment the bulk magnetisation will experience a tendency to revert to its equilibrium situation. The process of regaining equilibrium over a period of time is known relaxation. In NMR there are three important modes of relaxation:

- a) Spin-lattice relaxation (or longitudinal relaxation) causes the component of the bulk magnetisation along z-axis to return to its equilibrium. For homogeneous solid samples, this process is generally exponential with a relaxation time constant  $T_1$ .
- b) Spin-spin relaxation (or transverse relaxation) causes the decay of the magnetisation in the x-y plane. In general, for solids, transverse relaxation is unlikely to be single exponential with a relaxation time constant  $T_2$ .
- c) Spin-lattice relaxation in the rotating frame describes the return to equilibrium of transverse magnetisation in the presence of spin-locking from an RF

magnetic field, where values of relaxation time constant  $T_{1\rho}$  in cross-polarisation experiments.

For quadrupolar nuclei ( $I > 1/2$ ), the rates of longitudinal and transverse relaxation are, commonly, not single exponential functions.

The dominant cause of relaxation is the fluctuation in the local field at the excited nucleus. Molecular motion generally causes this fluctuation and can be characterised by a time correlation function

$$G(t) \propto e^{-\frac{t}{\tau_c}} \quad 2.14$$

where  $\tau_c$  is the correlation time and is the time constant that characterises the motion in question.

The Fourier transform of the correlation function (Equation 2.15) is called the spectral density

$$J(\nu) \propto \int_{-\infty}^{\infty} G(t) e^{-i2\pi\nu t} dt \quad 2.15$$

where  $\nu$  is frequency. Spectral density can be written in terms of correlation time dependence as

$$J(\nu) = \frac{2\tau_c}{1+(2\pi\nu\tau_c)^2} \quad 2.16$$

The expression above allows two motional regimes to be identified. The first one is the *extreme narrowing condition* where  $2\pi\nu\tau_c \ll 1$  then  $J(\nu) \approx 2\tau_c$  and the relaxation rates are proportional to  $\tau_c$ . This regime applies for fast molecular motion. The second is the *rigid lattice limit* where  $2\pi\nu\tau_c \gg 1$  so that  $J(\nu)$  becomes proportional to  $\tau_c^{-1}$  (and so do the relaxation rates) and applies to slow motions. The latter regime is of

interest for quadrupolar nuclei because it is here that multi-exponential relaxation is observed (Chapter 6).

## 2.2.4 Fourier Transform NMR

For many years the main technique for recording NMR spectra was continuous wave (CW) NMR [23]. This technique involves sweeping the applied magnetic field,  $B_0$ , or frequency,  $\omega_{rf}$ , and observing each transition as it comes into resonance. The main disadvantage of CW NMR is the long time required to record a single spectrum. This method has been superseded by Fourier transform NMR [24] in which pulses are used to induce a precessing magnetisation. The resulting precession of bulk magnetisation induces a voltage in the receiver coil. This current is the time-domain NMR signal, known as the free induction decay (FID), which arises as the result of the superposition of many oscillating waves of differing frequencies, amplitudes, phases and decay constants.

The time-domain signal of a single frequency  $\Omega$  can be written,

$$s(t) = C \exp(i\Omega t) \exp(-t/T_2) \exp(i\phi) \quad 2.17$$

where  $C$  is an overall scaling factor,  $\exp(-t/T_2)$  accounts for the relaxation and  $\exp(i\phi)$  is an arbitrary phase factor dependent on instrumental influences.

The free induction decay is converted into a spectrum in the normal frequency domain by calculation of its Fourier transform. This transformation is given by [24]

$$S(\omega) = \int_0^{\infty} s(t) \exp(-i\omega t) dt \quad 2.18$$

The time-domain signal  $s(t)$  is converted to a the frequency-domain spectrum  $S(\omega)$ .

In practice, the FID decays to zero from relaxation processes ( $T_2 \neq \infty$ ) and the resulting spectrum comprises a real and an imaginary component assuming  $\phi = 0$ ,

$$S(\omega) = A(\Delta\omega) - iD(\Delta\omega) \quad 2.19$$

where

$$A(\Delta\omega) = \frac{\frac{1}{T_2}}{\left(\frac{1}{T_2}\right)^2 + (\Delta\omega)^2} \quad 2.20$$

$$D(\omega) = \frac{\Delta\omega}{\left(\frac{1}{T_2}\right)^2 + (\Delta\omega)^2} \quad 2.21$$

represent absorptive and dispersive Lorentzian functions. Here,  $1/T_2$  is the decay rate constant in  $\text{rad s}^{-1}$  for transverse relaxation. The frequency offset  $\Delta\omega = \omega - \Omega$  is measured with respect to the centre of the resonance,  $\Omega$ . The real part,  $A(\Delta\omega)$ , of the spectrum contains absorptive Lorentzian lineshapes centred on frequency  $\Omega$  with a full-width at half-height equal to  $2/T_2$  (measured in  $\text{rad s}^{-1}$ ) while the imaginary part,  $D(\Delta\omega)$ , is the corresponding dispersive Lorentzian (see Figure 2.1). In practice these lineshapes are not purely absorptive or dispersive if  $\phi \neq 0$ , and so a “phase correction” is applied by taking linear combinations of the two lineshapes.

### 2.2.5 Instrumentation

A simple NMR experiment consists of a sequence of four events: initialisation, excitation, detection and finally processing and display. In the first event, before the experiment starts, the computer sends instructions to the pulse generator and to the RF (radiofrequency) generator, setting up the reference frequency, the sampling frequency and the number of sampled points, etc. (see Figure 2.2). Secondly, sample excitation occurs, where the pulse generator executes a timed sequence of

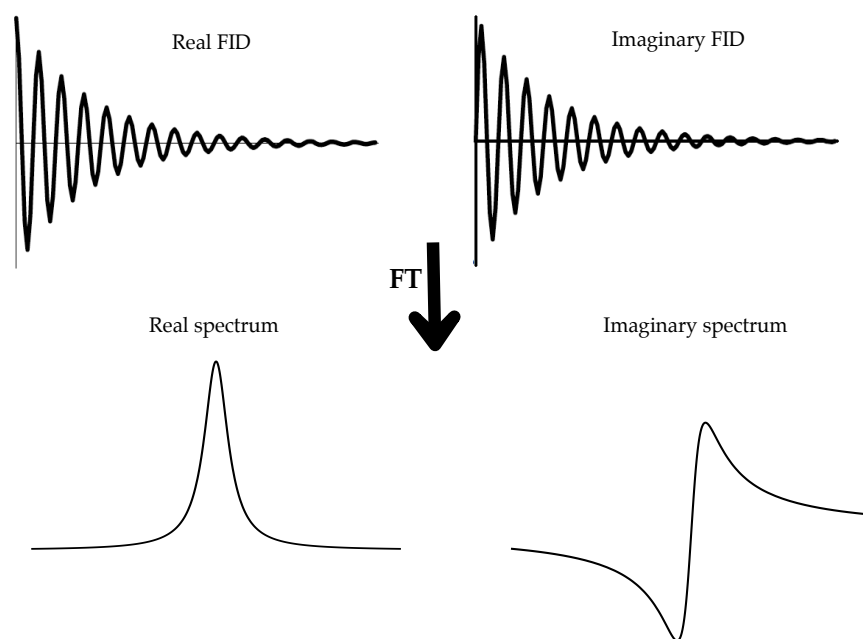


**Figure 2.1. A complex Fourier transform (FT) performed on the real and imaginary components of an exponentially decaying FID results in absorptive and dispersive Lorentzian lineshape, respectively.**

instructions to set the phase of the RF generator and open the switch. An RF pulse travels into the probe from RF amplifier.

Following this, the pulse is switched off and detection starts. The precession of the nuclear spin magnetisation sets up oscillations in the tuned circuit, which gives rise to a radiofrequency NMR signal (the free induction decay, FID). The free induction decay (FID) is the observable time-domain NMR signal generated by non-equilibrium nuclear spin magnetisation precessing about the magnetic field.

This signal is amplified by a RF amplifier, and converted down in frequency by the quadrature receiver (detector), and then the pulse generator issues an instruction to the ADC (analogue to digital converter), which proceeds to digitise receiver outputs.

Finally, the digitised time-domain signal stored in the computer memory is subjected to various mathematical operations or processing such as Fourier transform. Fourier transform (FT) turns a time-domain signal, the FID, into a frequency-domain signal

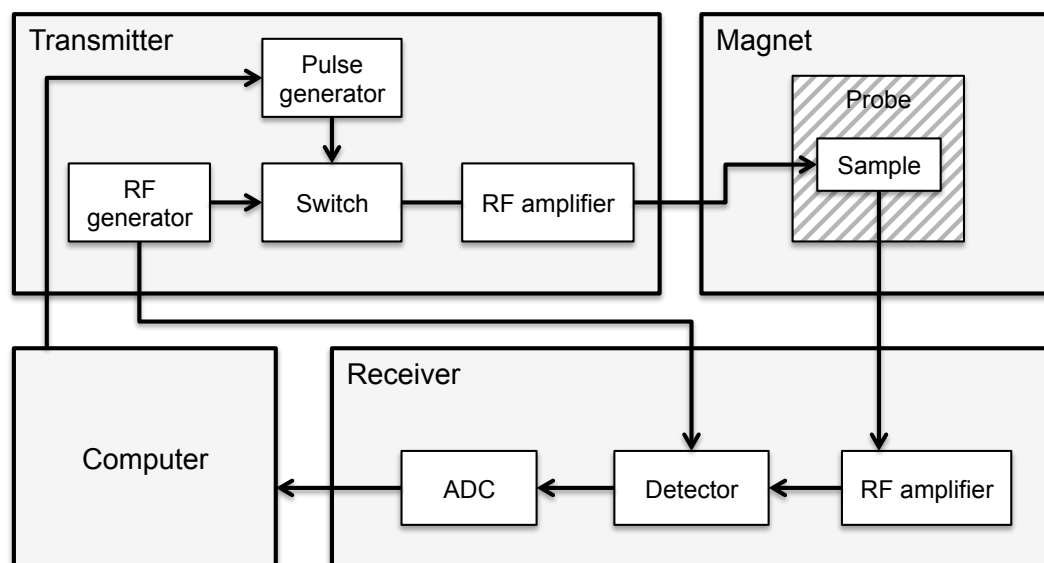


**Figure 2.2. Main components of an NMR spectrometer**

(see Section 2.2.4). Subsequently the NMR spectrum may be displayed on the computer screen to be processed by a user [21].

## 2.2.6 Solution-state NMR

The purpose of this section is to give an introductory insight into some important concepts used in solution-state NMR that are applied principally in Chapter 7.

### 2.2.6.1 The spin echo

An NMR signal will decay after an excitation pulse owing to effects that cause different spins in a sample to precess at different frequencies. Two factors are responsible: spin-spin relaxation induced by intra- or intermolecular magnetic fields and the spatial inhomogeneity of the static  $B_0$  field. In solution-state NMR, this dephasing can result principally from the latter reason; an inhomogeneous  $B_0$  field, where different volumes of the sample will have different precession frequencies according to the field they experience. It is a very common practice in NMR experiments to insert a pulse sequence into periods of free precession to refocus the

precession arising from  $B_0$  inhomogeneity. Usually this is done by the use of a spin-echo pulse sequence. The most popular sequence is the Hahn or Carr-Purcell echo,  $90^\circ - \tau - 180^\circ$ , where a  $90^\circ$  pulse is used to excite single-quantum coherence. A  $180^\circ$  pulse is applied after duration  $\tau$ . After a further period of free precession of duration  $\tau$  a spin echo is formed.

### 2.2.6.2 Water suppression

The presence of high concentration of solvent (molar range) compared to low concentration of solutes in NMR samples (millimolar to micromolar range) is a common problem in  $^1\text{H}$  experiments. This situation leads to a variety of problems such as overlapping resonances of interest by the intense solvent signal and saturation of the NMR receiver causing poor quality spectra. When desirable, the use of deuterated solvents instead of protonated ones is a simple solution to reduce solvent resonances. However, this method is not generally applicable for protein samples, in which protonated solvent (e.g., water) is required for the observation of exchangeable protons (e.g., amide protons). The last four decades has seen a progressive technique development to undertake solvent suppression to meet demanding requirements. Of all the pulse sequence suppression methods, the frequency differentiation-based methods are the most versatile [25]. Frequency differentiation methods are based on selective excitation and/or inversion with/without the application of pulsed magnetic gradients. The most prevalent frequency differentiation methods are:

- a) Pre-saturation. Pre-saturation related suppression methods are based on the selective saturation of the solvent resonances by a low-power selective RF pulse on the solvent resonances. One of the main drawbacks of pre-saturation related methods is when signals that resonate very close to the solvent signal may be partially saturated by the RF field applied [25].

b) WATERGATE and excitation sculpting. The WATERGATE (WATER suppression by Gradient-Tailored Excitation) technique [26] relies on a selective spin-echo pulse (which inverts all the resonances except the solvent resonances) flanked by two symmetrical pulsed field gradients (PFGs). This method evolved from the realisation that echo techniques provided superior phase properties compared with conventional selective phase properties [27]. However, one of the difficulties with a gradient echo is spectral phase distortion because the phase of the magnetisation is affected by the phase properties of the spin-echo pulse. This difficulty is overcome by applying a Double Pulsed Field Gradient Spin Echo (DPFGSE) first proposed by Hwang and Shaka [28] under the name *Excitation Sculpting*. It turns out that the phase of the magnetisation excited by this sequence is independent of the phase properties of the spin-echo's pulses [29].

### 2.2.6.3 Nuclear Overhauser Effect

All substances possess a variety of internal spin interactions: chemical shift terms (one-spin), quadrupolar couplings, J-couplings (two-spin), spin-rotation interactions (one-spin) and dipole-dipole couplings (two-spin). The study of the through-space dipole-dipole couplings of spin pairs in a molecule can tie down the molecular structure and conformation unambiguously where these couplings may be either intramolecular or intermolecular [21]. Dipolar couplings do not usually produce observable splittings in solution NMR spectra because they are averaged to zero by rapid tumbling of a molecule.

A remarkable phenomenon known as the nuclear Overhauser effect (NOE) [30] can provide us with information about these dipole-dipole interactions. This effect may be defined as the change in intensity of one resonance when the spin transitions of another are perturbed from their equilibrium populations, usually by saturation or by population inversion.

The most simple system to understand the origin of the NOE is a two homonuclear spin  $I=1/2$  system. Consider that both nuclei do not possess scalar coupling but are sufficiently close in space to share a dipolar coupling. Six possible spin-lattice relaxation pathways can be identified for a two-spin system (Figure 2.3). Four of these correspond to the single-quantum transitions involving the flip of a single spin. The transitions probabilities are represented by the label  $W$  where the subscript corresponds to the  $\Delta m_I$  for the transition and the superscript the spin (I or S). The other two transitions ( $W_0$  and  $W_2$ ) involve the simultaneous flipping of both I and S spins. Although these transitions do occur, they cannot be directly observed by an NMR experiment, unlike single-spin flips, because the overall change in magnetic quantum number does not equal one [31]. If the single-quantum transitions for spin S are saturated by a continuous RF field  $W_0$  and  $W_2$  are able to act as relaxation pathways. This phenomenon is the origin of the NOE.

The  $W_2$  process will remove spins from the  $\beta\beta$  state and transfer them to the  $\alpha\alpha$  state in an attempt to recover the population differences across the S transitions. This process results in a net increase in I-spin resonance intensities in the spectrum (positive NOE). Similarly, the  $W_0$  process will transfer spins from the  $\beta\alpha$  to the  $\alpha\beta$  state to regain the spin population differences across the S transitions. In this situation there will be a decrease in population across I transitions therefore there will be a net reduction in the I spin resonance intensities in the spectrum (negative NOE). The NOE enhancement factor definition ( $\epsilon_{\text{NOE}}$ ) is given by

$$\epsilon_{\text{NOE}} = 1 + \frac{\gamma_I}{\gamma_S} \left[ \frac{W_2 - W_1}{W_0 + 2W_1^S + W_2} \right] = \frac{\gamma_I}{\gamma_S} \frac{\sigma_{IS}}{\rho_{IS}} \quad 2.22$$

where  $\gamma_I$  and  $\gamma_S$  are the gyromagnetic ratios of the two spins,  $\sigma_{IS}$  represents the cross-relaxation rate constant for two spins and  $\rho_{IS}$  is the total dipolar longitudinal relaxation constant of spin I.

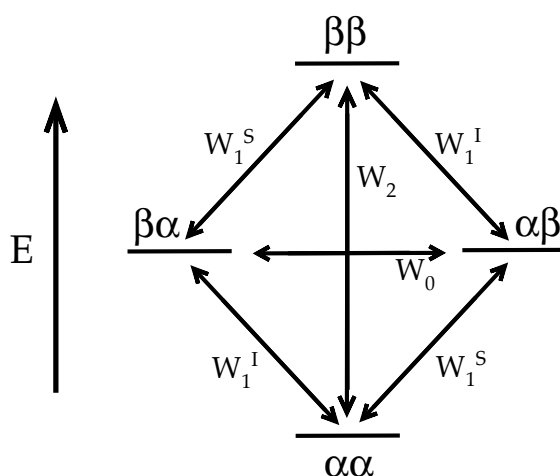


**Figure 2.3. Transitions in a two-spin system where  $\alpha\alpha$ ,  $\alpha\beta$ ,  $\beta\alpha$  and  $\beta\beta$  are spin states and the double-arrows represent the transitions between states.**

Rapid molecular tumbling, corresponding to a short correlation time  $\tau_c$  favours the higher energy  $W_2$  process in the *extreme narrowing condition*. Contrary, slow molecular tumbling (long correlation time) favours the lower energy  $W_0$  process in the *rigid lattice limit*.

The principal techniques that exploit the NOE are [31]:

- a) Nuclear Overhauser Effect (NOE) Difference. This technique establishes NOEs and hence spatial proximity between protons. It is suitable for small molecules, for which NOEs are positive. It is possible to detect steady-state or equilibrium NOEs generated from saturation of a target.
- b) Nuclear Overhauser Effect Spectroscopy (NOESY). One- or two-dimensional technique that establishes NOEs and hence spatial proximity between protons. It is suitable for small and large molecules for which NOEs are positive and negative, respectively, but may fail for mid-sized molecules (zero NOE). The method detects transient NOEs generated from the interversion of a target. The pulse sequence for this experiment consists of three  $90^\circ$  pulses (Figure

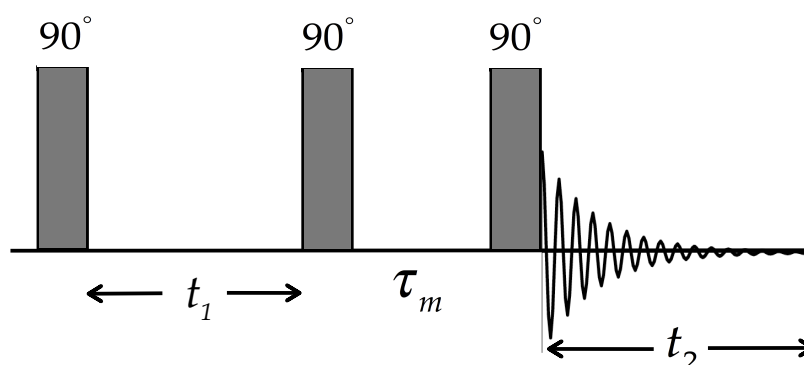


**Figure 2.4. NOESY experiment.**

2.4), the second and the third separated by a fixed delay  $\tau_m$  during which z magnetisation is transferred between neighbouring spins via the NOE.

- c) ROTating-frame nuclear Overhauser Effect Spectroscopy (ROESY). One- or two-dimensional technique that establishes NOEs and hence spatial proximity between protons. Suitable for any molecule but often essential for mid-sized molecules. NOEs are positive for all molecules sizes. The method is used to observe transient NOEs in the rotating frame.
- d) Heteronuclear nuclear Overhauser Effect Spectroscopy (HOESY). Two-dimensional technique that establishes NOEs and consequently spatial proximity between different nuclides (e.g.,  $\{^1\text{H}, ^{13}\text{C}\}$ ).

## 2.2.7 Solid-state NMR

### 2.2.7.1 Magic-Angle Spinning

When a conglomerate of nuclei in a solid sample is placed into a magnetic field, no nucleus resonates at precisely the same frequency as another, and hence the frequency range of resonances will be quite broad. This broad frequency range is due to orientation dependence within the chemical shift anisotropy, dipolar couplings and quadrupolar effects.

A complementary technique called magic angle spinning (MAS) [32] is the single most used technique in solid-state NMR. The technique relies on the rapid rotation of the solid sample around an axis which subtends the magic angle of  $54.74^\circ$  (Figure 2.5) to the applied magnetic field. This technique allows the elimination of anisotropic interactions (chemical shift anisotropies and direct dipole-dipole couplings) resulting in high-resolution NMR signals.

The molecular orientation dependence of nuclear spin interaction is proportional to the form  $(3\cos^2\vartheta - 1)$  (see Equation 2.11) where  $\vartheta$  is the angle which describes the orientation of the spin interaction tensor (Figure 2.5) relative to the applied magnetic field  $\mathbf{B}_0$ . If the sample is spun about an axis inclined at an angle  $\vartheta_R$  to the applied field,  $\mathbf{B}_0$ , then  $\vartheta$  varies with time as the molecule rotates with the sample. The average of the orientation dependence of nuclear spin interaction can be shown to be

$$\langle 3\cos^2\vartheta - 1 \rangle = \frac{1}{2}(3\cos^2\vartheta_R - 1)(3\cos^2\beta) \quad 2.23$$

where the angles  $\beta$  and  $\vartheta_R$  are defined in Figure 2.5. If  $\vartheta_R$  is set to  $54.74^\circ$ , then  $(3\cos^2\vartheta_R - 1) = 0$  and the effects of anisotropies vanish since  $\langle 3\cos^2\vartheta - 1 \rangle$  is zero also.

### 2.2.7.2 Cross-Polarisation

In 1962, the cross-polarisation phenomenon was first observed by Hartmann and Hahn [33], and later in 1972 the technique was adapted by Pines, Gibby and Waugh [34], to improve the sensitivity of nuclei with a low gyromagnetic ratio or low natural abundance.

A cross-polarisation pulse sequence consists of the application of a simple  $90^\circ$  pulse to the abundant spin (nucleus I, generally  $^1\text{H}$ ), aligning the magnetisation of the nuclei along the rotating-frame y-axis. Next, both nuclei (I and S) are continuously and simultaneously irradiated with a “spin lock” pulse along the y-axis. During this

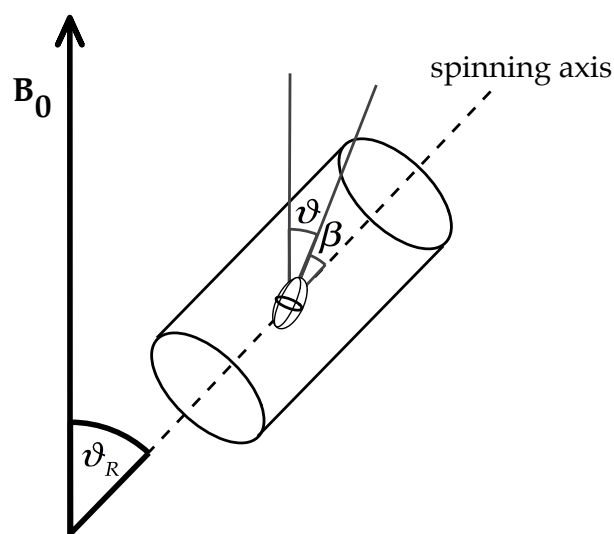


**Figure 2.5.** This diagram shows the angles  $\vartheta$ ,  $\vartheta_R$  and  $\beta$ , relevant to the magic-angle spinning experiment. The rotor - represented by a cylinder - is inclined at  $\vartheta_R \approx 54.74^\circ$  relative to  $B_0$ . The ellipsoid in the middle of the rotor represents the principal axis system (PAS). The dashed line represents the axis of rotation of the sample.

period, due to the dipolar interactions between the two spins, the magnetisation of the nucleus I is transferred to the nucleus S. This time period, during which cross-polarisation takes place, is known as the contact time. Subsequently, the FID is recorded (Figure 2.6a).

Cross-polarisation is often used in conjunction with MAS (CPMAS), a combination that was first demonstrated by Schaefer and Stejskal [35]. However, despite the use of MAS, the observation of some nuclei, such as  $^{13}\text{C}$  with a natural abundance of 1.1% (Table 2.1), is complicated owing to the strong heteronuclear dipolar coupling to protons, resulting in a broad spectrum. The effects of these couplings can be easily removed by RF irradiation of the protons, called decoupling. The method consists of applying continuous irradiation of very high power at the frequency of the proton resonance during the FID acquisition [12].

For a static sample, it can be shown that the transfer of magnetisation between the two set of spins will take place during the period of simultaneous spin-locking when a unique “Hartmann-Hahn” matching condition is satisfied

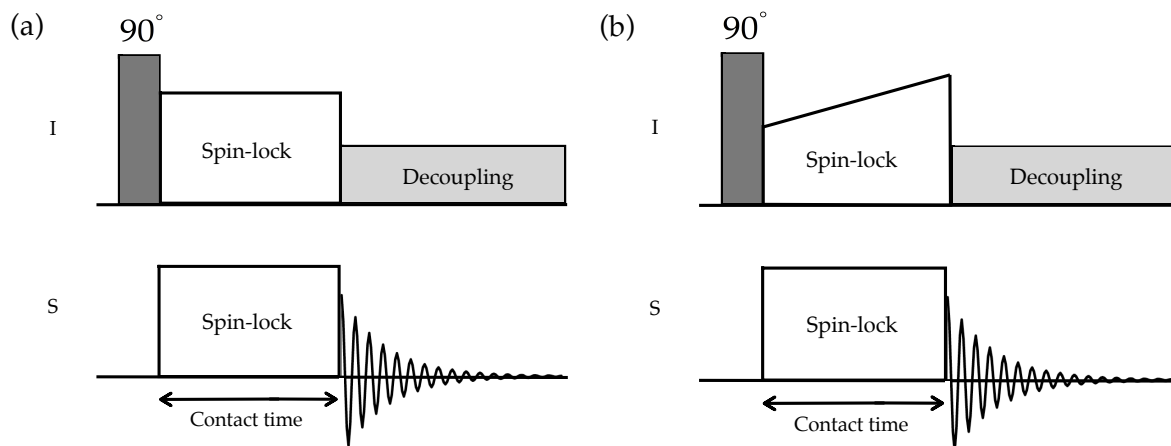


**Figure 2.6.** Representation of (a) the conventional cross-polarisation pulse sequence and (b) cross-polarisation ramped pulse sequence.

$$\gamma^I B_1^I = \gamma^S B_1^S \quad 2.24$$

where  $\gamma^I$  and  $\gamma^S$  are the gyromagnetic ratios of the I and S spins, and  $B_1^I$  and  $B_1^S$  are the strengths of the radiofrequency fields applied to the I and S spins, respectively. The application of MAS during cross-polarisation is desirable for the acquisition of high-resolution spectra, but sample rotation will introduce a time dependence into the dipolar interaction that mediates the polarisation transfer. As a consequence, optimum polarisation is not obtained at the conventional Hartmann-Hahn condition given in Equation 2.24. The new match condition under magic-angle spinning becomes (see Equation 2.5) [36]

$$\omega_{1I} - \omega_{1S} = \pm n\omega_R \quad 2.25$$

where  $\omega_{1I}$  and  $\omega_{1S}$  are the inherent nutation rates,  $\omega_R$  is the spinning frequency, and  $n$  is an integer, usually 1 or 2. The matching condition is no longer at the centerband,  $n = 0$  (Equation 2.14), but shifted to sidebands either side of the normal condition. Consequently, it is necessary to optimise the cross-polarisation conditions at the target spin rate. At high spin rates the matching conditions become narrower and more delicate than at slow rates [10].

The simplest solution to the problems related with the sensitive nature of the matching condition is to use ramped cross-polarisation (Figure 2.6b). Ramped cross-polarisation varies the RF nutation rate on one of the channels, sweeping the RF amplitude through the matching condition [10].

### *Heteronuclear correlation (HETCOR)*

Two-dimensional NMR experiments find such wide utility in chemical research because they map out interactions within or between molecules of interest. The interactions that can be observed by two-dimensional techniques are through-bond coupling, through-space coupling and chemical exchange.

The name HETCOR (from HETeronuclear CORrelation) is given to the two dimensional experiment which aims to correlate the resonances of a pair of heteronuclei within a sample through a coupling interaction, i.e., correlating  $^{13}\text{C}$  with  $^1\text{H}$  via a  $J$  coupling. Heteronuclear correlation via the dipolar interaction is particularly straightforward in solids since the necessary magnetisation transfer can generally be achieved using cross-polarisation [10].

The HETCOR experiment starts with the preparation period, a simple  $90^\circ$  pulse applied to the I spin, which creates transverse magnetisation that evolves for the evolution period,  $t_1$ , before cross-polarisation starts in a mixing time, followed by detection of the S-spin FID (with or without decoupling) (Figure 2.7).

## **2.3 Dynamic processes in proteins**

Protein dynamics play a crucial role in many important biological processes, such as ligand binding, allosteric regulation, protein folding, signaling and enzymatic catalysis [37]. A wide range of motions in terms of both time and distance scales are spanned by these processes. Many spectroscopic and computational techniques have been developed to monitor various aspects of protein dynamics.

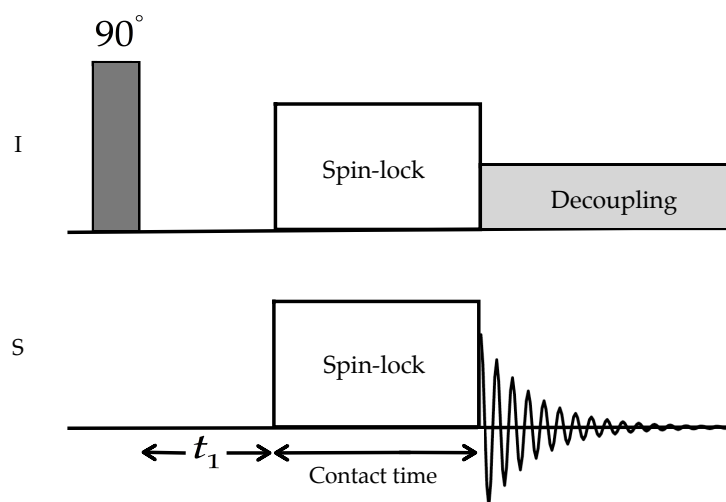


**Figure 2.7. Two-dimensional HETCOR experiment with I-spin decoupling.**

### 2.3.1 NMR approaches

As mentioned earlier in Section 2.1, NMR is capable of providing information about molecular dynamics. The clear advantage of NMR methods is that they can deliver timescales, together with atomic resolution, in contrast with other high-resolution methodologies such as X-ray crystallography or electron microscopy.

Biological functions span a range of timescales depending on the underlying conformational changes of cellular proteins. These changes can be studied using an array of NMR experiments that are like windows into the dynamic landscape of a protein [38]. NMR dynamics measurements can correlate changes in enthalpy and entropy of a protein to its function. Figure 2.8 shows how NMR can probe dynamics on timescales similar to processes involved in each function. Dynamic NMR can be organised into slow, intermediate and fast exchanges, compared to a time commonly referred to as the *NMR timescale*. The commonly used NMR timescale is that of direct peaks observation. In the case of a two-site exchange, if the exchange is slow, the separate sites are observable. In intermediate exchange the lines are significantly broadened and may even have started to coalesce. In the fast exchange limit the

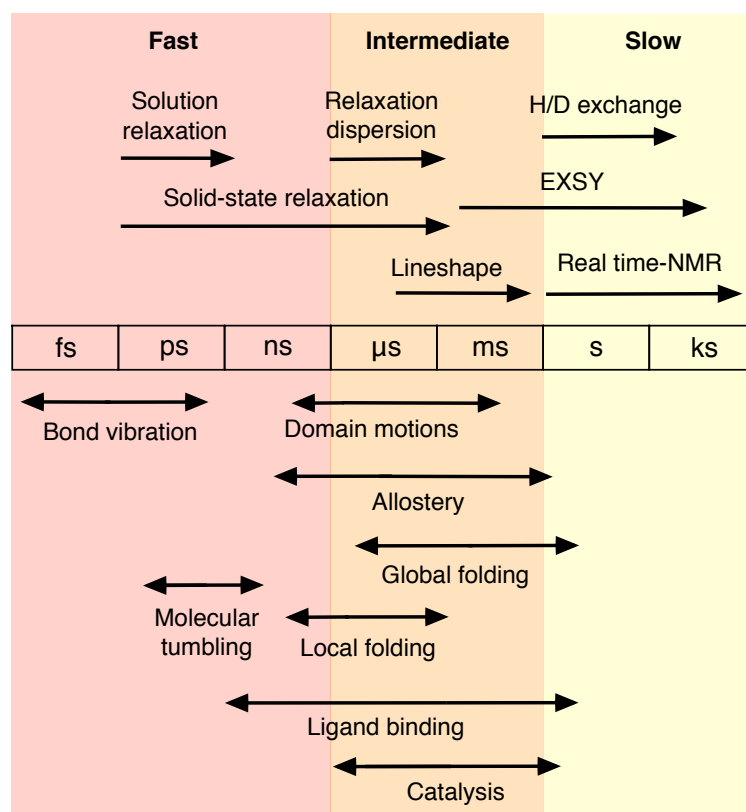


**Figure 2.8. Timescale of dynamic processes in proteins (bottom) and the NMR approaches to probe them (top) from references [37, 40, 41].**

signals have coalesced and only a single sharp line is observed at the average chemical shift.

The motional correlation time  $\tau_c$  (see Section 2.2.3) can be obtained by different NMR approaches depending on the timescale (see Figure 2.8). One of the simplest NMR approaches for the measurement of slow motion dynamics is real-time (RT) NMR. Dynamic processes on the second timescale are directly detected by quantifying the time-dependence of NMR signal intensities [39]. Physical processes on this timescale include protein folding and solvent hydrogen-exchange.

EXchange SpectroscopY (EXSY) can quantify dynamic processes in the 10-5000 ms time window [42]. Physical processes in this time window include conformational changes such as domain movement and ligand binding.

Intermediate motion dynamics events between the microsecond to millisecond time window, can be probed by lineshape analysis. This approach derives from well-defined theoretical work by McConnell [43]. Typically, a series of spectra are acquired along a titration coordinate such as ligand concentration, temperature or pH to observe their incremental effect upon the three NMR observables (chemical shift, intensity and linewidth).

Another NMR approach for measurements of intermediate motions dynamics is Carr-Purcell-Meiboom-Gill (CPMG) relaxation dispersion NMR spectroscopy. This experiment is a particularly a powerful tool to obtain high-resolution structural information about protein folding events on the millisecond timescale [44].

Fast motions can only be deduced from NMR relaxation measurements. NMR relaxation times depend on the fluctuations of the nuclear interactions (such as nuclear dipoles, chemical shift anisotropies or quadrupolar interactions) with respect to the static magnetic field due to the overall rotational diffusion of the protein as well as local fast motions in the protein [45]. The precise range of applicability for relaxation is different in solution and solid state. In solution, relaxation methods report on motions from picoseconds to the correlation time of the overall rotational diffusion (correlation time increases with the size of protein but generally falls within the picosecond-nanosecond range). In the solid state where overall tumbling is absent, the relaxation may be used to characterise amplitudes and time scales of motions from picoseconds to milliseconds. Furthermore, the absence of overall tumbling in the solid state removes the intrinsic limitation on the size of proteins that can be studied by NMR [41].

The longitudinal relaxation rate constant ( $R_1 = 1/T_1$ ), transverse relaxation rate constant ( $R_2 = 1/T_2$ ), and the nuclear Overhauser effect are generally measured to evaluate different relaxation processes in proteins (e.g., backbone NH group dynamics). All of these parameters are typically measured using two-dimensional

(HSQC type) experiments in which the intensities of the peaks are modulated as a function of a time delay placed at a point in the sequence when the relevant relaxation process is active [46]. These experiments normally require incorporation of specific isotopic labels.

The use of computational tools such as molecular dynamics to correlate NMR relaxation measurements is becoming increasingly useful for a better interpretation of the experimental data [47, 48].

Currently, the solid-state relaxation methodology toolbox is still not as rich its solution-state equivalent. One of the main reasons behind this problem is that relaxation rates measured in solid state are generally affected not only by processes such as random thermal fluctuations (which is the case in solution) but also processes originating from the incomplete averaging of strongly coupled networks of anisotropic interactions in solid proteins. One approach to remove such anisotropic broadening involves mechanical rotation of the samples around the so-called magic angle (see Section 2.2.7.1). A complementary approach to reduce the effect that the multiple couplings to proton have is to chemically remove protons and replacing them with deuterons (i.e., perdeuteration) [41].

The majority of traditional NMR methodologies to measure fast motions in protein are applied to spin  $I = 1/2$  nuclei. A significant number of biologically relevant elements in protein dynamics (e.g., allosteric modulation) have nuclides that possess spin quantum numbers greater than  $1/2$  (e.g.,  $^{23}\text{Na}$ ,  $^{35}\text{Cl}$  and  $^{43}\text{Ca}$ ) and thereby possess nuclear quadrupole moments. The quadrupolar interaction is usually much stronger than other interactions causing relaxation. This means that the quadrupolar mechanism normally dominates the relaxation and not other interactions. Relaxation of quadrupolar nuclei has been studied in solution using multiple-quantum filtered NMR methods [49, 50] and in Chapter 6 we attempt to apply these methods under

MAS to hybrid liquid-solid samples with the aim of investigating ion- and water-binding to immobilised enzymes.

### 2.3.2 Other approaches

Other atomic resolution methods such as X-ray and neutron diffraction also report on dynamics. X-ray diffraction generally reports on global changes in protein size and shape in a time-resolved manner and neutron diffraction on amplitudes and time scales for hydrogen atomic positions in proteins. X-ray crystallography itself yields some dynamic information. This information is extracted from temperature factors (B factors) [51].

Lower resolution techniques such as Mössbauer [52], Raman [53] and two-dimensional infrared [54] spectroscopy also provide new insights into protein dynamics. Fluorescence is an important tool to understanding protein dynamics both in the ensemble and in single molecules [55].

Computer simulations such as molecular dynamics, serve as a theoretical basis for predicting protein motion, analysing inputs from the wide variety of experimental techniques such as NMR, and probing dynamic information beyond what can be assessed experimentally [37].

## 2.4 Analysis of protein-ligand interactions

Protein-ligand interactions are fundamental to almost all processes occurring in living organisms. Enzyme catalysis involves diverse protein-ligand interaction, including substrate and cofactor binding to the enzyme. There are many techniques to characterise protein binding and new methods emerge every few years. In a general sense characterisation methods can be divided into two main categories: biophysical and computational. Here a general description of the most important techniques is given. Section 2.5.3 explores in more detail the different tools for

analysis of protein interactions (i.e., enzyme-surface and enzyme-ligand interactions) for immobilised enzyme systems.

### 2.4.1 Biophysical methods

To detect experimentally the formation of a complex between a ligand and a target protein, a measurable response, or signal, and an appropriate detection technology are required. Signals can arise from an intrinsic interaction from the ligand, the target, ligand-target complex or a combination of them all. In the absence of intrinsic interactions, one approach to studying these interactions is the attachment of a label (probe) to one of the species involved. Labelling can be advantageous in giving more sensitivity and specificity to the experiments [56].

Several biophysical experimental techniques have been used with the purpose of studying protein-ligand interactions. There are direct techniques to detect binding such as nuclear magnetic resonance (NMR), surface plasmon resonance (SPR), mass spectroscopy and X-ray crystallography or indirect methods such as thermal shift or isothermal titration calorimetry.

#### 2.4.1.1 NMR approaches

Several NMR techniques have been developed to detect binding. NMR is typically used in two distinct configurations with the purpose of studying protein interactions: monitoring the ligand or the protein. The immediately visible NMR evidence that the binding has occurred is likely to be either a change in the resonance frequency of a nucleus in the ligand or the protein, or a change in a linewidth. Chemical shift changes result from a change in the environment of the reporter nucleus. They can be obvious and readily observable. A change in linewidth (or more directly the relaxation rate constant  $1/T_1$  or  $1/T_2$ ) may result from a change in the motional characteristic of the reporter nucleus.

### *Protein-Detected NMR Techniques*

Monitoring the protein brings much more information as the structural and dynamics implications of binding can be evaluated [57].

Two-dimensional NOE experiments to evaluate backbone chains (e.g.,  $\{^1\text{H}-^{15}\text{N}\}$  HSQC) and SAR (structure-activity relationship) experiments to detect changes in the chemical shifts have been used in the past for monitoring the protein after a ligand event [58]. These methodologies require  $^{15}\text{N}$  and/or  $^{13}\text{C}$  labelling.

### *Ligand-Detected NMR Techniques*

When the ligand is monitored, any modification of its spectrum in the presence of protein implies an interaction. This approach can be quite fast and sensitive but not very informative in terms of the interaction geometry. Ligand examination has the technical advantage of not requiring labelled protein. The size of the protein does not limit this technique, and in many examples, larger proteins provide better sensitivity because binding of a large protein causes a more distinguishable change to the observable signals [59]. Ligand-based methods are attractive because they are broadly applicable, impose few constraints on the composition of the target protein and do not require isotopic labelling of the protein or ligands. Such experiments include relaxation experiments, diffusion experiments (DOSY) and methods involving magnetisation transfer (STD-NMR, NOE pumping, waterLOGSY, SALMON, transferred-NOE and INPHARMA) [60].

#### 2.4.1.2 Other approaches

Surface plasmon resonance (SPR) involves immobilising the protein on a sensor surface before a ligand is flowed over the surface. Binding events are measured by monitoring change in resonance angle (angle of minimum reflectivity) for the immobilised component. Observed binding levels and binding rates can be

interpreted in different ways to provide information on the specificity, kinetics and affinity of the interaction, thermodynamics or on the concentration of a molecule.

Mass spectroscopy (MS) is another technique to study protein-ligand complexes. The strengths of MS are supreme sensitivity as well as accuracy of molecular weight determination. In all MS techniques, the sample is vaporised, ionised, and accelerated through an electric field. The trajectory that molecules fly on depends on their molecular weight and their charge. The most obvious method to study protein complexes using MS is determine the molecular mass of these complexes, and hence the stoichiometry of a complex. In addition to molecular mass determinations, MS also offers other methods to study protein interactions. For example, an interesting application of MS is in study of kinetics of protein complex formation and dissociation, or subunit exchange, where the appearance of new molecular mass species can be monitored after mixing [61].

As was mentioned earlier in Section 2.1, protein structures are typically determined using X-ray crystallography. A key step in the study of protein-ligand interaction using X-ray crystallography is obtaining co-crystals structures of protein-complexes. Soaking and co-crystallisation are the two most widely used approaches to obtain them. These methodologies require the ligand to bind to the protein either before or after crystallisation. In soaking, the ligand is incubated with preformed crystals of either the ligand-free protein or cocrystals of a previously bound ligand that can be displaced with a new one. In the cocrystallisation method, the protein is incubated with excess ligand to form a complex prior to setting up the crystallisation experiments [56].

The thermal shift (TS) technique measures the change in thermal unfolding temperature of the protein caused by ligand binding (via a fluorescent dye that preferentially binds to the unfolded state). As the temperature of the sample is increased and the protein unfolds, the dye binds to the more exposed hydrophobic

regions of the protein and an increase in fluorescence signal is detected. The stability ( $T_m$ ) of the protein can be measured from the midpoint of this thermal unfolding curve. Ligand binding to native protein results in an increase in stability and a measurable increase in  $T_m$  [56].

When a protein interacts with a ligand, usually, heat is either released or absorbed. The determination of this heat gives necessary insight into the nature of an interaction. Isothermal titration calorimetry (ITC) is the only technique that measures this heat change and therefore gives detailed thermodynamic information about the binding process. The energy released or absorbed is measured when a ligand is titrated into a cell where the protein is located. The heat change is proportional to the amount of ligand bound and the binding enthalpy [56].

### **2.5 Immobilisation of enzymes**

As noted above enzymes, as catalysts, possess the astonishing quality of leading to product formation at mild and environmentally friendly conditions with a high specificity. A core technology is the immobilisation of enzymes – the conversion of the soluble protein molecules into a solid particle form that can be easily separated from the reaction mixture. This allows the expensive enzyme catalyst to be recovered and re-used and avoids protein contamination of the product streams.

In 1972, Wingard [62] defined immobilisation as the process where the enzyme is confined or located in a defined region of space, to yield to insoluble forms which retain their catalytic activity and can be reused repeatedly. Later this definition was extended to be that process which restricts, in whole or in part, the degrees of freedom of movement of enzymes, organelles, cells, etc. by binding to a support or other means [63].

The main advantages of immobilisation are derivative reusability (thus reducing the costs of the process) and obtaining a product uncontaminated by the catalyst.

At a molecular level there are some disadvantages to using this process. Some of these drawbacks stem from the alteration of the native conformation of the enzyme and the heterogeneity of the enzyme-support system where different protein fractions can be immobilised with a number of bonds to the support. Also, from a performance point of view, it is common to observe loss of activity of the enzyme during the immobilisation and the biocatalyst produced is more expensive than the free enzyme.

The success of an immobilisation procedure is based on the ability of the support to bind the enzyme and efficiently express the activity: however there is no ideal support universal for all enzymes [64].

Since the advent of immobilisation of single enzymes in the 1940s, innumerable methods have been developed.

### **2.5.1 Methods of immobilisation**

There are a large number of methods of immobilisation that can be broadly divided into those that involve the interaction of the enzyme with a matrix (usually through a chemical bond) and those in which the enzyme is contained within a restricted space [65].

Among the most popular immobilisation methods (Figure 2.9), there are two that involve the interaction with a matrix or carrier: covalent and non-covalent immobilisation. The latter case is more commonly known as adsorption. Other methods involve the use of the enzyme without a carrier, such as cross-linked enzyme aggregate (CLEA) and cross-linked enzyme crystal (CLEC). Also there are methods that involve the confinement of the enzyme, involving entrapment inside a gel and retention by a membrane.

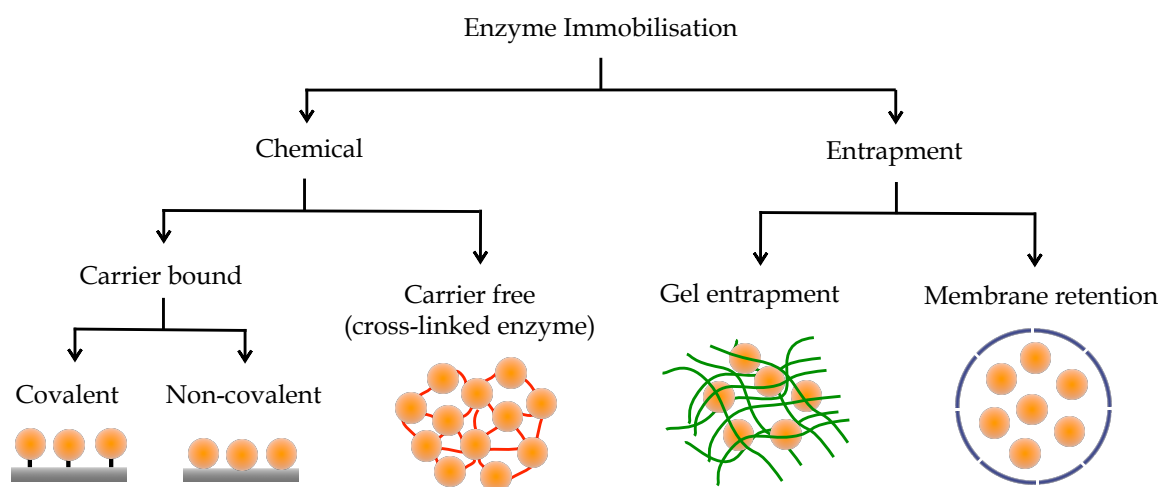


**Figure 2.9. Methods of enzyme immobilisation.** The enzyme is labelled in colour yellow, the surface of the carrier in grey, the covalent linkage in black, the cross-linking agent in red, the gel matrix in green and the semipermeable membrane in blue.

### 2.5.1.1 Covalent enzyme immobilisation

Covalent immobilisation was the second method of immobilisation developed after adsorption. The immobilisation methods through covalent bonding usually provide the strongest support-enzyme linkages, compared with other types of immobilisation such as adsorption [66]. Therefore, through covalent immobilisation methods, it is possible to minimise losses of enzyme from the matrix.

In general, covalent binding of an enzyme to a carrier is based on chemical reaction between the reactive amino acid residues (RARs) located on the enzyme surface and active functionalities also known as carrier bound groups (CAGs) (Figure 2.10) that are attached to the carrier surface. To achieve efficient linkage, the functionality of carrier and/or the enzyme must be activated before immobilisation. Often, carriers are activated before their use for binding enzymes [66].

#### *Factors affecting covalently immobilised enzyme performance*

Covalent binding is considered to be a radical method of immobilisation. This is because of the irreversible nature of the binding, fixing the enzyme conformation and

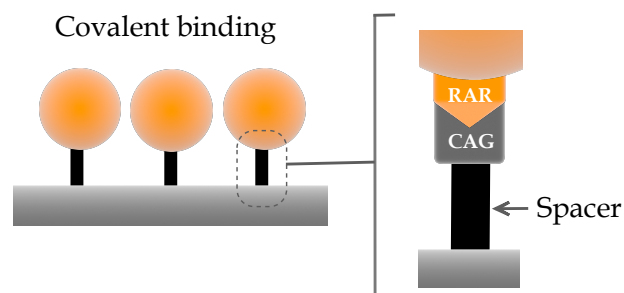


**Figure 2.10.** Elements involved in the covalent binding of an enzyme to a support. RAR stands for reactive amino acid residue and CAG for carrier bound group. Colour scheme is the same used in Figure 2.9.

modifying the enzyme chemically. Enzyme performance (i.e., selectivity and stability) can be significantly improved using this method in comparison with native enzyme or other immobilisation methods. Generally, the multiple linkages in covalent binding decrease the activity of immobilised enzyme compared with free enzyme.

The performance of the biocatalyst can be affected for different properties of the components of the composite system (Figure 2.10) [66]. Table 2.2 summarises these properties and the thesis Sections where information about them can be found. Enzyme conformation, orientation and distribution on immobilised systems are discussed in the Summary Chapter of this thesis (Chapter 8). Chapter 8 also contains further discussions for some of the other properties included in Table 2.2.

## 2.5.2 System

### 2.5.2.1 Carrier

Physical and chemical properties of the carrier are significant in the process of the attachment of the enzyme. Since the 1960s, it was recognised that the success of immobilising an enzyme was largely dependent on the physical and chemical properties of the whole system [67].

**Table 2.2. Properties of the components of covalent enzyme immobilisation that can affect the performance of the biocatalyst.**

Properties	Section
physical nature of the carrier (i.e., pore size, particle size, porosity, shape, etc.)	3.1
chemical nature of the carrier (chemical composition of the backbone, active functionality, other non-active functionality)	3.1
nature of the linkage or binding chemistry	3.3.2
nature and the length of the spacer	3.3.1
number of bonds formed between the enzyme and the carrier	2.5.2
conformation of the enzyme	Chapter 8
enzyme orientation	Chapter 8
enzyme distribution	Chapter 8

*Physical properties*

The physical characteristics of the support (such as mean particle diameter, swelling behaviour, mechanical strength, and compression behaviour) will be of major importance for the performance of the immobilised systems and will determine the type of reactor used under technical conditions. In particular, the pore size determines the total surface area and thus critically affects the capacity for binding of enzymes. Particle size does not really affect the total surface, unless for very small particle sizes (about microns). Nonporous supports show few diffusional limitations but have a low loading capacity. Therefore, porous supports are generally preferred because the high surface area allows for a higher enzyme loading and the immobilised enzyme receives greater protection from the environment [7]. The

surface of a carrier might include external and internal surfaces. For enzyme immobilisation, a large internal surface is highly desirable for high loadings.

The accessible surface is the surface area accessible to the enzymes to be immobilised and depends directly on the pore size of the carrier. Therefore, the pore size becomes a crucial physical property in order to obtain a successful immobilisation. It has been observed that minimum requirements exist relating to the size of the pores in the carrier. The pore size should be big enough to let the enzyme enter, have freedom of movement to change its conformation and mitigate diffusion limitations [66]. Previous studies reported optimum pore sizes for maximal binding capacity and activity retention between 5 and 10 times of the protein globular size. In general, it was found that when the pore size is bigger than optimum pore size, a decrease in the enzyme loading is expected [68]. This is because the surface available for enzyme occupation usually decreased with increasing the support pore size.

### *Chemical properties*

The chemical nature of the carrier involves the chemical composition of the backbone, the surface chemistry, the nature of the spacer, active or inactive functional pendant groups on the surface and hydrophilicity or hydrophobicity of the support.

It has been demonstrated that it is very difficult to predict which carrier bound binding group (CAG) is the best-suited for a given enzyme because many factors can affect the binding process (i.e., nature of the backbone and immobilisation conditions) [66].

The space arms that link the CAG are of crucial importance. They can affect the immobilisation efficiency and increase or decrease the enzyme stability. A higher molecular mobility in the presence of spacers can lead to an improvement in the performance of the immobilisation [69]. On the other hand, it is well known that

stability of covalently immobilised enzyme is related to the number of bonds formed between the enzyme and the carrier [70, 71] making the unfolding of the peptide chains much more difficult in this more “rigid” system than the native enzyme. Obviously, high binding density leads to an increase in the number of bonds between the support and the enzyme and therefore in a rigidification of the system that is not beneficial in terms of enzymatic activity.

### 2.5.2.2 Reactive enzyme residues

There are two essential requirements to achieve an efficient covalent binding between the enzyme and the carrier. The first one is the matching between the reactivity of the functional groups of the selected carrier and the enzyme residues in the aqueous medium and the second is ensuring that functional groups involved in the immobilisation are sterically accessible to each other in the medium chosen (aqueous or organic).

Not all free side chain (R) residues of the 20 amino acids can be used in covalent binding. Only half of them have a reactive group that can be involved in this type of immobilisation. The most important residues involved in immobilisation through covalent binding are lysine (lys), glutamic acid (glu), aspartic acid (asp), tyrosine (tyr), cysteine (cys), N-terminus and C-terminus of proteins (Table 2.3).

Lysines bear a primary amine moiety and although their side chains are protonated under physiological pH, they can still react as nucleophiles. ( $\epsilon$ )-amino groups of lysine and amino groups of N-terminal amino acids can react with a variety of reagents bearing reactive amino acid residues (i.e., N-hydroxysuccinimide esters, isothiocyanates, aldehydes) producing a covalent bond [72].

Another approach relies on the selective modification of carboxylic groups present on glutamic acid, aspartic acid and C-terminus of a protein. This method uses a

pre-activation of the carboxylic groups in order to produce an amide bond between the terminal functionality and pendant amines on a support [73].

Phenol groups present on tyrosine can also react as nucleophiles. The addition of a diazonium salt produces an azo bond, that can be further reduced and transformed into a stable benzoxazine [74]. Cysteine residues can be covalently bonded to a support using the thiol side chain. The thiol moiety is more nucleophilic than a primary amine, especially at a pH below 9, where the amine is protonated. However, free thiols are relatively rare in proteins (Table 2.3) and they are often found as an oxidised dimer, known as a disulfide form. There are other factors, besides reactivity, to consider as possible determinants of which groups might be more involved in covalent attachment to a solid support. One factor is the relative content of the amino acids in the protein molecule. Table 2.3 shows the average amino acid composition of proteins [75] for some of those amino acids with reactive groups.

There also exists a difference in the hydrophobic nature among amino acids. A ranking of hydrophobicity of the most important reactive amino acid in covalent binding<sup>2</sup> is shown in Table 2.3.

The position of the active amino acids on the enzyme is an important factor to consider. In general, hydrophobic amino acids are located in the core of the protein or buried zone, and less hydrophobic residues are preferentially in an exposed zone. However, the extent of exposure of the amino acids can be varied, depending on the properties of the medium and the enzyme itself. More frequently used reactive amino acid residues (RARs) are in general located on the surface of the enzyme in an aqueous environment as Lys, Glu, Asp, Arg, N- and C-terminal amino acids.

---

<sup>2</sup> These values represent the mean ranking of amino acids polarities according 38 published hydrophobicity scales [75]. The lower ranking numbers represent the most hydrophobic amino acids, and higher values represent the most hydrophilic amino acids.

**Table 2.3. Properties of amino acids involved in covalent binding<sup>3</sup>.**

Amino acid	Occurrence in proteins / %	Ranking of amino acid hydrophobicity
Glu	6.3	3
Lys	5.8	5
Asp	5.2	4
Tyr	3.3	2
Cys	1.8	1

### 2.5.3 Evaluation of immobilised enzyme

The aim of the present section is to give an overview of available methodologies that have been utilised to gain knowledge on different aspects of immobilised enzymes.

#### 2.5.3.1 Immobilisation process

In general, the process of covalent immobilisation of an enzyme consists basically in two main elements; the free enzyme (external solution) and the support or carrier.

The most common method to monitor the protein immobilisation is to retrieve samples from the external solution (supernatant) at different times during immobilisation process and measure the amount of enzyme remaining in the surrounding solution commonly by absorption spectroscopy (see Section 4.3). This indirect approach usually requires manual sampling and results in a low time resolution. Also, if only a small fraction of protein is immobilised, the loading measured will be extremely inaccurate because it is a difference measurement.

---

<sup>3</sup> Frequency of occurrence of each amino acid residue in the primary structure of 105,990 protein sequences [75].

There are not many studies whose aim is to measure the amount of the protein directly. Fluorescence microscopy has been used for this purpose [76]. There are also examples of the use of thermogravimetric analysis (TGA) to determine protein immobilised [77]. TGA is a common method to characterise materials by measuring changes in physical and chemical properties, such as phase transition, dehydration and decomposition, as function of temperature. With this technique the loss of weight upon heating a dried sample is used to determine the protein loading. By increasing the temperature protein degradation is induced, leading to the evaporation of organic material from the inorganic support.

Recently, Quartz Crystal Microbalance with Dissipation monitoring (QCM-D) have been used to study the immobilisation process with much higher time resolution than the indirect approach. The QCM-D technique measures the mass added to the quartz crystal with a time resolution in the sub-second range [78].

### 2.5.3.2 Location of immobilised enzyme

Some techniques can allow information to be obtained about where the enzyme is located (inside the pores or external surface) after the process of immobilisation. Techniques used for this purpose on immobilised enzymes are N<sub>2</sub> adsorption [79, 80] and X-ray diffraction (XRD) [79]. For N<sub>2</sub> adsorption, the pore volume can be evaluated before and after the immobilisation and pore occupation can be determined. XRD can give qualitative information about changes in the pore interiors before and after immobilisation. These techniques are referred as indirect techniques. There are also direct techniques that measure enzyme molecules localised inside the material. These techniques are fluorescence microscopy [81] and transmission electron microscopy in combination with immunogold staining (TEM-IGS) [82].

The results from indirect techniques should be carefully interpreted. For example, in the case of nitrogen adsorption the reduced pore space after immobilisation process is not necessarily due to proteins occupying the pores but may also be explained by proteins blocking the pore openings, which in turn may hinder the nitrogen gas to enter.

### 2.5.3.3 Conformational changes

The conformational stability of protein structures can easily be affected by immobilisation as a consequence of the interactions with the support surface which often lead to enhanced or lowered enzyme activity [83]. Some methods can detect overall changes in protein structure, which can be an indicative measures of both unfolding and changes in enzyme activity.

Circular dichroism (CD) is a well established method for studying conformational changes in protein secondary structures. The results are generally presented as changes in the percentages of the protein composed of  $\alpha$ -helix,  $\beta$ -sheets, turns and random coils [84]. The presence of solid particles in samples may cause absorption flattening and differential light scattering perturbing the typical CD peaks. Different approaches have been applied to overcome these problems in the study of immobilised enzymes such as computational simulation corrections [85], use of nanosized supports [86, 87] and soluble polymers as carriers [88].

Fourier transform infrared spectroscopy (FTIR) has been widely used to study changes in protein secondary structure [89, 90]. Deconvolution of the spectra allows the determination of the fractions of organised secondary structures similar to the information given from CD spectra. FTIR has also been applied to immobilised enzymes confirming a maintained enzyme structure upon immobilisation [91, 92] or defining a  $\alpha$ -helix/ $\beta$ -sheet ratio as a function of temperature [93].

Fluorescence spectroscopy has also been used to study conformational changes on immobilised enzymes, specifically tryptophan fluorescence. The fluorescence spectrum of the amino acid tryptophan is dependent on the polarity of the surrounding solution [94]. Due to the hydrophobicity of tryptophan, the aromatic amino acid residue is often buried inside the protein. Therefore, unfolding of the protein will expose tryptophan to the surrounding solution, which can be detected as a shift in the fluorescence spectrum. Tryptophan fluorescence spectra have been used to prove a stabilising effect of immobilised enzymes compared to free enzyme [95, 96].

### 2.5.3.4 Enzyme-surface interactions

There are three important aspects in terms of protein-surface interactions on immobilised enzymes: structure, orientation and dynamics. Orientation and three-dimensional structure of immobilised enzymes are crucial to ensure high enzyme stability and activity. Most immobilisation procedures do not actively control the orientation of the enzymes, resulting in the inevitable burying and inaccessibility of some active sites. Some methods address the study of these aspects such as FTIR, computational simulations and solid-state NMR.

FTIR is not only useful detecting conformational changes, but can also be used for detecting bond formation to the surface, therefore can be used to characterise formation of protein-surface interactions after immobilisation [97-100].

Computer simulations of molecular dynamics have been used to model surface interactions on immobilised enzyme systems. These studies are focused in protein modeling of the enzyme structure and calculation of charge distribution on the surface at different pH [101-103]. This information can partly be used to predict how strongly enzymes can bind to the surface and how the strength depends on the environmental conditions upon immobilisation [101]. Some attempts to simulate the

interactions of proteins in confined environments such as nanotubes or micelles had been explored [104, 105]. Other approaches have been focused on modeling enzymes on surfaces where information of enzyme orientation can be retrieved [99, 106]. However, it remains to further develop the models to better mimic those systems allowing a better prediction of how enzyme structure is affected by the confinement into pores. With this requirement in mind, several studies have attempted modeling pore shaped nanostructures using molecular dynamics [107, 108].

Solid-state NMR is a popular technique to characterise supports used for enzyme immobilisation [109-111]. These studies do not include characterisation after the immobilisation process. To our knowledge, so far only one study had covered the analysis of enzyme-surface interactions by solid-state NMR after the process of immobilisation [1]. This publication derives from work included in this thesis in Chapter 5.

Potentially, solid-state NMR can study immobilised enzyme dynamics indirectly indicating the strength of the interaction between the enzyme and the support, based on the hypothesis that proteins that bind strongly will be less mobile than those that are not tightly associated with the surface. Side chain and backbone dynamics can be studied using a combination of relaxation measurement ( $T_1$ ,  $T_2$ ,  $T_{1\rho}$  and cross-polarisation efficiency) as well as  $^2\text{H}$  dynamics. Some reviews about the study of membrane proteins [112] and biomineralisation proteins [113, 114] show the potential capabilities of solid-state NMR for the study of immobilised enzymes.

### 2.5.3.5 Enzyme-ligand interactions

The most popular methodologies to study protein-ligand interactions were discussed in Section 2.4. Many of these methodologies are not possible to apply to heterogeneous systems such as immobilised enzymes. However, ITC has been

successfully applied in the activity analysis of different enzymes in the free state [115, 116] and immobilised on solid supports [117, 118].

Frontal affinity chromatography (FAC) has been used to study binding properties of several molecules to immobilised trypsin [119, 120]. Frontal analysis is a chromatographic method where the sample is continuously infused over a stationary phase, rather than injected in a low-volume plug. FAC has the advantage that it is extremely reproducible and could be able to identify strong (nM range) as well as weak-binding molecules (mM range).

Solid-state NMR is a promising technique to monitor enzyme-ligand interactions on immobilised enzymes. By detecting spectral changes, residue-specific details of the enzyme-ligand interaction can be obtained. Interactions between ligand and labelled membrane proteins have been described in the past using solid-state NMR [121-123]. Until now, no solid-state NMR studies of ligand interactions on immobilised enzymes have been reported in literature.

## CHAPTER 3

# Selection of the system of study

To attain the objectives outlined in Chapter 1 it is imperative, as a first step, to define a system of study. The model systems studied in this thesis must comply with certain requirements. These requirements are primarily based on defining the immobilised enzyme system as simply as possible. The different elements of such a systems are discussed in this section.

### 3.1 Type of Support

Certain desirable features exist for the selection of the type of support, which should be:

- Inorganic; because they generally have no carbon atoms, a lower concentration of hydrogen atoms and a higher mechanical strength than organic supports - these features directly affect the execution of NMR experiments.
- Widely used as an enzyme support.
- Well characterised through solid-state NMR.

The selected supports were silica and alumina to comply fully with these three requirements.

The carrier bound group (CAG) selected was the epoxide group. The oxirane functionality is reactive with several amino acid residues (e.g., amino, carboxyl, hydroxyl, mercapto, phenol, imidazole and indole groups).

Inconveniently, the silica and alumina supports were found to catalyse the hydrolysis of one of the inhibitors of interest (a R-BF<sub>3</sub>K salt – see Section 3.2.2.3); therefore a third support was selected: Eupergit®, a synthetic organic polymer was used for the studies of interactions between immobilised enzyme and ligands (see Chapter 7).

### 3.1.1 Porous support materials

Porous supports have received significant attention in enzyme immobilisation as a result of their high surface areas together with their ability to encapsulate enzymes within the pores, providing a stable environment.

Figure 1.1 illustrates the scale and the level of complexity of an enzyme immobilised on a porous support material (approximate scale). The diagram shows a support particle of 15 µm of diameter (Figure 1.1a) and a pore size of 20 nm (Figure 1.1b). The diameter of the enzyme molecule in Figure 1.1c is around 5 nm.

An ideal support behaviour for a catalyst is one where the rate of the catalysed reaction is directly proportional to the surface area available for catalysis, assuming that all the surface is catalytically active. In addition to the surface area, it is essential to establish the pore diameter and the distribution range of the pore diameters, as part of the internal surface may not be accessible if the pore diameter is too small [124].

The surface area of porous material can be classified into internal surface and external surface. The former is the total surface including that contributed by the pores, while the latter refers only to the outer surface. The internal surface is

generally about 100 to 1000 times the external surface for macroporous carriers, depending on the diameter of the particles and the pores. Thus, for such supports the enzyme loading on the external surface can be neglected in comparison with the overall enzyme loading [125].

Numerous methods currently exist for determining properties in porous materials. Pore size distributions can be obtained using gas adsorption [126, 127], differential scanning calorimetry (DSC) thermoporosimetry [128], mercury intrusion porosimetry (MIP) [129] and NMR cryoporometry [130].

The most commonly used methods for determining pore size distributions are gas adsorption and MIP. Often non-destructive testing is preferred and mercury intrusion fails in this regard because the measurement process damages the pore matrix and makes it impossible to reuse the sample. Gas adsorption, NMR cryoporometry and DSC have the immediate advantage in that the samples remain undamaged and therefore can be measured again and recovered. All three methods rely on placing a liquid in the pores and measuring the change in the thermodynamic properties [131].

Gas adsorption relies on the Kelvin relationship. The surface area of a porous material is determined by determining the volume of a monolayer of an inert gas (typically N<sub>2</sub>, He or Ar) adsorbed by the support, usually using the BET method described by Brunauer, Emmett and Teller [126]. The adsorption-desorption isotherms obtained can be classified into six types, I-VI [132]. The shape of the isotherm can be used to provide details of the structure of the material being analysed. These details can include pore geometry, internal pore diameter, and pore size distribution and pore volume of the material. The results obtained by adsorption methods can be confirmed or clarified using X-ray diffraction (XRD) or transmission electron microscopy (TEM) [133]. Adsorption methods have been adopted as the principal methods to characterise porous materials. IUPAC [132] classify porous

materials by pore width as microporous, mesoporous or macroporous when the pore diameter are less than 2 nm, between 2 and 50 nm and greater than 50 nm, respectively.

Both NMR cryoporometry and DSC thermoporosimetry rely on the Gibbs-Thomson equation concerning the relationship between the characteristic pore length scale and the change in the freezing point of the liquid, or melting point of its solid crystal, due to confinement within the porous matrix.

NMR cryoporometry is a method suitable for measuring pore sizes and pore size distributions in the range of less than 30 Å to over 3000 Å pore diameter. The technique involves freezing a liquid in the pores and measuring the melting temperature by NMR. Since the melting point is depressed for crystals of small size, the melting point depression gives a measurement of pore size. Accurate measurements of the sample temperature are necessary for this approach [131].

### **3.1.2 Metal-oxide-based supports**

From the early days of enzyme immobilisation oxide-based materials have been used [134]. Some of the advantages of using these types of support are their tunable physical features (e.g., porosity, particle size). Also, inorganic supports in general are not susceptible to biological attack and usually their morphology remains unchanged under different conditions of solvent or pH [135].

#### **3.1.2.1 Silica**

Silicon dioxide ( $\text{SiO}_2$ ) usually exists as a three-dimensional polymer with regular units of tetrahedral  $\text{SiO}_4$  sharing vertices with each other in an infinite lattice of siloxane bridges Si-O-Si. The most abundant form of  $\text{SiO}_2$  is in crystalline arrangement (i.e., quartz) forming a tetrahedral structure [136].

Conventional oxide-based supports possess a broad pore size distribution, low surface area and low thermal stability. These carriers were used extensively for more than seven decades [135]. The synthesis of ordered mesoporous materials with uniform pore size distribution was started as early as the 1970s [137-139] but went almost unnoticed. Intensive research in the area of mesoporous silica supports began in 1990s [140, 141]. Since then, a very large number of different mesoporous materials have been developed [142]. These tunable materials are generally prepared by controlled hydrolysis of tetraethyl orthosilicate or sodium silicate in the presence of surfactants in a solvent solution. The surfactants act as templates of the pores and help in the formation of a highly ordered organic-inorganic liquid-crystal phase (mesophase or mesostructure). The removal of the surfactant from the mesostructure by calcination at high temperatures or other physical or chemical treatments results in the formation of mesopores in the structure [143].

The use of this type of material as a support for enzyme immobilisation results in high enzyme loadings. In addition, the enzyme molecules inside the pore channels are protected from microbiological attack as well as from physical and mechanical damage [144].

Usually, silica surfaces show two main chemical functions: silanols (Si-OH) and siloxanes (Si-O-Si). The existence of four different types of coordinated-Si are postulated: isolated ( $Q_3$ ), geminal ( $Q_2$ ), bulk ( $Q_4$ ) and  $Q_1$ . This last species is postulated but its real existence is not yet generally accepted. Figure 3.1 shows a representation of the bare silica surface. The coexistence on the silica surface of both hydrophobic (siloxanes) and hydrophilic sites (silanols) on silica surface, particularly the latter, explain the adsorptive properties of many silica-based materials [144]. Solid-state NMR techniques can reveal the surface structure of silica-based supports competently [136].

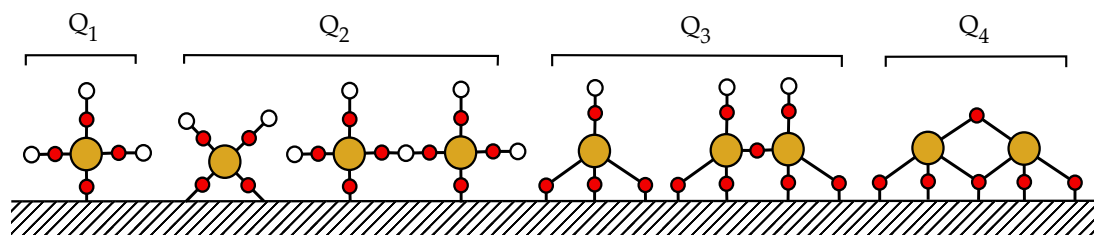


**Figure 3.1.** Scheme of silica surface with  $Q_1$ ,  $Q_2$ ,  $Q_3$ ,  $Q_4$  notation for  $SiO_4$  centers.

### 3.1.2.2 Alumina

Bauxite is the major source of alumina ( $Al_2O_3$ ) worldwide. The process of producing pure alumina from bauxite ore (by the Bayer process) has changed very little since 1893. The different aluminium minerals present in bauxite (e.g., gibbsite, boehmite) are selectively extracted from the insoluble components (e.g., quartz, iron, clay, titanium oxide) [145].

The dehydroxylation by heating treatment of aluminium trihydrates (gibbsite, bayerite and nordstrandite), monohydrate (boehmite) or hydroxide gels (the most important is pseudoboehmite) leads through different sorts of intermediate hydrates (transition aluminas) to anhydrous  $\alpha$ -alumina (Figure 3.2) [146]. At least six different transition alumina phases ( $\chi$ ,  $\delta$ ,  $\gamma$ ,  $\eta$ ,  $\kappa$ ,  $\theta$ ) have been claimed using various techniques, including  $^{27}Al$  MAS NMR [147, 148]. From these transitions,  $\gamma$ -alumina is perhaps the most extensively studied and used in catalysis because of its high porosity and specific surface. The structure of  $\gamma$ -alumina is traditionally considered as a cubic defect spinel type. The defective nature derives from the presence of only trivalent Al cations in the spinel-like structure [149].

From an enzyme immobilisation point of view,  $\gamma$ -alumina could represent an interesting alternative to silica-based supports [144].

The history of controlled synthesis of mesoporous alumina has been far more tortuous than for mesoporous silica-based materials. In 2002, Zhang and Pinnavaia

## Selection of the system of study

---

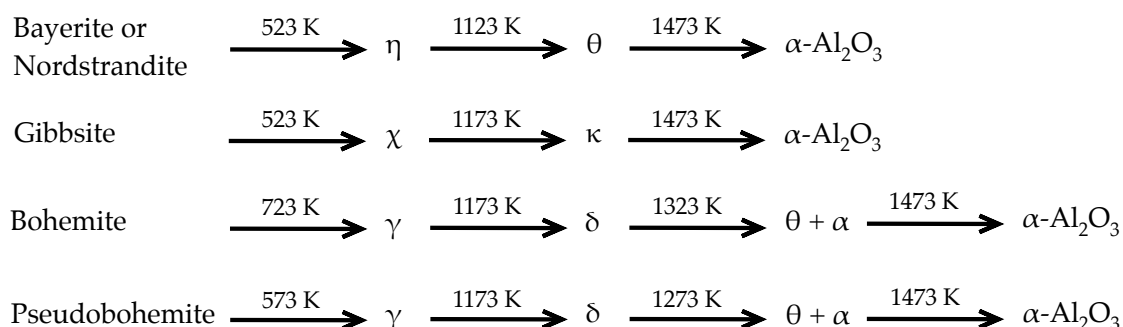


**Figure 3.2. Thermal transformation sequence of aluminium trihydroxides and monohydroxides.**

[150] reported the first successful synthesis of  $\gamma$ -alumina with a uniform pore size distribution by condensation of aluminium alkoxide in the presence of neutral polyethylene oxide surfactants. Since then, similar procedures have been developed for the synthesis of mesostructured alumina [151]. Nowadays, it is possible to find a wide variety of mesoporous aluminas commercially available with customised pore size and particle size distributions (e.g., PURALOX®, CATALOX®).

An interesting property of aluminas is their amphoteric character. They possess acidic and basic properties that are controlled by the surface groups. Upon exposure to a moist environment at low temperature ( $< 500\text{ K}$ ) the surface of a metal oxide undergoes a series of chemical reactions that are largely dictated by the chemistry of the cations. The first step in surface hydration involves the formation of surface hydroxyl groups followed by molecular adsorption. Protons attached to bridging oxygen sites behave as Brønsted acids, whereas the  $\text{OH}^-$  ions adsorbed to the cation sites behave as Brønsted bases. Additionally, the degree of unsaturation of  $\text{Al}^{+3}$  ions sites defines the strength of their Lewis acid character on surface.

Among the different surface model and site configurations reported in the literature, the model proposed by Knözinger and Ratnamasy [152] in the late 1970s is still the most accepted (Figure 3.3) where a minimum of five different OH configurations should be expected to exist on the surface of  $\gamma$ -alumina.

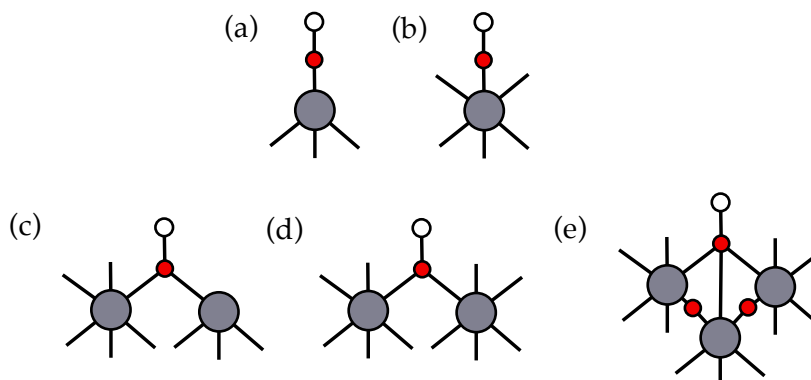


**Figure 3.3.** Types of OH- groups on the surface of alumina. (a) A terminal OH group is coordinated to a single tetrahedral Al<sup>3+</sup> cation, (b) the OH group is coordinated to a single cation in an octahedral interstice, (c) a bridging OH group links a tetrahedral and an octahedral cation; (d) the OH group links two cations in octahedral positions, and (e) the OH group is coordinated to the three cations in octahedral interstices [152].

### 3.1.3 Oxirane functional polymers

Many types of polymer bearing active functionalities have been studied for enzyme immobilisation. They include carriers bearing the functionalities such as acyl azide, acid anhydride, epoxy, isothiocyanate, aldehyde, activated esters, etc. [66, 72].

The first examples of synthetic polymers bearing oxirane functional groups for enzyme immobilisation can be dated to the mid-1970s [153, 154]. Since then, their capabilities as supports for industrial application have been proven [6, 155-158].

#### 3.1.3.1 Eupergit®

A popular and commercially available acrylic resin with epoxide pendant groups is Eupergit®, widely used as enzymatic support [159]. Eupergit® is a macroporous copolymer of N, N'-methylene-bis-(methacrylamide), glycidyl methacrylate, allyl glycidyl ether and methacrylamide (Figure 3.4a) with an average particle size of 180 µm [155]. It is a relatively hydrophilic polymer with a water retention capacity of 3 g

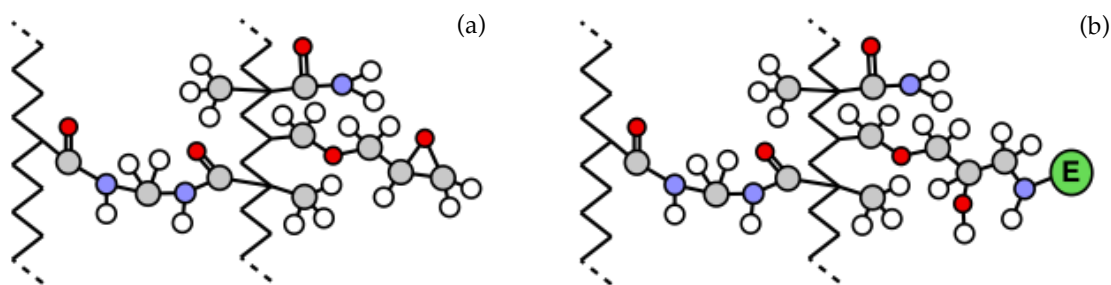


**Figure 3.4. Eupergit® support before (a) and after (b) immobilisation.**

of water per gram of polymer, and is very stable chemically over a pH range from 0 to 14.

Two different pore sizes have been produced by Evonik Industries (previously by Röhm and Haas), Eupergit® C and C 250 L (Appendix A, Table A.3). Both Eupergit® C and C 250 L are microporous, epoxy-activated acrylic beads with a diameter of 100-250  $\mu\text{m}$ . They differ in the content of oxirane groups and in their porosity. While Eupergit® C has an average pore size of 100  $\text{Å}$  and an oxirane density of 600  $\mu\text{mol g}^{-1}$  dry beads, Eupergit® C 250 L has larger pores (1000  $\text{Å}$ ) and a lower oxirane density (300  $\mu\text{mol g}^{-1}$  dry beads) [159]. The main advantages of immobilisation on Eupergit® is the increase in resistance to thermal and pH denaturation, and to the shear forces under reactor condition (i.e., stirred tank). Changes in pH and salt concentration have no effect on matrix swelling and it is therefore a good support candidate for fixed bed reactors. The enzyme loading is usually 10-100 mg protein  $\text{g}^{-1}$  carrier with activity retention usually below 50% [159].

### 3.2 Enzyme

$\alpha$ -Chymotrypsin was chosen as a convenient enzyme model in this thesis on which to test out methods used in Chapter 5 to Chapter 7. Also the availability of known fluorinated inhibitors was one factor (see Section 3.2.2.3).

The enzyme immobilisation methodology selected must be a well studied process. Therefore, the immobilisation of  $\alpha$ -chymotrypsin onto silica particles was chosen as the primary system. The immobilisation of the enzyme to the solid support is via covalent binding with the selected graft molecule (GOPS).

### 3.2.1 $\alpha$ -Chymotrypsin

#### 3.2.1.1 General features of structure and action

$\alpha$ -Chymotrypsin (Figure 3.5) has been extensively studied because it is small (25 kDa), easily obtainable in large quantities and relatively stable.  $\alpha$ -Chymotrypsin is produced in the pancreas and plays a role in digestion by hydrolysing polypeptide chains that contain aromatic amino acids. This enzyme was one of the first four enzyme structures to be solved by X-ray crystallography [160] and NMR studies [161] of these proteases were underway by the early 1970s. The polypeptide chain of  $\alpha$ -chymotrypsin comprises 245 amino acids arranged in two six-stranded beta barrels. The active site is located between the two barrels [162, 163]. The active site is generally divided into catalytic, substrate recognition and zymogen activation domain component that are common to all chymotrypsin-like serine proteases [164]. These three processes involve many of the same structural features and are intricately interlaced.

The  $\alpha$ -chymotrypsin possesses its optimum activity at pH 8.2 and its isoelectric point is 9.1. The molecule is a compact ellipsoid of dimensions  $51 \times 40 \times 40 \text{ \AA}$  [165].

$\alpha$ -Chymotrypsin is a serine protease, one of the most widely studied groups of proteases. These enzymes cleave peptide bonds by the attack of an activated serine residue on the carbonyl group of the bond. Serine proteases are classically categorised by their substrate specificity: trypsin-like (Lys/Arg preferred), chymotrypsin-like (large hydrophobic residues such Phe/Tyr/Leu) or elastase-like

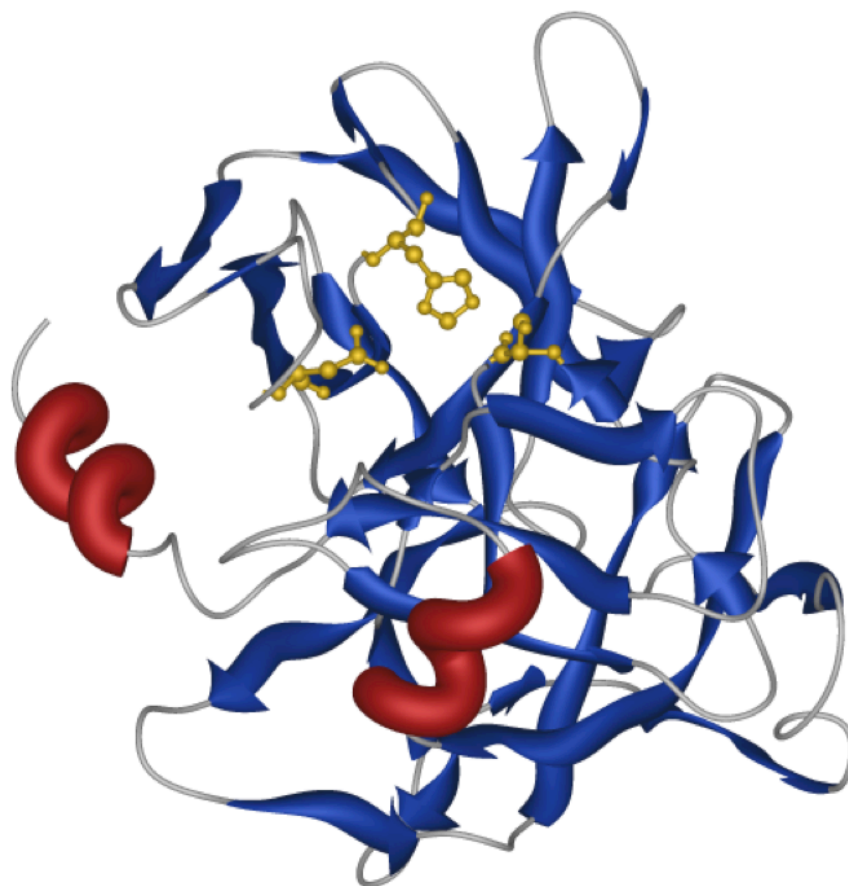


**Figure 3.5. Structure of  $\alpha$ -Chymotrypsin (PDB code 1CHG) [168]. This figure was produced with iMol v 0.4.**

(small hydrophobic residues such as Ala/Val) [166]. Serine proteases that do not belong to any of those categories are the subtilisins, which possess a broad specificity.  $\alpha$ -Chymotrypsin belongs to the chymotrypsin-like family, the largest group, and contains a deep hydrophobic pocket as is shown in Figure 3.5, which results in the enzymes specifically binding to substrates/inhibitors containing an aromatic and/or hydrophobic group that can fit into this pocket. The catalytic triad consists of His57, Asp102 and Ser195 [167] (Figure 3.6). In Figure 3.5 these three residues are labelled in yellow.

Currently, there are three different catalytic mechanism theories of how the triad works in serine proteases: the conventional (Figure 3.7), the low-barrier H-bond and

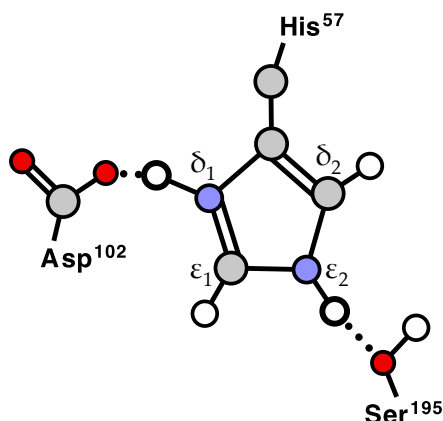


**Figure 3.6.** Scheme of catalytic triad of resting serine protease at low pH proposed by reference [162].

more recently the imidazole ring flip theory. The strongest theory to explain the mechanism of the catalytic triad of serine proteases is the charge-relay model of Blow *et al.* [162] (see Figure 3.7).

Since 1969 [162] there have been more than forty years of studies in this field and yet a detailed picture is still not completely clear about the structure and chemical properties of the triad. At that time all the theory around serine active site was supported by X-ray diffraction data. X-ray crystallography has been essential to unveil the mechanism of the catalytic triad on serine proteases but controversies in this field have arisen, some of them deriving from a major big pitfall of the technique; the high salt concentrations needed.

Further NMR studies supported the theory of Blow *et al.* (see Section 3.2.1.4) which postulates that the triad functioned as a ‘charge relay system’ where protons were relayed towards a buried aspartic acid in the hydrophobic interior of the protein (Asp102) and where electrons were relayed towards the serine residue 195 producing the net effect of a strong nucleophile (Ser195).

## Selection of the system of study

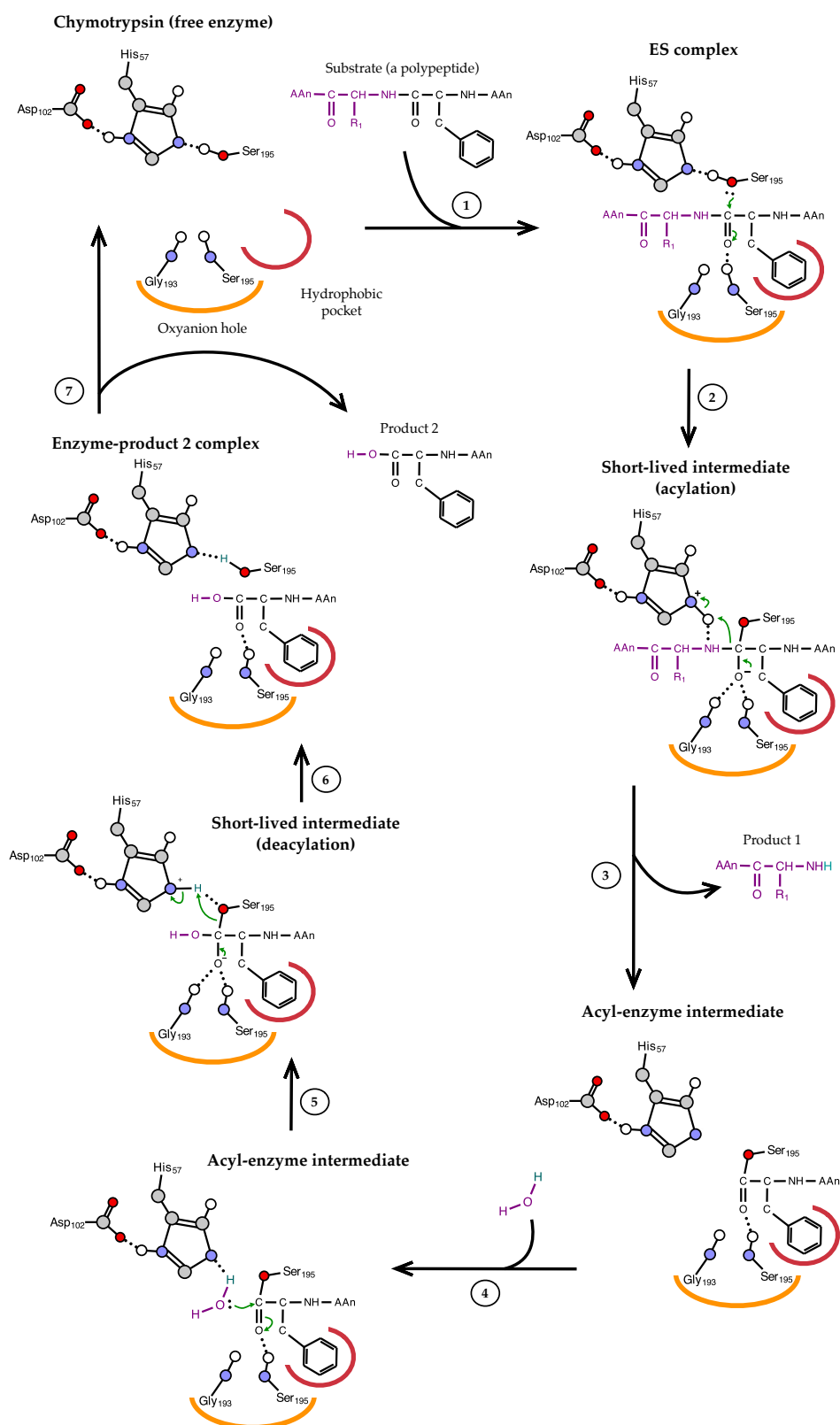


Figure 3.7. Conventional mechanism of hydrolytic cleavage of a peptide bond by chymotrypsin.

### 3.2.1.2 Conventional mechanism

Figure 3.7 summarises the conventional hydrolytic cleavage mechanism [169] of a peptide bond by chymotrypsin. First (step ①) the substrate binds the active site of the enzyme; the side chain of the residue adjacent to the peptide bond to be cleaved nestles in a hydrophobic pocket on the enzyme; the peptide bond is positioned for attack. After this (step ②), the interaction of Ser195 and His57 generate a strong nucleophilic alkoxide ion on Ser195 and the ion attacks the peptide carbonyl group forming a tetrahedral intermediate enzyme. This is accompanied by formation of a short-lived negative charge on the carbonyl oxygen of the substrate that is stabilised by hydrogen bonding in the oxyanion hole.

Afterwards (step ③) the instability of the negative charge on the substrate carbonyl oxygen leads to collapse of the tetrahedral intermediate; re-formation of a double bond with carbon displaces the bond between carbon and the amino group of the peptide linkage thereby breaking the peptide bond and forming an acyl-enzyme intermediate. The amino leaving group is protonated by His57, facilitating its displacement. In step ④ an incoming water molecule is deprotonated, generating a strongly nucleophilic hydroxide ion. A second tetrahedral intermediate is generated by an attack of hydroxide on the ester linkage of the acyl-enzyme, with oxygen in the oxyanion hole again taking on a negative charge. The deacylation, step ⑤ and ⑥, collapses the tetrahedral intermediate and forms a carboxylate anion and displaces Ser195. Finally in step ⑦ the release of the second product is followed by the regeneration of the active site [169].

### 3.2.1.3 Catalytic components

#### *The Oxyanion Hole*

The oxyanion hole was first noted by Henderson [170]. The hole is formed by the backbone NHs of Gly193 and Ser195. These atoms form a pocket of positive charge

that activates the carbonyl of the scissile peptide bond and stabilises the negatively charged oxyanion of the tetrahedral intermediate (Figure 3.7) [170, 171]. Crystal structures of several transition state analogue complexes confirm this interaction [172-174].

### *The Substrate Recognition Sites*

The active site of proteases contains several S pockets, which accommodate consecutive amino acids (called P sites) towards the N-terminal of the peptide. In a similar way, S' and P' sites exist towards the C-terminal from S1' and P1', respectively (Figure 3.8). These sites determine the substrate specificity through the size, shape and charge of the side chains involved. The compatibility and fit between the S sites in the substrate-binding pocket and the substrate P sites are influenced by the three-dimensional structure of the substrate when it is bound to the enzyme.

The S1 site is a pocket adjacent to Ser195, formed by residues 189-195, 214-220 and 225-228. The residues at positions 189, 216 and 226 usually determine specificity [175, 176]. The specificity of chymotrypsin correlates with the hydrophobicity of the P1 residue, with P1 as Phe preferred over Ala by 50000 times [177]. The combination of Ser189, Gly216 and Gly226 create a deep hydrophobic pocket (Figure 3.7) in chymotrypsin [163].

Enzyme-substrate interactions are not restricted only to the S1 site. Often in serine proteases there are additional binding pockets for the backbone of the peptide substrate. In chymotrypsin hydrogen bonds are formed between the peptide substrate and polypeptide binding site formed by residues 214-216. The polypeptide binding site also forms one wall of the S1 site and the residue 214 (Ser) forms a hydrogen bond to His57 showing the intertwined connection between all processes on the active site.

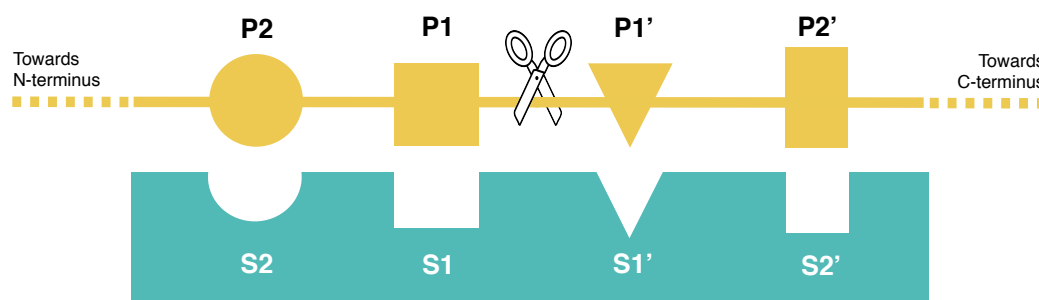


**Figure 3.8.** The substrate recognition sites of proteases. The active site of a protease (blue) is composed of several substrate-binding subsites (S). The nomenclature of the S sites (S1, S2, S1' and S2') is concordant with the P sites of the peptide substrate (yellow). S<sub>n</sub> sites are amino-terminal to the scissile bond (indicated by scissors) and S<sub>n</sub>' sites are carboxy-terminal to the scissile bond.

### *Zymogen Activation Domain*

Chymotrypsin is synthesised as an inactive precursor or zymogen where the latter has different segments deformed. These deformed regions include the S1 site and the oxyanion hole, which explains the low activity of the zymogen. A proteolytic process activates the zymogen releasing the N-terminal Ile16 [178]. The new N-terminus forms a buried salt bridge with Asp194 that induces a conformational change activating the enzyme. An interesting fact is that loss of activity at high pH is attributed to the deprotonation of the N-terminus and the disruption of the Ile16-Asp194 salt bridge changing the conformation to an inactive zymogen-like conformation [179, 180].

#### 3.2.1.4 NMR observation of active site <sup>1</sup>H signals

The current understanding of active site H-bonding in serine proteases has been revealed principally by NMR and X-ray crystallography. This section summarise the most important contributions in the study of hydrogen bonds in the active site of serine proteases – focused on chymotrypsin-like proteases – by NMR spectroscopy.

### *Asp<sup>102</sup>-His<sup>57</sup> H-bond*

An important discovery was made in 1972 by Robillard and Shulman [161]: the first direct observation of a single proton signal from the active site of chymotrypsin and chymotrypsinogen (zymogen or precursor of chymotrypsin), using continuous-wave (CW) solution-state <sup>1</sup>H NMR. The signal was titrated from ~ 18 to ~ 15 ppm with increasing pH, exhibiting a pKa value of 7.5. They assigned this signal to the proton in the Asp102-His57 H-bond [162] due to two observations: the signal seems invariable in serine proteases (e.g., trypsin, trypsinogen, subtilisin) but not in other proteins, and alkylation of His57 at N<sup>ε2</sup> causes the signal to become pH independent. This assignment was supported by subsequent NMR studies [181-183].

### *His<sup>57</sup>-Ser<sup>195</sup> H-bond*

As has been mentioned previously, the tetrahedral intermediate formation is crucial for the catalytic activity of serine proteases. One of the players in this configuration is the His57-Ser195 couple. When Robillard and Shulman [161, 184, 185] discovered the Asp102-His57 H-bonded proton resonance at low field, they failed to detect a corresponding high frequency signal for the His57-Ser195 H-bond.

Markley and Westler [186] accomplished the direct observation, more favourable at low pH, of the His57-Ser195 H-bonded proton. This proton resonates at a chemical shift of ~ 13 ppm [187]. Its visibility is favoured at low, rather than high, pH. Probably, this effect is due to slowing or preventing of acid-base mechanisms at low pH.

### *His<sup>57</sup>-Ser<sup>214</sup> H-bond*

Among chymotrypsin-like proteases, a backbone amino acid – Ser214 – contributes to the substrate binding. In Figure 3.9 it is possible to observe that this residue does not belong to the catalytic triad.

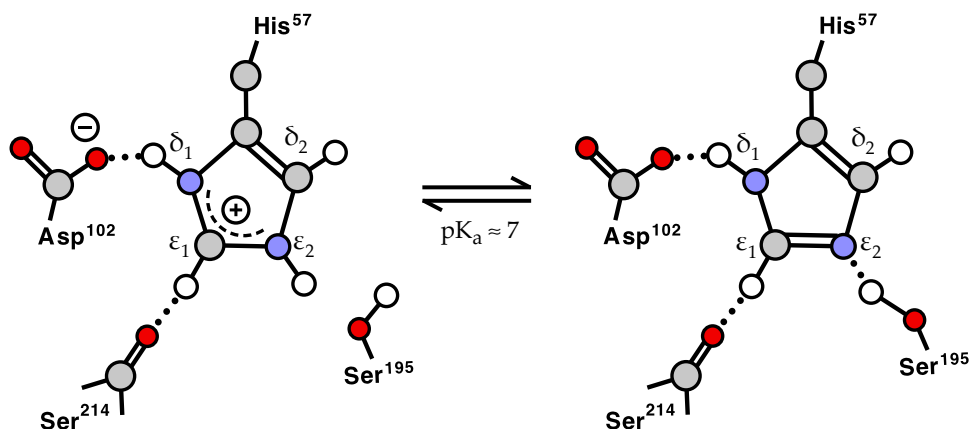


Figure 3.9. Scheme of current model of active site of resting serine protease.

The proton donor in an H-bond is thought to be very electronegative, e.g., O or N. Although carbon is not particularly electronegative, the idea that carbon-bound protons can act as H-bond donors was first proposed more than 60 years ago [188, 189] starting the controversy about the existence of this type of H-bond. In the early 1960s evidence of this kind of bond was provided in biological molecules [190]. Finally, after several years of debate, the belief that carbon-bound protons can act as H-bond donors has now become widely accepted [191, 192].

Derewenda *et al.* [193] proposed the existence of an additional H-bond in the serine proteases triad between the C<sup>ε1</sup>-H proton of His57 and a backbone carbonyl oxygen atom from the residue 214 (Figure 3.9) after analysis of more than 30 X-ray structures of different serine hydrolases. In 2000, Ash *et al.* [194] linked an unusual high frequency proton resonance with the interpretation that such chemical shift reflected the existence of carbon-H donated H-bonds. This proton signal resonates at 9.22 ppm for a protonated His57 in a  $\alpha$ -lytic protease. Not many further studies have been able to prove the existence of this bond.

### 3.2.2 Enzyme interactions

#### 3.2.2.1 Water

To perform their functionalities, enzymes require certain levels of water to sustain their conformational structures and this affects the ionisation and mobility of groups at the protein surface. Water molecules are also important in the interaction of enzymes with their reactants and products, either because they must be displaced in the process, or in some cases when they make bridging interactions. The presence of water does not always lead to positive results as regards enzyme performance. It is well known that extra water contributes to a decrease in the thermostability of the enzyme [195].

To understand from a mechanistic point of view the importance of water on an enzyme it would be ideal to know the amount of water bound to the enzyme molecules and, if possible, their location [196]. This task is not an easy one. Also it depends of the medium used: aqueous or organic.

Karl-Fischer analysis can give some information about the water in the system in an organic solution. The experiment has a restricted sensitivity and should be carefully designed so as to obtain information from real bound state water and not from the whole system [195]. Crystallography has been proven to be a useful technique for observing water in proteins [197] but with the usual drawbacks of the technique (e.g., high concentrations of salts on the structure and rigid conformation).

The extent of interaction between protein and water can also be monitored by studying the dynamic processes affecting proteins (see Section 2.3). Molecular dynamics simulations [198-200], supported by fluorescence spectroscopy [201, 202], inelastic neutron scattering [203] and NMR [204] experiments report rotational correlation times ranging for water-protein interactions from a few picoseconds for bulk water [199], up to nanoseconds for surface, and tens of nanoseconds for buried

water [204]. NMR provides several tools for examining events that occur on these different time scales, based on relaxation approaches, that are discussed in Section 2.3.1.

NMR methods can give qualitative and/or quantitative information about the water in both liquid and solid systems without the requirement of a crystalline order. Among the many different approaches used in NMR to study protein hydration, three interesting examples are: multiple-quantum relaxation of  $^{17}\text{O}$  nuclei [205-208] (discussed in Section 6.3), magnetic relaxation dispersion of  $^2\text{H}$  and  $^{17}\text{O}$  [209] and intermolecular  $^1\text{H}$ - $^1\text{H}$  nuclear Overhauser effects (NOEs)[210].

The type of support used for enzyme immobilisation can also have a role in the water dependent properties of a reaction system. This is due to the properties of the matrix, such as pore size, surface area and hydrophobicity of the support.

### 3.2.2.2 Ions

#### *Role of $\text{Ca}^{2+}$ in $\alpha$ -Chymotrypsin function*

Calcium ions are involved in a variety of important biological functions, many of which are accomplished through interactions with proteins.  $\text{Ca}^{2+}$  interacts with a number of extracellular proteins to confer thermal stability, protection against autolysis and is required for the activity of a number of enzymes. It has been known for many years that calcium ions stabilise chymotrypsin towards autolysis and denaturation [211, 212].

The existence of monomeric and polymeric forms of  $\alpha$ -chymotrypsin in solution is well established. The dimerisation of  $\alpha$ -chymotrypsin inactivates the enzyme since this binding involves the active site (acyl-enzyme dimers) [213]. Calcium ions have an inhibitory effect on this process impeding the dimerisation. Some evidence shows [214] that this effect is due to a displacement of the monomer-dimer equilibrium by

the specific interaction of the metal ion with a single site on the monomeric enzyme. Therefore, it is recommended, when free enzyme is used, that a relatively low concentration of  $\text{CaCl}_2$  (20 mM) is included to prevent dimerisation of the enzyme and therefore autolysis.

### *Role of $\text{Na}^+$ in $\alpha$ -Chymotrypsin function*

In Chapter 6, a TQF (triple quantum filtered) NMR experiment is used to study ion binding to biological molecules in solution [215]. Regulation of activity through metal ion complexation plays a key role in many enzyme-catalysed reactions.

$\text{Na}^+$  is the most abundant metal ion in extracellular fluids and second highest in abundance in ocean water after  $\text{Cl}^-$ . Molecular evolution has driven the incorporation of selective cation binding sites into many enzymes to enhance the activity, diversity, and/or stability of many enzymes [216].

Some experimental evidence exists to suggest that ion binding in enzymes substantially influences the enzyme-catalysed reaction. Ion binding may stabilise surface-exposed residues to increase overall thermal stability with little or no effect on catalysis. Cation binding has been noted to enhance the stability of a number of enzymes of mesophilic origin [216].

It is known that for S1 peptidases, a group of which  $\alpha$ -chymotrypsin is a member, the  $\text{Na}^+$  site lies immediately adjacent to Asp189 in the hydrophobic pocket (S1) of the enzyme and establishes a direct link with substrate binding. Furthermore, the  $\text{Na}^+$  binding influences the extended binding site of the enzyme [216].

Dang *et al.* [217] report that the catalytic activities of several serine proteases are enhanced allosterically by  $\text{Na}^+$  binding. This allosteric effect is due to the nature of residue 225 [217, 218]. Residue 225 is either a proline or tyrosine in the vast majority of serine proteases [219]. In the case of  $\alpha$ -chymotrypsin the residue 225 is proline,

and it is found in more ancestral proteases and practically all chymotrypsin-like proteases [220].

### 3.2.2.3 Inhibitors

Any compound that decreases the catalytic activity of an enzyme is by definition an inhibitor. In terms of inhibitor kinetics there are two large groups of inhibitors: reversible and irreversible.

Reversible inhibitors can bind to enzymes through weak non-covalent interactions such as ionic bonds, hydrophobic interactions and hydrogen bonds. Reversible inhibitors are properly classified according to the catalytic step with which they interact: competitive, uncompetitive and mixed type inhibitors. A competitive inhibitor competes with the substrate for the active site of an enzyme. While this type of inhibitor occupies the active site no substrate can bind to the enzyme. Increasing the concentration of substrate can overcome this type of inhibition. Uncompetitive inhibitors affect the chemical processing of the bound substrate in the active site without interfering with substrate binding. A mixed inhibitor binds at a site distinct from the substrate active site but also it binds at the active site.

The irreversible inhibitors are those that bind covalently causing chemical changes to the active site of enzymes and cannot be reversed. They often contain electrophilic groups (i.e., aldehydes, alkenes or phenyl sulphonates) that are able to react with amino acid side chains to form covalent adducts. The amino acid residues act as nucleophiles such as hydroxyl or sulfhydryl groups (e.g., amino acids serine, cysteine, threonine or tyrosine).

In general, non-covalent reversible inhibitors are preferred candidates for inhibition studies because they provide better selectivity and should cause fewer side effects than covalent inhibitors [221]. Non-covalent inhibitors are much more difficult to design. Possible methods for generating non-covalent inhibitors include designing

transition-state analogues (mimicking the transition state during substrate hydrolysis) or substrate variants (structures that retain functionality and scissile bond of the substrate destabilising transition states), but not substrate analogues, which generally produce covalent inhibitors [222].

The strength of the binding between an enzyme and a reversible inhibitor is defined by the dissociation constant,  $K_d$

$$K_d = \frac{[E_{free}][I_{free}]}{[EI_{bound}]} \quad 3.1$$

where  $[E_{free}]$ ,  $[I_{free}]$  and  $[EI_{bound}]$  are the concentrations of the free enzyme, free inhibitor and enzyme-inhibitor complex, respectively.

### *Serine protease inhibitors*

Serine proteases are ubiquitous in many biological processes and their deregulation is linked to many diseases (e.g., cancer, cardiovascular diseases, AIDS, hepatitis C) [223]. Therefore, there is significant interest in the area of protease-targeted therapies focused on drug discovery of inhibitors targeting serine proteases [221]. Organophosphates, sulphonyl fluorides, coumarins and boronic acids are some of the most widely used inhibitors of proteases. In this section boronic acids and their derivatives will be reviewed as inhibitors of chymotrypsin-like proteases.

### **Boron-containing inhibitors**

In the 1970s, boronic acids were first used as enzyme inhibitors for serine proteases [224-227]. The boron atom in boronic acid is usually  $sp^2$  hybridised (neutral, trivalent and planar) with an empty  $p$ -orbital. When the acid is in an aqueous solution, oxygen from water fills the empty orbital of boron and releases a proton to generate  $sp^3$  hybridised boron (tetravalent and tetrahedral), making it a Lewis acid (Figure 3.10a).

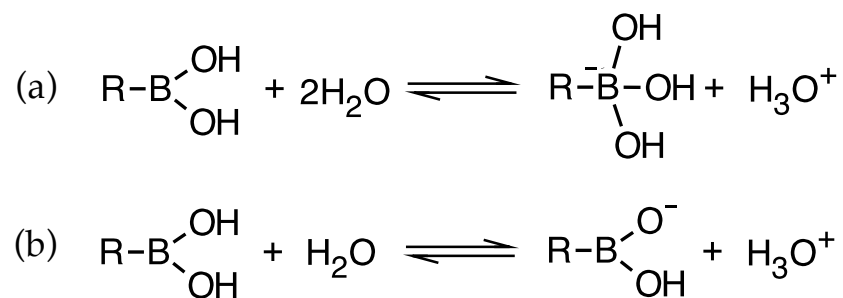


**Figure 3.10. Ionisation equilibrium of boronic acids in water as a (a) Lewis acid or as a (b) Brønsted acid.**

Only in exceptional cases do boronic acids act as Brønsted acids (Figure 3.10b) (e.g., coordination of hydroxide ion to boron in heterocyclic boronic acids) [228].

The tetrahedral geometry of  $sp^3$  hybridised boron in boronic acids is the one that can mimic the enzyme-catalysed substrate tetrahedral transition state and the reason why boronic acid compounds can be used as enzyme inhibitors.

Aryl and arylalkyl boronic acids were the first boronic acids reported to be strong competitive inhibitors of chymotrypsin [183, 224, 226, 229-231] with dissociation constants,  $K_d$ , in the millimolar order.

Robillard and Shulman [184] in 1974 reported the first study of different boronic acids (boric acid, phenylboronic acid and 2-phenylethylboronic acid) complexes with the active site of serine proteases by  $^1\text{H}$  NMR. They observed that the high frequency proton in the Asp102-His57 H-bond moved to an intermediate position (15-16 ppm) between low and the high pH chemical shifts.

The design and synthesis of more potent, reversible and selective boronic acids possessing specific peptide moieties have been developed since. Some of these successful transition state analogues of  $\alpha$ -chymotrypsin are benzamidomethaneboronic acid (Figure 3.11a) [232] and 1-acetamido-2-phenylethaneboronic acid (Figure 3.11c) [233], with dissociation constants,  $K_d$ , of around the nanomolar range. Matesson *et al.* [233] found that R

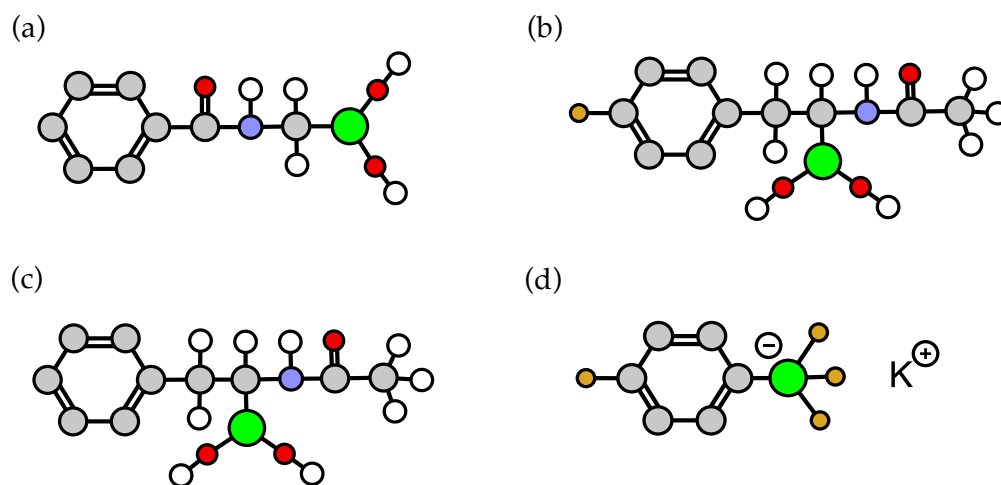


**Figure 3.11.** Structure of some boron-containing inhibitors of  $\alpha$ -chymotrypsin. (a) benzamidomethaneboronic acid, (b) 1-acetamido-2-(4-fluorophenyl)ethane-1-boronic acid, (c) 1-acetamido-2-phenylethane-boronic acid, and (d) potassium 4-fluorophenyltrifluoroborate. Aromatic protons are not included for structure simplicity.

isomers of the phenylalanine derivative inhibitor (Figure 3.11c) bind tighter than S isomers. The performance of this analogue as inhibitor of  $\alpha$ -chymotrypsin was slightly better than benzamidomethane boronic acid at same pH.

Some years later, Bachovchin *et al.* [234] observed that not all boronic acids inhibitors behave in the same way as transition state mimics. Using  $^{15}\text{N}$  NMR they examined the active site of  $\alpha$ -lytic protease in presence of different boronic acids. They concluded that boronic acids that resemble the structure of natural substrates of serine proteases, such as phenylalanine, form complexes in which the imidazole ring of the active site is protonated. In these complexes both N-H protons are strongly hydrogen bonded – type 1 complexes – and tend to have high affinities for the enzyme (Figure 3.12a). Boronic acids with structures that are not well related to that of the substrate tend to coordinate covalently between  $\text{N}^{\epsilon 2}$  of His57. These boronic acids form type 2 complexes with the active site, resulting in a histidine-boronate adduct with lower binding affinities (Figure 3.12b) [234].

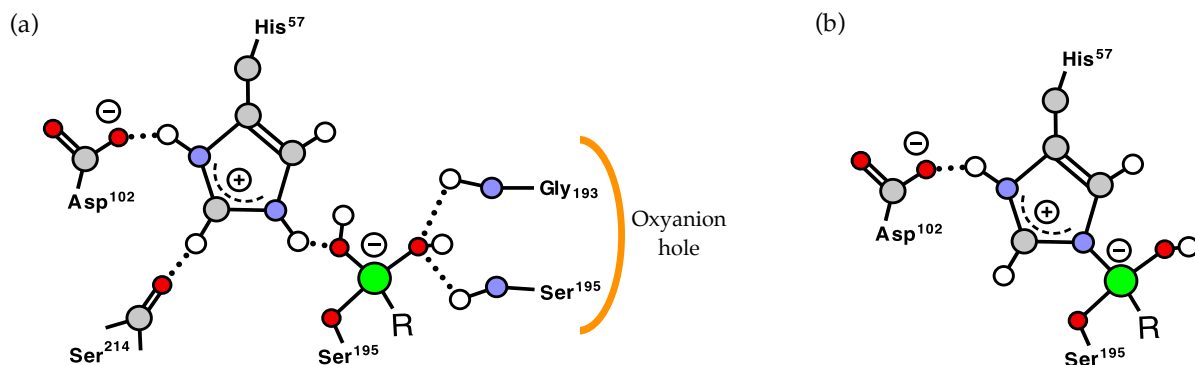


**Figure 3.12.** Scheme of serine protease boronic acid complexes. (a) Type 1 (serine adduct) and (b) type 2 (histidine adduct).

Type 1 complexes should exhibit two signals in the low-field region of the  $^1\text{H}$  NMR spectrum. On a  $\alpha$ -lytic protease, using BoroVal (MeO-Suc-Ala-Ala-Pro-boro-Val-OH) as inhibitor, the  $\text{N}^{\delta^1}\text{-H}$  and  $\text{N}^{\epsilon^2}\text{-H}$  protons for type 1 complexes resonate at  $\sim 16.0$  and  $\sim 16.5$  ppm, respectively. Both signals were assigned unambiguously by  $^{15}\text{N}$  NMR [234]. The fact that  $\text{N}^{\epsilon^2}\text{-H}$  resonates further at higher frequency than  $\text{N}^{\delta^1}\text{-H}$  indicates that  $\text{N}^{\epsilon^2}\text{-H}$  forms the stronger of the two H-bonds. In 1995, Zhong *et al.* [235] observed similar results for BoroPhe (MeO-Suc-Ala-Ala-Pro-boro-Phe-OH) and BoroVal-chymotrypsin complexes with two pH invariable chemical shifts. They assumed the assignment by Bachovchin *et al.* [234] of  $\text{N}^{\delta^1}\text{-H}$  and  $\text{N}^{\epsilon^2}\text{-H}$  protons at  $\sim 16.0$  and  $\sim 17.0$  ppm, correspondingly. In 1998, Bao *et al.* [236] studied the complexes of chymotrypsin and subtilisin with BoroPhe. This research exposed the fact that the assignments adopted in the study of Bachovchin and co-workers's for  $\alpha$ -lytic protease [234] for  $\text{N}^{\delta^1}\text{-H}$  and  $\text{N}^{\epsilon^2}\text{-H}$  protons were probably confused with other serine proteases complexes [235]. Bao *et al.* conclude that the higher frequency proton signal belongs to  $\text{N}^{\delta^1}\text{-H}$  and the lower frequency signal to  $\text{N}^{\epsilon^2}\text{-H}$ , reversing previous beliefs for chymotrypsin-peptideboronate serine adducts complex.

Type 2 inhibitors gave rise to a single pH independent resonance at low frequency ( $\sim 15.5$  ppm) for  $\alpha$ -lytic protease inhibited by benzeneboronic acid [234]. These results are consistent with Robillard and Shulman's early  $^1\text{H}$  NMR work [184] on a

boric acid-chymotrypsin complex. This showed a single high frequency resonance at  $\sim 15$  ppm, confirming that this complex behaves as a His adduct.

$^{19}\text{F}$  NMR has been proven as an effective probe for biological interactions. The  $^{19}\text{F}$  nucleus has excellent NMR properties that are comparable to those of the proton NMR (Table 2.1). Strong dipolar coupling allows  $^{19}\text{F}$ - $^{19}\text{F}$  and  $^1\text{H}$ - $^{19}\text{F}$  nuclear Overhauser effects to be measured [237]. One of the most useful and simple features of  $^{19}\text{F}$  nucleus is the intrinsic sensitivity of its chemical shift to changes in the local chemical environment, with a range of  $\sim 400$  ppm against 15 ppm for the  $^1\text{H}$  nucleus [238].

Sylvia and Gerig [239, 240] were among the promoters of an interesting approach to studying boronic acids interacting with serine proteases. They attached a fluorine atom to the phenyl ring of 1-acetamido-2-phenylethaneboronic acid (Figure 3.11b) so that information could be conveniently obtained from the fluorine-containing  $\alpha$ -chymotrypsin-inhibitor complex. The  $^{19}\text{F}$  NMR spectrum of such a system exhibited two resonances, one at the chemical shift characteristic of the inhibitor in the absence of the protein and another 2.34 ppm to higher frequency. They assumed that the high frequency signal arose from inhibitor molecules bound to the enzyme.

Fluorine relaxation in labelled proteins is dominated by proton-fluorine dipolar interactions which can be studied using heteronuclear  $\{^{19}\text{F}, ^1\text{H}\}$  NOE [241]. With this in mind, Sylvia and Gerig [239] carried out a two-dimensional  $\{^{19}\text{F}, ^1\text{H}\}$  NOE experiment of  $\alpha$ -chymotrypsin in the presence of the fluorine-containing inhibitor (Figure 3.11b). H-F cross peaks were observed with the fluorine signal representing the bound inhibitor (Figure 3.13). The highest frequency cross peak at  $\sim 6.9$  ppm in Figure 3.13, is very likely to be a result of an intra molecular NOE effect between the aromatic protons of the fluoroaromatic ring of the inhibitor. Similar results were obtained by Hammond, using a fluorine-containing carbazate [242], for an acylated

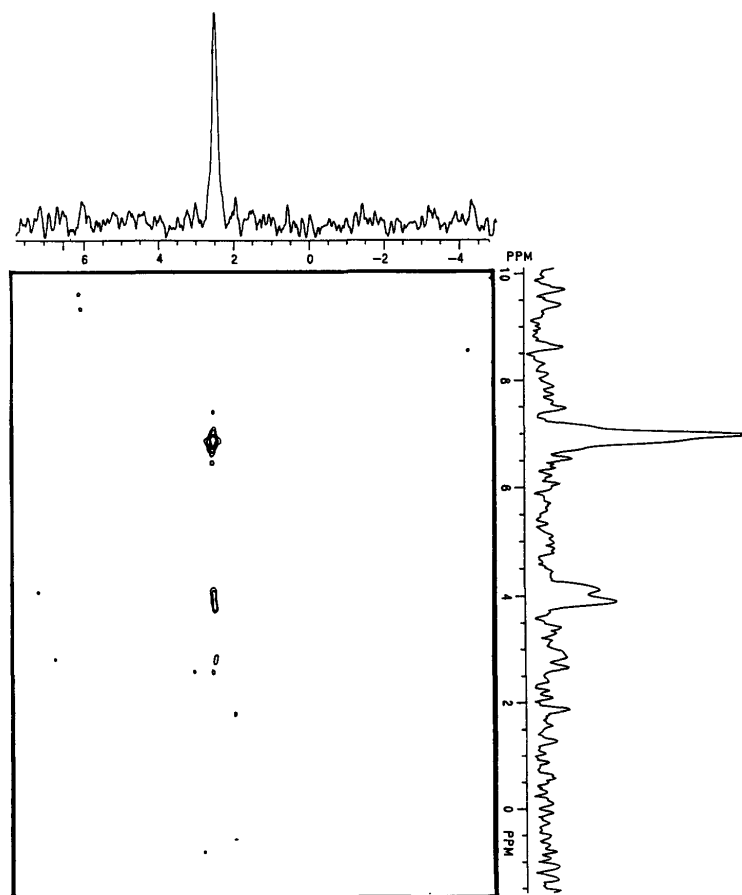


**Figure 3.13.** Two-dimensional  $\{^{19}\text{F}, ^1\text{H}\}$  spectrum of  $\alpha$ -chymotrypsin-(R)-1-acetamido-2-(4-fluorophenyl)ethane-1-boronic acid complex from reference [239] at 282 MHz. The concentrations of enzyme and inhibitor were 1.5 and 3.0 mM, respectively. The mixing time was 200 ms.

form of  $\alpha$ -chymotrypsin. These results suggest that the other cross peaks on the twodimensional spectrum are possibly related to the hydrophobic pocket.

The studies by Sylvia and Gerig [240] of the enzyme-inhibitor complex at different pHs by  $^1\text{H}$  NMR gave similar results to those obtained by Zhong et al. [235] with another type 1 boronic acid inhibitor.

Organotrifluoroborates are a new class of air-stable boronic acid derivatives. They are not sensitive to oxygen or moisture and are more stable than their corresponding organoboronic acid or ester [243]. The majority of the applications of organotrifluoroborate are located in the area of organic synthesis [244]. Recently, it

has been discovered that trifluoroborates can play a role in therapeutic applications such as analgesics [245], for the treatment of thyroid dysfunctions [246], and as inhibitor of serine proteases [247]. A disadvantage of R-BF<sub>3</sub>K salts is their instability in the presence of silica-gel [248] or other “fluorophiles” such as alumina [249]. There is a rapid equilibrium with free fluoride ions and the fluorophile binds the free fluoride ions pulling the equilibrium over towards hydrolysis.

In 2005, Smoum and co-workers [247] evaluated the inhibitory activity of different boronic acids and their respective salts on serine proteases. The salts were found to be noncovalent, competitive and reversible inhibitors of serine proteases. They exhibited an increase of inhibition by at least an order of magnitude over the corresponding boronates for  $\alpha$ -chymotrypsin and trypsin, with dissociation constants in the millimolar order. One of these organoborate salts, trifluoro-4-fluorophenylboronate (Figure 3.11d), was studied by <sup>19</sup>F NMR in the same contribution (Figure 3.14). Four signals arise from a mixture of  $\alpha$ -chymotrypsin and the organotrifluoroborate. They assigned two of these signals to the fluorines in the unbound inhibitor: -136 (F-B) and -114 ppm (aromatic).

The other two resonances were assumed as the bound inhibitor to the enzyme at -133 (F-B) and -107 ppm (aromatic). These assignments are not supported with complementary NMR data. Smoum *et al.* [247] postulate that the high frequency shift between the free and the bound state of the inhibitor arise from the formation of a hydrogen bond between the oxyanion hole and N-H and O-H groups from the active site (Figure 3.15).

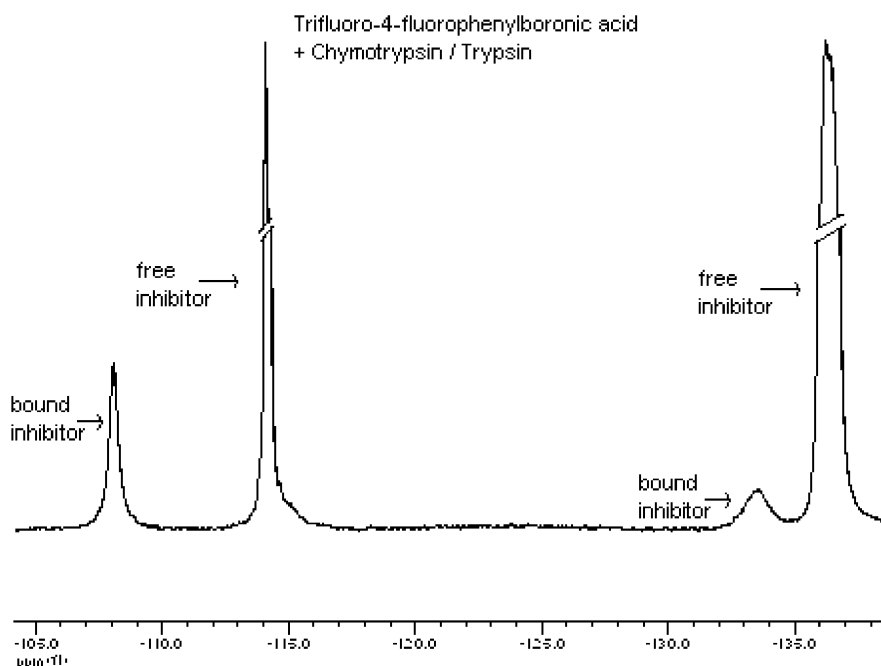


Figure 3.14.  $^{19}\text{F}$  NMR spectrum of  $\alpha$ -chymotrypsin and trifluoro-4-fluorophenyl-boronate from reference [247] at 282 MHz. The concentration of enzyme and inhibitor used were 0.08 mM and 0.602 mM, respectively.

### 3.3 Method of Immobilisation

As seen in section 2.5.1, there are many methods of immobilisation. The covalent binding method was selected to be the method by which the enzyme is directly attached to the support. Being an irreversible method, there is no risk of enzyme leaching during experimentation. In this section, the method of immobilisation will be discussed, including the surface functionalisation of silica and alumina supports and the mechanism of immobilisation between the enzyme and the selected carrier bound group – CAG (oxirane group).

#### 3.3.1 Functionalisation of metal-oxide-based supports

The method most often used to functionalise inorganic support surfaces is to silanise an organosilane onto the surface of the support. The modification of silica surfaces by



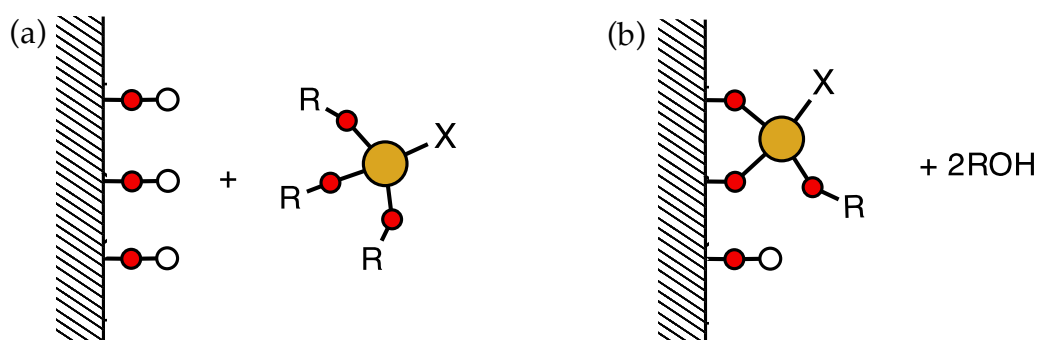


**Figure 3.16. Scheme of surface functionalisation of metal-oxide-based supports using trialkoxyorganosilanes. (a) Before and (b) after silanisation.**

generally preferred because it achieves higher loadings of functionalised surface than aqueous silanisation [250].

When a non-silica-based support is used instead, such as  $\text{Al}_2\text{O}_3$ , a quite similar reaction takes place and a covalent organosilane coating is formed [144]. An exceptional case is represented by  $\text{ZrO}_2$ , which under those conditions is incapable of forming Zr-O-Si bonds [253].

### 3.3.1.1 Oxirane functional metal-oxide-based supports

Some of the most widespread organosilanes used for functionalisation of inorganic supports for protein immobilisation are represented in Figure 3.17. Functionalised supports are usually not capable of reacting directly with the proteins. Only epoxy- or aldehyde-functionalised supports can directly couple with reactive amino acid residues (RARs) from the enzyme. In all the other cases, the support needs to be activated. Commonly, the activation consists of inserting an electrophilic function on the support surface [144].

A popular and commercially available organosilane used in surface modification is 3-(glycidoxypropyl)trimethoxysilane. Figure 3.18 shows a representation of the different species expected on functionalised surface with GOPS. A similar surface is expected when the same organosilane is tethered to an  $\text{Al}_2\text{O}_3$  surface. All these

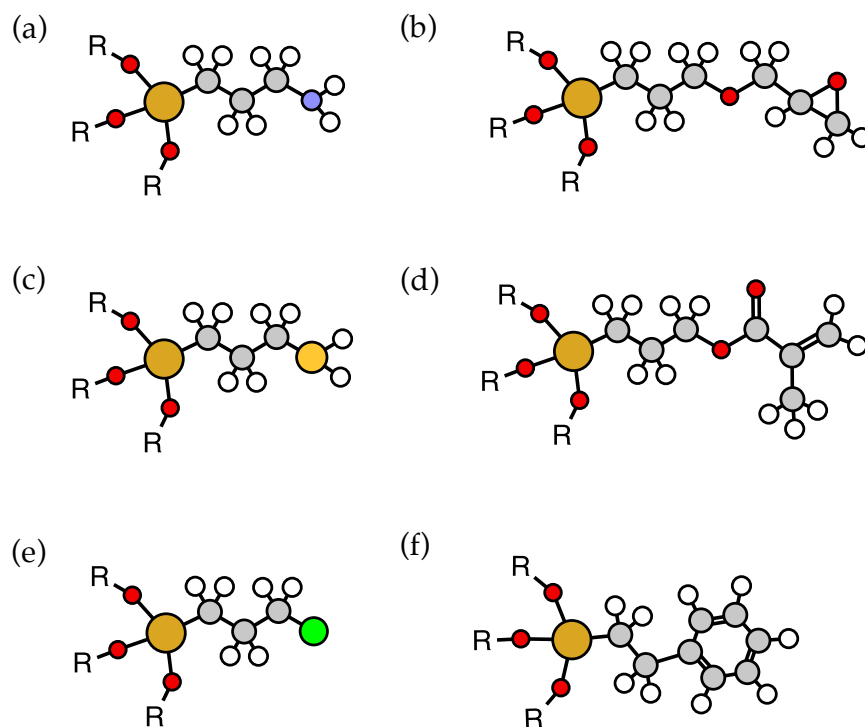


**Figure 3.17.** Organosilanes used in the functionalisation of metal-oxide-based supports. (a) (3-Aminopropyl)triethoxysilane, (b) (3-glycidyloxypropyl)triethoxysilane, (c) (3-mercaptopropyl)trimethoxysilane, (d) 3-(trimethoxysilyl)propyl methacrylate, (e) (3-chloropropyl)triethoxysilane, and (f) trimethoxy(2-phenylethyl)silane.

species can be observed by  $^{29}\text{Si}$  NMR, and by  $^{13}\text{C}$  NMR it is possible to observe the different carbons on the chain.

### 3.3.2 Mechanism of covalent binding via epoxide groups

The reaction type between epoxide groups and reactive amino acid residues (RARs) from the protein is a nucleophilic substitution. Protonation makes the epoxide group more electrophilic and creates a better leaving group. This makes the ring more susceptible to nucleophilic attack.

Epoxide groups can react with three different RARs: sulphhydryl group of cysteine, phenolic hydroxyl groups of tyrosine and amino groups of N-terminal amino acids and  $\epsilon$ -amino groups of lysine. Epoxy groups are quite stable especially at neutral pH

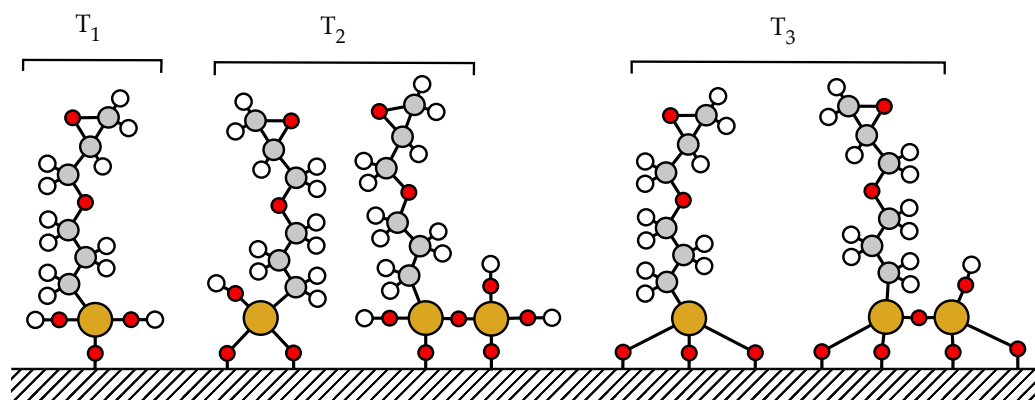


**Figure 3.18.** Scheme of epoxide-silica surface with T1, T2, T3 notation for R-SiO<sub>3</sub> centers, where R is an aliphatic carbon side chain.

and consequently are not highly reactive in mild conditions. Due to this, original epoxy supports hardly immobilise large amounts of protein. To overcome this problem, immobilisation in the presence of high ionic strengths has been used [254-258]. This is because the immobilisation occurs in two steps. Firstly, the enzyme is hydrophobically adsorbed on the surface due to a salt-induced hydrophobic interaction, followed by the covalent attachment between the nucleophile groups of the enzyme and the epoxy groups. The increase in protein concentration near the reactive epoxy groups leads to an increase in the rate of reaction.

In general, the most targeted reactive amino acid residue (RAR) in proteins for covalent binding is undeniably -NH<sub>2</sub>, both N-terminal  $\alpha$ -amino group and lysine  $\epsilon$ -amino group. This is for several reasons: it is widespread in almost all proteins, reactivity is optimal, lysine usually has a minor mechanistic relevance and is therefore not fundamental for retention of catalytic activity, a preferential exposed distribution of lysine residues (especially in an aqueous system) [259].

At the end of the immobilisation process, the remaining carrier bound group (CAG) can be easily blocked, if necessary, with thiol or amino compounds in mild conditions [260].

## CHAPTER 4

# Experimental

This chapter covers the analytical and experimental protocols used. Appendix F contains a list of the chemicals utilised in the protocols described in this section.

### 4.1 Quantification of Epoxide Groups

The amount of epoxide content (epoxy equivalent weight, EEW) on organosilane modified support and Eupergit® was determined by the non-aqueous titration of oxirane groups according the modified Dubertaki method. In 1956, Durbetaki [261] reported an analytical procedure to titrate  $\alpha$ -epoxy compounds with hydrogen bromide (HBr) in glacial acetic using crystal violet as an indicator. The method involves a two-step electrophilic addition: protonation and secondly anion addition ( $\text{Br}^-$ ). Despite this method being rapid and capable of good results, the reagent HBr, which fumes profusely in air, requires special handling and frequent restandardisation for accurate analysis. The problem of HBr storage is avoided in a useful variation of the Dubertaki method [262, 263]. In this modification HBr is prepared in situ by treatment of a quaternary ammonium halide with standard perchloric acid ( $\text{HClO}_4$ ).

### 4.1.1 Preparation of reagents

- Crystal violet indicator solution (0.1 %): 0.1 g of crystal violet was dissolved in 100 ml in a 250 ml beaker.
- Perchloric acid solution: A solution of 0.1 M perchloric acid was prepared in glacial acetic acid ( $\text{CH}_3\text{COOH}$ ) by adding 8.5 ml of 72% perchloric acid and 20 ml of acetic anhydride ( $(\text{CH}_3\text{CO})_2\text{O}$ ) to 400 ml of glacial acetic acid in a 1000 ml volumetric flask. The mixture was diluted to full mark with glacial acetic acid.
- Tetraethylammonium bromide solution: The indicator solution was prepared by dissolving 100 g of tetraethylammonium bromide ( $\text{NEt}_4\text{Br}$ ) in 400 ml of glacial acetic acid. Finally, 3-5 drops of the crystal violet indicator solution were added to the previous mixture.

### 4.1.2 Procedure

Standardisation of perchloric acid solution: potassium hydrogen phthalate ( $\text{HOOC}_6\text{H}_4\text{COOK}$ ) was dried overnight at 100 °C (0.2 g). The dry salt was weighed on an analytical balance and recorded with accuracy to four decimal places, and finally placed into a 150 ml beaker. Glacial acetic acid (50 ml) was added on low heat until the sample was dissolved. After cooling, another 50 ml of acetic acid was added to wash down the sides of the beaker. Crystal violet indicator was added (3-5 drops). The mixture was titrated under magnetic stirring with the perchloric acid until a yellow green end point was reached. The amount of tritane added was recorded to the nearest 0.05 ml.

Molarity of perchloric acid was calculated according to

$$N = \frac{K * 1000}{MW_K * V_P} \quad 4.1$$

where  $K$  is the weight of potassium hydrogen phthalate (g),  $MW_K$  is the molecular weight of potassium hydrogen phthalate ( $204.2 \text{ g mol}^{-1}$ ),  $V_p$  is volume of perchloric acid solution added (ml) and  $N$  is molarity of perchloric acid solution.

Determination of epoxy equivalent weight (EEW): Approximately 1 g of sample was weighed in a 50 ml beaker. The sample weight was recorded on an analytical balance. Next, 5-6 drops of crystal violet indicator were added. The mixture was titrated under magnetic stirring with standardised perchloric acid until the color changed from crystal violet to green. The volume of perchloric acid used was recorded to the nearest 0.1 ml.

Epoxy equivalent weight was defined according to

$$EEW = \frac{S}{V_s * N} \quad 4.2$$

where  $S$  is weight of the sample (g),  $V_s$  is perchloric acid titer volume (ml) and EEW is epoxy equivalent weight (kg sample/mol epoxide group).

### 4.2 Protein Analysis

Quantification of proteins has been carried out using the colourimetric method of Bradford [264], which involves the binding of Coomassie Brilliant Blue G-250 to the residues of arginine and hydrophobic aminoacids present in protein. This union produces a change in the absorption maximum and can be monitored at 595 nm. It is a quick and reproducible method, and does not experience interference due to the presence of amino acids in the media. The process is complete in fifteen minutes and is stable for up to one hour.

Protein concentration is obtained by interpolation with a calibration curve calibrated with bovine serum albumin (BSA), which relates the concentration of albumin to the

absorbance at 595 nm. The concentration of BSA used for the calibration curve should be between 0.01 and 0.1 mg/ml (Appendix B, Figure B.1).

### 4.2.1 Preparation of reagents

- BSA stock solution (1 mg/ml): BSA (250 mg) was dissolved in 250 ml of distilled water. Subsequently, the solution was aliquoted in Eppendorf vials using small volumes of approximately 500  $\mu$ l and stored at  $-20$  °C.
- Bradford reagent: 100 mg Coomassie Brilliant Blue G-250 ( $\geq 90\%$ ) were dissolved in 50 ml of ethanol 95%. 100 ml of orthophosphoric acid 85% (w/w) were added slowly and diluted to 1 L with deionised water. The Bradford reagent was stored at room temperature protected from light.

### 4.2.2 Procedure

Standard curve: From BSA stock solution (1 mg ml<sup>-1</sup>) several dilutions were prepared using 0.010 M potassium phosphate buffer (pH = 7.0), with concentrations between 0.02 and 0.14 mg protein per ml. For each dilution, 5 ml of Bradford reagent was added per 0.5 ml of BSA stock solution diluted. The mixtures were well mixed and after 15 minutes the absorbance was measured at 595 nm in a spectrophotometer against a blank reagent prepared with 0.010 M potassium phosphate buffer (pH = 7.0) to finally build the standard curve.

Sample: Bradford reagent (5 ml) was added to 0.5 ml of a sample solution suitably diluted with buffer in order to be within the range of protein concentration of the standard curve. The mixture was well mixed and after 15 minutes the absorbance was measured at 595 nm in a spectrophotometer against a reagent blank prepared with buffer.

### 4.3 Immobilised Protein Determination

The immobilised protein quantity was determined by measuring the difference between the total protein content in the initial enzyme solution contacted and soluble protein at the end of immobilisation process in the supernatant. The enzyme solution and the support were separated by centrifugation at 5000 rpm.

### 4.4 Enzyme Activity Determination

The determination of hydrolytic activity of  $\alpha$ -chymotrypsin was carried out according to methodology developed by Vandermeers, Lelotte and Christophe [265] who described an automated method by constant pH titration using a pHstat to measure the reaction.  $\alpha$ -Chymotrypsin hydrolyses the synthetic substrate N-acetyl-L-tyrosine ethyl ester (ATEE) releasing acid (N-acetyl-L-tyrosine). The amount of acid liberated (at pH = 7.0 and 25 °C) is measured by titration with sodium hydroxide, recorded as a function of time.

An international unit (IU) is defined as the amount of enzyme able to hydrolyse 1  $\mu$ mol of ATEE at 25 °C per minute under the assay conditions indicated.

#### 4.4.1 Preparation of reagents

- ATEE solution (50 mM): ATEE (134.6 mg) was dissolved in 3 ml of ethanol and diluted to 10 ml with 5 mM Tris-HCl buffer (pH = 7.0) containing 20 mM CaCl<sub>2</sub>.
- Titration solution: A 50 mM NaOH standardised solution was prepared.
- Free enzyme solution: A 0.1% (w/v)  $\alpha$ -chymotrypsin solution in 1 mM HCl (in order to avoid autolysis phenomena) was prepared.

- Immobilised enzyme suspension: A suspension of immobilised enzyme with an amount that has the same amount of protein as the free enzyme solution, according to section 4.2 and 4.3, was prepared. The suspension was diluted properly with 1 mM HCl.

### 4.4.2 Procedure

A 10 ml volume of 50 mM ATEE in 5 mM Tris-HCl, pH = 7.0, containing 20 mM CaCl<sub>2</sub>, was placed into a reaction vessel under magnetic stirring at 25 °C. The reaction was started by addition of 50 µl of free enzyme solution or immobilised enzyme suspension, in 1 mM HCl, and the pH was maintained constantly at 7.0 by continuous addition of 50 mM NaOH as titrant. One unit of activity was defined as the amount of enzyme that hydrolyses 1 µmol ATEE per min under standard conditions of assay (pH = 7.0, 25 °C).

Enzyme activity was calculated according to

$$A = \frac{S * C_{NaOH}}{C_{enz} * V_{enz}} \quad 4.3$$

where  $A$  is the specific activity of free enzyme (E) solution or immobilised enzyme (IE) suspension (IU/mg E or IU/mg IE),  $S$  is the slope obtained in the titration curve (ml NaOH/min),  $C_{NaOH}$  is the concentration of titration solution (mM),  $C_{enz}$  is the concentration of free enzyme solution or immobilised enzyme suspension (mg E/ml or mg IE/ml), and  $V_{enz}$  is the volume of free enzyme solution or immobilised enzyme suspension added (ml).

### 4.5 Immobilisation Procedure

Daiso kindly donated for this project porous silica with different pore sizes (Appendix A, Table A.1). It was primarily decided to use the support with greater

surface area because this condition might be expected to allow the immobilisation of an increased amount of enzyme than supports with a lower area. Therefore, most of the experiments shown in this report so far have been developed with the support with pore size of 60 Å or 100 Å.

Alumina supports were donated by SASOL Germany (Appendix A, Table A.2).

### 4.5.1 Activation of Support

#### 4.5.1.1 Synthesis of epoxide-activated silica

The epoxide-activated silica was prepared essentially according to a procedure described by Herman *et al.* [260]. Daisogel silica with various pore sizes (10 g) was dried for 24 h at 200 °C. The dry silica was suspended in 160 ml of dry toluene and degassed by sonication under vacuum for half hour. A tenfold theoretical excess of GOPS was added. This excess was calculated assuming four silanol groups per square nanometer of silica surface using the surface area data supplied by Daiso Co., Ltd (Appendix A, Table A.1). The mixture was refluxed gently for 4 hr. After cooling and filtration of the reaction mixture the silica was washed with 500 ml of toluene, 250 ml of tetrahydrofuran (THF) and 500 ml of methanol, and then dried under vacuum at 40 °C overnight.

#### 4.5.1.2 Synthesis of epoxide-activated alumina

An identical protocol as that used for the silica-based supports was used for the preparation of epoxide-activated alumina supports. SASOL aluminas are provided in boehmite form. The desired transition phase is  $\gamma$ -alumina, therefore it is necessary to dehydrate the support before the functionalisation. The supplier advises calcination of the sample at 550 °C (823 K) for 3 hours to obtain the  $\gamma$  transition.

### 4.5.2 Covalent Binding of the Enzyme

Essentially, the same protocol was used to immobilise the enzyme onto epoxide silica, onto epoxide alumina, and onto Eupergit®.

The protocols described in this section are based on the work of Wheatley and Schmidt [254] and Felix and Descorps [256], which reveal that high salt concentration during immobilisation increases the amount of protein immobilised onto an epoxy silica support, as mentioned in Section 3.3.2. This enhancement is thought to occur because of a salt-induced hydrophobic interaction between the protein and the surface of the stationary phase. The increase in concentration of the protein near the reactive epoxy groups leads to an increase in the rate of reaction between the nucleophilic groups on protein and the epoxide [255].

#### 4.5.2.1 Procedure

Protein immobilisation was performed based on the work of Wheatley and Schmidt [254] and Felix and Descorps [256].  $\alpha$ -Chymotrypsin from bovine pancreas (Type II) was dissolved in 0.010 M potassium phosphate, pH 8.0 and 1.88 M ammonium sulfate, resulting in 10 mg ml<sup>-1</sup> protein solution. A 500  $\mu$ l volume of the above solution was combined with 50 mg of support<sup>4</sup> in a 1.5 ml capped vial. The mixture was agitated for 40 h by orbital rotation at room temperature. The conjugated support was centrifuged at 3000 rpm for 1.5 min and washed twice with 500  $\mu$ l of 0.010 M potassium phosphate, pH = 7.0, subsequently with 1 ml of 0.010 M sodium acetate, pH 4.5, containing 0.3 M sodium chloride, and ultimately the immobilised enzyme was equilibrated with 1 ml of 0.10 M potassium phosphate, pH = 6.0.

As is discussed in Section 3.3.2, the process of immobilisation involves two steps: adsorption of the protein followed by a covalent reaction between reactive amino

---

<sup>4</sup> Epoxide silica, epoxide alumina or Eupergit®

acid residues (RARs) and epoxide groups. It is logical to assume that not all protein molecules will be immobilised covalently; some of them will be loosely adsorbed and washed out after completion of the immobilisation. For this reason, the protein content was measured in the washings after the end of the immobilisation (last part of the *procedure* in Section 4.5.2). Measurements were conducted for the epoxide-silica and alumina systems but the amounts of protein in the washings were negligible (less than 1% of the total protein contacted). Only the measurements for immobilised enzyme on Eupergit® were included in this thesis (Section 5.3.3) because they presented a significant amount of protein in the washings.

For the immobilisation process, the use of ammonium sulfate was evaluated for all different types of supports (epoxide silica, epoxide alumina and Eupergit®). The enzyme loading was estimated in order to obtain a high yield of immobilisation (protein and activity yield) and high specific activity.

At the end of the immobilisation, wet samples were dried under vacuum at room temperature overnight.

Immobilisation yields are defined according to the Equations 4.4 and 4.5.

$$\text{Protein yield (\%)} = \frac{C_i - C_f}{C_i} * 100 \quad 4.4$$

$$\text{Activity yield (\%)} = \frac{A_{EI} * M_s}{A * M_E} * 100 \quad 4.5$$

where  $C_i$  is the concentration of proteins in solution at the beginning of immobilisation ( $\text{mg ml}^{-1}$ ), and  $C_f$  is the concentration of proteins in solution at the end of immobilisation ( $\text{mg ml}^{-1}$ ).

where  $A_{EI}$  is the specific activity of the immobilised enzyme ( $\text{IU/mg support}$ ),  $M_s$  is the mass of support contacted ( $\text{mg support}$ ),  $A$  is the specific activity of the free

enzyme (IU/mg enzyme commercial powder), and  $M_E$  is the mass of enzyme contacted per mass of support (mg protein/mg support).

A third parameter was included: retention of activity, defined according to

$$\text{Retention of activity (\%)} = \frac{A_{EI}/M_{EI}}{A/P_c} * 100 \quad 4.6$$

where  $M_{EI}$  is the mass of immobilised enzyme per mass of support (mg protein/mg support) and  $P_c$  is the protein fraction content of the commercial enzyme powder.

### 4.6 Sample storing

Samples were stored in plastic boxes with moisture indicator silica beads at  $-20$  °C. The silica is used as a desiccant to control the environment humidity to avoid the degradation of the samples. The moisture indicator in the silica consists in the impregnation of silica beads with cobalt chloride, which changes from blue to pink as the desiccant becomes saturated with water. These silica beads are available commercially under the name silica gel blue. After becoming saturated (pink), the desiccant can be reactivated for reuse by heating at  $100$  °C overnight.

### 4.7 Nuclear Magnetic Resonance

General details are provided in this section. Further information can be found at the start of Chapter 5 to Chapter 7 where experimental details for the samples investigated in the chapter are presented.

#### 4.7.1 Solution-State

The spectra were recorded on two spectrometers: a Bruker Avance 400 MHz spectrometer equipped with a narrowbore 9.4 T and a Bruker Avance III 600 MHz spectrometer equipped with a narrowbore 14.1 T magnet; these provide  $^1\text{H}$

resonance frequencies of approximately 400 and 600 MHz, respectively. Samples were held in borosilicate glass (Type 1 Class A) NMR tubes. Samples that release fluoride anions were held in PTFE-FEP copolymer tubes inserts to avoid interactions (etching) with the NMR glass tube. Studied nuclei were  $^1\text{H}$ ,  $^{19}\text{F}$ ,  $^{11}\text{B}$  and  $^{13}\text{C}$  (Table 2.1). Chemical shifts are recorded in ppm relative to tetramethylsilane (TMS) for  $^{13}\text{C}$  and  $^1\text{H}$ , trichlorofluoromethane ( $\text{CFCl}_3$ ) for  $^{19}\text{F}$  and trimethyl borate ( $\text{C}_3\text{H}_9\text{BO}_3$ ) for  $^{11}\text{B}$ .

### 4.7.2 Solid-State with Magic Angle Spinning

The spectra were recorded on three spectrometers: a Bruker Avance 400 MHz spectrometer equipped with a widebore 9.4 T magnet, a Bruker Avance III 600 MHz spectrometer equipped with a widebore 14.1 T magnet, and a Bruker Avance III 850 MHz spectrometer with a widebore 20 T magnet; these provide  $^1\text{H}$  resonance frequencies of approximately 400, 600 and 850 MHz, respectively. Probe assemblies support the transmitter/receiver coil, tuning circuits and sample, and are inserted directly into the magnet bore. The dry powder samples were packed into a conventional MAS rotor and samples containing liquid into a CRAMPS rotor with a polytetrafluoroethylene (PTFE) spacer to avoid sample leakage. The rotors and caps are made from zirconium oxide and Kel-F (polymerised  $\text{FCIC}=\text{CF}_2$ ), respectively. Studied nuclei were  $^1\text{H}$ ,  $^{19}\text{F}$ ,  $^{29}\text{Si}$ ,  $^{13}\text{C}$ , and  $^{23}\text{Na}$  (Table 2.1). Chemical shifts are recorded in ppm relative to tetramethylsilane (TMS) for  $^{29}\text{Si}$ ,  $^{13}\text{C}$  and  $^1\text{H}$  and trichlorofluoromethane ( $\text{CFCl}_3$ ) for  $^{19}\text{F}$ .

## CHAPTER 5

# Structural Characterisation of the Immobilised Enzyme and its Supports

The systems of study chosen (Chapter 3) were:  $\alpha$ -chymotrypsin covalently immobilised on functionalised silica and alumina particles (glycidoxypropyltrimethoxysilane, GOPS, grafted onto the surface of inorganic supports), and Eupergit®. Inorganic supports (silica and alumina) are studied both before (Section 5.2) and after (Section 5.3) functionalisation with the chosen organosilane (GOPS). Eupergit® is included from Section 5.3 onwards because it is an activated support and it is not necessary to use any additional treatment before immobilising the enzyme onto it. The results for the three systems after immobilisation are discussed in Section 5.4.

### 5.1 Experimental details

#### 5.1.1 NMR experiments

All NMR spectra presented in this Chapter were recorded from solid samples. Experiments were performed on either a Bruker Avance I 400 MHz spectrometer equipped with a widebore 9.4 T magnet or a Bruker Avance III 850 MHz spectrometer with a widebore 20 T magnet, yielding  $^1\text{H}$  resonance frequencies of approximately 400 and 850 MHz, respectively.

Powdered samples (dry samples) were packed into 4 mm and 1.3 mm ZrO<sub>2</sub> rotors. Samples were rotated at rates between 10 and 15 kHz in a 4 mm MAS probe or 60 kHz in a 1.3 mm MAS probe.

When liquids needed to be added to the powder (wet sample), then a 4 mm “CRAMPS-type” MAS rotor was used with a PTFE spacer to help contain the fluid. For containment of liquids in 1.3 mm ZrO<sub>2</sub> rotor, soft silicone plugs were used in the top and bottom of the rotor, in addition to the normal end caps.

Chemicals shifts are quoted relative to TMS for <sup>29</sup>Si, <sup>13</sup>C and <sup>1</sup>H and to Al(H<sub>2</sub>O)<sub>6</sub><sup>3+</sup> for <sup>27</sup>Al. For <sup>13</sup>C, <sup>27</sup>Al or <sup>29</sup>Si NMR, cross-polarisation was generally used, with a 50-100% linear ramp on the <sup>1</sup>H channel for variable contact times between 1 to 5 ms (Figure 2.6b). Further experimental details such as pulse length, recycle delay and number of transients can be found in the text and figure captions.

### 5.1.2 Sample preparation

Preparation of the supports and the immobilised enzyme is explained in detail in Chapter 4. Wet samples were stored at 3 °C and discarded after one week of preparation. Dry samples were stored in the conditions described in Section 4.6. Immobilised enzyme samples were discarded after six months of preparation.

## 5.2 Characterisation of the Supports

### 5.2.1 Bare silica

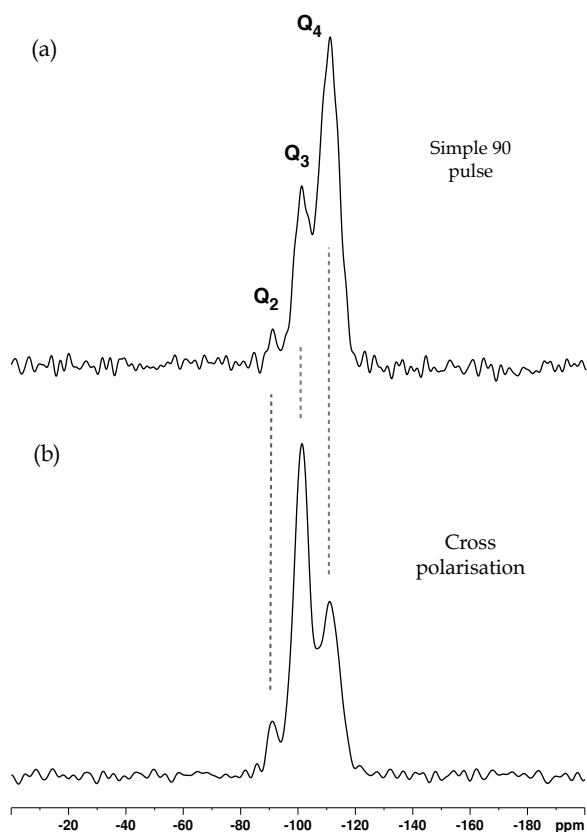
Daiso Co. Ltd kindly donated silica supports of different pore sizes used in this thesis. The technical data supplied for these silica supports by Daiso is summarised in Table A.1 (Appendix A).

Figure 5.1 shows  $^{29}\text{Si}$  MAS NMR spectra of bare silica without and with cross-polarisation, with 15 and 2.5 hours of collection time, respectively. The  $^{29}\text{Si}$  MAS NMR spectrum (Figure 5.1a) reveals three different resonances that belong to silicon species expected in bare silica: Si-coordinated  $\text{Q}_2$ ,  $\text{Q}_3$  and  $\text{Q}_4$  (Figure 3.1). According to Maciel and Sindorf [266] the peak at  $-90$  ppm corresponds to surface silicon atoms with two siloxane bonds and two silanol groups ( $\text{Q}_2$ ); similarly, the resonance at  $-100$  ppm is attributed to surface silicon atoms with three siloxane bonds and one silanol group ( $\text{Q}_3$ ); while the peak at  $-110$  ppm is attributed to silicon atoms with four siloxane bonds ( $\text{Q}_4$ ).

As the current understanding of the structure of silica is that hydrogen atoms occur almost exclusively on the surface [267], cross-polarisation ( $^1\text{H} \rightarrow ^{29}\text{Si}$ ) can be considered to be a surface-selective method. The  $^{29}\text{Si}$  CPMAS spectrum (Figure 5.1b) confirms the presence of  $\text{Q}_2$ ,  $\text{Q}_3$  and  $\text{Q}_4$   $^{29}\text{Si}$  species. An enhancing effect by magnetisation transfer from nearby dipole-dipole-coupled protons is observable for those  $^{29}\text{Si}$  species which are in close contact with protons. These species are  $\text{Q}_2$  and  $\text{Q}_3$  and a smaller proportion of  $\text{Q}_4$  species that are close to the surface.

For the spectrum recorded using a single  $90^\circ$  pulse (Figure 5.1a), the area  $A$  under a  $^{29}\text{Si}$  peak will be approximately quantitative and it is possible to note that  $A(\text{Q}_4) > A(\text{Q}_3) > A(\text{Q}_2)$ , as expected, with the bulk of the silica comprising  $\text{Q}_4$  units. In contrast, in the spectrum recorded using  $^{29}\text{Si}$  CPMAS experiment, the signal intensities reflect the homo- and the heteronuclear dipolar couplings, H-H and H-Si, as well as the numbers of each species.

One obvious advantage of cross-polarisation with respect to direct polarisation is the time gain because interval times are now governed by the longitudinal relaxation times of  $^1\text{H}$  rather than of  $^{29}\text{Si}$ . This effect is observed in the lengths of the relaxation intervals used to obtain the spectra in Figure 5.1; 180 seconds of relaxation delay for



**Figure 5.1.**  $^{29}\text{Si}$  (a) simple  $90^\circ$  pulse MAS ( $90^\circ$  pulse length of  $3\ \mu\text{s}$ , relaxation interval of 180 s, averaging of 300 transients) and (b) CPMAS spectra of dry bare silica ( $100\ \text{\AA}$ ) ( $90^\circ$  pulse length of  $6.2\ \mu\text{s}$ , contact time of 5 ms, relaxation interval of 3 s, averaging of 3000 transients) at  $B_0 = 9.4\ \text{T}$  and a MAS rate of  $\omega_R/2\pi = 10\ \text{kHz}$ .  $^1\text{H}$  decoupling was not used.

the direct polarisation experiment (Figure 5.1a) and 3 seconds in the case of the cross-polarisation experiment (Figure 5.1b).

### 5.2.2 Bare alumina

Alumina supports with different pore size were donated by Sasol, Germany. The technical data for these alumina supports are given in Table A.2 (Appendix A). The aluminas were supplied in the form of boehmite, needing a further calcination to become  $\gamma$ -alumina.

Dehydration of pore-variable boehmites gives rise to different transition aluminas (Figure 3.2) where the most useful of them for the purpose stated in this thesis is

$\gamma$ -alumina. This is because it has a favourable combination of various characteristics such as surface area, pore size and pore-size distribution. The dehydration of boehmites supplied by Sasol was studied using  $^{27}\text{Al}$  MAS NMR, before and after calcination at 550 °C for 3 hours (Figure 5.2). The use of direct- and cross-polarisation was evaluated.

Figure 5.2a and Figure 5.2c show  $^{27}\text{Al}$  MAS NMR spectra of bare boehmite (TH-80) before calcination without and with cross-polarisation, respectively. The spectra reveal a single resonance at 10 ppm that is attributed to octahedrally coordinated aluminium sites ( $\text{Al}^{\text{VI}}$ ), where it is possible to note that boehmite is composed exclusively of  $\text{Al}^{\text{VI}}$  within the bulk and surface [268].

Compared to silica, the  $\gamma$ -alumina structure is much more complex, as seen in Section 3.1.2. Bearing in mind that only aluminium that is coupled to the hydroxyl group, will give signals in the  $^1\text{H} \rightarrow ^{27}\text{Al}$  CPMAS experiment, it is important know the predominant location of the H-species in alumina. Controversies arise about the location of hydrogen in the  $\gamma$ -alumina structure, with the majority of these studies claiming that a considerable amount of hydrogen is present in the bulk of  $\gamma$ -alumina as protons trapped in octahedral and tetrahedral vacancies within the bulk anion lattice [269-272]. Contrarily, a more recent study claims that no interstitial hydrogen can be found in  $\gamma$ -alumina [273].

As a consequence of the discussion above, the results of cross-polarisation experiments applied to alumina materials should be interpreted cautiously and the CPMAS technique should not be referred to as “surface-selective” because there is no certainty of this. However, a preferential surface distribution has been observed for these materials [274] where over 60% of H-species are located on the surface and the rest in the bulk.

In terms of cross-polarisation efficiency, the application of  $^1\text{H} \rightarrow ^{27}\text{Al}$  CPMAS NMR is more complicated when compared to  $^1\text{H} \rightarrow ^{29}\text{Si}$  CPMAS, as it involves transfer

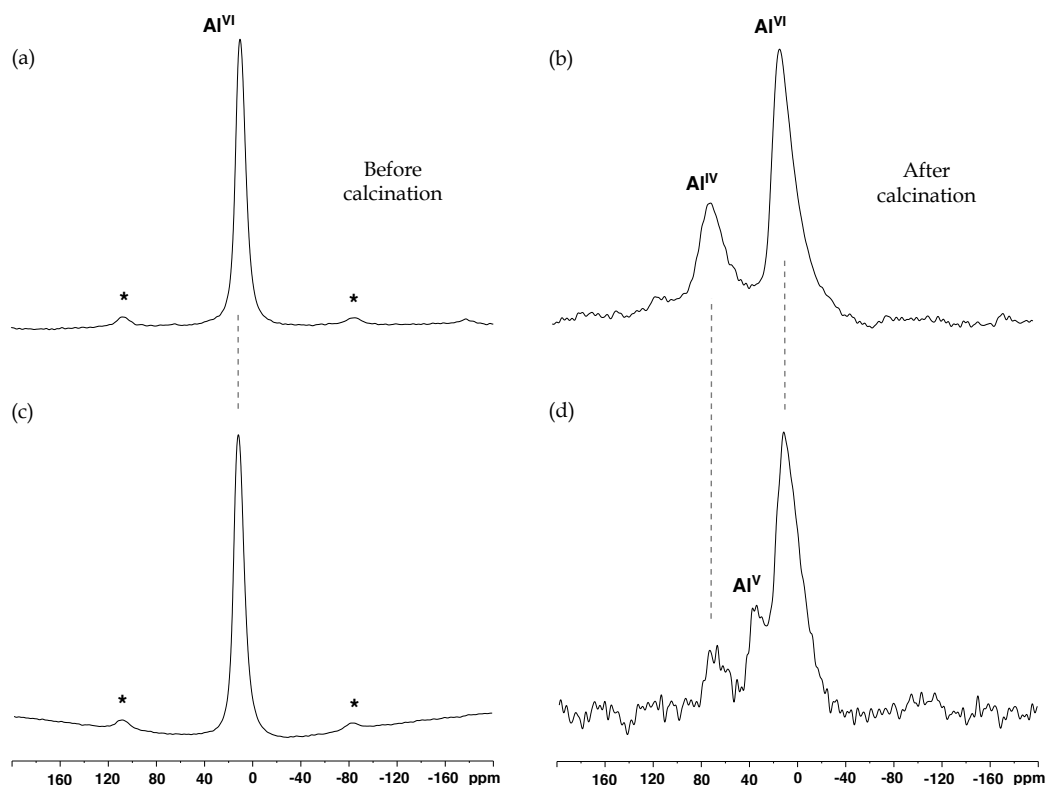


Figure 5.2.  $^{27}\text{Al}$  simple  $90^\circ$  pulse MAS NMR spectra of dry TH-80 alumina (a) before and (b) after calcination ( $90^\circ$  pulse length of  $5\ \mu\text{s}$ , relaxation interval of  $5\ \text{s}$ , averaging 4 transients).  $^{27}\text{Al}$  CPMAS NMR spectra of dry TH-80 alumina (c) before and (d) after calcination ( $90^\circ$  pulse length of  $5.6\ \mu\text{s}$ , contact time of  $0.5\ \text{ms}$ , relaxation interval of  $2\ \text{s}$ , averaging 1024 transients). All spectra were recorded at  $B_0 = 9.4\ \text{T}$  and a MAS rate of  $\omega_R/2\pi = 10\ \text{kHz}$ .  $^1\text{H}$  decoupling was not used. Spinning sidebands are indicated by asterisks.

between a half-integer nucleus ( $^1\text{H}$ ) and a quadrupolar nucleus ( $^{27}\text{Al}$ ). Only a small fraction of the quadrupolar nuclei can be Hartmann-Hahn matched with protons, therefore signal enhancements in the CPMAS NMR spectra for quadrupolar nuclei are generally poor or even insignificant [275]. This effect is observed in the spectra shown in Figure 5.2 where a higher number of transients is needed for CPMAS compared with the direct polarisation experiments to obtain a desirable signal-to-noise ratio.

After the thermal treatment, it is expected that the specific surface of the alumina will increase and therefore there will be an increase in aluminium species with a different

coordination geometry. The spectrum recorded using a single  $90^\circ$  pulse (Figure 5.2b), shows two aluminium species,  $\text{Al}^{\text{IV}}$  and  $\text{Al}^{\text{VI}}$ , at 68 and 10 ppm, respectively, whereas the spectrum recorded using  $^{27}\text{Al}$  CPMAS experiment also shows pentacoordinated aluminium ( $\text{Al}^{\text{V}}$ ) at 35 ppm (Figure 5.2d). These resonances are in agreement with other  $^{27}\text{Al}$  MAS NMR alumina studies [276, 277]. From Figure 5.2b is possible to note that the dominant species in  $\gamma$ -alumina are tetrahedral and octahedral where  $A(\text{Al}^{\text{VI}}) > A(\text{Al}^{\text{IV}})$ . The bulk of  $\gamma$ -alumina contains both hexacoordinated ( $\text{Al}^{\text{VI}}$ ) and tetraordinated ( $\text{Al}^{\text{IV}}$ ) alumina sites, with the former being more abundant than the latter. [278, 279]. Around only 1.5% of Al atoms are pentacoordinated in  $\gamma$ -alumina [280]. This coordination number,  $\text{Al}^{\text{V}}$ , is not yet well understood, but many authors refer to it as being caused either by substitution of lattice oxygens in octahedral symmetry by hydroxyl groups or by oxygen defects adjacent to an aluminium centre [269, 281]. Other researchers have tentatively assigned Al atoms at the external surface of alumina particles to pentahedral sites [282].

In the cross-polarisation experiment (Figure 5.2d) the  $\text{Al}^{\text{V}}$  peak is well separated and clearly resolved suggesting that this type of Al atom is preferentially located on the surface of  $\gamma$ -alumina. In 2007, Kwak *et al* [283] found strong evidence that pentacoordinated aluminium is exclusively located on the surface of  $\gamma$ -alumina. Recently, De Paëpe's research group confirmed these results using dynamic nuclear polarisation [284]. It is possible to conclude that  $\text{Al}^{\text{V}}$  sites are exclusively located in the surface of  $\gamma$ -alumina with the data presented in Figure 5.2 and the recent literature mentioned above.

Identical spectra were obtained for SB-1, TH-100 and TH-200 aluminas before and after calcination. Therefore, only TH-80 spectra were included in this thesis.

## 5.3 Characterisation of the Immobilised Enzymes

### 5.3.1 Epoxide-silica

After the functionalisation with GOPS, a modified surface with epoxide groups is obtained (Figure 3.18). As can be seen from Figure 5.3, the smaller the pore size (larger surface area) the greater the epoxide content, with the exception of 60 Å where the activation process could have been affected by diffusional restrictions due to the small pore size.

Figure 5.4a shows the  $^{29}\text{Si}$  CPMAS NMR spectrum of functionalised silica. The new species were assigned according to those previously reported by Bayer *et al.* [285] for chemically modified silica gels where all new Si species have one alkyl group but siloxane and silanol vary. The peak at -48 ppm corresponds to surface silicon atoms with one siloxane bond and two silanol groups ( $T_1$ ), similarly the resonance at -56 ppm is ascribed to surface silicon atoms with two siloxane bonds and one silanol group ( $T_2$ ), while the resonance at -67 ppm is assigned to surface silicon atoms with three siloxane bonds and no silanol group ( $T_3$ ).

It must be remember that the success of cross-polarisation depends on the dipolar coupling interaction between proximate protons and the nucleus observed. Therefore, in the case of  $^1\text{H} \rightarrow ^{29}\text{Si}$  CPMAS, it is plausible to suggest that the efficiency of the cross-polarisation experiment will decrease after grafting organic moieties on to the surface (GOPS silanisation).

$^{13}\text{C}$  CPMAS NMR spectra of epoxide-silica (100 and 300 Å pore size) are presented in Figure 5.5a and Figure 5.5c, respectively. The new species related with GOPS tethered to silica surface were assigned in agreement with previous studies [285, 286]. Figure 5.5a shows the carbon labels for each epoxide-silica species. Figure 5.6 shows the notation that was used here for the carbon assignments.

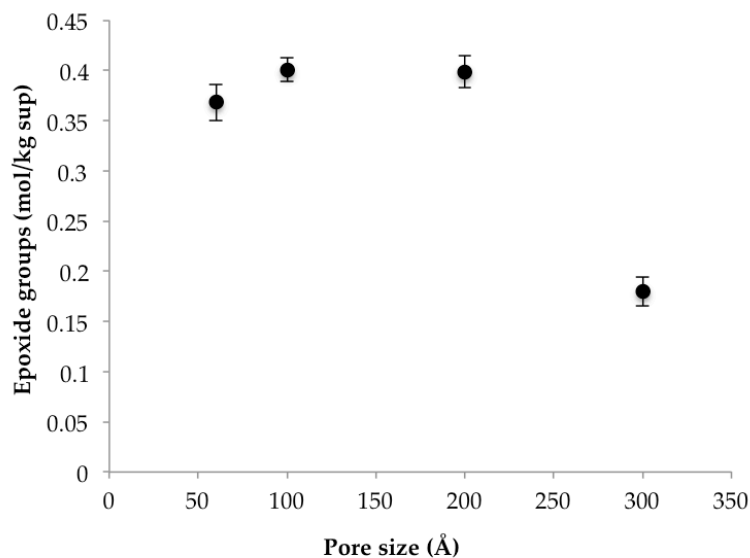


**Figure 5.3.** Epoxide content after functionalisation with GOPS for silica with 60, 100, 200 and 300 Å pore size.

The addition of liquid D<sub>2</sub>O (10 ml of D<sub>2</sub>O per 0.5 g epoxide-silica, at least 3 h prior to NMR measurements) to the powdered epoxide-silica (100 Å pore size) sample (in the CRAMPS-type rotor) has a very significant effect on the <sup>1</sup>H MAS spectrum, as shown in Figure 5.7. There is displacement of bound H<sub>2</sub>O and exchange of acidic protons (i.e., in Si-OH groups) for deuterons, leading to the disappearance of some of the broad and intense <sup>1</sup>H peaks in the spectrum of the dry epoxide-silica.

Furthermore, a narrowing of the remaining <sup>1</sup>H resonances is very noticeable, especially in the expansion in Figure 5.7b, which is presumably a result of the greater mobility of the GOPS linker in the presence of a solvent. As expected, the protons closest to the surface (H1 and H2) are narrowed less than those further away, which have greater mobility. It should be noted that this addition of a solvent is significant as it mimics the environment in which a solid biocatalyst will be utilised in practice.

The epoxide-silica sample has been treated with D<sub>2</sub>O (see Figure 5.7) so that only non-exchangeable <sup>1</sup>H nuclei related with the grafted linker remained. This treatment

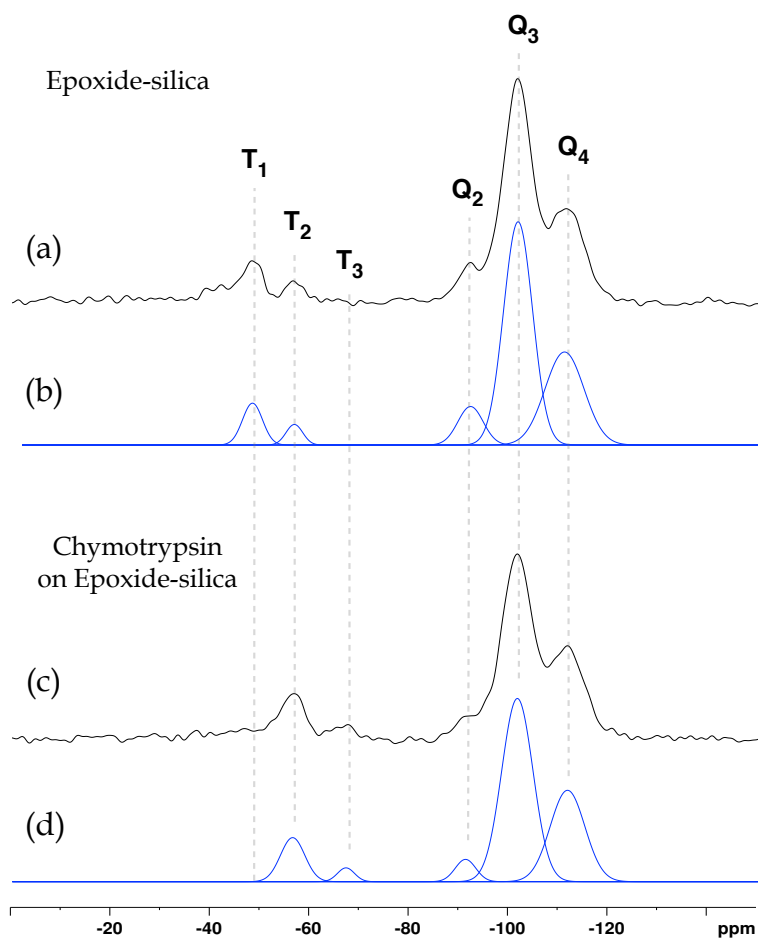


**Figure 5.4.** <sup>29</sup>Si CPMAS NMR spectra of (a) dry epoxide-silica (100 Å) and (c) dry immobilised enzyme (90° pulse length of 3 μs, contact time of 5 ms, relaxation interval of 3 s, averaging 512 transients). All spectra were recorded at  $B_0 = 20$  T and MAS rate of  $\omega_R/2\pi = 10$  kHz, using 90 kHz SPINAL-64 <sup>1</sup>H decoupling during acquisition. The blue lines represent deconvoluted <sup>29</sup>Si CPMAS NMR spectra of (b) dry epoxide-silica and (d) dry immobilised enzyme fitted using Gaussian line shape analysis. Results of deconvolution analysis are presented in Table 5.3.

avoids getting broad and large peaks, principally, due to residual water and Si-OH groups (Figure 5.7).

The immobilisation of the enzyme was conducted under the conditions mentioned in section 4.5 for different pore sizes of silica particles (60, 100, 200 and 300 Å). The commercial enzymatic powder used in all immobilisations had a protein content of 78.1% and its hydrolytic activity was 412.3 IU/mg powder.

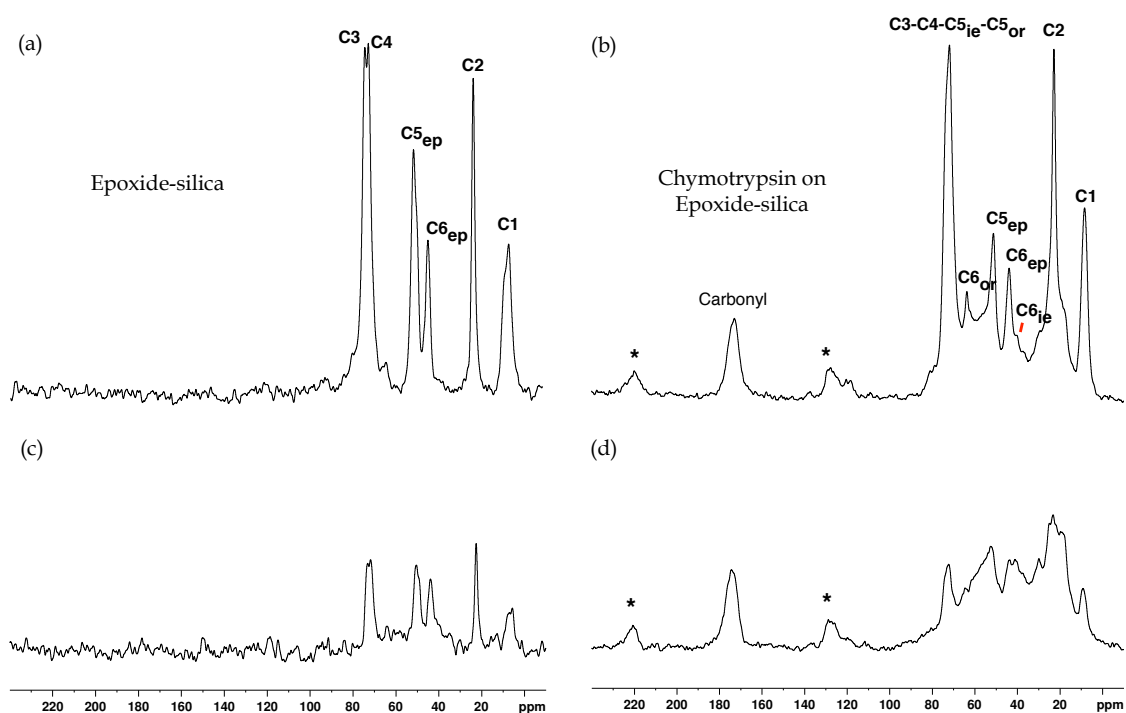


**Figure 5.5.**  $^{13}\text{C}$  CPMAS NMR spectra with  $^1\text{H}$  decoupling of (a) dry epoxide-silica 100 Å, (b) dry immobilised enzyme on epoxide-silica 100 Å, (c) dry epoxide-silica 300 Å and (d) dry immobilised enzyme on epoxide-silica 300 Å ( $90^\circ$  pulse length of 3  $\mu\text{s}$ , contact time of 1 ms, relaxation interval of 3 s, averaging 20000 transients). All spectra were recorded at  $B_0 = 20$  T and a MAS rate of  $\omega_R/2\pi = 14$  kHz, using 90 kHz SPINAL-64  $^1\text{H}$  decoupling during acquisition. Spinning sidebands are indicated by asterisks.

Immobilisation results are presented in Table 5.1 and Table 5.2. Differences in the protocols in the literature [254, 256] lead to different suggested immobilisation pHs (pH 7.0 and 8.0). Table 5.1 summarises the results without and with ammonium sulfate at pH 7.0 and 8.0 where it is very clear that the addition of salt highly favours an increase in the amount of protein immobilised. Loading is also higher at pH 8.0. As has been mentioned in Section 3.3.2, immobilisation in presence of high ionic strengths increases the reactivity of epoxide groups with reactive amino acid residues (RARs).

It is important to note that small values of immobilised protein (e.g., 13.77 mg prot/g sup in Table 5.1) may include large error values because the protein quantification is

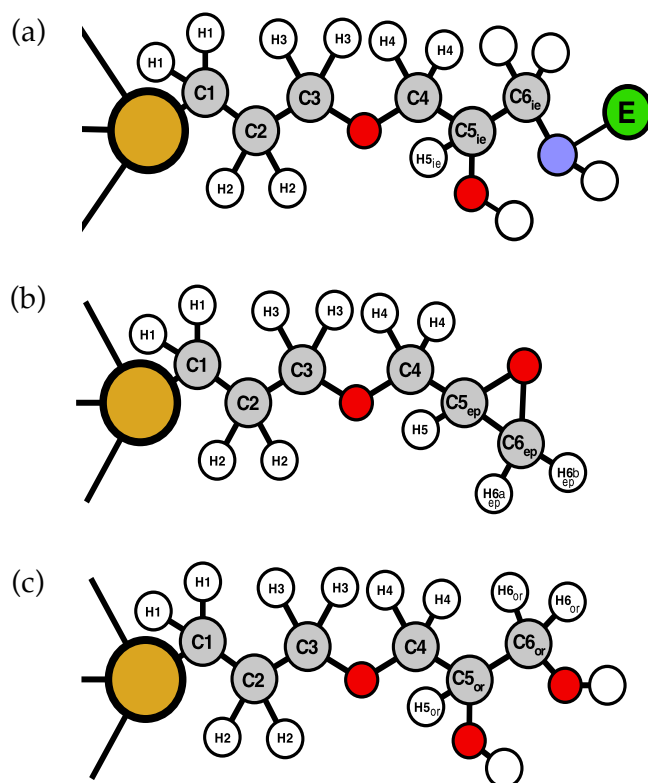


**Figure 5.6. (a) Scheme of  $\alpha$ -chymotrypsin covalently immobilised in epoxide-silica. (b) Scheme of GOPS grafted on to silica surface. (c) Scheme of opened epoxide ring. Subscript ie: immobilised enzyme, ep: epoxide and or: open ring.**

obtained as a difference between supernatant concentrations at the start and the end of the immobilisation procedure.

The principal issue for studying immobilised enzymes using solid-state MAS NMR is the low sensitivity, which on the one hand is due to the relatively small quantity of protein present - relatively - in the sample, and consequently in the rotor, and on the other to the low  $^{13}\text{C}$  abundance.  $^{13}\text{C}$  enrichment is not considered in this thesis, for the reasons discussed in Chapter 1, therefore samples with the highest amount of protein are preferred.

The highest amount of immobilised protein in Table 5.1 was achieved at pH 8.0 and in presence of salt. For these conditions the immobilisation takes around 20 min to be completed. In contrast, without ammonium sulfate the process takes more than 40

**Table 5.1. Immobilisation results of  $\alpha$ -chymotrypsin on epoxide-silica 60 Å.**

Immobilisation procedure	Contacted load / (mg prot/g support)	Immobilised protein / (mg prot/g support)	Protein yield / %	Immobilised enzyme activity / (IU/g)	Activity yield / %	Retention activity / %
pH 7.0 without ammonium sulfate	80.8 ± 2.1	13.7 ± 7.2	17.0 ± 8.3	1360 ± 30	3.23 ± 0.13	18.7 ± 1.2
pH 7.0 with ammonium sulfate (1.88 M)	79.1 ± 2.4	36.6 ± 4.3	46.3 ± 2.4	19040 ± 23	45.1 ± 0.2	98.3 ± 1.4
pH 8.0 with ammonium sulphate (1.88 M)	81.6 ± 2.3	44.2 ± 3.4	54.2 ± 3.5	18850 ± 20	44.6 ± 0.2	80.6 ± 1.3

hours finish. The kinetics of immobilisation on epoxide-silica (60 Å pore size) are shown in Figure C.1 (Appendix C).

Table 5.2 shows the results of immobilisation at pH 8 and with ammonium sulfate (previous conditions selected) for the four different pore sizes available. The highest amount of protein achieved was for a pore size of 100 Å with 68.52 mg/g sup and 95% of retained activity.

The protein yield parameter can be very useful to determine if the biocatalyst produced is close to reaching the maximum amount of protein possible (saturation point). For example, in Table 5.2 it is possible to notice that, excluding 60 Å pore size support, all immobilised enzymes reach around a 100% of protein yield. This means that the maximum of protein is not reached yet with a contacted load of around 70 mg prot/g support. An important suggestion for future studies using this support is to evaluate a higher contact loading.

**Table 5.2. Immobilisation results of  $\alpha$ -chymotrypsin on epoxide-silica with different pore size at pH 8 with ammonium sulfate (1.88 M).**

Pore size / Å	Contacted load / (mg prot/g support)	Immobilised protein / (mg/g support)	Protein yield / %
60	69.3 $\pm$ 3.4	31.2 $\pm$ 2.3	54.8 $\pm$ 3.5
100	69.0 $\pm$ 3.8	68.5 $\pm$ 3.1	99.6 $\pm$ 4.3
200	69.3 $\pm$ 4.2	67.7 $\pm$ 4.7	99.4 $\pm$ 6.2
300	69.3 $\pm$ 2.5	66.4 $\pm$ 3.3	97.8 $\pm$ 4.7

Figure 5.4c and Figure 5.5b show  $^{29}\text{Si}$  and  $^{13}\text{C}$  CPMAS NMR spectra of immobilised enzyme on epoxide-silica (100 Å pore size), respectively. A scheme of  $\alpha$ -chymotrypsin covalently immobilised on epoxide-silica is shown in Figure 5.6a. Carbonyl groups and, probably,  $\epsilon$ -carbon from lysine residues ( $\text{C}_{6\text{ie}}$ ) from enzyme can be observed in the immobilised  $\alpha$ -chymotrypsin spectrum (Figure 5.5b).

The  $^{29}\text{Si}$  CPMAS NMR spectra (Figure 5.4a and Figure 5.4c) were deconvoluted by fitting Gaussian lineshapes, adjusting their intensity, width and frequency shift (Figure 5.4b and Figure 5.4d). Table 5.3 presents the results of the deconvoluted and integrated Gaussian curves for epoxide-silica and immobilised enzyme spectra. These results are reported as percentages.

Unexpectedly, the  $^{29}\text{Si}$  CPMAS NMR spectra shown in Figure 5.4b reveal changes in the surface species of epoxide-silica after the enzyme immobilisation, a process that is distant from silicon atoms. These changes are confirmed by the results obtained from the deconvolution of the spectra (Table 5.3).

On the basis of the  $^{29}\text{Si}$  CPMAS NMR spectra, it is possible to calculate the degree of polycondensation of  $\text{Q}_n$  or  $\text{T}_n$  species by deconvolution which may be estimated using the formulae

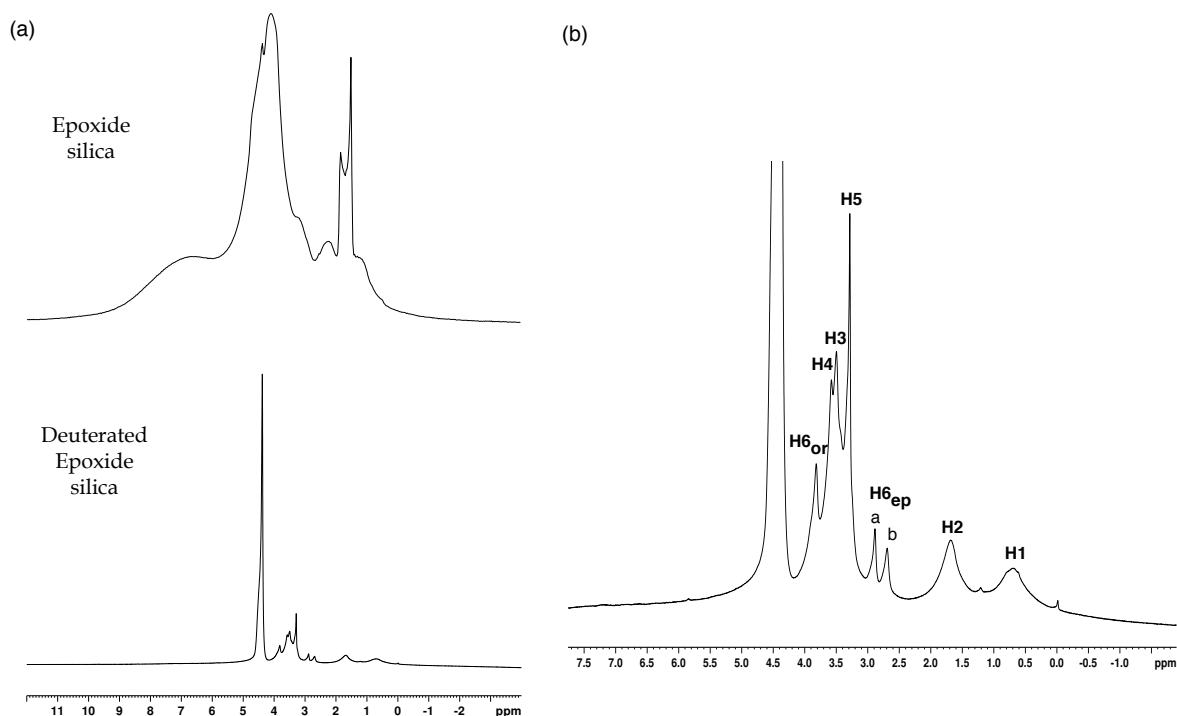


Figure 5.7. (a)  $^1\text{H}$  MAS NMR of dry epoxide-silica and wet epoxide-silica in  $\text{D}_2\text{O}$  recorded at 9.4 T (20 kHz MAS rate,  $90^\circ$  pulse length of  $5.5 \mu\text{s}$ , relaxation interval of 6 s, averaging of 64 transients). (b) Close section  $^1\text{H}$  MAS NMR of wet epoxide-silica in  $\text{D}_2\text{O}$  at  $B_0 = 9.4$  T. The full linewidth at half-height is 289 Hz for H1, 238 Hz for H2, 51 Hz for  $\text{H6}_{\text{epa}}$  and 68 Hz for  $\text{H6}_{\text{epb}}$ .

$$\text{Degree of condensation } Q_n (\%) = \frac{\sum_{i=1}^4 i(Q_i)}{4} \quad 5.1$$

$$\text{Degree of condensation } T_n (\%) = \frac{\sum_{i=1}^3 i(T_i)}{3} \quad 5.2$$

where  $Q_i$  and  $T_i$  are the percentages of the corresponding sites obtained from deconvolution of the  $^{29}\text{Si}$  CPMAS NMR spectra (Table 5.3) and  $i$  is the respective number of condensed siloxane groups.

After the immobilisation procedure, it can be observed that the  $T_1$  peak is negligible,  $T_2$  is significantly increased and  $T_3$  has appeared for the first time; small changes can

**Table 5.3. Results of deconvolution analysis of  $^{29}\text{Si}$  CPMAS NMR spectra before and after immobilisation on epoxide-silica.**

Sample	Q <sub>2</sub> /%	Q <sub>3</sub> /%	Q <sub>4</sub> /%	T <sub>1</sub> /%	T <sub>2</sub> /%	T <sub>3</sub> /%
Epoxide-silica	7.82 ± 0.11	51.9 ± 0.7	29.1 ± 0.4	6.70 ± 0.97	2.76 ± 0.04	-
	8.80 ± 0.12 <sup>a</sup>	58.4 ± 0.7 <sup>a</sup>	32.7 ± 0.4 <sup>a</sup>	70.82 ± 0.99 <sup>b</sup>	29.1 ± 0.4 <sup>b</sup>	-
Chymotrypsin on Epoxide- silica	4.04 ± 0.04	50.60 ± 0.52	27.9 ± 0.2	-	9.39 ± 0.09	2.06 ± 0.02
	4.89 ± 0.05 <sup>a</sup>	61.3 ± 0.6 <sup>a</sup>	33.8 ± 0.3 <sup>a</sup>	-	82.0 ± 0.8 <sup>b</sup>	17.9 ± 0.1 <sup>b</sup>

<sup>a</sup> percentages are normalised to 100% for Q<sub>n</sub> species (Q<sub>2</sub>, Q<sub>3</sub> and Q<sub>4</sub>)

<sup>b</sup> percentages are normalised to 100% for T<sub>n</sub> species (T<sub>1</sub>, T<sub>2</sub> and T<sub>3</sub>)

also be observed in the Si-coordinated Q<sub>2</sub>, Q<sub>3</sub> and Q<sub>4</sub> species. The degree of condensation for T<sub>n</sub> and Q<sub>n</sub> species confirm these observations (see Table 5.4). A condensation increase of 30% was obtained for T<sub>n</sub> species after immobilisation and just 1% for Q<sub>n</sub> species.

These changes are because residual Si-OH groups become cross-linked to give Si-O-Si. The same changes were observed if GOPS-modified silica was incubated in aqueous conditions, as in the immobilisation procedure, but with no enzyme present. The hydrolysis and condensation (cross-linking process) of organofunctional alkoxy silanes is a well-known process used in industry to increase adhesive strength [287]. However, it has not been extensively studied on surfaces and not at all in the type of system studied here. It is interesting that silanol groups do not condense to the maximum possible extent during the initial GOPS modification but require the extended aqueous incubation during immobilisation.

Another reaction promoted by the aqueous conditions of the immobilisation is the nucleophilic attack by water molecules on the oxirane functional groups [288], thereby yielding a diol (see Figure 5.6c); this can be noted from the relative increase in intensity of C<sub>6or</sub> and the decrease of oxirane carbons (the C<sub>5ep</sub> and C<sub>6ep</sub> decrease is

**Table 5.4. Degree of condensation of Q<sub>n</sub> and T<sub>n</sub>.**

Sample	Degree of condensation Q <sup>n</sup> / %	Degree of condensation T <sup>n</sup> / %
Epoxide-silica	80.9 ± 1.1	43.0 ± 0.6
Chymotrypsin on Epoxide-silica	82.2 ± 0.8	72.5 ± 0.7

also due to the immobilisation of the enzyme) (Figure 5.5a and b). The same behaviour has been observed also in absence of the enzyme. Also, the epoxide group can be opened by nucleophilic attack by ammonia (NH<sub>3</sub>) from the immobilisation buffer, yielding primary amines.

<sup>13</sup>C CPMAS NMR spectra before and after immobilisation of α-chymotrypsin are presented in Figure 5.5 for both 100 and 300 Å silicas. It can be seen from Figure 5.5a and c that the NMR results confirm the difference in the epoxide content found by the modified Dubertaki method (Figure 5.3), which were 0.40 and 0.18 mol kg<sup>-1</sup> for 100 and 300 Å, respectively. Furthermore, after immobilisation of the enzyme, the <sup>13</sup>C spectra of 100 and 300 Å silicas show similar intensity to the α-chymotrypsin carbonyl groups at 175 ppm (Figure 5.5b and d). The area under the carbonyl peak for the immobilised enzyme on epoxide-silica of 100 Å pore size has an absolute value of 3.7 × 10<sup>6</sup> and for 300 Å pore size an absolute value of 3.4 × 10<sup>6</sup>. These results are in agreement with the results for biochemical quantification of the immobilised protein (Table 5.2), where both pore sizes achieved similar protein content at the end of the immobilisation procedure. Although CPMAS signal intensities are generally not quantitative, it should be noted that here we are comparing <sup>13</sup>C intensities of samples that differ only in the silica pore size; we are comparing absolute intensities in Figure 5.5a and c and, separately, in Figure 5.5b and d. The <sup>13</sup>C signals from the GOPS tethered to the epoxide-silica (100 Å pore size) in Figure 5.5a and b have been

assigned with the aid of a  $\{^1\text{H}, ^{13}\text{C}\}$  HETCOR experiment and are in agreement with previous studies [286, 287]. Figure 5.6 shows the notation used here for the carbon assignment.

To aid assignment of  $^1\text{H}$  and  $^{13}\text{C}$  MAS NMR spectra, two-dimensional  $\{^1\text{H}, ^{13}\text{C}\}$  HETCOR spectra of the epoxide-silica and solid biocatalyst samples (both 100 Å pore size) were recorded and are shown in Figure 5.8 (only  $^{13}\text{C}$  shifts below 100 ppm are displayed). Two-dimensional correlation peaks here indicate the presence of a dipolar coupling and hence spatial proximity between  $^1\text{H}$  and  $^{13}\text{C}$  pairs. The  $^{13}\text{C}$  projections of the two spectra are also shown, and to aid assignment, the  $^1\text{H}$  MAS spectrum of the epoxide-silica sample with added  $\text{D}_2\text{O}$  from Figure 5.7 is also presented. Analysing the results of the support system and solid biocatalyst jointly, it was possible to assign the  $^{13}\text{C}$  and  $^1\text{H}$  NMR spectra in Figure 5.5 and Figure 5.7 as shown, according to the numbering schemes in Figure 5.6.

### 5.3.2 Epoxide-alumina

The functionalisation of calcined alumina was conducted using the same protocol as for silica. A set of aluminas with various pore sizes were grafted on the surface with GOPS in a non-aqueous reflux system (Section 4.5.1). The epoxide content for different alumina supports after the functionalisation with the organosilane are summarised in Figure 5.9. The trend is similar to that found using silica supports; the smaller the pore, the greater the epoxide content. Apparently, alumina with a pore size of 50 Å does not show diffusional restrictions, unlike that found for silica with 60 Å pores size. This effect could be possible due to a better pore distribution (i.e., a narrower range of pore sizes) on the alumina support. These parameters were not provided by the suppliers of silica and alumina and not measured in the present thesis. It is strongly recommended that future studies include the characterisation of the supports by methods such as BET, TEM or XRD.

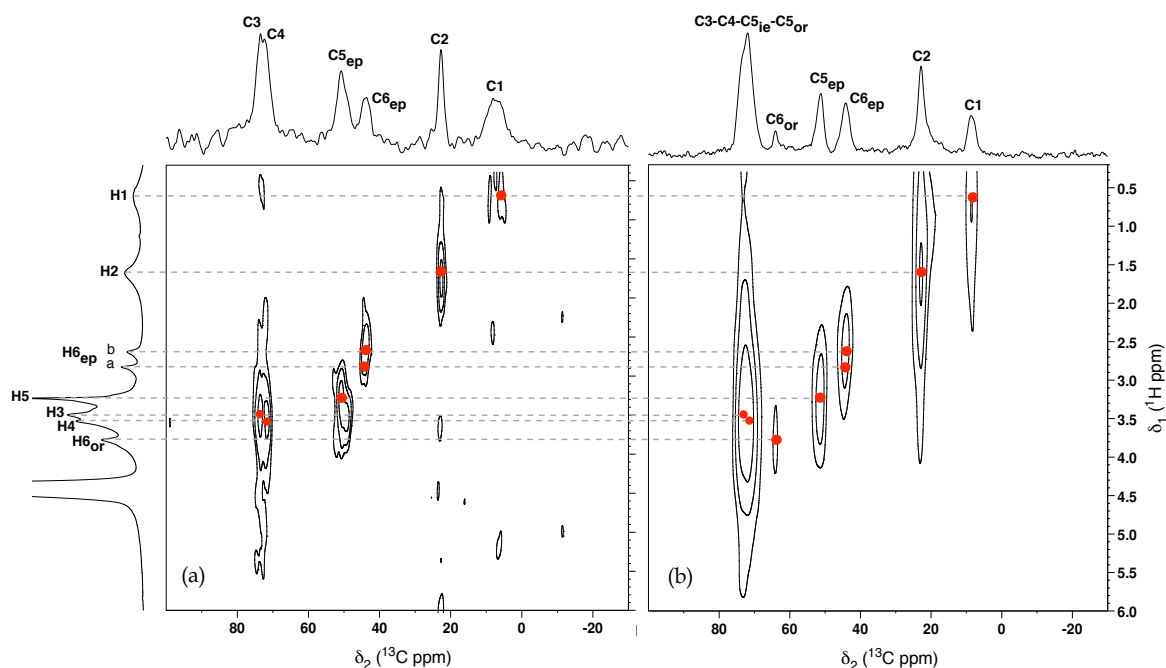
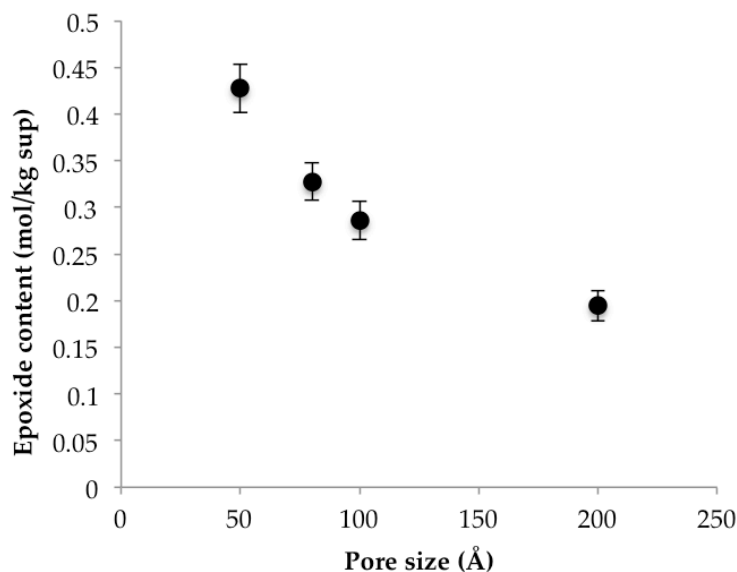


Figure 5.8. Two-dimensional  $\{^1\text{H}, ^{13}\text{C}\}$  HETCOR spectra with  $^1\text{H}$  decoupling of (a) dry epoxide-silica and (b) dry immobilised enzyme  $100 \text{ \AA}$  at  $B_0 = 20 \text{ T}$  and a MAS rate of  $\omega_R/2\pi = 14 \text{ kHz}$ , using  $90 \text{ kHz}$  SPINAL-64  $^1\text{H}$  decoupling during acquisition. Spectra were recorded with the pulse sequence shown in Figure 2.7 by averaging 128 transients for each of the 24  $t_1$  increments of  $150 \mu\text{s}$  ( $90^\circ$  pulse length of  $3 \mu\text{s}$ , contact time of  $1 \text{ ms}$ , relaxation interval of  $3 \text{ s}$ ).

Figure 5.10 shows  $^{27}\text{Al}$  MAS NMR spectra of epoxide-alumina (TH-80) without cross-polarisation (Figure 5.10a) and with (Figure 5.10c). There is no visible difference between the cross-polarisation experiment and the simple  $90^\circ$  pulse. Pentacoordinated alumina sites are no longer present on the surface after the immobilisation procedure. The disappearance of  $\text{Al}^{\text{V}}$  after immobilisation is probably because of the interaction of water molecules from the immobilisation buffer with pentacoordinated alumina sites converting these sites to octahedral aluminium. This result supports the idea of the exclusive presence of  $\text{Al}^{\text{V}}$  on the surface of alumina, discussed in Section 5.2.2, since the interaction of water and  $\text{Al}^{\text{V}}$  is restricted to the surface only.



**Figure 5.9.** Epoxide content after functionalisation with GOPS for alumina 50 Å (SB-1), 80 Å (TH-80), 100 Å (TH-100) and 200 Å (TH-200) pore size.

$^{29}\text{Si}$  CPMAS NMR spectra of GOPS-treated alumina are presented in Figure 5.10b. It is possible to note that the signal-to-noise ratio is much lower than for epoxide-silica systems (Figure 5.4), even using a 20 T magnet. This is not a surprise because in the alumina epoxide system the only source of silicon atoms is from the molecules of GOPS tethered to the surface.

$^{13}\text{C}$  CPMAS NMR spectra before and after immobilisation of  $\alpha$ -chymotrypsin on epoxide-alumina are shown in Figure 5.11. The same species as were found for epoxide-silica were identified in this system (Figure 5.5a and b).

The addition of liquid  $\text{D}_2\text{O}$  (100 ml  $\text{D}_2\text{O}$  per 0.5 g of epoxide-alumina, at least 3 h prior to NMR recording) was also studied for epoxide-alumina with 80 Å of pore size (Figure 5.12). No difference was observed in the proton species between epoxide-silica (Figure 5.7) and epoxide-alumina.

The immobilisation of enzyme on epoxide-alumina with different pore sizes (50, 80, 100 and 200 Å) was achieved. The initial conditions used were the optimum conditions obtained for epoxide-silica discussed in Section 5.3.1 (pH 8.0 with

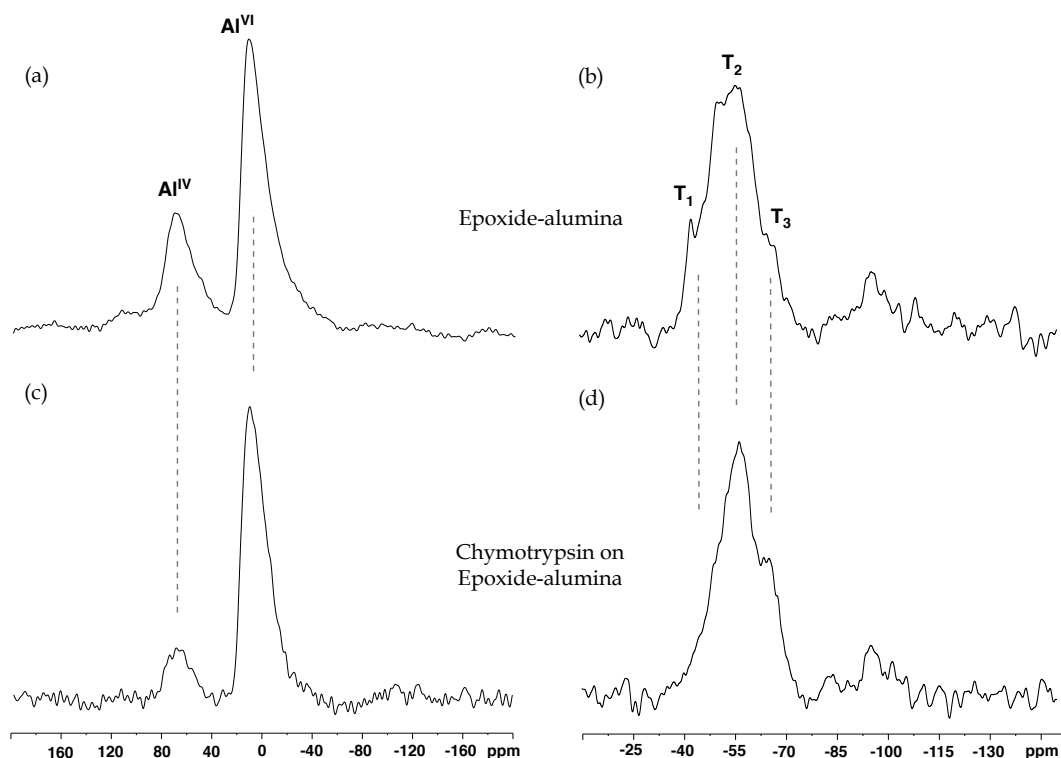


**Figure 5.10.**  $^{27}\text{Al}$  simple  $90^\circ$  pulse MAS ( $90^\circ$  pulse length of  $5\ \mu\text{s}$ , relaxation interval of  $5\ \text{s}$ , averaging 4 transients) and CPMAS NMR spectra ( $90^\circ$  pulse length of  $5.6\ \mu\text{s}$ , contact time of  $0.5\ \text{ms}$ , relaxation interval of  $2\ \text{s}$ , averaging 1024 transients) of (a) dry epoxide-alumina and (c) dry immobilised enzyme ( $80\ \text{\AA}$  pore size) at  $9.4\ \text{T}$  and a MAS rate of  $\omega_{\text{R}}/2\pi$   $10\ \text{kHz}$ ,  $^1\text{H}$  decoupling was not used.  $^{29}\text{Si}$  CPMAS NMR of (b) dry epoxide-alumina and (d) dry immobilised enzyme ( $80\ \text{\AA}$  pore size) ( $90^\circ$  pulse length of  $3.3\ \mu\text{s}$ , contact time of  $5\ \text{ms}$ , relaxation interval of  $3\ \text{s}$ , averaging 6057 transients) at  $B_0 = 20\ \text{T}$  and a MAS rate of  $\omega_{\text{R}}/2\pi = 10\ \text{kHz}$ , using  $90\ \text{kHz}$  SPINAL-64  $^1\text{H}$  decoupling during acquisition.

ammonium sulfate). Table 5.5 and Table 5.6 summarise the results for these immobilisations. In Table 5.5 it is possible to note that the highest amount of protein immobilised was obtained for an alumina pore size of  $80\ \text{\AA}$  (TH-80).

The immobilisation kinetics for all different pore sizes are shown in Figure C.2 (Appendix C). It is noticeable that the time required to immobilise the enzyme on epoxide-alumina increases for smaller pores. This trend seems reasonable because the access of the protein will be restricted during the immobilisation process for smaller pores and the coverage of the surface available within these pores will be

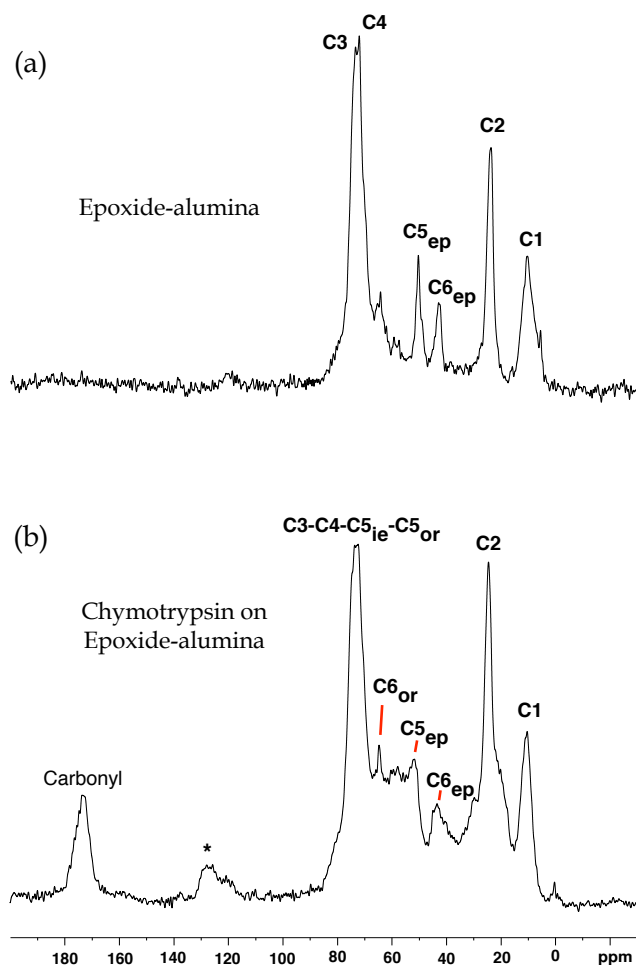


**Figure 5.11.**  $^{13}\text{C}$  CPMAS NMR spectra of (a) dry epoxide-alumina and (b) dry immobilised enzyme on same support (80 Å pore size) ( $90^\circ$  pulse length of 3  $\mu\text{s}$ , contact time of 1 ms, relaxation interval of 3 s, averaging 20000 transients) at  $B_0 = 20$  T and a MAS rate of  $\omega_R/2\pi = 14$  kHz, using 90 kHz SPINAL-64  $^1\text{H}$  decoupling during acquisition. Spinning sideband is indicated by asterisk.

hampered by internal diffusion. The procedure of immobilisation of  $\alpha$ -chymotrypsin on epoxide-silica with a pore size of 50 Å pore size took approximately 50 hours, for a pore size of 80 Å around 20 hours, for a pore size of 100 Å about 10 hours and, finally, for the largest pore available (200 Å) less than 5 hours. Similar behaviour was observed in the immobilisation on epoxide-silica for different pore sizes.

The enzymatic activity results for alumina systems were intriguing (Table 5.6). Very low activities were obtained at normal conditions of the activity assay described in

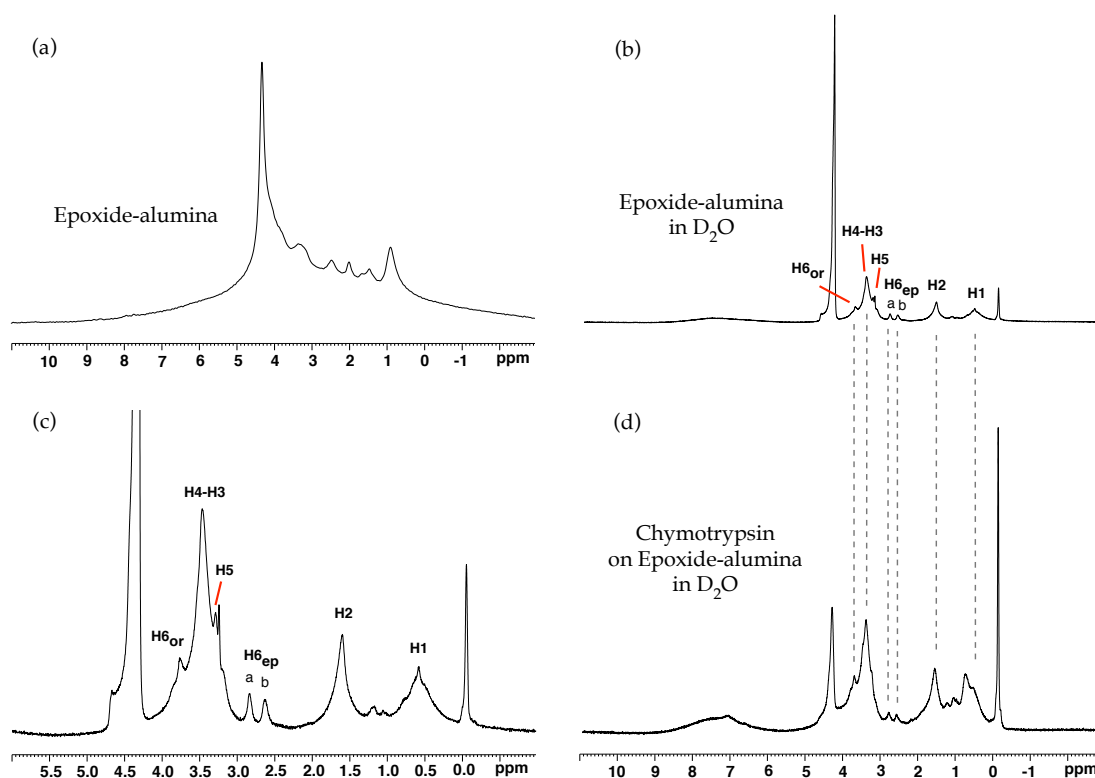


**Figure 5.12.**  $^1\text{H}$  MAS NMR spectra of (a) dry epoxide-alumina, (b) wet epoxide-alumina in  $\text{D}_2\text{O}$  and (d) wet enzyme immobilised on epoxide-alumina at  $B_0 = 20$  T ( $90^\circ$  pulse length of  $1.8 \mu\text{s}$ , relaxation interval of 4 s, averaging 256 transients). (c) Expanded region of  $^1\text{H}$  MAS NMR spectrum of wet epoxide-alumina in  $\text{D}_2\text{O}$  at  $B_0 = 20$  T. The MAS rate was  $\omega_R/2\pi = 60$  kHz.

Section 4.4 (pH 7 and  $25^\circ\text{C}$ ) compared with immobilised enzyme on epoxide-silica (Table 5.1).

It has been reported that several mono- and divalent cations, particularly sodium (Section 3.2.2.2) and calcium, bind proteolytic enzymes, inducing conformational changes which affect the catalytic activity of proteinases and/or the recognition process by their protein inhibitors [289-291]. Aluminium, as other metals, can act as an enzyme inhibitor. Aluminium strongly influences the binding properties of  $\alpha$ -chymotrypsin, affecting both substrate and the inhibitor recognition process [292]. The experimental data of Angeletti *et al.* [292] demonstrate that the modulative effect of aluminium is due to a simultaneous occupancy of the substrate and metal-binding sites. The substrate binding brings about a modification of the ionic environment of

**Table 5.5. Immobilisation results of  $\alpha$ -chymotrypsin on epoxide-alumina with different pore sizes.**

Pore size / Å	Contact load / (mg prot/g support)	Immobilised protein / (mg/g support)	Protein yield / %
50	81.5 ± 3.3	47.9 ± 2.2	58.8 ± 3.3
80	81.8 ± 2.4	64.2 ± 2.8	78.4 ± 2.2
100	80.4 ± 2.1	61.5 ± 1.4	76.5 ± 1.7
200	81.4 ± 3.7	59.3 ± 2.7	72.8 ± 2.4

the enzyme molecule, favouring aluminium binding. This situation induces a threefold decrease in the affinity of the enzyme for the macromolecular protein inhibitor bovine pancreatic trypsin inhibitor (BPTI) in presence of  $Al^{3+}$ . In the same study the pH effect was studied. They observed that upon increasing the pH from 7.0 to 8.5, the dissociation constant between  $Al^{3+}$  and the enzyme increases too. With this background the results shown in Table 5.6 seem plausible.

With the purpose of observing if the inhibition of aluminium is dependent or not on pH, different pH values were evaluated in the activity assay. Table 5.6 shows the enzymatic activity that took place at pH 7.0, 9.0 and 10.0 for all immobilised enzymes on epoxide-alumina. The results show a clear pH dependence on the enzymatic activity of enzyme immobilised on alumina-based supports, suggesting that protonated residues on the protein modulate the aluminium-linked effect.

Another contribution that could explain the pH dependence on the enzymatic activity could be a negative charge on the alumina surface in aqueous media. This attracts  $H^+$  ions and leads to a lower microenvironmental pH, and therefore an apparent shift in the enzyme pH profile to a higher pH.

Similarly to silica systems, cross-linking between residual Al-OH and alkyl silicon atoms ( $T_1$ ,  $T_2$  and  $T_3$ ) on epoxide-alumina surface takes place during the

**Table 5.6. Activity results at different pHs for immobilised enzyme on epoxide-alumina.**

Pore size / Å	Immobilised enzyme activity / (IU/g)			Activity yield / %			Retention activity / %		
	pH 7	pH 9	pH 10	pH 7	pH 9	pH 10	pH 7	pH 9	pH 10
50	21 ± 12	276 ± 10	350 ± 20	0.07 ± 0.01	0.84 ± 0.03	1.07 ± 0.06	0.09 ± 0.01	1.12 ± 0.04	1.42 ± 0.08
80	93 ± 15	776 ± 23	732 ± 10	0.28 ± 0.04	2.36 ± 0.07	2.23 ± 0.03	0.28 ± 0.04	2.35 ± 0.06	2.22 ± 0.02
100	93 ± 13	1005 ± 14	1005 ± 12	0.29 ± 0.04	3.11 ± 0.04	3.11 ± 0.03	0.29 ± 0.04	3.17 ± 0.04	3.17 ± 0.04
200	104 ± 11	1116 ± 12	420 ± 14	0.32 ± 0.03	3.41 ± 0.03	3.41 ± 0.12	0.34 ± 0.04	3.66 ± 0.03	1.38 ± 0.04

immobilisation in aqueous conditions (Figure 5.10b and Figure 5.10d). The  $^{29}\text{Si}$  peak around -100 ppm ( $Q_3$ ) before and after immobilisation in Figure 5.10b and Figure 5.10d can be attributed to impurities in the alumina support.

Figure 5.11 shows  $^{13}\text{C}$  CPMAS NMR before and after immobilisation of  $\alpha$ -chymotrypsin on epoxide-alumina (80 Å pore size). By comparison with Figure 5.5 (silica systems) and Figure 5.11 (alumina systems), no significant differences are observed after the immobilisation.

With the purpose of confirming whether the assignment for silica epoxide systems can be applied to epoxide-alumina systems, two-dimensional  $\{^1\text{H}, ^{13}\text{C}\}$  HETCOR spectra were recorded and are shown in Figure 5.13 (only  $^{13}\text{C}$  shifts below 100 ppm are displayed). The  $^{13}\text{C}$  projections of the two spectra are also shown. The  $^1\text{H}$  MAS NMR spectrum of the epoxide-alumina sample with added  $\text{D}_2\text{O}$  from Figure 5.12 is also presented. For both metal-oxide supported biocatalysts, the  $\{^1\text{H}, ^{13}\text{C}\}$  HETCOR spectra (Figure 5.8 and Figure 5.13) are comparable and the assignments are identical for the  $^{13}\text{C}$  and  $^1\text{H}$  peaks.

In general, the structural characterisation of both inorganic supports has shown quite similar results. In contrast, their performances as biocatalysts were completely

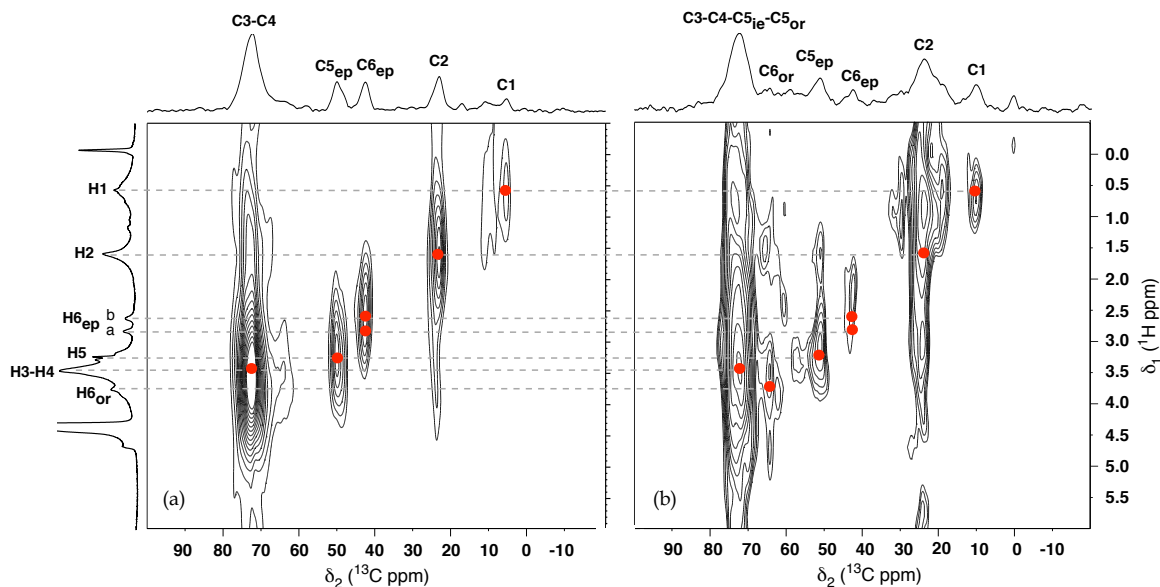


**Figure 5.13.** Two-dimensional  $\{^1\text{H}, ^{13}\text{C}\}$  HETCOR spectra of (a) dry epoxide-alumina and (b) dry immobilised enzyme on epoxide-alumina at  $B_0 = 20$  T and a MAS rate of  $\omega_R/2\pi = 10$  kHz, using 90 kHz SPINAL-64  $^1\text{H}$  decoupling during acquisition. Spectra were recorded with the pulse sequence shown in Figure 2.7 by averaging 256 transients for each of the 25  $t_1$  increments of 50  $\mu\text{s}$  ( $90^\circ$  pulse length of 3.5  $\mu\text{s}$ , contact time of 1 ms, relaxation interval of 3 s, averaging 20400 transients). Epoxide-alumina used had a pore size of 80  $\text{\AA}$  (TH-80).

different. The use of alumina supports is not recommended for immobilisation of  $\alpha$ -chymotrypsin if a high enzymatic activity is desirable.

### 5.3.3 Eupergit®

Eupergit® is a trademark of Evonik Industries. There are two different types of this support: Eupergit® C and 250 L (Appendix A, Table A.3). As a the result of a market driven decision, production of Eupergit® C was discontinued years ago and it is therefore no longer commercially available. This meant that Eupergit® 250 L alone was available for use in the present research. From this point onwards the term Eupergit® will be used to refer to Eupergit® 250 L unless otherwise stated. Eupergit® was generously donated by Evonik industries.

The epoxide content of Eupergit® by the modified Dubertaki method was 0.67 mol kg<sup>-1</sup> of support. This commercial support exhibits a higher amount of oxirane groups per mass than the metal-oxide-based supports (around 0.4 mol kg<sup>-1</sup> sup) described earlier in this Chapter.

Of the supports chosen in this thesis, Eupergit® becomes the most challenging to characterise by NMR due to the complexity of its nature as a polymer (3.1.3.1). The cross-linking agent used to manufacture the acrylic resin does not contain aromatic groups (personal communication with Dr Stefan Menzler who is in charge of the production of Eupergit® currently).

The <sup>13</sup>C CPMAS NMR spectra of Eupergit® are shown in Figure 5.14. The peak at 181 ppm corresponds to carbonyl groups, whereas the resonance at 67 ppm is assigned to carbon singly bonded to an oxygen atom (C-O) and the peak at 56 ppm relates to not-terminal epoxide carbon (C<sub>Ep</sub>). The resonance at 46 ppm corresponds to either a terminal epoxide carbon, a carbon bonded to nitrogen atoms or methyl carbons (C<sub>EpT</sub>, C-N or CH<sub>3</sub>). The broad peak at 20 ppm is attributed principally to backbone carbons in the polymer (C<sub>BB</sub>).

As observed before with epoxide-silica and epoxide-alumina, the addition of D<sub>2</sub>O to Eupergit® has a significant effect on the <sup>1</sup>H spectrum in narrowing signals and exchanging acidic protons (100 ml of D<sub>2</sub>O per 0.5 g of Eupergit®, at least 3 h prior to NMR recording) (Figure 5.15). The proton resonances from the epoxide ring (H<sub>ep</sub>) are visible after the addition of heavy water (Figure 5.15b) at 3.8 and 3.2 ppm. In the same spectrum a very sharp signal arises at 1 ppm, probably corresponding to methyl protons.

The immobilisation of α-chymotrypsin on Eupergit® was optimised. Some of the factors studied were the presence of ammonium sulfate at different concentrations and contacted loads of enzyme.

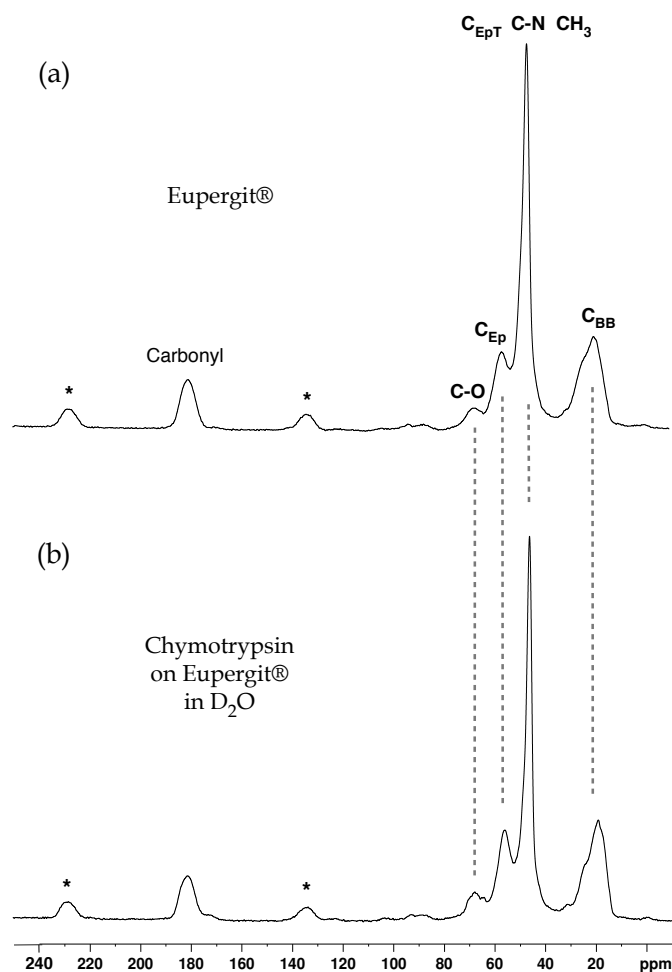


**Figure 5.14.**  $^{13}\text{C}$  CPMAS NMR spectra with  $^1\text{H}$  decoupling of (a) dry Eupergit® and (b) dry immobilised enzyme on Eupergit® ( $90^\circ$  pulse length of  $3.5\ \mu\text{s}$ , contact time of  $1\ \text{ms}$ , relaxation interval of  $3\ \text{s}$ , averaging 20400 transients) at  $B_0 = 20\ \text{T}$  and a MAS rate of  $\omega_R/2\pi = 15\ \text{kHz}$ , using  $90\ \text{kHz}$  SPINAL-64  $^1\text{H}$  decoupling during acquisition. Spinning sidebands are indicated by asterisks.

Again, the presence of ammonium sulfate shows favourable effects on the amount of protein immobilised (Table 5.7), almost doubling the protein yield. The immobilisation kinetics for these two immobilisations are shown in Figure C.3 (Appendix C). More than 60 hours are needed to complete the immobilisation without the use of ammonium sulfate. When ammonium sulfate was used the immobilisation process only took around the half of the time.

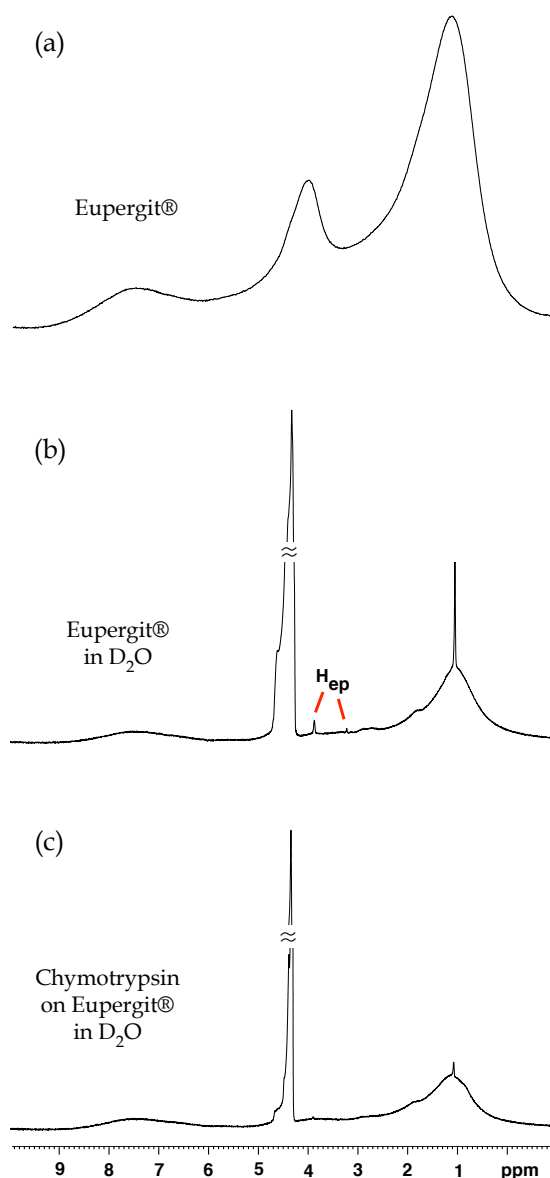


**Figure 5.15.** <sup>1</sup>H MAS NMR spectra (a) of dry Eupergit®, (b) wet Eupergit® in D<sub>2</sub>O and (c) wet immobilised enzyme on Eupergit® in D<sub>2</sub>O (90° pulse length of 1.8 μs, relaxation interval of 4 s, averaging 256 transients) at  $B_0 = 20$  T and a MAS rate of  $\omega_R/2\pi = 10$  kHz. The solvent peak has been truncated.

The use of different concentrations of ammonium sulfate was evaluated (Table 5.8) showing no clear optimum concentration. The contacted load used is still far from a concentration indicating saturation, even using over 100 mg of protein per g of support. This effect is possibly because of the higher oxirane density of Eupergit® compared with epoxide-silica or epoxide-alumina. An increase in the immobilised

**Table 5.7. Immobilisation results of  $\alpha$ -chymotrypsin on Eupergit® at pH 8.**

Immobilisation procedure	Contacted load / (mg prot/g support)	Immobilised protein / (mg/g support)	Protein yield / %
without ammonium sulfate	52.8 ± 4.2	26.7 ± 2.7	50.7 ± 4.3
with ammonium sulphate (1.88 M)	56.7 ± 3.6	55.1 ± 3.5	94.7 ± 5.1

**Table 5.8. Immobilisation results of  $\alpha$ -chymotrypsin on Eupergit® at different salt concentrations at pH 8.0.**

Salt concentration / M	Contacted load / (mg prot/g support)	Immobilised protein / (mg/g support)	Protein yield / %	Immobilised enzyme activity / (IU/g)	Activity yield / %	Retention activity / %
1.5	116.5 ± 5.2	111.4 ± 5.7	95.6 ± 4.3	571 ± 13	0.95 ± 0.02	1.00 ± 0.02
2.0	122.1 ± 4.4	115.8 ± 4.5	94.8 ± 3.1	399 ± 11	0.63 ± 0.01	0.67 ± 0.02
2.5	136.9 ± 4.1	135.8 ± 4.8	99.1 ± 3.9	402 ± 17	0.57 ± 0.02	0.58 ± 0.02

enzyme content can be due to an increase in the binding density [293]. However, the same positive effect can have negative repercussions in the form of a reduction of in activity retention, presumably because of rigidification of the conformation of the enzyme [294]. The multipoint covalent attachment has shown a significant increase in the thermostability of  $\alpha$ -chymotrypsin immobilised on Eupergit® C [295] but, intriguingly, in the same publication the retention of activity for this biocatalyst is not provided.

Interestingly, in Table 5.8 it is possible to observe that the activity of the immobilised enzyme at pH 8 decreases when a higher salt concentration has been used during the immobilisation. This is probably for the same reasons stated above: an increase of the

binding points between the enzyme and the support, leading to an observable decrease in the retention of activity.

As was mentioned in Section 4.5.2, the results for Eupergit® for the evaluation of the protein content in the washings were measured. The washings correction was significant in this case, and has been used. The immobilisation results for this system are summarised in Table 5.9.

Bearing in mind the points above, not all the protein adsorbed was immobilised by covalent binding because at least 6% of the protein is lost during the washing procedure. Non-covalent adsorption was higher for this support than for epoxide-silica and epoxide-alumina.

Figure 5.14 shows  $^{13}\text{C}$  CPMAS NMR spectra before and after immobilisation of  $\alpha$ -chymotrypsin at pH 8.0 with a protein loading of  $152 \text{ mg prot g}^{-1}$  support. No significant differences can be perceived because the high complexity of the Eupergit® spectrum obscures the signals from the protein. The parameters for both experiments in Figure 5.14 are the same, and thus are comparable. Presumably, the signal from the protein is very small compared with the significant background from the support, hence impeding observation of any differences in the spectra. This effect is noted, for example, in the signal from carbonyl groups, where at least some increase in intensity was expected but not found.

The effect of the addition of  $\text{D}_2\text{O}$  to an immobilised enzyme on Eupergit® was studied. Figure 5.15 shows  $^1\text{H}$  MAS NMR spectra before and after immobilisation with  $\text{D}_2\text{O}$  (5% w/v, at least 3 h prior to NMR recording). It is noticeable that the intensity of epoxide protons decreases after the immobilisation. This could be an effect of the immobilisation of the protein through the epoxide or the nucleophilic attack of water during the immobilisation procedure (as was noted earlier for silica and alumina systems).

**Table 5.9. Immobilisation results of  $\alpha$ -chymotrypsin on Eupergit® at pH 8 and with ammonium sulfate (2.0 M).**

Contacted load / (mg prot/ g support)	Immobilised protein / (mg/g support)		Protein yield / %		Immobilised enzyme activity / (IU/g)	Activity yield / %	Retention activity / %	
	Before	After	Before	After			Before	After
54.6	54.3 ± 3.1	53.0 ± 2.3	99.4 ± 5.6	96.9 ± 4.3	180 ± 12	0.64 ± 0.04	0.64 ± 0.04	0.66 ± 0.04
105.2	103.0 ± 4.6	96.3 ± 3.7	97.9 ± 4.4	91.5 ± 3.8	508 ± 14	0.94 ± 0.02	0.96 ± 0.02	1.02 ± 0.03
152.4	131.1 ± 2.3	108.6 ± 3.2	85.9 ± 2.7	71.2 ± 2.5	379 ± 20	0.48 ± 0.04	0.56 ± 0.03	0.68 ± 0.03

## 5.4 Discussion

Solid-state NMR has certain limitations as a characterisation tool of porous supports. One drawback of this technique is that it is not possible to obtain information about the size or distribution of pores. Gas adsorption analysis is the more conventional technique used for this purpose (see Section 3.1.1). Additional studies using adsorption methods could be beneficial in order to compare the metal-oxide systems and make better conclusions about the performance of these supports. Conclusions could be drawn that derive from information gained from examining the relative activity performance of the biocatalyst and the pore size distribution.

Another limitation of the use of solid-state NMR is the absence of information about the location of the immobilised enzyme. However, it is usually assumed for these types of systems that the majority of the enzyme is inside the pores because the internal surface is much larger than the external surface. The use of complementary techniques such as gas adsorption, XRD, FTIR or TEM could be extremely beneficial in providing further insights about the distribution of the protein within the supports.

Despite these pitfalls, solid-state NMR has proven its capabilities as a useful technique for characterising the surface interaction before and after silanisation of the oxide-metals supports used in this thesis. In addition, the use of FTIR and TGA could be used as complementary techniques to analyse the grafting procedure.

The use of solid-state NMR to characterise Eupergit® systems is less informative when compared to its use for silica and alumina systems. The main reason is the organic nature of Eupergit®. Future solid-state NMR studies of enzymes immobilised on polymers (and also on inorganic supports) should explore approaches other than cross-polarisation. In the cross-polarisation method, enhancement of  $^{13}\text{C}$  magnetisation is effective for immobile components in a polymer where there are relatively strong dipolar couplings. Therefore, there is a chance that mobile regions of the polymer have been missed in the CPMAS NMR spectra. Other solid-state NMR methods such as pulse saturation transfer under MAS or low decoupling under MAS can enhance the  $^{13}\text{C}$  signal of the mobile components in this type of system [296].

An interesting approach, not explored in this thesis, is the study of the enzyme-surface interactions by relaxation measurements using solid-state NMR. Potentially, solid-state NMR can be used to study the immobilised enzyme dynamics by indicating the strength of the dipolar interaction through relaxation measurements (e.g.,  $T_1$  or  $T_{1\rho}$ ) performed on the both the protein backbone and its side chains. This approach is based on the hypothesis that proteins that bind strongly will be less mobile than those that are not tightly associated with the surface. This tactic has been exploited for analogous systems to immobilised enzymes, such as membrane proteins and biomineralisation proteins (see Section 2.5.3.4).

Computer simulation methods such as molecular dynamics can also provide information about enzyme-surface interactions. Some work has been done for

immobilised proteins on surfaces (see Section 2.5.3.4). However, further development is needed to obtain more accurate predictions for such systems.

In addition to the NMR studies, the protein quantitation is an important step to fully characterise these systems after immobilisation. Here, the protein quantitation was conducted by a traditional difference method. This indirect method is not suited for fast immobilisation processes (see Appendix C, Figure C.2d) because it requires manual sampling and results in a low time resolution, typically tens of minutes. Table 5.10 shows other methodologies that can quantify protein concentration directly in real time. The additional use of these direct methods for protein quantification could be beneficial but not essential for future studies.

### 5.5 Conclusions

It has been shown that solid-state NMR can be used to characterise the metal-oxide-based supports (silica and alumina) used in an immobilised enzyme model biocatalyst and can also be used to follow changes in the surface environment upon coupling of the covalent linker (GOPS) and the enzyme ( $\alpha$ -chymotrypsin). In particular,  $^{29}\text{Si}$  CPMAS NMR spectra reveal changes in the surface species upon immobilisation, arising from cross-linking between silanol groups. Using one- and two-dimensional  $^{13}\text{C}$  CPMAS NMR, it was possible to achieve a full assignment of  $^{13}\text{C}$  and  $^1\text{H}$  species from the linker before and after covalent immobilisation of the enzyme. Although most of the focus of the work described in this Chapter has been upon the characterisation of the metal-oxide-based support and covalent linker, it was possible to observe carbonyl groups in the  $\alpha$ -chymotrypsin enzyme using  $^{13}\text{C}$  CPMAS NMR.

On the other hand, the information from the structural characterisation of the Eupergit® system by solid-state NMR was not as useful as for the other two metal-based biocatalysts. The complexity of the polymer, with an abundance of  $^{13}\text{C}$

**Table 5.10. Methods for quantification of immobilised protein.**

Method	References
Difference Method	[264], [297], [298]
QCM-D <sup>1</sup>	[78]
Fluorescence Microscopy	[76]

<sup>1</sup> Applicable only to immobilised enzyme on Quartz crystals

species from the support, makes it very difficult get a deep insight into the system. However, information on <sup>1</sup>H signals from the epoxide ring was noticeable before and after the immobilisation.

Finally, although the primary goal of this Chapter was the characterisation of the systems by solid-state NMR, some results from biochemical assays about the optimisation of the immobilisation process provided interesting information. For example, the effect of a high ionic strength during the immobilisation of protein is not a well known effect for metal-oxide-based supports, despite the popularity of the same approach for immobilisation on oxirane functional polymers.

## CHAPTER 6

# Quadrupolar Relaxation Studies of Immobilised Enzymes

There has been widespread interest in using NMR of spin  $I = 3/2$  nuclei, such as  ${}^7\text{Li}$ ,  ${}^{23}\text{Na}$ ,  ${}^{35}\text{Cl}$  and  ${}^{39}\text{K}$ , and spin  $I = 5/2$  nuclei, such as  ${}^{17}\text{O}$ ,  ${}^{25}\text{Mg}$ ,  ${}^{67}\text{Zn}$ ,  ${}^{85}\text{Rb}$  and  ${}^{127}\text{I}$ , to study the vital roles played by ions in many important biological processes.

The two main areas of interest have been the study of these nuclei in intracellular environments [299] and of their binding to biological molecules in solution [215]. In both cases the nuclei often exhibit multiexponential transverse and longitudinal quadrupolar relaxation [300] if the extreme narrowing condition is not fulfilled (i.e., if conditions of restricted mobility exist),

$$\omega_0\tau_c \geq 1 \tag{6.1}$$

As was mentioned in Section 2.3.1, the quadrupolar relaxation mechanism normally dominates the relaxation process and, therefore, the line shapes and widths of the NMR peaks observed from such nuclei. To a certain extent, quadrupolar NMR is advantageous because, effectively, only a single relaxation mechanism is in operation.

Multiple-quantum NMR experiments have been used to investigate multiexponential relaxation since 1986 [301, 302] when it was first discovered that multiple-quantum

coherences could be excited in liquid samples whose spectrum consisted only of a single resonance at a chemical shift characteristic of the aqueous ion.

In this chapter the study of the relaxation behaviour for different immobilised enzymes in the presence of sodium cations and water is explored. The theory behind multiple-quantum experiments for spins  $I = 3/2$  and  $I = 5/2$  will be outlined.

Principally, our interest in the study of quadrupolar relaxation lies in the study of water interactions with immobilised enzymes. It is generally assumed that in the presence of macromolecules, water can be located in the bulk, surface or buried (see Section 3.2.2.1). When immobilised enzymes are employed in non-aqueous media at low water activity, with bulk phases based on organic liquids, supercritical fluids or gas phases, residual water molecules bound to the enzyme are crucial in this case for the continuing function of the enzyme. The importance of these enzyme interactions is discussed in Section 3.2.2. The potential users of the methods developed in this chapter will be interested in determining the number of bound water molecules and the strength of their interaction with the immobilised enzyme at low water activity. Consequently, the fractions of free and bound water represent interesting information and potentially could be addressed using MQ-filtered  $^{17}\text{O}$  NMR. It is important to note that the systems tested here correspond to aqueous systems, where this is a matter of definition as well as of experimental measurement.

We decided to start with  $^{23}\text{Na}$  NMR – cheaper, more sensitive, and theoretically simpler than for spin  $I = 5/2$  – before moving on to  $^{17}\text{O}$  NMR. However,  $^{23}\text{Na}$  NMR relaxation study of sodium ions with immobilised enzyme is also an interesting system to evaluate.

The application of the techniques presented in this chapter to solid-liquid hybrids samples (see Section 6.1.2) using solid-state MAS NMR is completely novel.

## 6.1 Experimental details

### 6.1.1 NMR experiments

All NMR spectra presented in this chapter were recorded using the methodology of solid-state NMR, although many of the samples were solid-liquid composites.  $^{23}\text{Na}$  NMR experiments were performed on a Bruker Avance I 400 MHz spectrometer equipped with a widebore 9.4 T magnet and  $^{17}\text{O}$  NMR experiments on a Bruker Avance III 850 MHz spectrometer with a widebore 20 T magnet, yielding  $^1\text{H}$  resonance frequencies of approximately 400 and 850 MHz, respectively. All samples treated in this chapter contain liquids, therefore samples were packed into a 4 mm “CRAMPS-type” MAS rotor with a PTFE spacer to help contain the fluid. Samples were rotated at 10 kHz in a 4 mm MAS probe. Further experimental details such as pulse sequence, pulse length, free-precession delay, recycle delay and number of transients can be found in the text and figure captions.

### 6.1.2 Sample preparation

Samples were approximately 50% biocatalyst and 50% liquid by weight. The liquid was a solution of aqueous NaCl (0.03 M) for  $^{23}\text{Na}$  NMR experiments (Section 6.2) and 70%  $^{17}\text{O}$  enriched water for  $^{17}\text{O}$  NMR experiments (Section 6.3). The biocatalyst used in these experiments was immobilised enzyme ( $\alpha$ -chymotrypsin) on epoxide-silica of different pore sizes. Samples were stored at 3 °C and discarded after one week in case of possible microbiological contamination. Biocatalyst samples were the same preparations as the ones characterised in Chapter 5: immobilised-enzyme on epoxide-silica.

## 6.2 The Triple-Quantum Filter Experiment for $^{23}\text{Na}$ (Spin $I = 3/2$ )

The most frequently studied spin  $I = 3/2$  nucleus, especially *in vivo*, is  $^{23}\text{Na}$  because of its 100% natural abundance, high biological concentration and favourable gyromagnetic ratio (see Table 2.1).

The regulation of activity through metal ion complexation plays a key role in many enzyme-catalysed reactions [216]. In serine proteases there exists a specific site where  $\text{Na}^+$  binds to the enzyme, affecting positively the activity of these enzymes (Section 3.2.2.2). Although our main interest in  $^{23}\text{Na}$  TQF NMR experiments is to perform a trial run before moving on to  $^{17}\text{O}$  NMR experiments, the obtention of information about the behaviour of sodium cations in the presence of immobilised enzyme, also provides us with information that could potentially be of interest to us.

The  $\text{Na}^+$  interaction with the enzyme can be catalogued as an allosteric effect. Allostery can be defined as the regulation of protein function, structure and/or flexibility induced by the binding of a ligand, at a site away from the active site. The timescales of dynamics implicated in allostery often range from nanoseconds to milliseconds (see Figure 2.8) [303]. Here, a novel approach to the study of the quadrupolar relaxation behaviour of  $\text{Na}^+$  in the presence of a solid-liquid composite sample (i.e., immobilised enzyme in presence of a solution of  $\text{NaCl}$ ) by solid-state MAS NMR, using a solution-state NMR method [49], is presented.

When  $^{23}\text{Na}$  is transiently bound to the protein (i.e., under conditions of restricted mobility), electric field gradients created at the  $^{23}\text{Na}$  nucleus act as an effective relaxation mechanism and the outer transitions ( $m_I = -3/2 \leftrightarrow m_I = -1/2$  and  $m_I = +1/2 \leftrightarrow m_I = +3/2$ ) relax more quickly than the inner transition ( $m_I = -1/2 \leftrightarrow m_I = +1/2$ ). Jaccard *et al.* [301] and Pekar and Leigh [302] have independently shown that, when  $\text{Na}^+$  has two distinct relaxation rates for the inner and the outer transitions, the normal coherence transfer selection rule can be violated and MQ transitions become possible.

It has been shown that biexponentially relaxing spin  $I=3/2$  nuclei can be filtered through a state of multiple-quantum coherence, therefore providing unambiguous evidence of the presence of biexponential relaxation [301, 302]. NMR studies employing  $^{23}\text{Na}$  triple-quantum filter experiments have been used in the past to study sodium ion binding to biological molecules in solution [205, 304, 305].

The published theory behind triple-quantum filter experiments for  $I=3/2$  nuclei is written in terms of irreducible spherical tensor operators. A full description of these is beyond the scope of this section, which is the application of multiple-quantum experiments to the systems of interest (i.e., immobilised enzymes). Further details about the theory behind the study of relaxation for spin  $I=3/2$  through multiple-quantum techniques can be found in reference [301].

In brief, in the irreducible tensor operator basis the density operator  $\sigma(t)$  – the “state of the spin system” – for an isolated spin of quantum number  $I$  can be expressed as a linear combination of tensor operators

$$\sigma(t) = \sum_{l=0}^{2S} \sum_{p=-l}^l b_{l,p}(t) T_{l,p} \quad 6.2$$

where  $T_{l,p}$  denotes an irreducible spherical tensor operator of rank  $l$  and order  $p$ . The expansion of Equation 6.2 is especially useful in the description of multiple-quantum NMR experiments since the ranks ( $l$ ) and coherence order ( $p$ ) are readily identifiable.

If a number of uninteresting constants are ignored, the tensor operators for a spin  $I=3/2$  nucleus immediately after a  $90^\circ$  excitation pulse (“at  $t=0$ ”) are:

$$\sigma(t=0) = (T_{1,-1} - T_{1,+1}) \quad 6.3$$

That is, the initial transverse magnetisation is single quantum ( $p = \pm 1$ ) and in phase ( $l=1$ ). If the time evolution of the density operator occurs as a result of

biexponential transverse relaxation then, after time  $t$ , the new density operator  $\sigma(t)$  is given in tensor operator form by [301]

$$\sigma(t) = f_{11}^{(1)}(t)(T_{1,-1} - T_{1,+1}) + f_{31}^{(1)}(t)(T_{3,-1} - T_{3,+1}) \quad 6.4$$

where

$$f_{11}^{(1)}(t) = \frac{1}{5} \left( 3 \exp\{-R_f^{(1)}t\} + 2 \exp\{-R_s^{(1)}t\} \right) \quad 6.5$$

$$f_{31}^{(1)}(t) = \frac{\sqrt{6}}{5} \left( \exp\{-R_f^{(1)}t\} - \exp\{-R_s^{(1)}t\} \right) \quad 6.6$$

Note that doubly-antiphase single-quantum magnetisation (represented by  $T_{3,\pm 1}$ ) has appeared and can be used to excite MQ coherences (pulses can change the order of a tensor but not its rank). For pure quadrupolar relaxation in the absence of exchange, the fast ( $R_f$ ) and slow ( $R_s$ ) transverse relaxation rate constants can be calculated as

$$R_f^{(1)} = C(J_0 + J_1) \quad 6.7$$

$$R_s^{(1)} = C(J_1 + J_2) \quad 6.8$$

where the spectral densities  $J_n$  and the constant  $C$  are given by

$$J_n = \frac{2\tau_c}{1 + (n\omega_0\tau_c)^2} \quad 6.9$$

$$C = \frac{1}{40} \left( \frac{e^2 q Q}{\hbar} \right)^2 \left( 1 + \frac{\eta^2}{3} \right) \quad 6.10$$

where  $\tau_c$  is the motional correlation time,  $\omega_0$  is the Larmor frequency,  $e$  is the electronic charge,  $q$  is the magnitude of the EFG,  $Q$  is the nuclear quadrupolar moment,  $\hbar$  is the reduced Planck constant and  $\eta$  is the quadrupolar asymmetry parameter that can take values between 0 and 1.

Since the constant  $C$  depends not only on the nuclear quadrupolar moment  $Q$ , but also on the chemical environment of the nucleus, quadrupole couplings can vary greatly for the same nucleus. The quadrupolar coupling constant is intimately connected with the type of valence surrounding the nucleus. Moreover, the nuclear quadrupole constant tensor (see Equations 2.12 and 2.13) contains useful chemical information on the disposition of bonding and nonbonding electrons which determine the electric field gradient [306].

In a normal, “one-pulse” NMR experiment only the relaxation function  $f_{11}(t)$  can be measured, which corresponds to the sum of two decaying exponentials. In contrast, a multiple-quantum filtration experiment (Figure 6.1), by filtering the magnetisation through  $T_{3,\pm 2}$  or  $T_{3,\pm 3}$ , additionally allows the transverse relaxation function  $f_{31}^{(1)}(t)$  to be measured [301, 302]. This function is the *difference* of two decaying exponentials, which can permit their easier deconvolution. Chung and Wimperis [49] have shown that the triple-quantum filter (TQF) experiment (filtration through  $T_{3,\pm 3}$ ) is 50% more sensitive than the double-quantum (DQF) experiment (filtration through  $T_{3,\pm 2}$ ).

### 6.2.1 TQF $^{23}\text{Na}$ NMR relaxation study of sodium ions with immobilised chymotrypsin

Having considered our interest in first testing  $^{23}\text{Na}$  multiple-quantum NMR, here TQF experiments were evaluated for various immobilised enzymes of different pore sizes. A solution of aqueous NaCl (0.03 M) was added to our sample, where the binding of the sodium ions to  $\alpha$ -chymotrypsin leads to long correlation times, so that the transverse relaxation becomes biexponential.

The pulse sequence shown in Figure 6.1 (triple-quantum filtration) was used to measure spin  $I = 3/2$  transverse relaxation.

Figure 6.2a-c shows the TQF  $^{23}\text{Na}$  MAS NMR spectra of immobilised  $\alpha$ -chymotrypsin on epoxide silica 100, 200 and 300 Å with 0.03 M NaCl. Fixed evolution times  $\tau_e$  of 3,

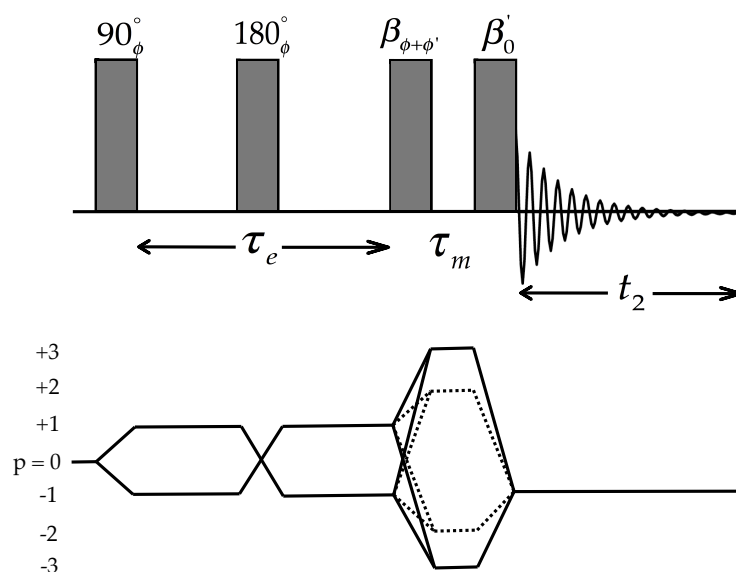


**Figure 6.1.** Pulse sequence and coherence pathway diagram for multiple-quantum filtration of spin  $I = 3/2$  nuclei to study biexponential transverse relaxation. Pulse phase  $\phi$  is stepped through the values the values  $0^\circ$ ,  $90^\circ$ ,  $180^\circ$  and  $270^\circ$  for double-quantum filtration (dashed coherence pathways) and through  $30^\circ$ ,  $90^\circ$ ,  $150^\circ$ ,  $210^\circ$ ,  $270^\circ$  and  $330^\circ$  for triple-quantum filtration (solid pathways).

7.2 and 13.8 ms were used, respectively, and 32768 acquisitions were taken for all samples. These TQF spectra correspond to  $F_{31}^{(1)}(\omega)$ , the Fourier transform of the time-domain function  $f_{31}(t)$ , and are the differences of two Lorentzian line shapes. Further experiments using TQF showed no signal from samples of epoxide silica without protein.

Figure 6.2d-f show the time-domain results obtained for immobilised  $\alpha$ -chymotrypsin with different pore sizes using the TQF pulse sequence. They show the peak amplitude plotted against  $\tau_e$ . The amplitudes of TQF spectra were measured for a range of values of  $\tau_e$  between 0 and 150 ms. This allows measurement of the time-domain function  $f_{31}(t)$  directly and, as a consequence of the  $180^\circ$  pulse in the middle of the  $\tau_e$  period, is free of most of the adverse effects of  $B_0$  inhomogeneity. The experimental time-domain data presented in Figure 6.2d-f were fitted to a biexponential model (Equation 6.11) using Mathematica software (Appendix E).

$$f_{13}^{(1)}(t) = A \frac{\sqrt{6}}{5} \left( \exp(-R_f^{(1)}t) - \exp(-R_s^{(1)}t) \right) \quad 6.11$$

where  $A$  is an amplitude factor.

The Fourier-Laplace transform was used to provide the matrix  $\mathbf{F}^{(1)}(\omega)$  directly, yielding the analytical frequency-domain lineshapes  $F_{11}^{(1)}(\omega)$  and  $F_{31}^{(1)}(\omega)$ , starting from the transverse relaxation matrix  $\mathbf{R}_{\text{tensor}}^{(1)}$  in the spherical tensor operator basis (Appendix D). The spectra presented in Figure 6.2a-c were fitted to the lineshape function  $F_{31}^{(1)}(\omega)$  (Equation 6.12) using a Mathematica routine (Appendix E).

$$F_{31}(\omega) = -\frac{\sqrt{6}C(J_2 - J_0)}{5(CJ_1 + CJ_2 + i\omega)(CJ_1 + CJ_0 + i\omega)} \quad 6.12$$

where  $J_n$  and  $C$  are defined in Equations 6.9 and 6.10, respectively. Only the real component of Equation 6.12,  $F_{31}^{(1)}(\omega)_{\text{real}}$  (Appendix D, Equation D.8), was used.

For convenience, the parameters extracted from the Mathematica routines were  $R_f^{(1)}$  and  $R_s^{(1)}$  for the time-domain data and  $\tau_c$  and  $C$  for frequency-domain. The calculation of the remaining dependent parameters was achieved using Equations 6.7 to 6.10.

Substantial differences in the values for  $R_s^{(1)}$  between the two method – frequency- and time-domain – were observed. Frequency and time-domain methods should converge to provide identical results within a negligible margin of error; nonetheless significant differences were found. A probable explanation for these differences might be the impact of  $B_0$  inhomogeneity, which will affect only the line shape fitting results, in particular the line width of the central component. For this reason, only the results obtained by the time-domain fitting are presented here (Table 6.1).

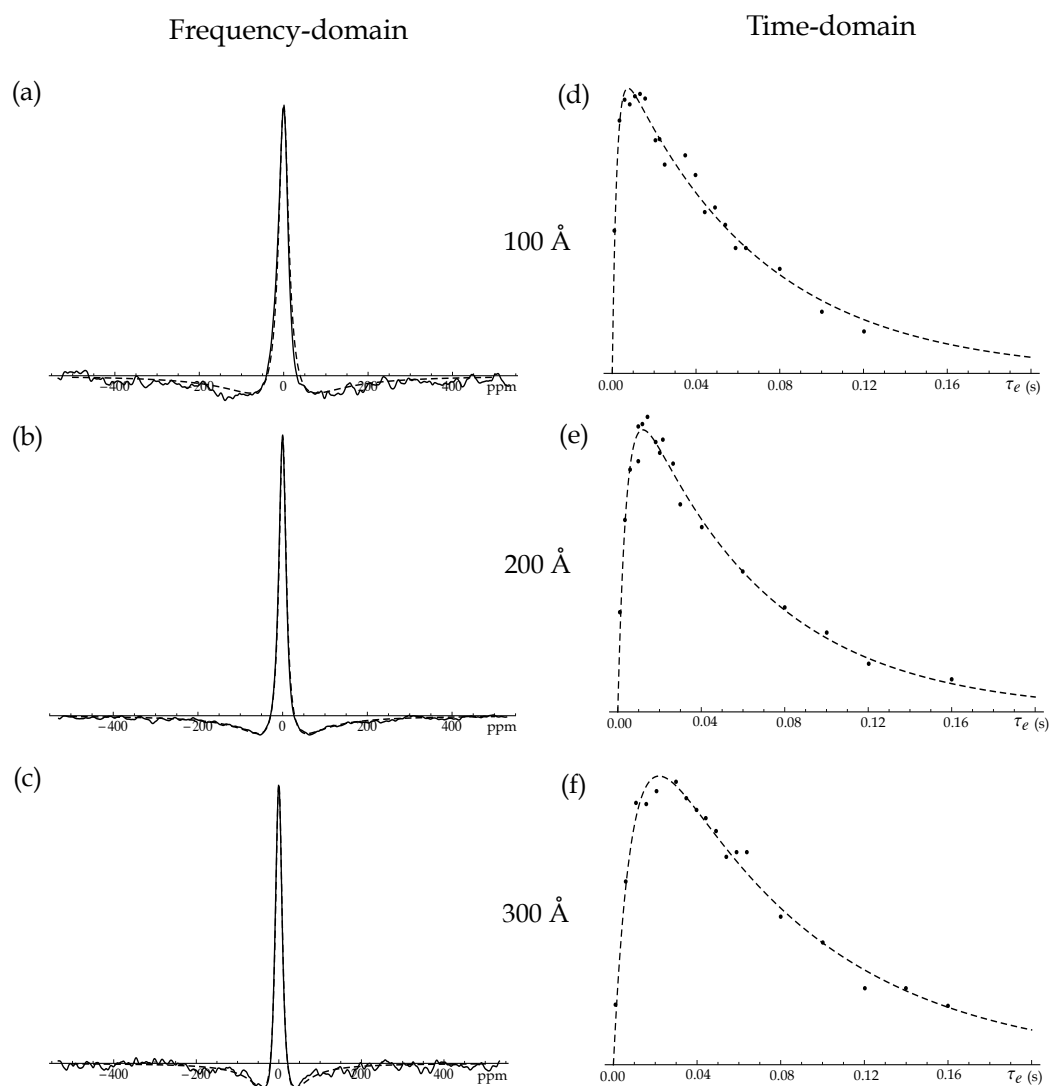


**Figure 6.2.** TQF  $^{23}\text{Na}$  MAS NMR spectra of immobilised enzyme of pore size (a) 100 Å, (b) 200 Å and (c) 300 Å with fixed  $\tau_e$  values of 10, 15 and 20 ms, respectively, recorded in presence of NaCl (0.03 M). TQF time-domain peak amplitude against  $\tau_e$  (s) plots of immobilised enzyme of pore size (d) 100 Å, (e) 200 Å and (f) 300 Å in presence of NaCl (0.03 M). All spectra were recorded with the pulse sequence shown in Figure 6.1 at  $B_0 = 9.4$  T and MAS rate of  $\omega_R/2\pi = 10$  kHz ( $90^\circ$  pulse length of  $5.5 \mu\text{s}$ ,  $\tau_m$  of  $2 \mu\text{s}$ , relaxation interval of  $0.2$  s, averaging 4096 transients). Computer fittings (dashed lines) were performed to experimental data (solid line in spectra and circles for time-domain plots).

Although difficult to interpret, the correlation time  $\tau_c$  of motion associated with relaxation is a parameter that is potentially of interest for our research. This parameter contains information about the dynamics of the protein as well as the bulk

**Table 6.1. Results for time-domain fitting of  $^{23}\text{Na}$  TQF NMR data from immobilised chymotrypsin with different pore sizes.  $R_f^{(1)}$ ,  $R_s^{(1)}$ ,  $C$  and  $\tau_c$  are defined in Equations 6.7-6.10.**

Pore size /Å	$R_f^{(1)}$ / s <sup>-1</sup>	$R_s^{(1)}$ / s <sup>-1</sup>	$C$ / s <sup>-2</sup>	$\tau_c$ / ns	R <sup>2</sup>
100	980 ± 20	33 ± 1	(5.3 ± 0.1) × 10 <sup>10</sup>	9 ± 0.2	0.9970
200	484 ± 18	32 ± 1	(3.7 ± 0.1) × 10 <sup>10</sup>	6 ± 0.2	0.9972
300	226 ± 20	25 ± 2	(2.3 ± 0.2) × 10 <sup>10</sup>	4 ± 0.4	0.9974

physical characteristics of the solvent. A novel aspect of the experiments performed in this chapter is that the protein is tethered to a solid. Therefore the correlation time should not reflect rotational diffusion of the protein molecule, because the protein is “static”. It is usually assumed that sodium ions are in fast exchange between free solution and the bound state. In this case the obtained  $\tau_c$  values are more likely due to the distortion of the water coordination sphere that takes place as the Na<sup>+</sup> binds and unbinds – this will cause a fluctuation of the quadrupolar coupling that will be “rotation-like” and so will possess a definable correlation time. Of course, there is the possibility of a contribution from local motion in the protein or perhaps a rocking motion on the surface.

As can be seen from Table 6.1, the correlation times  $\tau_c$  obtained show a decreasing trend when the pore size is increased. When the protein is immobilised, the relaxation effect depends instead on the internal molecule residence time rather than on free tumbling of protein molecules [307]. Therefore as an effect of pore size, the internal residence times are reduced when it is larger. However, these data must be interpreted with caution due to the little knowledge about relaxation phenomena on proteins in restricted or inhibited motion environments. The correlation times in this type of system will be dictated by the residence time of the ligand and also by the restricted movement of the immobilised protein.

The values of correlation time showed in Table 6.1 were calculated assuming no fast chemical exchange in the systems. It is clear that a non-chemical exchange approach is unrealistic. An attempt to obtain correlation time  $\tau_c$  assuming fast chemical exchange between bound sodium ions and free solution was performed. The values obtained did not make sense in terms of their magnitude (less than 1 ns) and therefore these results were omitted. A motional model that includes such fast chemical exchange is used for the spin  $I = 5/2$  systems in Section 6.3.1.

### 6.3 Four-Quantum and Five-Quantum Evolution Experiments for $^{17}\text{O}$ -labelled (Spin $I = 5/2$ )

Water plays an important role in enzyme structure and function. Water molecules affect the ionisation and mobility of groups or residue chains on the protein surface (Section 3.2.2.1). The study of the structural and dynamic details of the immobilised enzyme-water interaction is covered here. With this purpose, enriched  $^{17}\text{O}$ -water was used and the  $^{17}\text{O}$  NMR relaxation behaviour in presence of immobilised enzyme was studied. As was mentioned earlier in this chapter, the fractions of free and bound water in presence of immobilised enzyme are of interest to us and could be addressed using MQ-filtered  $^{17}\text{O}$  NMR.

With a spin quantum number of  $I = 5/2$ ,  $^{17}\text{O}$  is the only magnetic nuclide of oxygen. Despite its low abundance and low gyromagnetic ratio (Table 2.1), this nuclide has attracted considerable interest as a means of probing the environment of water in biological systems [308].

In general, spin  $I = 5/2$  nuclei are less favourable to study than spin  $I = 3/2$  nuclei as a consequence of far more complicated relaxation dynamics. As with spin  $I = 3/2$  systems, it is possible to use multiple-quantum filtration experiments to study relaxation in spin  $I = 5/2$ . However, to obtain quantitative parameters from such studies (e.g., relaxation rate constants, fraction of bound water, etc.) requires the use

of complex iterative fitting techniques as, unlike in the  $I = 3/2$  case, both the amplitudes and line widths of the (now) three components depend on  $\tau_c$ . A much simpler alternative is to monitor the relaxation of fifth-rank four-quantum and five-quantum coherences [309]. These exhibit exponential decays under all motional conditions and a simple exponential fitting (see Figure 6.6) of both is all that is required to extract the two independent variables: correlation time and exchange-averaged quadrupolar coupling constant.

The scope of this section is the application of multiple-quantum evolution experiments to immobilised enzymes. Further details about the theory behind the study of relaxation for spin  $I = 5/2$  through multiple-quantum techniques can be found in reference [50].

The pulse sequence used to measure spin  $I = 5/2$  four-quantum and five-quantum relaxation is shown in Figure 6.3. In this sequence the multiple-quantum coherence is allowed to evolve during the mixing period  $\tau_m$  so that its exponential decay can be measured.

If a number of uninteresting constants are ignored, the spin  $I = 5/2$  tensor operators at the start of the mixing period,  $t_m = 0$  for the rank  $l = 5$  four-quantum and five-quantum coherences are

$$\sigma_{4Q}(t_m = 0) = (T_{5,-4} - T_{5,+4}) \quad 6.13$$

$$\sigma_{5Q}(t_m = 0) = (T_{5,-5} - T_{5,+5}) \quad 6.14$$

Thus, after a time  $t_m$ , the new density operators for four-quantum and five-quantum coherence can be written

$$\sigma_{4Q}(t) = f_{55}^{(4)}(t_m)(T_{5,-4} - T_{5,+4}) \quad 6.15$$

$$\sigma_{5Q}(t) = f_{55}^{(5)}(t_m)(T_{5,-5} - T_{5,+5}) \quad 6.16$$

where

$$f_{55}^{(4)}(t_m) = \exp\{-R_2^{(4)}t\} \quad 6.17$$

$$f_{55}^{(5)}(t_m) = \exp\{-R_1^{(5)}t\} \quad 6.18$$

For pure quadrupolar relaxation in the absence of exchange, the two relaxation rate constants can be calculated as

$$R_2^{(4)} = C'(6J_0 + 2J_1 + 7J_2) \quad 6.19$$

$$R_1^{(5)} = C'(10J_1 + 5J_2) \quad 6.20$$

where  $C'$  is given for spin  $I = 5/2$  by

$$C' = \frac{3}{2000} \left( \frac{e^2 q Q}{\hbar} \right)^2 \left( 1 + \frac{\eta^2}{3} \right) \quad 6.21$$

and the spectral densities  $J_n$  by Equation 6.9.

Chemical exchange is an intrinsic feature of any system that involves ligand binding<sup>5</sup> to a macromolecule. The theory behind quadrupolar relaxation in the presence of chemical exchange has been treated in references [310, 311]. For quadrupolar nuclei it is possible to assume that there exist two exchanging populations of water molecules in fast chemical exchange, namely bulk water in the extreme narrowing limit and water bound in the slow-motion limit. The two correlation times will be very different; the relaxation rates of the quadrupolar nuclei at the bound site are much greater than at the free site, while their exchange lifetimes are much less.

$$R_1^{(5)} = R_f^{(5)} + (p_b / p_f) R_b^{(5)} \quad 6.22$$

---

<sup>5</sup> Ions, inhibitors and water can interact with macromolecules as ligands.

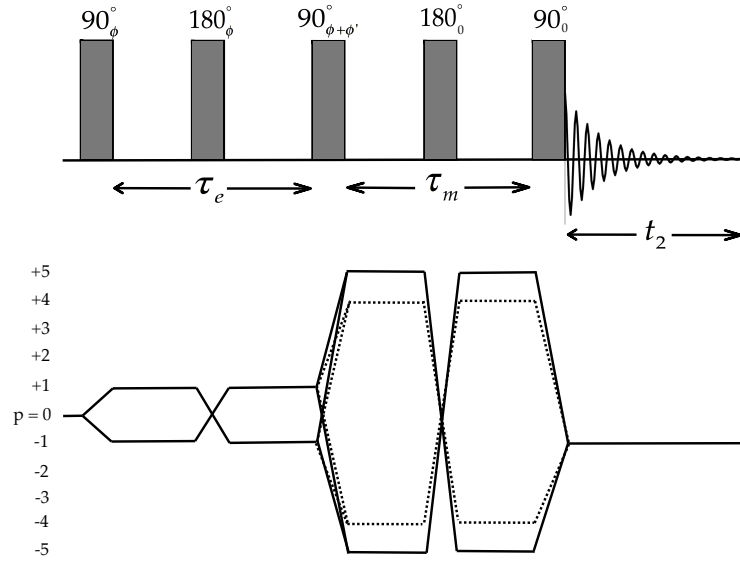


Figure 6.3. Pulse sequence and coherence pathway diagram for multiple-quantum evolution sequence for spin  $I = 5/2$  nuclei to measure four-quantum and five-quantum relaxation functions  $f_{55}^{(4)}(t_m)$  and  $f_{55}^{(5)}(t_m)$ . Pulse phase  $\phi$  is stepped through the values  $0^\circ$ ,  $45^\circ$ ,  $90^\circ$ ,  $135^\circ$ ,  $180^\circ$ ,  $225^\circ$ ,  $270^\circ$  and  $315^\circ$  for four-quantum (dashed coherence pathways) and through  $18^\circ$ ,  $54^\circ$ ,  $90^\circ$ ,  $126^\circ$ ,  $162^\circ$ ,  $198^\circ$ ,  $234^\circ$ ,  $270^\circ$ ,  $306^\circ$  and  $342^\circ$  for five-quantum coherence (solid pathways). The exponential four-quantum and five-quantum relaxation rates are measured by monitoring the amplitude of the observed signal as a function of the mixing time period  $\tau_m$ .

$$R_2^{(4)} = R_f^{(4)} + (p_b / p_f) R_b^{(4)} \quad 6.23$$

where  $R_f^{(5)}$  and  $R_f^{(4)}$  are the free-site relaxation rates,  $R_b^{(5)}$  and  $R_b^{(4)}$  are the bound-site relaxation rates, and  $p_b$  and  $p_f$  are the bound and free ion fractions.

The free-site relaxation rate constants  $R_f^{(5)}$  and  $R_f^{(4)}$  can be assumed to be negligible compared with the bound-site relaxation rate constants [50]

$$R_f^{(5)} \ll (p_b / p_f) R_b^{(5)} \quad 6.24$$

$$R_f^{(4)} \ll (p_b / p_f) R_b^{(4)} \quad 6.25$$

The ratio of the two bound-site relaxation rates is given by [50]

$$\alpha = \frac{R_1^{(5)}}{R_2^{(4)}} = \frac{(p_b/p_f)R_b^{(5)}}{(p_b/p_f)R_b^{(4)}} = \frac{40J_1 + 20J_2}{24J_0 + 8J_1 + 28J_2} \quad 6.26$$

With the spectral densities  $J_n$  given by Equation 6.9 the expression for  $\omega_0\tau_c$  can be solved

$$\omega_0\tau_c = \left( \frac{15(1-\alpha) + [5(1-\alpha)(45-13\alpha)]^{1/2}}{16\alpha} \right)^{1/2} \quad 6.27$$

With the measured quadrupolar constant  $C'$  from Equations 6.19 or 6.20 and assuming a value for the  $^{17}\text{O}$  quadrupolar constant of pure water  $C_w$ , the ratio between the bound and free ion fraction  $p_b/p_f$  can be calculated since

$$\frac{p_b}{p_f} = \frac{C'}{C_w} \quad 6.28$$

### 6.3.1 An $^{17}\text{O}$ multiple-quantum NMR relaxation study of water dynamics and interactions with immobilised chymotrypsin

The MAS NMR experiments described in this section were performed on immobilised chymotrypsin on epoxide silica of two different pore sizes (100 and 200 Å) in the presence of 70%  $^{17}\text{O}$  enriched water (added with mass approximately equal to that of the whole immobilised preparation).

Four-quantum and five-quantum evolution  $^{17}\text{O}$  NMR experiments were performed using the pulse sequence in Figure 6.3. The phase of the third pulse was  $\phi' = 0^\circ$  for four-quantum and  $\phi' = 90^\circ$  for five-quantum coherences. The following phase cycles were used in addition to those provided in Figure 6.3: a two-step phase cycle to counteract any imperfections of the first  $180^\circ$  pulse; a two-step phase cycle to counteract any imperfections of the second  $180^\circ$  pulse; and a four-step CYCLOPS

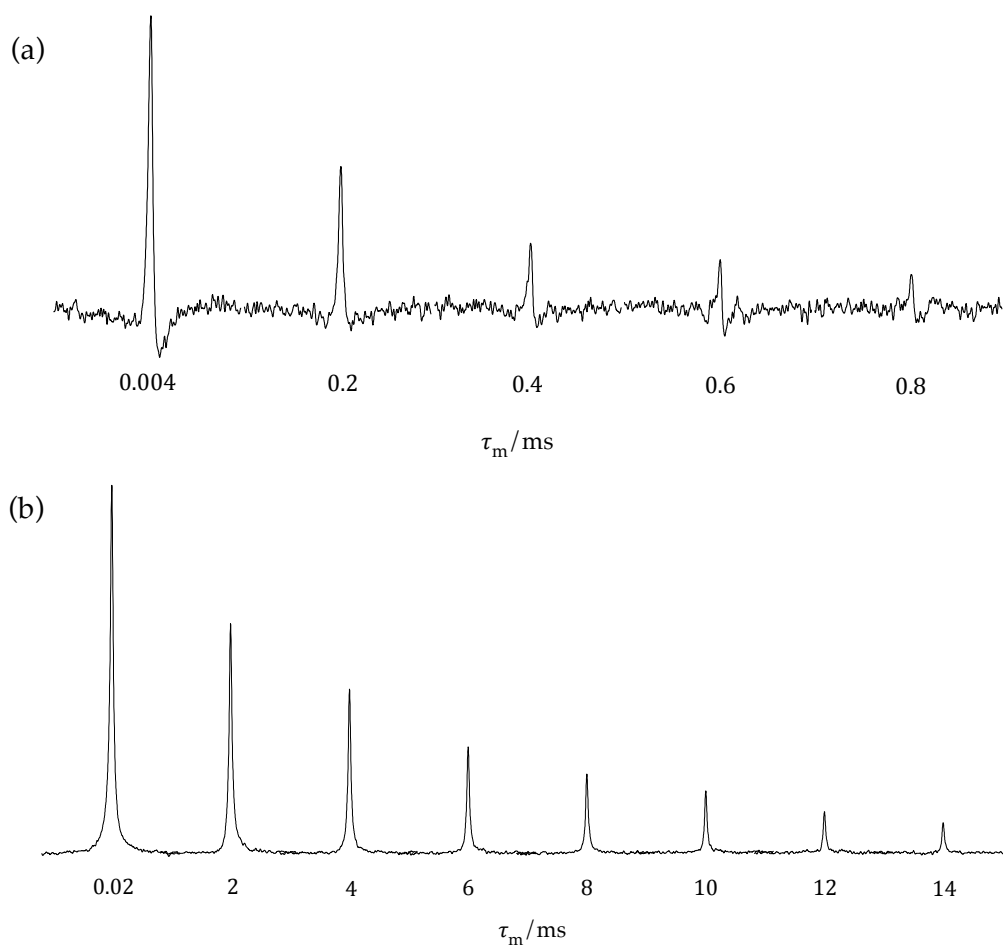


**Figure 6.4.** (a) Four-quantum and (b) five-quantum evolution  $^{17}\text{O}$  MAS NMR spectra of immobilised enzyme on epoxide silica with a pore size of  $100 \text{ \AA}$  in presence of  $^{17}\text{O}$  enriched water. The spectra shown were recorded with the pulse sequence shown in Figure 6.3 with a variable  $\tau_m$  at  $B_0 = 20 \text{ T}$  and MAS rate of  $\omega_R/2\pi = 10 \text{ kHz}$  ( $90^\circ$  pulse length of  $5.2 \mu\text{s}$ ,  $\tau_e$  of  $0.6 \text{ ms}$ , relaxation interval of  $0.1 \text{ s}$ , averaging 2400 transients).

phase cycle. Overall this resulted in a 128-step phase cycle for four-quantum and a 160-step phase cycle for the five-quantum evolution experiment [50].

Figure 6.4 shows the  $^{17}\text{O}$  NMR spectra obtained using the four-quantum and the five-quantum evolution experiments for chymotrypsin immobilised on epoxide silica with a pore size of  $100 \text{ \AA}$ . Likewise, Figure 6.5 shows the spectra for chymotrypsin immobilised on epoxide silica with a pore size of  $200 \text{ \AA}$ . The spectra are shown as a function of the mixing time  $\tau_m$ . The evolution period was fixed at the experimentally optimised values of  $\tau_e = 0.62$  and  $\tau_e = 1 \text{ ms}$  for  $100$  and  $200 \text{ \AA}$  pore size, respectively.

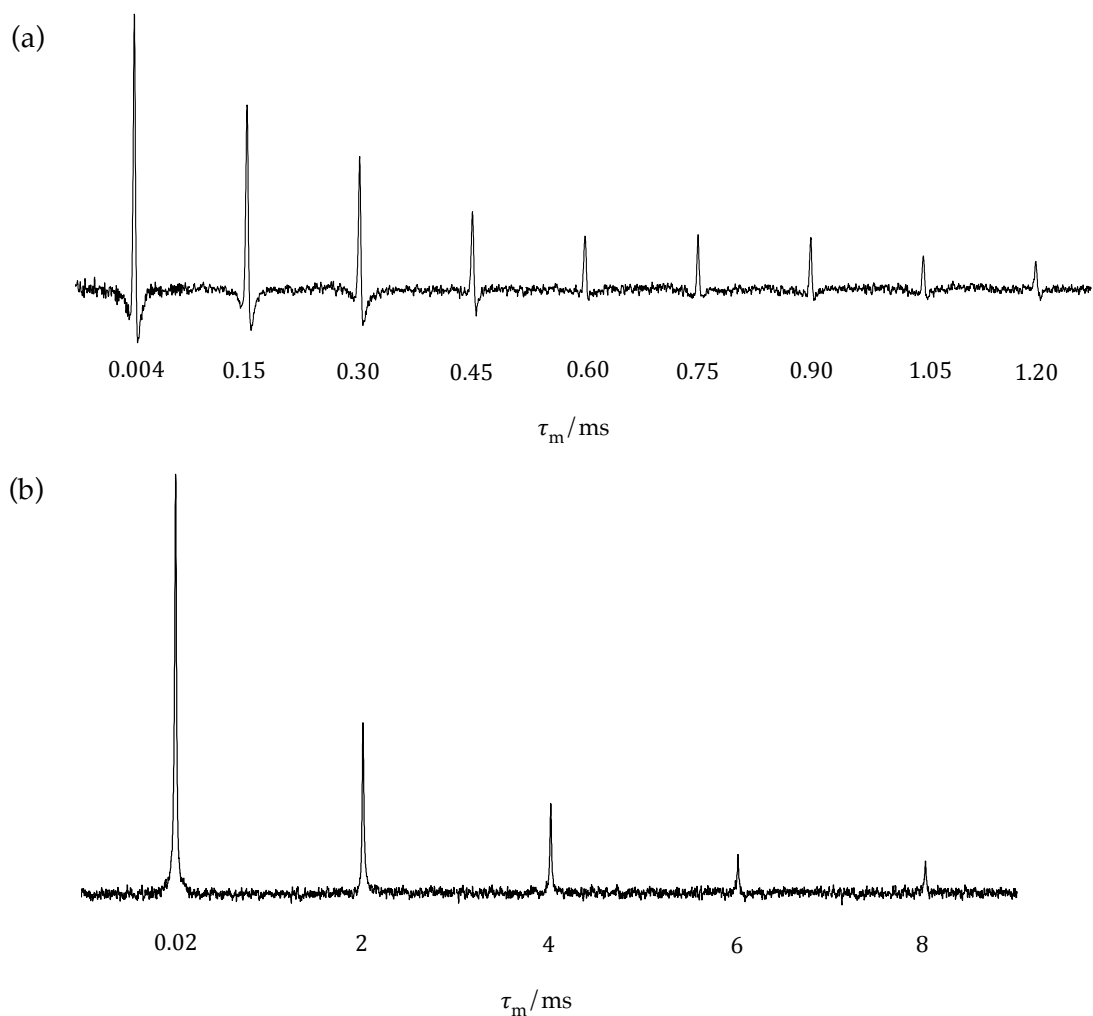


**Figure 6.5.** (a) Four-quantum and (b) five-quantum evolution  $^{17}\text{O}$  MAS NMR spectra of immobilised enzyme on epoxide silica with a pore size of  $200 \text{ \AA}$  in the presence of  $^{17}\text{O}$  enriched water recorded at  $B_0 = 20 \text{ T}$ . The spectra shown were recorded with the pulse sequence shown in Figure 6.3 with a variable  $\tau_m$  at  $B_0 = 9.4 \text{ T}$  and MAS rate of  $\omega_R/2\pi = 10 \text{ kHz}$  ( $90^\circ$  pulse length of  $5.2 \mu\text{s}$ ,  $\tau_e$  of  $1 \text{ ms}$ , relaxation interval of  $0.1 \text{ s}$ , averaging 2048 transients).

The four-quantum coherence is observed with lower sensitivity and shows a much faster relaxation rate. These results are in accordance with the analogous  $^{25}\text{Mg}$  NMR work of Chung and Wimperis in the solution state [50].

As described in Section 6.3, the correlation time and quadrupolar coupling constant can be extracted analytically from the exponential four-quantum and five-quantum

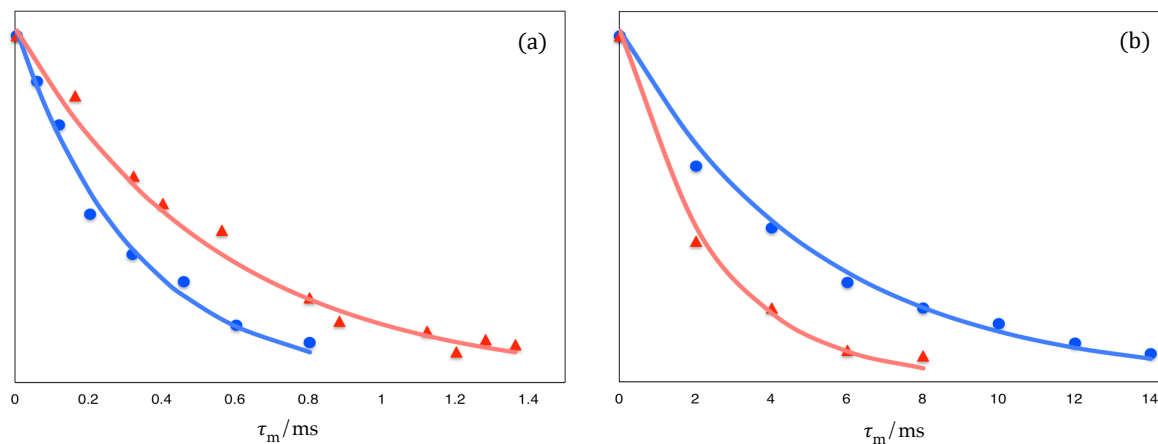


**Figure 6.6.**  $^{17}\text{O}$  peak amplitude as a function of  $\tau_m$  evolution time in (a) four-quantum NMR experiment and (b) a five-quantum NMR experiment. Data and fitted lines for immobilised chymotrypsin on epoxide silica with pore sizes 100 Å (blue circles) and 200 Å (red triangles). Note the change in  $\tau_m$  scale between (a) and (b).

relaxation rates. Peak amplitudes from Figure 6.4 and Figure 6.5 were fitted to a first-order decay as a function of time  $\tau_m$  (Figure 6.6). The fitting procedure was generated using Mathematica software to obtain relaxation rate constants.

These values obtained are shown in Table 6.2. By combining these two relaxation values, and assuming the theoretical treatment of Chung and Wimperis [50] to be valid (Equations 6.24 to 6.28), it is possible to obtain estimates of the correlation times of motions associated with relaxation, and the number of water molecules perturbed by interaction with the immobilised enzyme. This leads to the further values in Table 6.3 using a value of the quadrupolar coupling constant  $(e^2qQ/\hbar)(1+\eta^2/3)^{1/2}$  for liquid  $^{17}\text{O}$ -water of 7.7 MHz [312]. This enabled the fraction of bound  $p_b$  and free  $p_f$  water and the number of water molecules bound to the protein to be estimated (see Table 6.2). The number of water molecules bound per immobilised enzyme (mol/mol) can be calculated since the amount of  $^{17}\text{O}$  enriched water and immobilised enzyme in the sample were measured. The numbers of water molecules bound to the enzyme are plausible.

It is possible to obtain motional correlation times from these experiments and these are also given in Table 6.2. Earlier, in Section 3.2.2.1, it was mentioned that water molecules can be classified into three different categories according to their dynamical properties: bulk water with typical reorientational correlation time  $\tau_c$  of the order of picoseconds; water present on the surface of the protein which exhibits a partially restricted motion with  $\tau_c$  in the order of nanoseconds; and buried water molecules with  $\tau_c$  values typically of the order of  $10^{-8}$  seconds (tens of nanoseconds). The values for motional correlation times  $\tau_c$  obtained here (Table 6.2) fall within motional range for water present on the surface of the protein.

As with the  $^{23}\text{Na}$  TQF experiments, a decrease in  $\tau_c$  values was observed for  $^{17}\text{O}$  multiple-quantum experiments for immobilised enzymes with increasing pore sizes (Table 6.2). The idea that internal residence times are reduced when the pore of the support is larger, therefore reducing  $\tau_c$ , is corroborated by these results.

### 6.4 Discussion

Future studies should address the possibility of interactions between the ligands (i.e.,  $\text{Na}^+$  and  $\text{H}_2^{17}\text{O}$ ) and the support, which in this case is silica. Jang and Fuerstenau [313] observed a correlation time of 7 ns by  $^{23}\text{Na}$  spin-lattice relaxation studies for silica of pore size 100 Å in a NaCl solution. They concluded that this correlation time probably reflected the time needed for sodium ions to diffuse out of the pore region, rather than a motional restriction of the interfacial sodium ion due to binding.

**Table 6.2. Results for fitting and calculations for multiple-quantum evolution experiment of  $^{17}\text{O}$  NMR data from immobilised chymotrypsin with different pore sizes.  $R_2^{(4)}$ ,  $R_1^{(5)}$ ,  $C'$  and  $\tau_c$  are defined in Equations 6.23-6.28.**

Pore size / Å	$R_2^{(4)} / \text{s}^{-1}$	$R_1^{(5)} / \text{s}^{-1}$	$C' / \text{s}^{-2}$	$\tau_c / \text{ns}$	$\frac{p_b}{p_f}$	Bound water per enzyme / (mol/mol)	$R^2$
100	$6140 \pm 20$	$389 \pm 2$	$(1.71 \pm 0.01) \times 10^{10}$	$7.32 \pm 0.02$	$(20 \pm 0.12) \times 10^{-3}$	$345 \pm 2$	0.9983
200	$3610 \pm 12$	$814 \pm 3$	$(1.93 \pm 0.01) \times 10^{10}$	$3.59 \pm 0.01$	$(22 \pm 0.13) \times 10^{-3}$	$425 \pm 3$	0.9997

Additional control experiments of the bare supports and ligands should be included to evaluate if there is any interaction between them. These can be performed in a similar fashion to those used in [313] for inversion time recovery  $T_1$  experiments. This information will help in a better understanding of the interpretation of the motion times obtained. Also, it will help provide a more accurate value for the water molecules bound to the immobilised enzyme in the case of the  $^{17}\text{O}$  NMR experiments.

The magnitude of the correlation times obtained – in the range of nanoseconds – by  $^{23}\text{Na}$  and  $^{17}\text{O}$  multiple-quantum experiments is in accordance with what is expected for a small protein like  $\alpha$ -chymotrypsin [314]. Shimshick *et al.* [315] measured  $\tau_c$  for a phosphonyl  $\alpha$ -chymotrypsin with a nitroxide spin-label by Electron Paramagnetic Resonance (EPR), obtaining an experimental value of 12 ns. They argued that, due to the rigid body motion of the labelled enzyme, the correlation time must be 1.6 times smaller than the theoretical value predicted for a rigid sphere of the same mass and density as  $\alpha$ -chymotrypsin using the Debye equation (around 7.5 ns). Despite these results having similar magnitudes with the  $\tau_c$  values presented in Table 6.1 and Table 6.2, there is no a clear picture of the behaviour of the immobilised enzyme and the data must be interpreted with caution. This is mainly because our systems have a restricted mobility, where the enzyme is tethered on a solid surface.

The numbers of water molecules calculated by  $^{17}\text{O}$  NMR experiments are plausible for those surrounding the protein surface. For a fuller picture, it is also necessary also to consider the possibility of water molecules interacting with sites on the silica surface (ones not masked by the attached protein, silane coupling agent used as a first step of immobilisation or hydroxyl/amino groups on the hydrolysed epoxides). Another consideration is that not all the interactions between protein and water are the same: the binding of water to some sites on the protein is much stronger (e.g., around charged groups) than others. However, values between 300 and 400 water molecules are feasible numbers for a fully hydrated small protein like  $\alpha$ -chymotrypsin. Similar values have been obtained for water bound to small proteins in the free state by molecular dynamics, X-ray and neutron diffraction [198, 316, 317].

### 6.5 Conclusions

The relaxation phenomena associated with immobilised enzymes interacting with  $\text{Na}^+$  and water were studied. The multiple-quantum  $^{23}\text{Na}$  NMR experiment trial run was successfully performed enabling us to move on to multiple-quantum  $^{17}\text{O}$  NMR experiments. The later experiments were also performed successfully, providing us with the information required: the number of water molecules bound to the immobilised enzyme. The multiple-quantum techniques to follow transverse relaxation used in this Chapter have been proved to be useful for the evaluation of these systems.

For studies of spin  $I = 3/2$  it was observed that the frequency-domain method is not an effective means to derive information from the relaxation behaviour because relaxation rates are falsified by  $B_0$  inhomogeneity. The time-domain method provides a more reliable method for extracting information about relaxation phenomena.

Four-quantum and five-quantum evolution experiments were used to obtain information about the relaxation of spin  $I = 5/2$  in systems with  $^{17}\text{O}$  enriched water in the presence of immobilised enzyme. The decision to use this approach to measure transverse relaxation instead of TQF experiments was based on the simplicity of this method compared with the treatment for TQF for spin  $I = 5/2$ .

Potentially, the motional correlation time  $\tau_c$  is a valuable parameter for investigating systems where the protein is in an environment of restricted motion. However, it is important to keep in mind that this parameter does not reflect the “rotational” motion because the protein is tethered to the solid support. In this case  $\tau_c$  values are more likely due to fluctuation of the quadrupolar coupling. However, it is also possible that local motions in the protein make a contribution.

Regarding the values of the correlation time  $\tau_c$  obtained here, the results provided by the TQF  $^{23}\text{Na}$  NMR experiments are in the timescale expected for allosteric dynamics, which is in the range of nanosecond to millisecond. In the case of multiple-quantum  $^{17}\text{O}$  NMR experiments, the  $\tau_c$  values fall within the motional range for water present on the surface of the protein.

It is possible to say, that the aim of determining the number of bound water molecules to immobilised enzyme was successfully attained. The numbers of water molecules per immobilised enzyme (mol/mol) obtained by  $^{17}\text{O}$  NMR experiments are plausible numbers.

## CHAPTER 7

# Enzyme-Inhibitor Interaction Studies in Solution and in Solid State

Molecular recognition lies at the core of any biological process. These ligand-binding interactions are central to numerous biological processes such as signal transduction, physiological regulation, gene transcription and enzymatic reactions. Ligand-binding interactions involve both macromolecular complexes (i.e., protein-protein and protein-DNA) and complexes of small molecules with macromolecules. As many proteins regulate these key biological processes via interactions with small molecules, these protein receptors are often prime targets for therapeutic agents. Since serine proteases are concerned in the deregulation of biological processes linked to many diseases, the study of their interactions with ligands has a significance for drug development programmes.

In this Chapter, the accessibility of the enzyme active sites to ligands was measured by using two different fluorine-containing inhibitors of  $\alpha$ -chymotrypsin. A ligand-based NMR method (see Section 2.4.1.1) is evaluated here. Ligand examination has the technical advantage of not requiring labelled protein.  $^{19}\text{F}$  NMR has proven to be a powerful technique in the study of protein structure and dynamics because provides a relatively nonperturbing yet sensitive probe with no background signals.

The evaluation of the accessibility of the inhibitors to the biocatalysts provides insight into the enzyme-inhibitor interactions. The information extracted from these studies can lead to the development of methods to evaluate the conformational state of the enzyme in the preparation and observe if the enzyme is active or not.

The two chosen inhibitors are potassium 4-fluorophenyl trifluoroborate (PFPTB) and (R)-1-acetamido-2-(4-fluorophenyl)ethane-1-boronic acid (AFEB). They correspond to non-covalent reversible inhibitors. Reversible inhibitors are preferred in inhibition studies because they are generally less toxic than irreversible inhibitors and bind non-covalently to the active site of the enzyme.

Inhibitors with an inhibition constant,  $K_d$ , in the  $\mu\text{M}$  range are preferred over the mM range. The reason behind this is that the smaller the  $K_d$  value the greater the affinity of an inhibitor for its target. The first inhibitor selected (PFPTB) corresponds to an inhibitor with a  $K_d$  in the mM range. The second inhibitor used in this Chapter (AFEB) has a  $K_d$  in the  $\mu\text{M}$  range. It is in our interests the observation of differences in the spectra between two inhibitors with different  $K_d$ . These differences can lead in a better understanding of how inhibitors interact with the enzyme.

The characterisation of both inhibitors was conducted in this thesis by solution-state NMR (see Appendix G). The inhibitor utilised in Section 7.3 (PFPTB) was commercially available, as opposed to the inhibitor utilised in Section 7.4 (AFEB), which was synthesized by the research group of Professor Colin Gibson at the University of Strathclyde (more details in Appendix G.2) in collaboration with this project.

Despite the focus on solid-state NMR studies of this thesis, the majority of the work presented in this Chapter was performed using solution-state NMR experiments on free enzyme. The reason behind this is that there is currently no complete understanding of these ligand-enzyme systems in the solution state. Therefore, better insight is needed into such systems before turning to immobilised enzymes in

presence of ligands. Solution-state NMR studies were conducted first to test the ligand-enzyme systems for eventual comparison with the solid-state results of ligand-immobilised enzyme systems.

Approaches without the need of isotopic labelling were preferred for the reasons discussed in Chapter 1. The direct observation of low-field protons belonging to the active site of the enzyme by  $^1\text{H}$  NMR and a ligand-based approach were explored.

## 7.1 Experimental details

### 7.1.1.1 NMR experiments

The solution-state NMR spectra presented in this Chapter were recorded on two spectrometers: a Bruker Avance 400 MHz spectrometer equipped with a narrowbore 9.4 T and a Bruker Avance III 600 MHz spectrometer equipped with a narrowbore 14.1 T magnet, providing  $^1\text{H}$  resonance frequencies of approximately 400 and 600 MHz, respectively. The probe head was equipped to provide pulsed field gradients in the  $z$  direction. Solution samples were held in 5 mm borosilicate glass (Type 1 Class A) NMR tubes. To prevent etching of the glass by fluoride anions released from the inhibitor, the samples were held inside PTFE-FEP copolymer tubes inserts. The studied nuclei were  $^1\text{H}$ ,  $^{19}\text{F}$ ,  $^{11}\text{B}$  and  $^{13}\text{C}$  (Table 2.1). Chemical shifts were recorded in ppm relative to tetramethylsilane (TMS) for  $^{13}\text{C}$  and  $^1\text{H}$ , trichlorofluoromethane ( $\text{CFCl}_3$ ) for  $^{19}\text{F}$  and trimethyl borate ( $\text{C}_3\text{H}_9\text{BO}_3$ ) for  $^{11}\text{B}$ .  $^1\text{H}$  NMR data were acquired by using a double pulsed field gradient spin echo (DPFGSE) approach to eliminate the solvent resonance. For the DPFGE method, rectangular soft pulses were used for selective inversion at the solvent frequency together with sine-shaped gradient pulses (1 ms duration) in a ratio of 31:11. Further experimental details such as pulse sequence, pulse length, recycle delay and number of transients can be found in the text and figure captions.

The solid-state NMR spectra were recorded on a Bruker Avance III 600 MHz spectrometer equipped with a narrowbore 14.1 T magnet, providing a  $^1\text{H}$  resonance frequency of approximately 600 MHz. Samples were packed into 1.9 mm and 2.5 mm  $\text{ZrO}_2$  rotors and rotated at 38 kHz in a 1.9 mm MAS probe, and 20 kHz in a 2.5 mm MAS probe, respectively. To contain liquids inside rotors, soft silicone plugs were used. Further experimental details such as pulse sequence, pulse length, recycle delay and number of transients can be found in the text and figure captions.

#### 7.1.1.2 Sample preparation

Two types of samples were studied in this Chapter: the free enzyme and the immobilised enzyme samples. Free enzyme samples (solution samples) were studied by solution-state NMR, and immobilised enzyme samples (heterogeneous samples) by solid-state NMR. Solution samples consisted of a solution of 1.5 mM of  $\alpha$ -chymotrypsin and 20 mM  $\text{CaCl}_2$  (to avoid autolysis) with or without inhibitor (PFPTB or AFEB) in  $\text{H}_2\text{O}/\text{D}_2\text{O}$  (90:10). The concentration of PFPTB in the solution was 10 mM and 3 mM for AFEB. The dry immobilised (on Eupergit®) enzyme<sup>6</sup> was suspended in 200  $\mu\text{l}$  of a 10 mM HCl solution containing the inhibitor (PFPTB or AFEB) and then packed in the rotor. The same inhibitor concentration as for free enzyme samples was used in the immobilised enzyme samples. All samples were stored at 3 °C and discarded after one week in case of possible microbiological contamination.

Table 7.1 summarise the composition of the samples for the different experiments conducted in this Chapter.

---

<sup>6</sup> The amount of biocatalyst was calculated on the basis to have a similar concentration of enzyme as for free enzyme (solution) samples.

## 7.2 Solution-state NMR studies of the free enzyme

A  $^1\text{H}$  NMR spectrum of a protein of any size is a very complex piece of information to interpret as most of the signals overlap heavily.  $\alpha$ -Chymotrypsin is no exception as can be observed in Figure 7.1, which shows data from  $\alpha$ -chymotrypsin dissolved in distilled water (90%  $\text{H}_2\text{O}/10\%$   $\text{D}_2\text{O}$ ) in the presence of  $\text{CaCl}_2$ <sup>7</sup> at pH 2.3. This is the pH obtained after dissolution of  $\alpha$ -chymotrypsin without pH adjustment. In this Chapter all samples with free  $\alpha$ -chymotrypsin were prepared without adjustment of pH unless otherwise stated.

In 1972 an exceptional discovery was made: the first direct observation of a single proton signal from the active site of  $\alpha$ -chymotrypsin [161]. Since this discovery, the understanding of how the catalytic triad of serine proteases operates has improved enormously, as was discussed in Section 3.2.1. However, despite the large number of studies on the active site of serine proteases, questions relating to the catalytic mechanism have arisen recently (LBHB and ring-flip theory). A review about the story concerning the observation of H-bonding signals in the catalytic triad of chymotrypsin-like enzymes by solution-state NMR was included in Section 3.2.1.4.

---

<sup>7</sup> The effect of the presence of calcium ions for free  $\alpha$ -chymotrypsin is mentioned in 3.2.2.2.

**Table 7.1. Sample characteristics for experimental studies described in Chapter 7.**

Experiment	Enzyme	Inhibitor	NMR configuration
Figure 7.1, Figure 7.2a, Figure 7.8a	1.5 mM (20 mM CaCl <sub>2</sub> ) in H <sub>2</sub> O/D <sub>2</sub> O (90:10)	No	Solution-state NMR
Figure 7.2b, Figure 7.4, Figure 7.5	1.5 mM (20 mM CaCl <sub>2</sub> ) in H <sub>2</sub> O/D <sub>2</sub> O (90:10)	10 mM PFPTB	Solution-state NMR
Figure 7.6	0.6 gr of IE on Eupergit® in 10 mM HCl (200 µl total volume)	10 mM PFPTB	Solid-state NMR
Figure 7.8b, Figure 7.9, Figure 7.10, Figure 7.11	1.5 mM (20 mM CaCl <sub>2</sub> ) in H <sub>2</sub> O/D <sub>2</sub> O (90:10)	3 mM AFEB	Solution-state NMR
Figure 7.12	0.3 gr of IE on Eupergit® in 10 mM HCl (200 µl total volume)	3 mM AFEB	Solid-state NMR

Figure 7.2a shows the expansion of the spectrum shown in Figure 7.1 for a specific high-frequency region of the one-dimensional <sup>1</sup>H NMR spectrum of α-chymotrypsin between δ <sup>1</sup>H = 10 and 20 ppm, where it is possible to observe signals from protons bound in the enzyme active site. At low pH, it is possible to observe three signals in this region arising from the active site protons, two clearly resolved around δ <sup>1</sup>H = 18 ppm (18.5 and 18.2 ppm) and a quite broad one at δ <sup>1</sup>H = 13.1 ppm. The signals arising in the 18 ppm region correspond to N<sup>δ</sup><sub>1</sub>-H protons of the catalytic triad of α-chymotrypsin (see Figure 3.9). Bruylants *et al.* [318] concluded that the protonation state of Asp102 is responsible for the two signals observed for the His57 N<sup>δ</sup><sub>1</sub>-H at low pH. Based on the change in the relative intensities of the observed signals with pH, they assigned the higher frequency signal to the N<sup>δ</sup><sub>1</sub>-H proton of His57 in the presence of protonated Asp102 and the lower frequency signal to the same proton in the presence of deprotonated Asp102. The observation of these two signals in similar systems is not very common; the use of an extremely low pH helps in this respect.

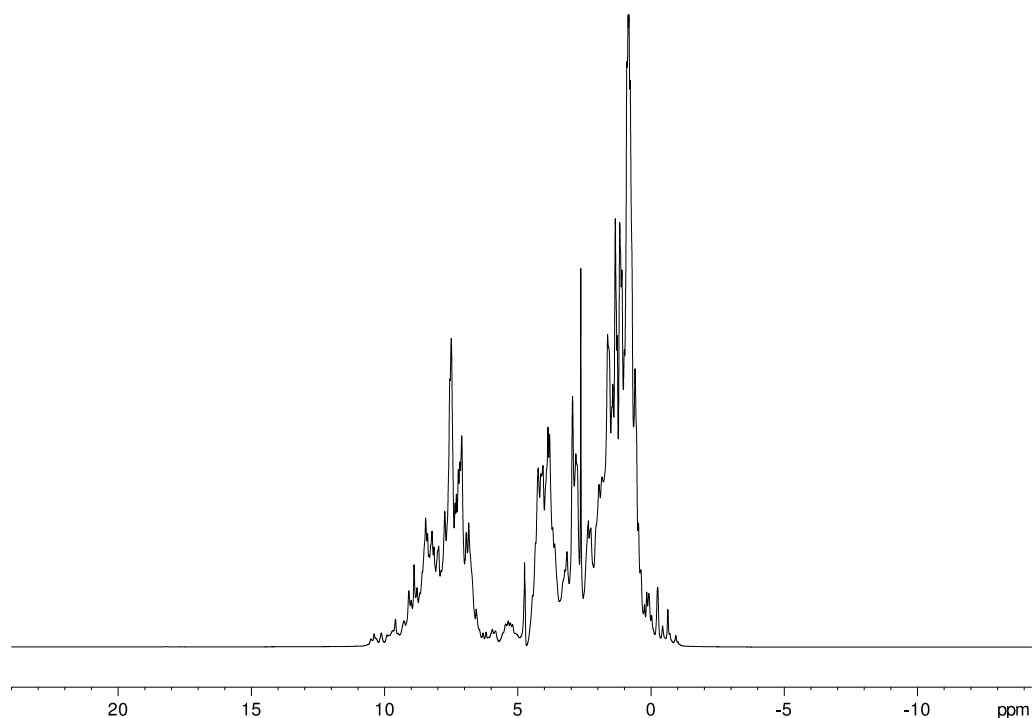


**Figure 7.1.**  $^1\text{H}$  NMR spectrum of free enzyme recorded using DPFGSE sequence at  $B_0 = 14.1$  T ( $90^\circ$  pulse length of  $9 \mu\text{s}$ , relaxation interval of  $1.4$  s, averaging 4800 transients). The free enzyme sample contains  $\alpha$ -chymotrypsin ( $1.5$  mM) with  $\text{CaCl}_2$  ( $20$  mM) at pH 2.3.

The signal at  $\delta \text{ } ^1\text{H} = 13.1$  ppm corresponds to the  $\text{N}^{\epsilon 2}\text{-H}$  proton (see Figure 3.9), which is known to resonate in this frequency range. This proton is possibly involved in fast exchange thereby causing the line broadening visible in Figure 7.2a.

The  $\text{C}^{\epsilon 1}\text{-H}$  proton signal of His57 reported previously by Ash *et al.* [194] at  $\delta \text{ } ^1\text{H} = 9.2$  ppm (Section 3.2.1.4) was not possible to distinguish due to the strong background in that region.

### 7.3 Interactions with potassium 4-fluorophenyl trifluoroborate

#### 7.3.1 Solution-state NMR studies of the free enzyme in presence of PFPTB

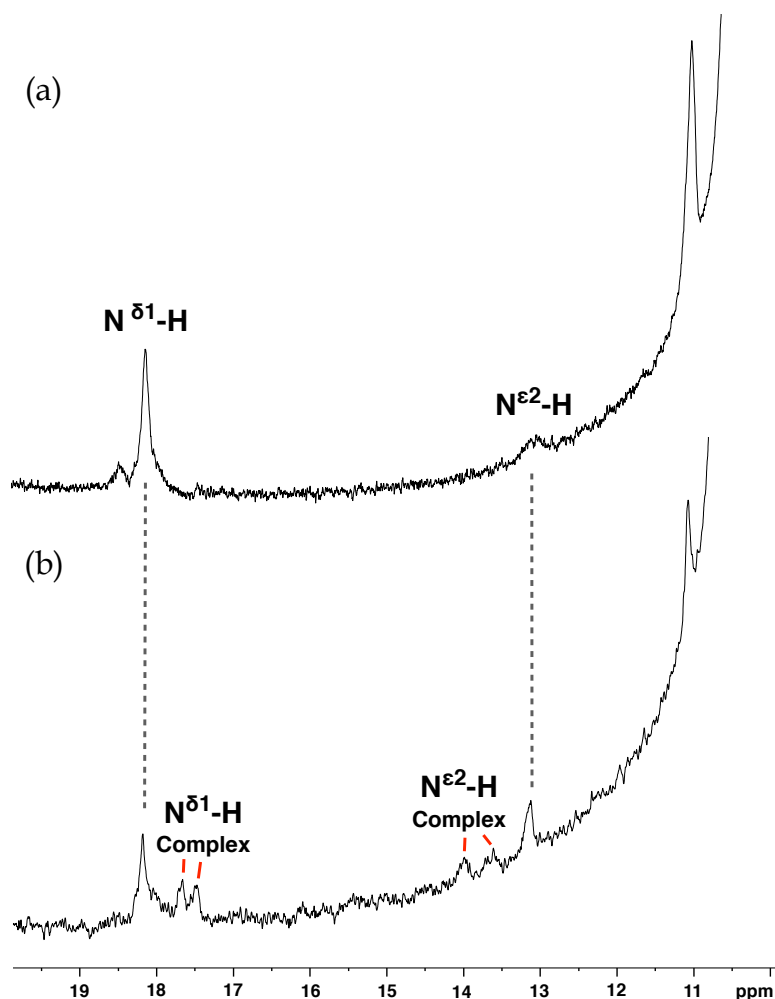


**Figure 7.2.**  $^1\text{H}$  NMR spectra of (a) free enzyme (b) and free enzyme in presence of 10 mM of PFPTB (inhibitor) at pH 2.3 recorded using DPFGSE sequence at  $B_0 = 14.1$  T ( $90^\circ$  pulse length of  $9 \mu\text{s}$ , relaxation interval of 1.4 s, averaging 30000 transients).

In 2005, Smoum *et al.* [247] reported the inhibitory effect of a series of trifluoro(organo)borates. They observed that the inhibitory effect was much more potent than the effect associated with the corresponding boronic acids (Section 3.2.2.3). One of these salts was potassium 4-fluorophenyl trifluoroborate (PFPTB) (Figure 7.3), which exhibited a reported inhibition constant,  $K_d$ , of 1.84 mM for  $\alpha$ -chymotrypsin.

The use of PFPTB as an inhibitor of  $\alpha$ -chymotrypsin has been studied in this thesis. The characterisation of PFPTB by solution-state NMR has been conducted and

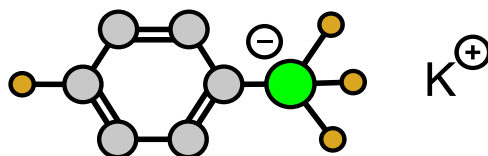


**Figure 7.3. Structure of 4-fluorophenyl trifluoroborate (PFPTB). Aromatic protons are not included for structure simplicity.**

Appendix G.1 summarises the NMR spectra of PFPTB and confirms that the structure of the commercial compound is the one expected.

Figure 7.2 shows the  $^1\text{H}$  NMR spectra with and without PTPTB. As well as the free active site appearing at  $\delta \text{ } ^1\text{H} = 18.2$  and  $13.1$  ppm in the presence of the inhibitor, two additional pairs of signals arise close to these two peaks. These two pairs of signals belong to the active site protons complexed to the inhibitor. The pair of signals arising at high frequency ( $\delta \text{ } ^1\text{H} = 17.6$  and  $17.5$  ppm) are assigned to the  $\text{N}^{\delta 1}\text{-H}$  proton, which is known to resonate in this frequency range. The pair of signals at the lower frequency ( $\delta \text{ } ^1\text{H} = 14.0$  and  $13.6$  ppm) are assigned to the  $\text{N}^{\epsilon 2}\text{-H}$  proton [234]. The observation of two signals for the inhibitor-chymotrypsin complex protons has not been reported before in the literature. This can be attributed to the difference in the environments of these two protons and could, for instance, be an effect associated with protonated and deprotonated residues arising from the very low pH used during these measurements (pH = 2.3) in the slow exchange regime. The signals from protonated and deprotonated  $\text{N}^{\delta 1}\text{-H}$  sites have residence lifetimes of at least 16 ms and in the case of the  $\text{N}^{\epsilon 2}\text{-H}$  proton of at least 4 ms. Further experiments, using a labelled enzyme, are necessary to lead to a clearer understanding of why these two sets of signals arise.

From the information obtained from the proton NMR spectrum (Figure 7.2b) it is possible to conclude that PTPTB acts as a type 1 inhibitor (Section 3.2.2.3). This can be noted from the presence of  $\text{N}^{\delta 1}\text{-H}$  and  $\text{N}^{\epsilon 2}\text{-H}$  protons in the inhibitor-enzyme complex forming a Ser adduct (Section 3.2.2.3). Type 2 complexes can be recognised

through the absence of responses associated with the N<sup>ε</sup>-H proton after the formation of a His adduct (Figure 3.12b).

The <sup>19</sup>F NMR spectrum of PTPTB in presence of α-chymotrypsin is presented in Figure 7.4. When compared with the <sup>19</sup>F NMR spectrum of PTPTB (Appendix G, Figure G.4), it can be seen that two new signals arise in addition to the two expected signals related to the free inhibitor ( $\delta^{19\text{F}} = -115.5$  and  $-137.4$  ppm) at  $\delta^{19\text{F}} = -109.4$  and  $-155.5$  ppm. In accordance with this result, it is known that chymotrypsin forms a fraction complexed with PTPTB at approximately 1:5 enzyme:inhibitor ratio [247]. This is observed in the area of the peaks for the aromatic fluorine in the free and bound states. Conclusions cannot be drawn from the signals arising from the boron-fluorine species. It is possible to observe that peak area ratios between boron-fluorine and aromatic fluorine species in the bound and free states are not proportional. This is probably due to the effect of the quadrupole moment of <sup>11</sup>B. T<sub>1</sub> relaxation effects on the intensities have been excluded.

Smoum *et al.* [247] studied the same system, also by solution-state <sup>19</sup>F NMR (Figure 3.14). They observed four signals in the spectrum of α-chymotrypsin (0.08 mM) in presence of PTPTB (0.6 M). Two signals were observed at  $\delta^{19\text{F}} = -136$  and  $-114$  ppm for the -BF<sub>3</sub> group and for the aromatic fluorine, respectively. They assumed that the signals observed in the one-dimensional <sup>19</sup>F NMR data that did not belong to the free inhibitor, (those at  $\delta^{19\text{F}} = -133$  and  $-107$  ppm) were from the complex inhibitor-enzyme. No additional evidence behind this conclusion is provided in the publication. The assignment of the signal at  $\delta^{19\text{F}} = -133$  ppm by Smoum *et al.* disagrees with our findings.

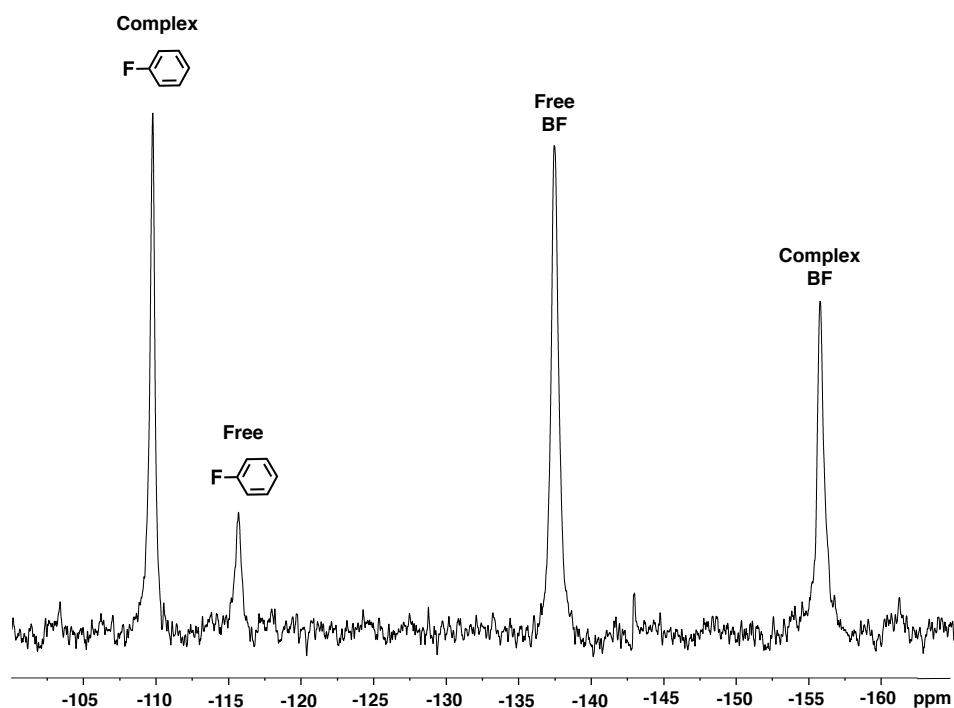


**Figure 7.4.**  $^{19}\text{F}$  NMR spectrum of 10 mM of PFPTB (inhibitor) in presence of 1.5 mM free enzyme at pH 2.3 at  $B_0 = 9.4$  T ( $90^\circ$  pulse length of 10  $\mu\text{s}$ , relaxation interval of 12 s, averaging 128 transients). WALTZ-16 was used for proton decoupling.

Interestingly, in the same publication by Smoum and co-workers [247], they postulated that there is no interaction between the fluorine in the phenyl ring and the catalytic triad of chymotrypsin (Figure 3.15). This postulate can be argued because it is well known that chymotrypsin has high specificity towards phenylalanine, whose aromatic ring is accommodated in a well preserved substrate recognition site of serine proteases, namely the hydrophobic pocket. Since PTPTB has an aromatic para-substituted fluorine, it is expected that two signals from this atom might be observed in the presence of inhibitor, one from the free state (free inhibitor) and one from the bound state (or enzyme-inhibitor complex).

A two-dimensional  $\{^{19}\text{F}, ^1\text{H}\}$  HOESY spectrum was recorded on  $\alpha$ -chymotrypsin in the presence of PTPTB (Figure 7.5). Unambiguously, the two-dimensional spectrum shows the spatial proximity of the  $\text{N}^{\delta 1}\text{-H}$  proton from the active site to two different

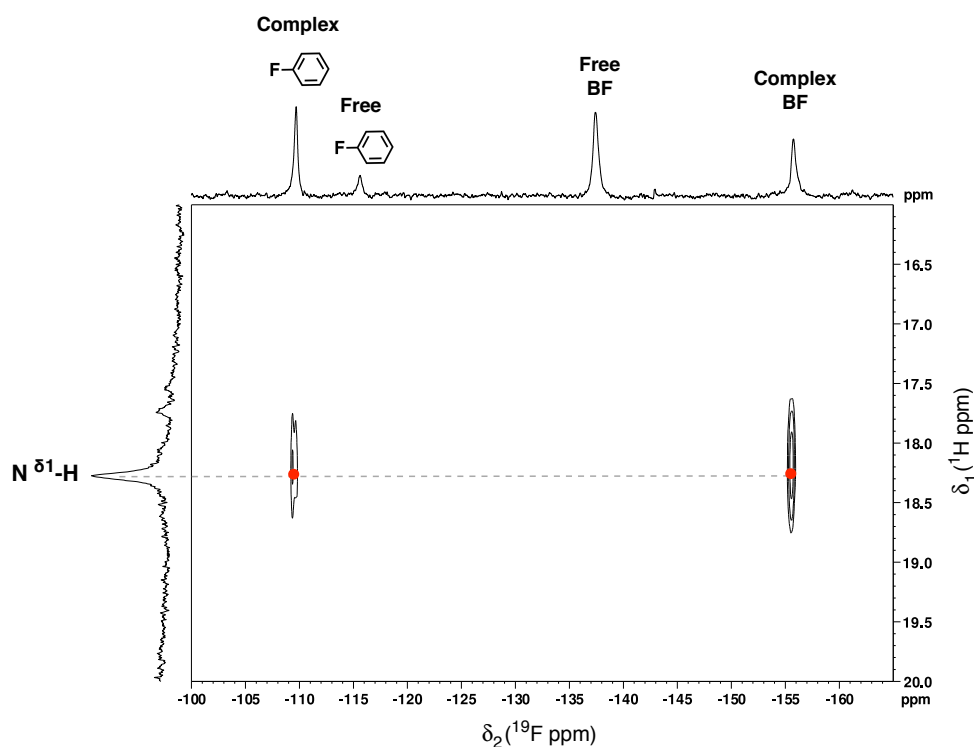


Figure 7.5.  $\{^{19}\text{F}, ^1\text{H}\}$  HOESY NMR of 10 mM of PFPTB (inhibitor) in presence of free enzyme at pH 2.3 at  $B_0 = 9.4$  T. Spectra were recorded by averaging 1024 transients for each of the 32  $t_1$  increments of 90  $\mu\text{s}$  ( $90^\circ$  pulse length of 10  $\mu\text{s}$ , relaxation interval of 8.5 s). The  $^{19}\text{F}$  NMR spectrum from Figure 7.4 and the  $^1\text{H}$  NMR spectrum from Figure 7.2b have been used in place of the  $^{19}\text{F}$  and  $^1\text{H}$  projection, respectively. The mixing time,  $\tau_m$ , used was 500 ms. WALTZ-16 was used for proton decoupling.

fluorine atoms. These two fluorine atoms can be assigned unequivocally as bound inhibitor complex signals from the fluorine atom bonded to the phenyl ring ( $\delta^{19}\text{F} = -109.4$  ppm) and from the fluorine atom bonded to the boron ( $\delta^{19}\text{F} = -155.7$  ppm).

The two-dimensional  $\{^{19}\text{F}, ^1\text{H}\}$  HOESY spectrum (Figure 7.5) proves the points stated above about the disagreements with the results of Smoum *et al.* The signals identified by Smoum *et al.* as issuing from the complex enzyme-inhibitor complex appear to have been incorrectly identified in one case. Our assignments for the enzyme-inhibitor complex only agree with the signal at -107 ppm as the aromatic fluorine resonance from the bound inhibitor. Possibly, Smoum *et al.* missed the signal at lower frequency at -155 ppm (see Figure 3.14) and therefore interpreted the signal at -133

ppm as from the bound inhibitor. The signal at  $-133$  ppm might correspond to an impurity in their inhibitor.

The B-F fluorine and the phenyl ring fluorine are close to the  $N^{\delta 1}$ -H proton. The phenyl ring of the inhibitor is probably positioned in the hydrophobic pocket. This pocket is part of the S1 site and close to the catalytic triad and, is therefore, close to the  $N^{\delta 1}$ -H proton (Section 3.2.1.3).

A fact to bear in mind is the gradual hydrolysis of PTPTB in an aqueous system. We observed by  $^{19}\text{F}$  NMR spectroscopy over time that a significant amount of fluorine atoms bonded to boron are hydrolysed. After four hours this effect is noticeable but does not affect signal intensities associated with the enzyme-inhibitor complex. When a borosilicate NMR tube is used in the presence of PTPTB, a very sharp peak appears at  $\delta \text{ }^{19}\text{F} = -128$  ppm. This peak is assigned to hexafluorosilicic anion ( $\text{SiF}_6^{-2}$ ) and increases over time. The first step in the etching process is the substitution of a surface SiOH group by a SiF group [319]. Species in which F is bonded to coordinated Si on the surface of the glass result from this first step. In the  $^{19}\text{F}$  NMR spectrum shown in Figure 7.4 it is possible to observe a signal at  $\delta \text{ }^{19}\text{F} = -143$  ppm that must correspond to these coordinated silicon atoms, which are known to resonate close to this frequency [320]. There is a rapid equilibrium with free fluoride ions released and the fluorophile (silica in the glass) binds the free fluoride ions, pulling the equilibrium over towards hydrolysis. All solution-state NMR data using PTPTB shown in this thesis are recorded using PTFE-FEP copolymer tube inserts (liner) inside standard borosilicate NMR tubes to avoid unwanted signals arising from the interactions (etching) with the NMR tube glass.

### 7.3.2 Solid-state NMR studies of the the immobilised enzyme in presence of PTPTB

Finally, after obtaining a better insight into  $\alpha$ -chymotrypsin in the presence of PTPTB in the solution state by NMR, a solid-state NMR spectrum was recorded for the same system (Figure 7.6). It was noted that the standard MAS probe used exhibited strong background signals for  $^{19}\text{F}$  due to the construction materials. Hence, to record this spectrum, a pulse sequence called EASY (elimination of artefacts in NMR spectroscopy) [321] was utilised to eliminate these background signals. In this pulse sequence, two FIDs are acquired sequentially. After the acquisition of the first transient (it contains the wanted NMR signal and the background artefacts), the same experiment is repeated immediately afterwards before the  $T_1$  waiting delay. This second scan contains only the signal arising from the background. The artefact-free NMR spectrum was obtained by taking the difference of these two spectra.

The concentration of inhibitor to immobilised enzyme was in a ratio 7:1 (similar to that used in the solution-state NMR experiments).

As can be seen from the solid-state  $^{19}\text{F}$  NMR spectrum in Figure 7.6, free inhibitor signals appear at  $\delta^{19}\text{F} = -115$  ppm (aromatic fluorine) and  $-137$  ppm ( $-\text{BF}$ ). The complexed inhibitor with the enzyme appears at  $-109$  ppm (aromatic fluorine) and at  $-149$  ppm ( $-\text{BF}$  group). Fluoride anions released from the inhibitor ( $-120$  ppm) appear to have triggered etching of the zirconia rotor. An almost negligible peak at  $-13$  ppm (region not shown in the  $^{19}\text{F}$  NMR spectrum in Figure 7.6) can be attributed to  $\text{H}_2\text{ZrF}_6$  and appears as a result of this etching reaction. Interestingly, a resonance at  $-129$  ppm also appears in Figure 7.6. This can be assigned to hexafluorosilicic acid. The presence of silica is required for the formation of this signal to occur, as in the case of the borosilicate NMR tubes discussed previously. Bruker has not released details of the composition of their zirconia rotors but other solid-state rotor manufacturers have reported their composition. Doty, for instance, have reported a

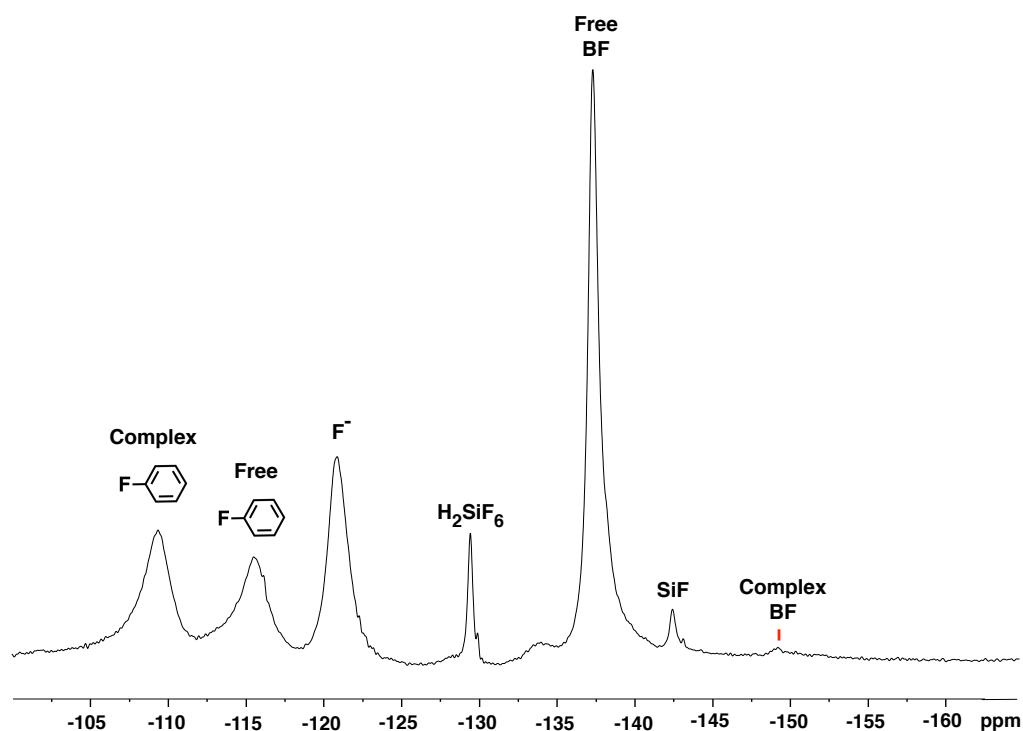


Figure 7.6.  $^{19}\text{F}$  MAS NMR spectrum of 10 mM of PTPTB (inhibitor) in presence of immobilised enzyme recorded at  $B_0 = 14$  T and a MAS rate of  $\omega_R/2\pi = 20$  kHz, using the EASY pulse sequence [321] ( $90^\circ$  pulse length of  $3.1 \mu\text{s}$ , relaxation interval of 8 s, averaging 63488 transients). The immobilised enzyme sample is  $\alpha$ -chymotrypsin immobilised on Eupergit®.

silicon atom concentration of approximately 200 ppm in their zirconia rotors. A similar composition for Bruker rotors would be expected. On this basis, signals arising from the etching of coordinated Si species from the rotor are plausible. In a similar manner to the  $^{19}\text{F}$  NMR spectrum obtained for free enzyme in the presence of PTPTB (Figure 7.4), it is possible to observe a resonance at -143 ppm in the  $^{19}\text{F}$  NMR spectrum of immobilised enzyme in the presence of the same inhibitor (Figure 7.6). This signal is assigned to fluorine bonded to coordinated Si from zirconia rotor impurities.

From the relative intensities of the signals from the free and bound aromatic fluorines in the spectrum shown in Figure 7.6, it is possible to say that the complex forms with an approximate ratio of 1:4 enzyme:PTPTB. Several factors can contribute

to the discrepancy between the ratios obtained from solution state (1:5) and solid state experiments. A possible reason is that an excess of inhibitor was packed in the MAS rotor as a result of the complications of having to work with such small volumes. However, the fact that the complex ratios are similar is a sign that the immobilised enzyme is active and the active site is accessible to the inhibitor and not hindered.

## **7.4 Interactions with (R)-1-acetamido-2-(4-fluorophenyl)ethane-1-boronic acid**

### **7.4.1 Solution-state NMR studies of the free enzyme in presence of AFEB**

Inhibitors with high affinity to targets and thus with smaller dissociation constants,  $K_d$ , are preferred over those with lower affinity and larger dissociation constants. A more specific inhibitor of  $\alpha$ -chymotrypsin is (R)-1-acetamido-2-(4-fluorophenyl)ethane-1-boronic acid (AFEB) (Figure 7.7) with a dissociation constant,  $K_d$ , of 0.6  $\mu$ M [239]. Sylvia and Gerig studied this inhibitor in the presence of  $\alpha$ -chymotrypsin [239, 240] (discussed in Section 3.2.2.3). They included the study of the effect of pH (between 8.7 and 4) on the high frequency  $^1\text{H}$  NMR signals from the enzyme active site. At pH = 4.0 a strong signal appears at  $\delta \text{ } ^1\text{H} = 13$  ppm together with a smaller signal at  $\delta \text{ } ^1\text{H} = 18$  ppm. The signals were assigned to  $\text{N}^{\epsilon 2}\text{-H}$  and  $\text{N}^{\delta 1}\text{-H}$  protons, respectively. A similar approach than the one proposed by Sylvia and Gerig [239, 240] to evaluate the interaction between chymotrypsin and AFEB is adopted in this Chapter to validate and confirm findings at pH 2.3.

The characterisation by solution-state NMR of AFEB was conducted and Appendix G.2 summarises the NMR spectra of AFEB, confirming that the structure of the synthesised compound is as expected.

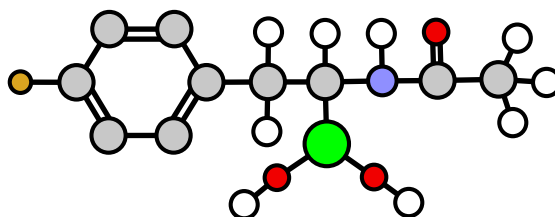


**Figure 7.7. Structure of 1-acetamido-2-(4-fluorophenyl)ethane-1-boronic acid (AFEB). Aromatic protons are not included for structure simplicity.**

Figure 7.8b shows the  $^1\text{H}$  NMR spectrum of  $\alpha$ -chymotrypsin in the presence of AFEB. Only two signals arise, at  $\delta \text{ } ^1\text{H} = 13$  ppm (split into two at 12.98 and 13.02 ppm) and 13.6 ppm. The concentration of  $\alpha$ -chymotrypsin in the measured sample, for which data are shown in Figure 7.8, was 1.5 mM. A two-fold excess of inhibitor was used. The strong peak at 13 ppm in the  $^1\text{H}$  NMR spectrum (Figure 7.8b) suggests slow exchange on the NMR timescale between free AFEB and that bound to the active site of  $\alpha$ -chymotrypsin. The result confirms tight binding between the inhibitor and the enzyme. It has been previously reported that this compound forms a 1:1 stoichiometric complex with  $\alpha$ -chymotrypsin [240].

The resonance at  $\delta \text{ } ^1\text{H} = 13$  ppm is assigned to proton  $\text{N}^{\text{e}2}\text{-H}$  of the free active site. A small signal appears next to this signal at 13.6 ppm. This resonance belongs to proton  $\text{N}^{\text{e}2}\text{-H}$  complexed with the inhibitor creating a serine adduct (Figure 3.12a). Thus AFEB is clearly a type 1 boronic-containing inhibitor. Interestingly, no further signals, those relating to proton  $\text{N}^{\text{e}1}\text{-H}$ , are visible to high frequency. This effect could be related to the low pH (2.3) in the sample and a fast exchange of this proton in particular. The significant difference in the signal-to-noise ratio between both spectra in Figure 7.8 confirms the slow rate exchange.

As for the previous system ( $\alpha$ -chymotrypsin in presence of PFPTB), the proton  $\text{C}^{\text{e}1}\text{-H}$  (around 9 ppm) was impossible to distinguish due to the strong  $^1\text{H}$  background around that region.

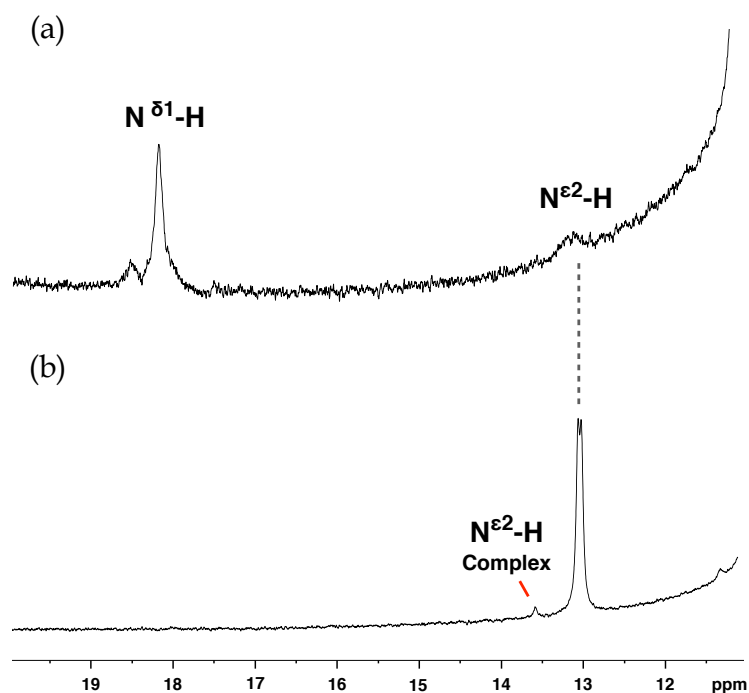


**Figure 7.8.** <sup>1</sup>H NMR spectra of (a)  $\alpha$ -chymotrypsin (1.5 mM) with CaCl<sub>2</sub> (20 mM) and (b)  $\alpha$ -chymotrypsin (1.5 mM) with CaCl<sub>2</sub> (20 mM) and 3 mM of AFEB at pH 2.3 using DPFSGE sequence recorded at  $B_0 = 14.1$  T ( $90^\circ$  pulse length of 9  $\mu$ s, relaxation interval of 1.4 s, averaging 4800 transients).

Figure 7.9 shows the <sup>19</sup>F NMR spectrum of  $\alpha$ -chymotrypsin in the presence of AFEB. Two signals appear, one of them at -117.6 ppm corresponding to the free inhibitor (Appendix G, Figure G.9) and the other at -115.4 ppm to the inhibitor bound to the active site of the enzyme. Approximately 25% of the inhibitor is bound to the active site (Figure 7.9), despite an anticipated of a ratio of 1:1 (50%) between the free and bound inhibitor. This discrepancy can be attributed to the presence in the sample of inactive enzyme with a damaged active site (around the half of the enzyme present in the sample). Sylvia and Gerig observed similar chemical shifts for the free and bound inhibitor, namely two signals with a shift separation of 2.3 ppm [239, 240].

Depending on the timescale of the ligand association-dissociation, information concerning binding kinetics and affinities can be accessed by using a variety of NMR techniques. In the case of slow binding kinetics, exchange spectroscopy (EXSY) can

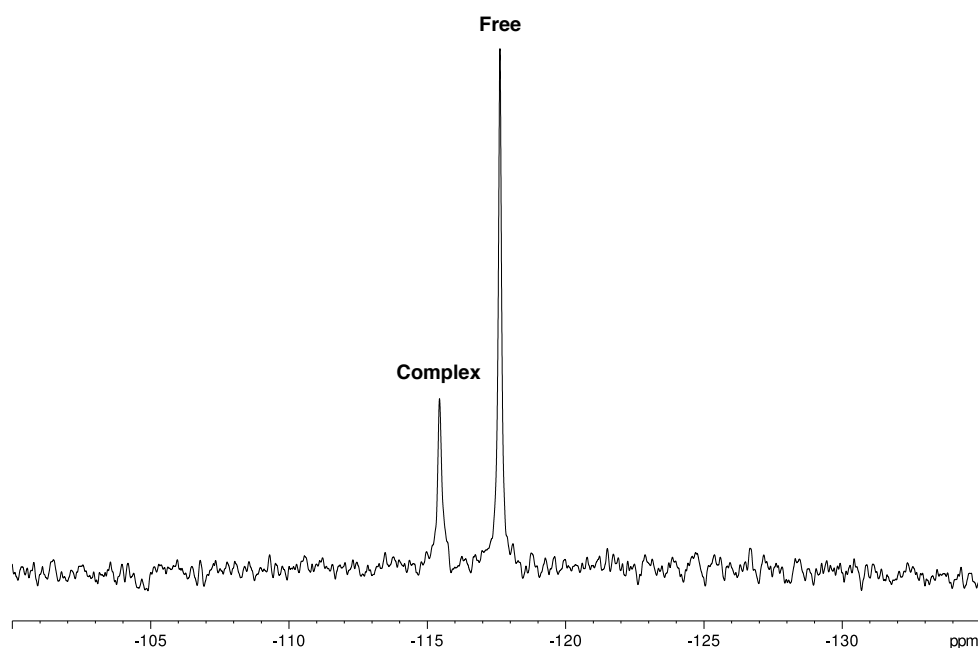


**Figure 7.9.**  $^{19}\text{F}$  NMR spectrum of  $\alpha$ -chymotrypsin (1.5 mM) with  $\text{CaCl}_2$  (20 mM) and 3 mM of AFEb at pH 2.3 at  $B_0 = 9.4$  T ( $90^\circ$  pulse length of 10  $\mu\text{s}$ , relaxation interval of 12 s, averaging 128 transients). WALTZ-16 was used for  $^1\text{H}$  decoupling.

provide qualitative mapping of exchange pathways in dynamic systems., with separate peaks observed for each exchanging species. The most popular EXSY method is the NOESY-based sequence [322]. Although the mechanism of chemical exchange and the NOE are quite unrelated, they both share a common characteristic, the transfer of longitudinal magnetisation.

Figure 7.10 shows the two-dimensional [323] EXSY NMR spectrum of  $\alpha$ -chymotrypsin in the presence of the inhibitor AFEb. Diagonal peaks (-117, -117 ppm and -115, -115 ppm) correspond to the self correlation peaks of the free and the bound state of the inhibitor, respectively. Off-diagonal cross-peaks (-117, -115 ppm and -115, -117 ppm) are produced by ligand association and dissociation during the mixing time,  $\tau_m$ .

The spectrum in Figure 7.10 confirms that the  $^{19}\text{F}$  peak at -115 ppm corresponds to the ligand in its bound state. No additional EXSY spectra were collected as a function of  $\tau_m$  and thus no quantitative information can be extracted relating to the

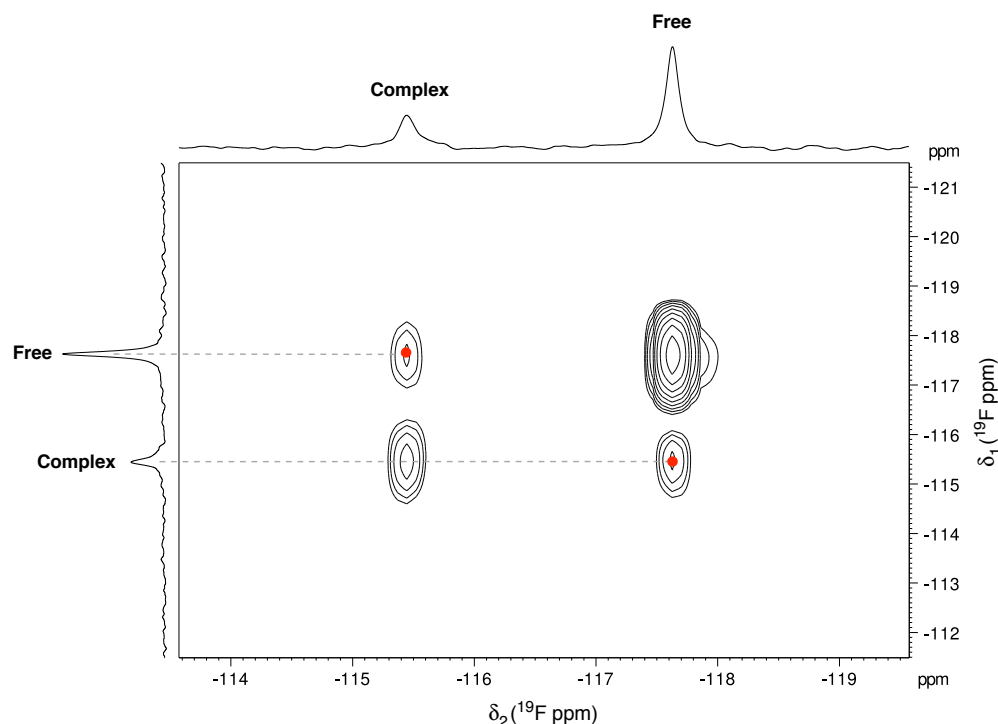


**Figure 7.10.** Two-dimensional  $\{^{19}\text{F}, ^{19}\text{F}\}$  EXSY NMR spectrum of  $\alpha$ -chymotrypsin (1.5 mM) with  $\text{CaCl}_2$  (20 mM) and 3 mM of AFEb at pH 2.3 at  $B_0 = 9.4$  T. Spectra were recorded by averaging 64 transients for each of the 128  $t_1$  increments of 33  $\mu\text{s}$  ( $90^\circ$  pulse length of 10  $\mu\text{s}$ , relaxation interval of 1.5 s). The  $^{19}\text{F}$  NMR spectrum from Figure 7.9 has been used in place of the  $^{19}\text{F}$  projections. A mixing time,  $\tau_m$ , of 500 ms was used.  $^1\text{H}$  decoupling was not used.

dissociation constants or rate of exchange. Further experiments using different mixing times could be useful to acquire a clearer insight into the dynamics of this system.

A two-dimensional  $\{^{19}\text{F}-^1\text{H}\}$  HOESY NMR spectrum was recorded on  $\alpha$ -chymotrypsin in the presence of AFEb (Figure 7.11). No cross-peaks were observed in the high-frequency proton chemical shift region of the spectrum (not shown). Since the two-dimensional  $\{^{19}\text{F}-^1\text{H}\}$  HOESY NMR spectrum for  $\alpha$ -chymotrypsin in the presence of PTPTB (Figure 7.5) only shows cross-peaks in the vicinity of 18 ppm in the  $^1\text{H}$  dimension, the situation arising in Figure 7.11 could be expected as no signal was found in the 18 ppm region of the  $^1\text{H}$  NMR spectrum for the enzyme-AFEb complex either (Figure 7.8b).

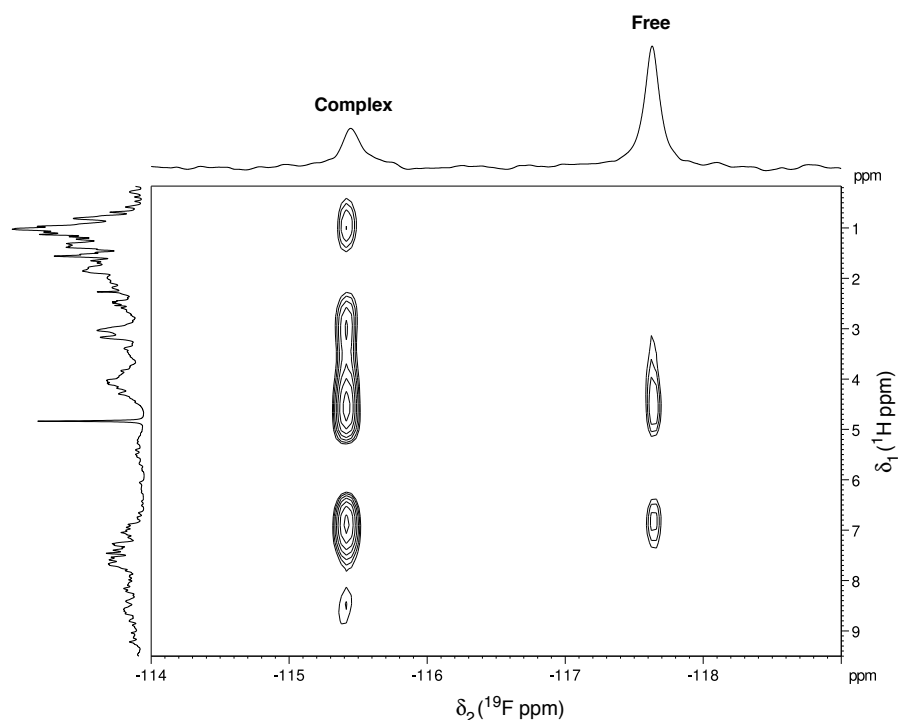


**Figure 7.11.** Two-dimensional  $\{^{19}\text{F}, ^1\text{H}\}$  HOESY NMR spectrum for  $\alpha$ -chymotrypsin (1.5 mM) with  $\text{CaCl}_2$  (20 mM) and 3 mM of AFEB at pH 2.3 at  $B_0 = 9.4$  T. Spectra were recorded by averaging 1024 transients for each of the 32  $t_1$  increments of 90  $\mu\text{s}$  ( $90^\circ$  pulse length of 10  $\mu\text{s}$ , relaxation interval of 8.5 s). The  $^{19}\text{F}$  NMR spectrum from Figure 7.9 and the  $^1\text{H}$  NMR spectrum from Figure 7.8b have been used in place of the  $^{19}\text{F}$  and  $^1\text{H}$  projection, respectively. The mixing time used was 500 ms. WALTZ-16 was used for  $^1\text{H}$  decoupling.

Interestingly, Figure 7.11 reveals several H-F cross-peaks that lie at lower frequencies in the proton dimension. Cross-peaks to the bound inhibitor fluorine signal are at the same proton chemical shifts as the cross-peaks to the free signal, as would be expected for a system in which there is chemical exchange between two forms. The spectrum shows an intramolecular cross peak between the fluorines and the aromatic protons which arises at  $\delta(^1\text{H}) = 6.8$  ppm. This NOE is noticeable for the free inhibitor (Appendix G, Figure G.11). Cross-peaks at  $\delta(^1\text{H})$  8.5, 4.6, 3.0 and 0.93 ppm are also observed in the  $\{^{19}\text{F}, ^1\text{H}\}$  HOESY correlation spectrum (Figure 7.11). These cross-peaks arise from intermolecular interactions between the enzyme and the inhibitor. The assignment of these protons is a difficult task since the  $^1\text{H}$  NMR spectrum of  $\alpha$ -chymotrypsin has not yet been fully assigned.

A simple search in the Protein Data Bank<sup>8</sup> under the search term “chymotrypsin” yields more than 200 results from X-ray crystallography whereas only four from NMR are available. All the results for the latter are related to the protein inhibitor structures and none to the chymotrypsin-like enzyme structure. The structure of  $\alpha$ -chymotrypsin has been completely elucidated by X-ray crystallography [168, 324, 325] and this is possibly the main reason for the lack of interest in NMR structural studies on this enzyme.

A two-dimensional  $\{^{19}\text{F}, ^1\text{H}\}$  HOESY NMR study of  $\alpha$ -chymotrypsin inhibited by 1-acetyl-4-fluorobenzyl carbazate [242] showed cross-peaks at 0.8 ppm and in the 3-5 ppm range for protons, correlated with a single  $^{19}\text{F}$  peak. The publication suggests that these signals arise through the interaction between the fluorophenyl ring and the hydrophobic pocket of  $\alpha$ -chymotrypsin. Later, in 1992, Sylvia and Gerig [239] detected similar interactions between AFEB and  $\alpha$ -chymotrypsin. They observed cross-peaks at  $\delta ^1\text{H} = 3.8, 4.1$  and  $6.9$  ppm (Figure 3.13) where only the first two arise from intermolecular interactions.

In Figure 7.11, an evident improvement in terms of resolution and sensitivity is achieved in the two-dimensional  $\{^{19}\text{F}, ^1\text{H}\}$  HOESY NMR spectrum of the inhibitor complexed to  $\alpha$ -chymotrypsin compared with similar data obtained by Hammond [242] and Sylvia and Gerig [239]. In all likelihood, the majority of these cross-peaks observed ( $\delta ^1\text{H} = 8.5, 4.6, 3.0$  and  $0.93$  ppm) belong to the S1 site (Section 3.2.1.3). The resonance at  $8.5$  ppm can be assigned to backbone HN protons and the signal at  $4.6$  ppm to  $\text{H}\alpha$ . Both could belong to Ser189, Gly216 and Gly226 from the hydrophobic pocket. These resonances comply with the random coil chemical shifts for these amino acids suggested by Wishart and Nip [326]. The cross-peak at  $\delta ^1\text{H} = 0.9$  ppm can be assigned to methyl groups of the protein. The signal at  $\delta ^1\text{H} = 3$  ppm possibly belongs to a  $\text{H}\beta$  proton. Bearing in mind that this signal should belong to a proton

---

<sup>8</sup> The Protein Data Bank (PDB) is a repository for structural data of biological macromolecules.

close to the active site or the S1 site, one possibility is that this proton is the H $\beta$  proton of His57<sup>9</sup>. Further studies with a protein that has been suitably isotopically enriched might provide access to the confirmation of the identity of this proton.

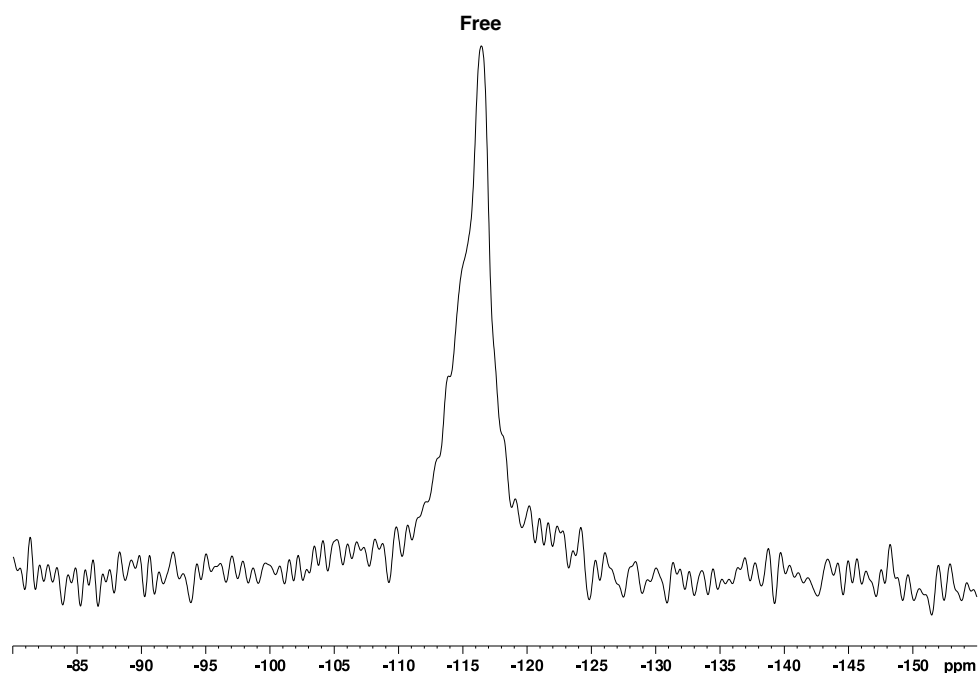
#### 7.4.2 Solid-state NMR studies of the immobilised enzyme in presence of AFEB

Figure 7.12 shows the solid-state <sup>19</sup>F MAS NMR spectrum of  $\alpha$ -chymotrypsin immobilised on Eupergit® in presence of AFEB. The concentration of inhibitor to immobilised enzyme was in a ratio 2:1 (as in the solution-state NMR experiments). The spectrum was recorded using EASY (elimination of artefacts in NMR spectroscopy) [321] to eliminate unwanted signals from the background arising from <sup>19</sup>F in the probe structure.

The strong signal at -117 ppm in Figure 7.12 is from the free inhibitor (AFEB). A high-frequency shoulder is noticeable in the expected region where the signal from the enzyme-inhibitor complex arises for the solution-state NMR experiment (-115 ppm signal in Figure 7.9). This shoulder can be interpreted as the poorly resolved signal from the inhibitor bounded to the enzyme. One suggestion for further solid-state NMR experiments on this system, would be to use a probe with a smaller rotor size than that used to obtain the spectrum in Figure 7.12, which was 1.9 mm. If a smaller rotor were to be used, higher MAS rates might be attained and the resolution of the spectrum would be possibly be improved. For instance, a probe with a 1.3 mm rotor size could achieve a spinning rate of 60 kHz. However, it is necessary to bear in mind that there is a compromise between sensitivity and resolution. In general, higher spinning rates (i.e., better resolution) involve the use of smaller rotors and consequently a smaller volume of sample and this affects the

---

<sup>9</sup> Chemical shifts from the Biological Magnetic Resonance Data Bank [327] of Histidine H $\beta$  protons are 3.18 and 3.11 ppm.



**Figure 7.12.**  $^{19}\text{F}$  MAS NMR spectrum of  $\alpha$ -chymotrypsin immobilised on Eupergit® in presence of 3 mM of AFEb (Inhibitor) recorded at  $B_0 = 14$  T and a spinning rate of  $\omega_R/2\pi = 38$  kHz, using the EASY pulse sequence [321] ( $90^\circ$  pulse length of 2.2  $\mu\text{s}$ , relaxation interval of 8 s, averaging 58928 transients).

sensitivity of the experiment (e.g., 1.3 mm rotor has a four times less sample volume than a 1.9 mm rotor size).

## 7.5 Discussion

It is important to raise the point that only a couple of the biophysical methods to evaluate binding events mentioned in Section 2.4.1.2 can be applied to immobilised enzyme systems (see Section 2.5.3.5). ITC has been successfully applied to studies of ligand interaction with immobilised enzymes [117, 118]. Another biophysical method used for this purpose is FAC [119, 120]. However, it is very clear that further development in biophysical techniques to analyse binding interactions on immobilised enzymes is needed.

Several NMR techniques have been developed to detect binding by monitoring the protein or the ligand (see Section 2.4.1.1). The majority of these techniques have only been applied to solution-state systems and some of them are not able to be utilised in solid state (e.g., diffusion experiments). Here,  $^{19}\text{F}$  ligand-detected and  $^1\text{H}$  protein-detected NMR studies were performed. Both studies exploit the simplicity of the use of non-isotopic labelled samples and can be applied either to non-supported systems (i.e., free enzyme) or to heterogeneous systems (i.e., immobilised enzyme).

In the present research, several efforts were made to observe the active-site protons of immobilised enzymes by solid-state NMR. However, no signals from these protons were obtained. One of the possible reasons for this is the low sensitivity of the experiments even using the highest field magnet that is available for solid-state NMR in the UK (20 Tesla). One is trying to observe just a few protons in a whole protein; to resolve them requires very fast MAS; and yet this necessitates the use of very small sample volumes, as noted above. Probably, with advances in solid-state NMR and the use of higher fields, at some point in the future it will be possible to observe these high-frequency protons from the active site of serine proteases in the solid state.

It is strongly advised that future studies include an analysis of enzyme kinetics for the systems evaluated in this thesis. These studies can be conducted by biophysical methods such as the measurement of initial enzymatic activity rate (see Section 4.4) at varying inhibitor concentrations, using non-linear regression methods to extract the dissociation constant ( $K_D$ ) [328]. NMR approaches can be utilised to measure this kinetic parameter for enzyme-ligand complexes [329]. A suitable  $^{19}\text{F}$  NMR approach for the detection of a dissociation constant in the range  $\mu\text{M}$  to  $\text{mM}$  is quantitative NOESY analysis. Scheuring *et al.* [330] measured the dissociation constant of a complex by using two-dimensional  $^{19}\text{F}$  NOESY experiments. Despite the fact that NOEs in the solid state are rare – owing to the general absence of motion on the correct timescale – the exploration of quantitative NOESY experiments for

immobilised enzymes could be an interesting approach, one which would eliminate the need for assembling a titration curve at different ligand concentrations.

## 7.6 Conclusions

Important information about the accessibility of inhibitors to the enzyme active site in the solution and the solid state was obtained. Significant insight was attained through the study of the enzyme in the presence of two different inhibitors using solution-state NMR.

The decision taken in this thesis to study the systems using solution-state NMR before moving to the study of immobilised enzyme by solid-state NMR was fully supported by the results obtained in Section 7.3. Further clarification was achieved, compared with the study by Smoum *et al.*, regarding the  $^{19}\text{F}$  NMR assignments for PFPTB in the presence of  $\alpha$ -chymotrypsin.

For the second inhibitor, AFEB, the assignments were in agreement with those obtained by Sylvia and Gerig. Better resolution and sensitivity were obtained for the spectra measured in this thesis compared with those of Sylvia and Gerig ( $^1\text{H}$ ,  $^{19}\text{F}$  and  $\{^{19}\text{F}-^1\text{H}\}$  HOESY NMR spectra).

The two-dimensional HOESY experiments for both inhibitors in the presence of the enzyme showed how the inhibitor interacts with different regions of the active site, revealing a clear difference between an inhibitor with a dissociation constant,  $K_d$ , in the millimolar range (PFPTB) compared with one in the nanomolar range (AFEB). Further experiments are necessary to better understand the cross-peak assignment revealed in both Sections 7.3 and 7.4.

It was possible to interpret the solid-state  $^{19}\text{F}$  NMR spectrum for the PFPTB-immobilised enzyme complex in accordance with the solution-state results from the free enzyme bound with the inhibitor.

Unfortunately, for the second system (immobilised enzyme in presence of AFEB) it was not possible to obtain a resolved solid-state  $^{19}\text{F}$  NMR spectrum as expected. Only the signal for the free inhibitor (AFEB) was observed. Lack of resolution in the spectrum led to the observation of a shoulder for the AFEB-immobilised enzyme complex.

## CHAPTER 8

### Summary

The lack of guidelines governing the selection of the immobilisation method and the expected performance of the immobilised enzyme for a specific application seriously hampers the application of a rational approach to the design robust immobilised enzymes [331]. One of the probable reasons why this situation arises is because, as has been stated in earlier sections in this thesis, not many analytical tools are available to characterise these heterogeneous systems. To date, catalytic activity provides the main source of information used to evaluate immobilised enzymes.

No single immobilisation method seems to be generally applicable if an optimised immobilised enzyme system is required. The immobilisation process depends on a broad spectrum of variables that involve the support, enzyme and medium of immobilisation. This intrinsic complexity is the main reason why their systematic study is not a straightforward task.

NMR spectroscopy is the only structural biology method that is capable of studying structure and dynamics at an atomic resolution. The main goal of this thesis was to evaluate how informative NMR can be in the study of immobilised enzyme systems and the limitations of its applicability. This contribution demonstrates the fact that solid-state NMR provides us with a powerful tool to study these systems. Structural characterisation of immobilised enzymes systems (Chapter 5) and their interactions

**Table 8.1. Methods to measure pore size and pore size distribution of porous materials.**

Method	References
Gas Adsorption Method	[126], [132]
Mercury Intrusion Porosimetry <sup>1</sup>	[332]
XRD <sup>2</sup>	[133]
NMR Cryoporometry	[130]
TEM	[133]

<sup>1</sup> Particularly good for macroporous supports

<sup>2</sup> Limited to regular structures such as zeolites

with ligands (Chapter 6 and Chapter 7) by NMR were covered. However, more research on this topic needs to be undertaken to exploit the technique's full potential.

Nevertheless, incorporation of other techniques to aim for a better understanding of immobilised enzymes could be extremely beneficial and is strongly advised for future studies. Table 8.1 to Table 8.3 summarise the current methods that can be applied to study these heterogeneous systems.

The characterisation of the systems<sup>10</sup> before and after enzyme immobilisation by solid-state NMR was covered in Chapter 5. One of the most interesting results from Chapter 5 was the observation of the carbonyl groups in the immobilised enzyme by <sup>13</sup>C CPMAS NMR. Further characterisation of the support materials is necessary. These studies should attempt the quantification of pore size, carrier bound group and enzyme distributions for bare supports and immobilised systems, correspondingly.

---

<sup>10</sup> The systems are silica, alumina and Eupergit® as enzymatic supports. The characterisation also includes the silanisation of silica and alumina with GOPS.

**Table 8.2. Methods for evaluating location and conformational changes on immobilised enzymes.**

Purpose	Method	References
Location of immobilised enzyme	Adsorption Method	[79, 80]
	XRD	[79]
	FTIR	[333]
	Fluorescence Microscopy	[81]
	TEM	[82]
Conformational changes on immobilised enzyme <sup>1</sup>	CD	[85, 88]
	FTIR	[91-93]
	Fluorescence Spectroscopy	[94-96]
	Solid-state NMR	[112] <sup>2</sup>

<sup>1</sup> Evaluation of the protein secondary structure

<sup>2</sup> References correspond to protein membrane studies

Pore size is an important factor for enzyme immobilisation. To reach high enzyme loading and to reduce diffusion constraints, the pore size should exceed the size of the enzyme [334]. Probably, for epoxide-silica systems the pore size is a controlling parameter for the immobilisation process, due to the high loading and activity obtained for these immobilised enzymes (see results in Section 5.3.1). However, if the pore size greatly exceeds the protein size, it may provoke another problem, namely diffusion constraints, when the enzyme can be too deeply embedded within the support particles, leading to lower retention of activity [334]. This could have happened in the Eupergit® systems where high loadings were obtained but extremely low activities were expressed (see results in Section 5.3.3). Furthermore, the distribution of binding sites on the carrier surface (i.e., carrier bound group distribution) influences the loading, activity and also the stability of the biocatalyst.

**Table 8.3. Methods for evaluating interactions of immobilised enzymes with the support and the ligands.**

Purpose	Methods	References
Enzyme-support interactions	Solid-state NMR	[1]
	FTIR	[97-100]
	MD	[99, 101-103, 106]
	ITC	[338]
Enzyme-ligand interactions	ITC	[117, 118]
	FAC	[119, 120]
	Solid-state NMR	[121-123] <sup>1</sup>

<sup>1</sup> References correspond for protein membrane studies

Some techniques that can be used for the purpose of measuring pore size and pore size distribution are listed in Table 8.1, with gas adsorption the most popular. However, an interesting approach involving the consistent use of NMR as the main technique would be to use NMR methods to characterise porous materials.

NMR cryoporometry [130] and NMR relaxometry [335, 336] have been used with the purpose of measuring pore size distribution in porous materials such as silica gels [337]. NMR relaxometry is based on the fact that water molecules in pores will move randomly due to Brownian motion and hence the transverse relaxation time  $T_2$  will be affected. Brownstein and Tarr [335] proposed a model to obtain porous parameters from the transverse relaxation.

As dissolved ions (e.g.,  $\text{Na}^+$ ) also move by Brownian motion, Rijniers *et al.* [339] showed that  $^{23}\text{Na}$  NMR relaxometry can be used to monitor pore size distributions in silica gels (i.e., Nucleosil).  $^{23}\text{Na}$  NMR relaxometry (e.g., CPMG experiments) can be explored to evaluate the supports. However, the treatment used by Rijniers *et al.*

should be followed with caution because it is based on the assumption that the system does not experience a net EFG, therefore no biexponential relaxation is expected. These experiments could be a valuable addition to the experiments used in Chapter 6 where relaxation studies were conducted. The evaluation of traditional  $^1\text{H}$  NMR relaxometry also represents an interesting approach.

Accessibility of the enzyme to the substrate can be deduced by information about the distribution and location of the enzyme within the support material. Among the methods used for this purpose (see Table 8.2), TEM is one of the most popular to literally observe enzyme location in immobilised systems. However, the solid-state multiple-quantum NMR experiments described in Chapter 6 were able, to some extent, to determine the accessibility of counter ion sites in the immobilised enzyme. For instance, correlation times for  $\text{Na}^+$  and labelled water decrease when the size of the pores increases.

One area not explored in this thesis was the direct evaluation of conformational changes. Table 8.2 summarise the methods that can be used to evaluate immobilised enzymes in terms of conformational changes. No solid-state NMR methodology has been applied to immobilised enzymes so far. However, advances in the structure determination of labelled membrane proteins by solid-state NMR have been made in recent years (see Table 8.2) and these could be applied to immobilised biocatalysts if there is interest in using labelled enzymes in the future.

As was mentioned earlier in Chapter 2, there are no methodologies for evaluating the interaction of ligands with immobilised enzymes. In Chapter 6 and Chapter 7, efforts to evaluate these interactions were made. Chapter 6 analyses the interaction with ions and water, while Chapter 7 describes the study of inhibitor interactions. The observation of a specific interaction with ligands can be interpreted, with a degree of caution, as confirmation that the protein is not unfolded and remains in an active structure.

In Chapter 6 information about the range of motional processes related with the interactions of Na<sup>+</sup> and labelled water with the immobilised enzyme was obtained by solid-state multiple-quantum NMR. In order to validate these results, control experiments with bare supports in the presence of these ligands (i.e., ions and water) are necessary. However, the results obtained fall inside the range of motion expected. In the case of Na<sup>+</sup> (<sup>23</sup>Na), the correlation times fall within the range of allosteric interactions and for labelled water, the counts of water molecules fall in the range of water present on the surface of the protein.

The interactions between enzyme and inhibitors were covered in Chapter 7. Although the main interest of this thesis was the study of immobilised enzyme systems, studies of free enzyme were conducted to evaluate their interactions with inhibitors. The reasoning behind this approach was to obtain an understanding of the free enzyme system first in order to better understand a more complicated system later: the immobilised enzyme. An improved understanding of the free enzyme in the presence of inhibitors was achieved – but not for immobilised systems. Our hope is that our efforts will provide a basis for future studies and will clarify the study of  $\alpha$ -chymotrypsin in the presence of PFPTB and AFEB. Nonetheless, advances in the study of inhibitors interacting with immobilised enzymes were achieved: the direct observation of signals arising from the bound inhibitor in the solid state was achieved.

The use of solid-state NMR represents one of the best options available to study ligand interactions in immobilised enzymes because it is a high-resolution approach, unlike ITC and FAC (see Table 8.3).

The incorporation of molecular dynamics simulations for evaluating the interactions of ligands with enzymes or even with the surfaces of the supports could help tremendously in gaining a better understanding of the meaning of NMR results (e.g., the correlation times obtained in Chapter 6). While enzyme-surface simulations can

be used to aid in the design of an appropriate support material (see Table 8.3), applications of molecular simulation methods to studying ligand interactions in enzymes immobilised onto porous supports are still limited. There are problems in correct treatment of solid surfaces during simulations.

Back to Figure 1.1, the diagram highlights that – currently – much of the detail of the state of the enzyme molecules is speculative. In this contribution our objective was to obtain a better insight about the state of the enzyme molecules on the support. To a certain extent this aim was achieved: it was possible to characterise the elements involved in the covalent attachment (Figure 2.10) and also, the accessibility of different ligands to the immobilised enzyme by NMR techniques.

Summarising, this research has extended the current knowledge of tools for understanding immobilised enzymes. However, results indicate that, in the future, NMR will not be used in this quest as a solitary technique. The development of hybrid methods will certainly be the most efficient way to evaluate these heterogeneous systems.

## APPENDIX A

### Technical data for supports materials

Daiso Co, Ltd (Osaka, Japan) has kindly donated the silica supports to use in this project. Table A.1 summarises the main characteristics of the supports.

Table A.1. Silica features.

Commercial name	Pore size / Å		Particle size / $\mu\text{m}$	Specific surface area / ( $\text{m}^2/\text{g}$ )	Pore volume / ( $\text{ml/g}$ )
	Å	nm			
SP-60-15P	60	6	14.0	452	0.68
SP-100-15P	92	9.2	13.5	436	1.00
SP-120-15P	123	12.3	15.1	335	1.03
SP-200-15P	208	20.8	13.9	209	1.08
SP-300-SP	291	29.1	14.2	105	0.97

Sasol Germany GmbH has provided the alumina supports. The Table A.2 summarises the principal characteristics of the supports.

Table A.3 summarises the principal characteristics of both types of Eupergit® supports. Evonik Industries has provided Eupergit® 250 L support. As a result of a market driven decision Eupergit® C has been discontinued several years ago and is no longer commercially available.

**Table A.2. Alumina features.**

Commercial name	Pore size / Å		Particle size / $\mu\text{m}$	Specific surface area / ( $\text{m}^2/\text{g}$ )	Pore volume / ( $\text{ml/g}$ )
	Å	nm			
Pural SB-1	50	5	45	241	0.5
Pural TH-80	80	8	45	203	not supplied
Pural TH-100	100	10	45	157	not supplied
Pural TH-200	200	20	45	130	not supplied

**Table A.3. Eupergit® features.**

Commercial name	Pore size / Å		Particle size / $\mu\text{m}$	Epoxide content / ( $\mu\text{mol/g}$ )
	Å	nm		
C	100	10	180	600
250 L	1000	100	180	300

## APPENDIX B

### BSA standard curve

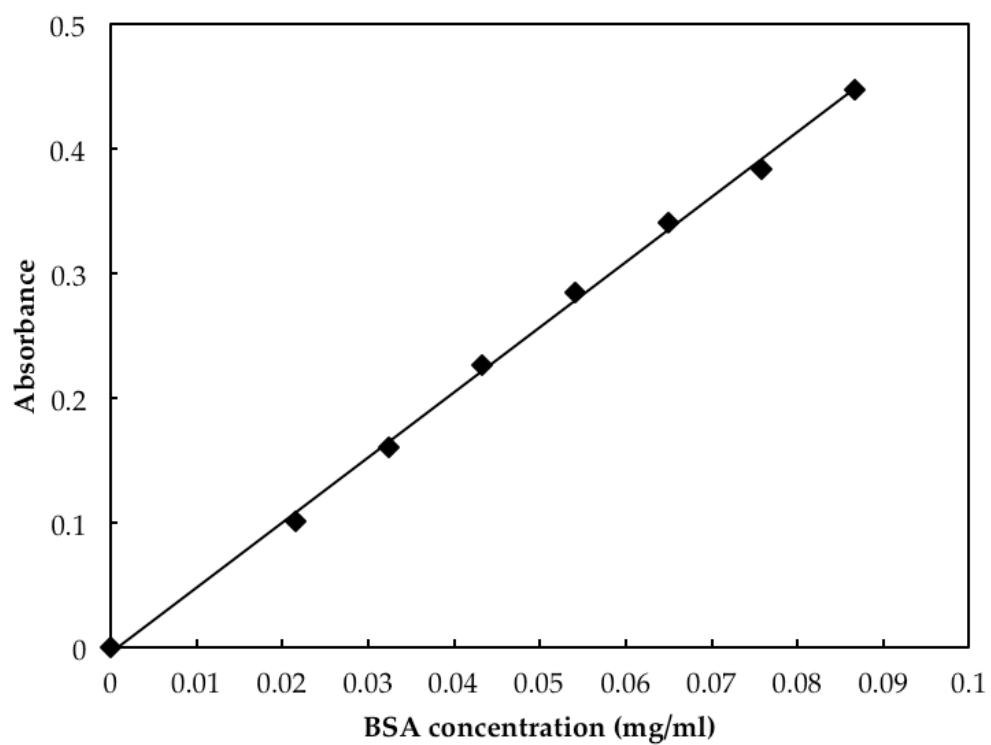


Figure B.1. BSA standard curve for calculation of protein concentration. Linear function:  $\text{Absorbance} = 5.22 \times \text{Protein concentration (mg/ml)} - 0.0043$ ,  $R^2 = 0.998$ .

## **APPENDIX C**

### **Immobilisation kinetics of $\alpha$ -chymotrypsin**

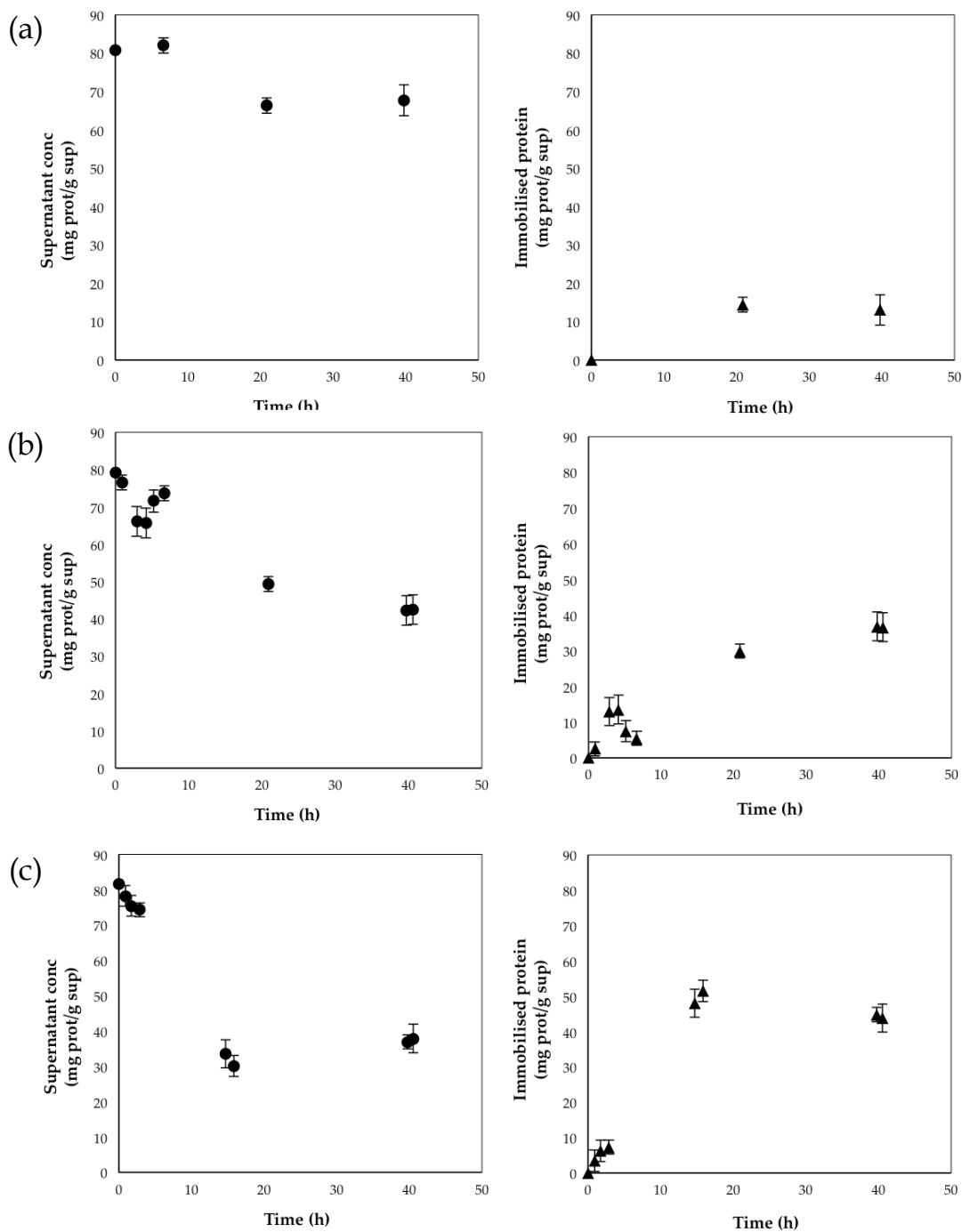


Figure C.1. Immobilisation kinetic of  $\alpha$ -chymotrypsin on epoxide silica 60 Å. (a) pH 7.0 without ammonium sulfate, (b) pH 7.0 with ammonium sulfate, (c) pH 8.0 with ammonium sulfate. Circles: concentration of protein in the supernatant support based on a function of time, triangles: amount of protein immobilised support based on a function of time.

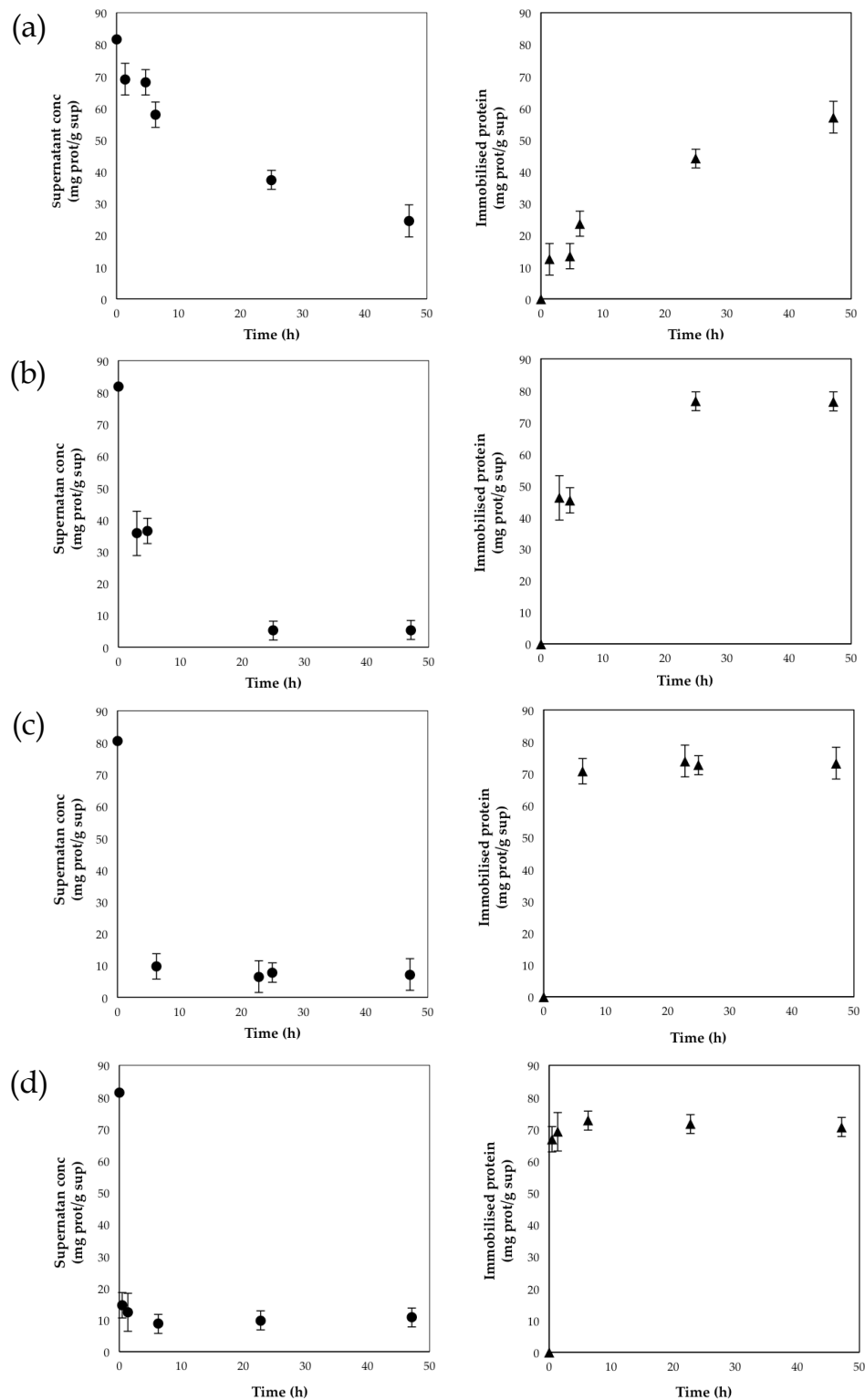
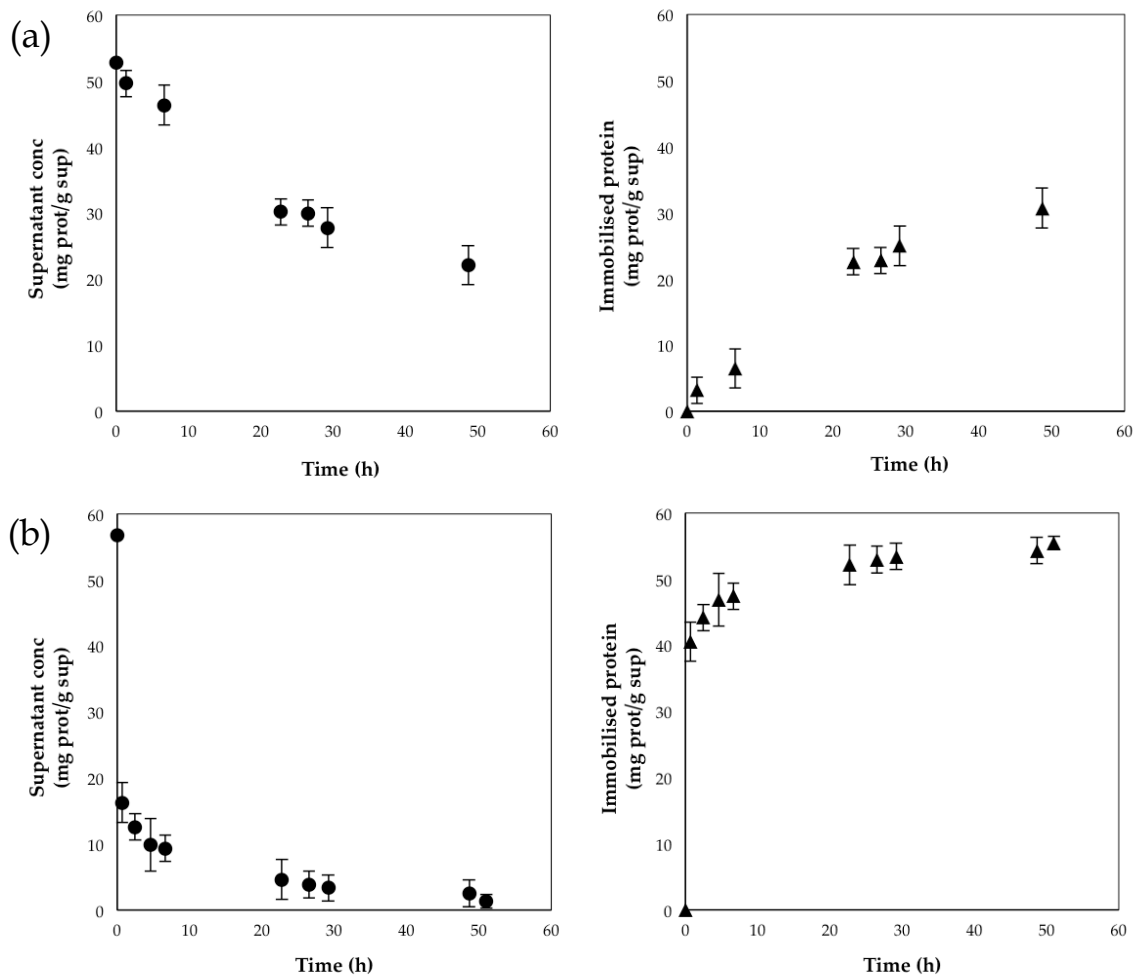


Figure C.2. Immobilisation kinetic of  $\alpha$ -chymotrypsin on epoxide alumina, at pH 8.0 with ammonium sulfate. (a) SB-1, (b) TH-80, (c) TH-100 and (d) TH-200 epoxide alumina. Circles: concentration of protein in the supernatant support based on a function of time, triangles: amount of protein immobilised support based on a function of time.



**Figure C.3. Immobilisation kinetic of  $\alpha$ -chymotrypsin on Eupergit®, at pH 8.0 (a) with ammonium sulfate (1.88 M) and (b) without. Circles: concentration of protein in the supernatant support based on a function of time, triangles: amount of protein immobilised support based on a function of time.**

## APPENDIX D

# Spin $I = 3/2$ Frequency-Domain Lineshape Functions for Evolution under Relaxation

The Fourier-Laplace Transform can be used to directly provide  $\mathbf{F}^{(1)}(\omega)$  and thereby to establish analytical frequency-domain lineshapes directly from the tensor basis matrix  $\mathbf{R}_{tensor}^{(1)}$ .

The term  $\exp(-R_{tensor}^{(1)} t)$  gives the time dependence for the interconversion of different forms of single-quantum coherence, including the conversion to observable magnetisation.

$$\mathbf{R}_{tensor}^{(1)} = \begin{pmatrix} \frac{1}{5}(3a+3b+2c) & 0 & \frac{1}{6}\sqrt{6}(a+b-c) \\ 0 & a-b & 0 \\ \frac{1}{5}\sqrt{6}(a+b-c) & 0 & \frac{1}{5}(2a+2b+3c) \end{pmatrix} \quad \mathbf{D.1}$$

The Fourier transform of these expressions will give the frequency-domain spectrum for each element of the basis set. Fourier transformation of  $\exp(-R_{tensor}^{(1)} t)$  term gives

$$\begin{aligned}
\mathbf{F}^{(1)}(\omega) &= \int_{-\infty}^{+\infty} \exp(-\mathbf{R}_{tensor}^{(1)} t) \exp(-i\omega t) dt \\
&= \int_{-\infty}^{+\infty} \exp(-\{\mathbf{R}_{tensor}^{(1)} + i\omega \mathbf{1}\} t) dt \\
&= \left[ \exp(-\{\mathbf{R}_{tensor}^{(1)} + i\omega \mathbf{1}\} t) (\mathbf{R}_{tensor}^{(1)} + i\omega \mathbf{1})^{-1} \right]_0^{\infty} \\
&= (\mathbf{R}_{tensor}^{(1)} - i\omega \mathbf{1})^{-1}
\end{aligned} \tag{D.2}$$

where  $\mathbf{1}$  is the unit matrix with the same dimension as  $\mathbf{R}_{tensor}^{(1)}$ .

$\mathbf{F}^{(1)}(\omega)$  becomes

$$\mathbf{F}^{(1)}(\omega) = \begin{pmatrix} F_{11}^{(1)}(\omega) & 0 & F_{13}^{(1)}(\omega) \\ 0 & F_{22}^{(1)}(\omega) & 0 \\ F_{31}^{(1)}(\omega) & 0 & F_{33}^{(1)}(\omega) \end{pmatrix} \tag{D.3}$$

Therefore,

$$\mathbf{F}^{(1)}(\omega) = \begin{pmatrix} \frac{2a+2b+3c-5i\omega}{5(a+b-i\omega)} & 0 & \frac{\sqrt{6}(a+b-c)}{5(a+b-i\omega)(-c+i\omega)} \\ 0 & \frac{1}{a-b-i\omega} & 0 \\ \frac{\sqrt{6}(a+b-c)}{5(a+b-i\omega)(-c+i\omega)} & 0 & \frac{3a+3b+2c-5i\omega}{5(a+b-i\omega)(-c+i\omega)} \end{pmatrix} \tag{D.4}$$

With

$$\begin{aligned}
a &= -C(J_0 + J_1 + J_2), \\
b &= CJ_2, \\
c &= -C(J_1 + J_2),
\end{aligned} \tag{D.5}$$

The standard multiple-quantum filtration experiment allows the transverse relaxation function  $F_{31}^{(1)}(\omega)$  to be measured.

$$\begin{aligned}
F_{31}^{(1)} &= \frac{\sqrt{6}(a+b-c)}{5(a+b-i\omega)(-c+i\omega)} \\
&= -\frac{\sqrt{6}C(J_2-J_0)}{5(CJ_1+CJ_2+i\omega)(CJ_1+CJ_0+i\omega)}
\end{aligned}
\tag{D.6}$$

with a real and imaginary components, respectively

$$F_{31}^{(1)}(\omega)_{real} = \frac{\sqrt{6}C(C^2J_0^2(J_1+J_2)+J_0(C^2J_1^2-C^2J_2^2-\omega^2)+J_2(-C^2J_1^2-C^2J_1J_2+\omega^2))}{5(C^2J_0^2+2C^2J_0J_1+C^2J_1^2+\omega^2)(C^2J_1^2+2C^2J_1J_2+C^2J_2^2+\omega^2)}
\tag{D.7}$$

$$F_{31}^{(1)}(\omega)_{imaginary} = \frac{\omega(2C^2J_0^2+4C^2J_0J_1+5C^2J_1^2+6C^2J_1J_2+3C^2J_2^2+5\omega^2)}{5(C^2J_0^2+2C^2J_0J_1+C^2J_1^2+\omega^2)(C^2J_1^2+2C^2J_1J_2+C^2J_2^2+\omega^2)}
\tag{D.8}$$

## **APPENDIX E**

### **Mathematica routines**

## E.1. Fitting routines for triple-quantum filter experiment

The lineshape fitting procedure routine for  $^{23}\text{Na}$  triple-quantum filter experiment of immobilised enzyme in epoxide silica with 200 Å pore size is shown below.

```
Directory[]
```

```
/Users/nicolefaure/Desktop
```

```
exp = Import["desktop/DATA.xlsx", {"Data", 1}]
```

A very large output was generated. Here is a sample of it:

```
{{{-510.535, -0.132019}, {-510.291, -0.137856}, {-510.046, -0.143593},  
<<4327>>, {548.697, -0.359594}, {548.941, -0.367711}}
```

Show Less

Show More

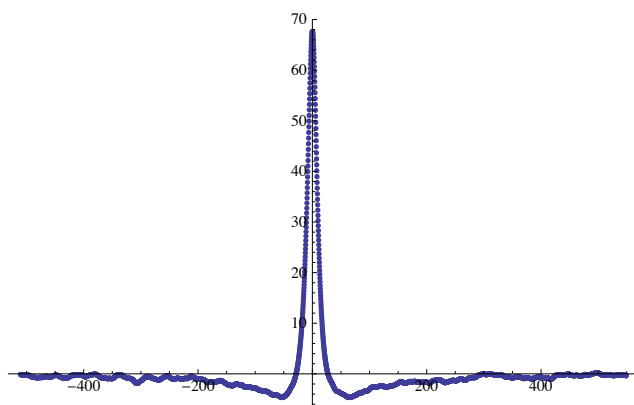
Show Full Output

Set Size Limit...

```
Dimensions[exp]
```

```
{4332, 2}
```

```
ListPlot[exp, PlotRange -> All]
```



```
model =
```

$$\frac{(a) \left( - \left( 8 \sqrt{6} k t^3 (w_0 + t^2 w_0^3)^2 \left( (1 + 4 t^2 w_0^2) (w + t^2 w w_0^2)^2 - 4 k^2 t^2 (4 + 12 t^2 w_0^2 + 5 t^4 w_0^4) \right) \right) \right)}{\left( 5 \left( 4 k^2 t^2 (2 + t^2 w_0^2)^2 + (w + t^2 w w_0^2)^2 \right) \left( 4 k^2 t^2 (2 + 5 t^2 w_0^2)^2 + w^2 (1 + 5 t^2 w_0^2 + 4 t^4 w_0^4)^2 \right) \right)}$$

$$- \left( 8 \sqrt{6} a k t^3 (6.65025 \times 10^8 + 2.94113 \times 10^{26} t^2)^2 \right. \\ \left. (-4 k^2 t^2 (4 + 5.3071 \times 10^{18} t^2 + 9.77962 \times 10^{35} t^4) + \right. \\ \left. (1 + 1.76903 \times 10^{18} t^2) (w + 4.42258 \times 10^{17} t^2 w)^2 \right) \left. \right) / \\ \left( 5 \left( 4 k^2 t^2 (2 + 2.21129 \times 10^{18} t^2)^2 + (1 + 2.21129 \times 10^{18} t^2 + 7.82369 \times 10^{35} t^4)^2 w^2 \right) \right. \\ \left. \left( 4 k^2 t^2 (2 + 4.42258 \times 10^{17} t^2)^2 + (w + 4.42258 \times 10^{17} t^2 w)^2 \right) \right)$$

```
w0 = 6.65025 * 108
```

```
6.65025 * 108
```

```
solv = FindFit[exp, model,
```

```
{a, 1712.}, {t, 4.663 * 10-9}, {k, 8.704 * 109}, w, MaxIterations -> 100]
```

```
{a -> 1686.06, t -> 4.08676 * 10-9, k -> 8.42251 * 109}
```

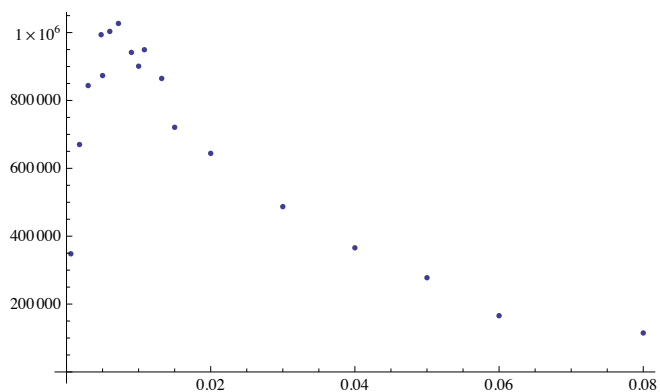
The time-domain fitting procedure routine for  $^{23}\text{Na}$  triple-quantum filter experiment of immobilised enzyme in epoxide silica with 200 Å pore size is shown below.

$$\text{model2} = a * \frac{\sqrt{6}}{5} \{e^{R1*t} - e^{R2*t}\}$$

$$\left\{ \frac{1}{5} \sqrt{6} a (e^{R1 t} - e^{R2 t}) \right\}$$

```
sim2 = Import["desktop/TQF200/TQF200.xlsx", {"Data", 19, Table[i, {i, 24, 41}], {1, 2}}]
ListPlot[sim2, PlotRange -> All]
```

```
{ {0.0018, 670177.}, {0.003, 843881.}, {0.005, 873331.},
  {0.006, 1.00344 × 106}, {0.0072, 1.02694 × 106}, {0.01, 900895.},
  {0.0006, 348168.}, {0.015, 720924.}, {0.02, 644086.}, {0.0048, 993773.},
  {0.0108, 949467.}, {0.03, 487110.}, {0.04, 365774.}, {0.06, 165718.},
  {0.05, 277678.}, {0.08, 114910.}, {0.009, 941599.}, {0.0132, 864903.} }
```



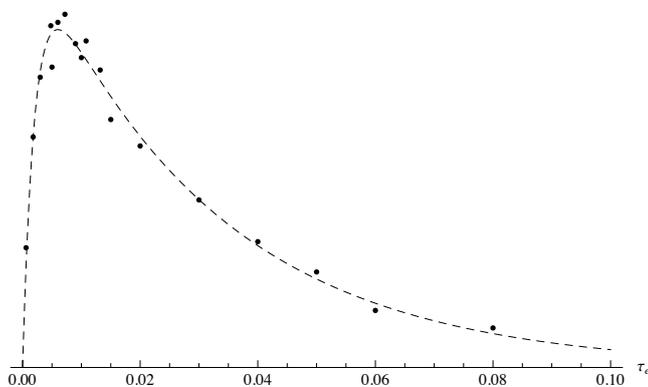
```
solv2["BestFit", "FitResiduals", "ParameterTable", "RSquared"]]
```

```
{-1.27506 × 106 (e-484.145 t - e-32.0238 t),  
{-57.0973, -16 021.8, -99 779.5, 21 088., 53 489.6, -14 704., 50 988.8, -66 888.3, -27 846.,  
25 201.3, 54 048.6, -753.535, 11 596.4, -20 948.1, 20 553.6, 16 529.3, 2146.65, 31 535.3},
```

	Estimate	Standard Error	t-Statistic	P-Value
a	-2.60272 × 10 <sup>6</sup>	90964.7	-28.6124	1.67254 × 10 <sup>-14</sup>
R1	-484.145	40.7222	-11.889	4.90783 × 10 <sup>-9</sup>
R2	-32.0238	2.0639	-15.5162	1.20293 × 10 <sup>-10</sup>

```
Show[
```

```
ListPlot[sim2, Axes → {True, False},  
AxesLabel → {τe, None}, PlotRange → All, PlotStyle → Black],  
Plot[Evaluate[model2 /. solv2], {t, 0, 0.1}, Axes → {True, False},  
PlotStyle → {Black, Dashed}, PlotRange → All]]
```



```
R1=slow
```

```
R2=fast
```

$$R2 = R2f + \frac{Pb}{Pb} R2b$$

$$R1 = R1f + \frac{Pb}{Pb} R1b$$

```
α = Evaluate[(R1 / R2) /. solv]
```

```
15.1183
```

```
teopt = Evaluate[Log[ $\frac{R2}{R1}$ ] /. solv]
```

```
0.00600703
```

$$tc = \frac{\sqrt{(1/8) (5 * \alpha - 9 + \sqrt{25 * \alpha^2 - 58 * \alpha + 49})}}{6.65025 * 10^8} // N$$

```
6.21114 × 10-9
```

The same calculations were performed using these routines for the different pore size systems.

## E.2. Fitting routine for four-quantum and five-quantum evolution experiment

The fitting procedure routine for  $^{17}\text{O}$  four-quantum evolution experiment of

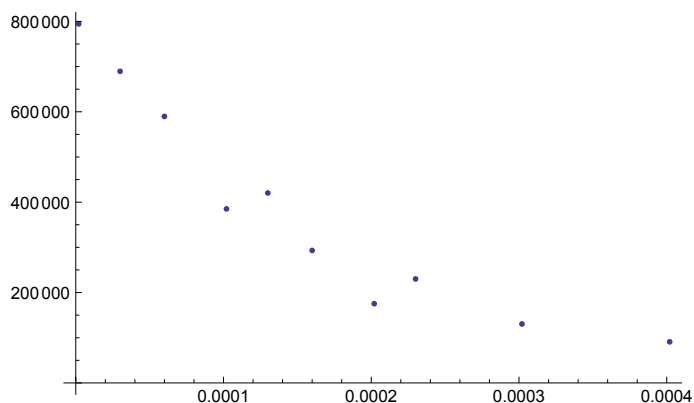
```
modell1 = a * {eR*t}
```

```
{a eR*t}
```

```
sim1 = Import["dropbox/NMR experiments/Relaxation/17O/TQF10017O.xls",  
  {"Data", 3, Table[i, {i, 3, 12}], {2, 3}}]
```

```
ListPlot[sim1, PlotRange -> All]
```

```
{{2. × 10-6, 794 400.}, {0.00003, 689 500.}, {0.00006, 589 700.}, {0.000102, 385 100.},  
  {0.00013, 420 300.}, {0.00016, 293 200.}, {0.000202, 175 300.},  
  {0.00023, 230 100.}, {0.000302, 130 500.}, {0.000402, 90 970.}}
```



```
solv1 = FindFit[sim1, modell1, {{a, -1.18`*^6}, {R, -500}}, t, MaxIterations -> 100]  
{a -> 815 729., R -> -6140.64}
```

```
solv2 = NonlinearModelFit[sim1, modell1,  
  {{a, -1.18`*^6}, {R, -500}}, t, MaxIterations -> 100]
```

```
FittedModel[ 815 729. e-6140.64 t ]
```

```
solv2[{"BestFit", "FitResiduals", "ParameterTable", "RSquared"}]
```

```
{815 729. e-6140.64 t, {-11 371.8, 11 014.8, 25 367.6, -50 941.1,  
  53 139.7, -12 186.9, -60 662.4, 31 412.2, 2809.62, 21 870.7},
```

	Estimate	Standard Error	t-Statistic	P-Value
a	815 729.	29 664.5	27.4985	3.29835 × 10 <sup>-9</sup> , 0.994117}
R	-6140.64	418.393	-14.6767	4.56196 × 10 <sup>-7</sup>

immobilised enzyme in epoxide silica with 100 Å pore size is shown below.

The fitting procedure routine for  $^{17}\text{O}$  five-quantum evolution experiment of immobilised enzyme in epoxide silica with 100 Å pore size is shown below.

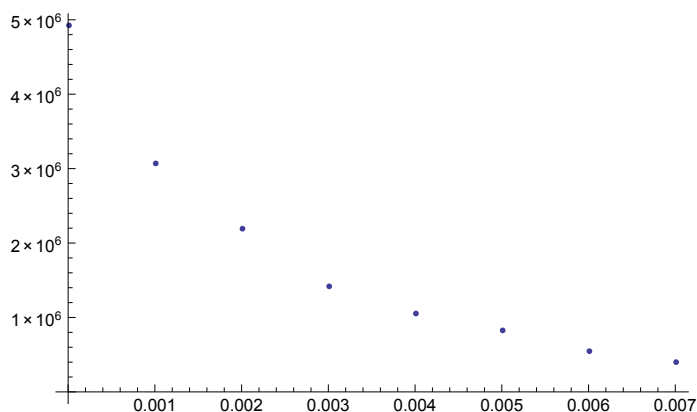
```
modell = a * {eR*t}
```

```
{a eR*t}
```

```
sim1 = Import["dropbox/NMR experiments/Relaxation/17O/TQF10017O.xls",  
  {"Data", 4, Table[i, {i, 3, 10}], {2, 3}}]
```

```
ListPlot[sim1, PlotRange -> All]
```

```
{{0.00001, 4.925 × 106}, {0.00101, 3.07 × 106},  
  {0.00201, 2.193 × 106}, {0.00301, 1.418 × 106}, {0.00401, 1.053 × 106},  
  {0.00501, 826 300.}, {0.00601, 547 200.}, {0.00701, 400 000.}}
```



```
solv1 = FindFit[sim1, modell, {{a, -1.18`*^6}, {R, -500}}, t, MaxIterations -> 100]  
{a -> 4.82515 × 106, R -> -388.739}
```

```
solv2 = NonlinearModelFit[sim1, modell,  
  {{a, -1.18`*^6}, {R, -500}}, t, MaxIterations -> 100]
```

```
FittedModel[ 4.82515 × 106 e-388.739t ]
```

```
solv2[{"BestFit", "FitResiduals", "ParameterTable", "RSquared"}]
```

```
{4.82515 × 106 e-388.739t,  
  {118 576., -188 330., -15 858.6, -79 410.3, 37 888.6, 138 144., 80 691.6, 83 748.6},
```

	Estimate	Standard Error	t-Statistic	P-Value
a	4.82515 × 10 <sup>6</sup>	110 641.	43.6109	9.73073 × 10 <sup>-9</sup> , 0.997892}
R	-388.739	15.6068	-24.9083	2.75595 × 10 <sup>-7</sup>

Finally,  $\alpha$  and  $\tau_c$  were evaluated for this system.

$$\alpha = \text{Evaluate} \left[ \left( R / -6140.64035589877 \right) /. \text{solvr1} \right]$$

$$0.0633059$$

$$\tau_c = \frac{\sqrt{\frac{15*(1-\alpha) + \sqrt{5(1-\alpha)(45-13\alpha)}}{16\alpha}}}{7.24125 * 10^8} // \text{N}$$

$$7.3169 \times 10^{-9}$$

The same calculations were performed using this routine for the different pore size systems.

## APPENDIX F

### List of chemicals

The information about the chemicals used in each section of the experimental Chapter (Chapter 4) is detailed in this Appendix. If a chemical is used in more than one section, it has been described only once (by appearance order).

#### F.1. Quantification of Epoxides Groups

Table F.1 shows the chemicals used in Section 4.1.

**Table F.1. List of chemicals used in quantification of epoxides groups.**

Substance	Chemical formula	Purity (%)	Supplier
Crystal violet	$C_{25}H_{30}N_3Cl$	90	Sigma-Aldrich
Perchloric acid	$HClO_4$	72	Sigma-Aldrich
Acetic acid	$CH_3CO_2H$	99.85 (glacial)	Sigma-Aldrich
Acetic anhydride	$(CH_3CO)_2O$	98	Sigma-Aldrich
Tetraethylammonium bromide	$(C_2H_5)_4N(Br)$	98	Sigma-Aldrich
Potassium hydrogen phthalate	$C_8H_5KO_4$	99	Alfa Aesar

## F.2. Protein Analysis, immobilised protein determination and evaluation of immobilised enzyme

Table F.2 shows the chemicals used in Sections 4.2, 4.3 and 4.5.

**Table F.2. List of chemicals used in Protein analysis, immobilised protein determination and evaluation of immobilised enzyme.**

Substance	Chemical formula	Purity (%)	Supplier
Bovine serum albumin	-	96	Sigma-Aldrich
Coomassie brilliant blue G-250	$C_{47}H_{48}N_3NaO_7S_2$	99	Thermo Scientific
Ethanol	$CH_3CH_2OH$	95	Acros Organics
Orthophosphoric acid	$H_3PO_4$	85	Acros Organics
Potassium phosphate monobasic	$KH_2PO_4$	98	Sigma-Aldrich
Potassium phosphate dibasic	$K_2HPO_4$	98	Sigma-Aldrich

### F.3. Enzyme activity determination and evaluation of immobilised enzyme

Table F.3 shows the chemicals used in Sections 4.4 and 4.5.

**Table F.3. List of chemicals used in enzyme activity determination and evaluation of immobilised enzyme.**

Substance	Chemical formula	Purity (%)	Supplier
N-Acetyl-L-tyrosine ethyl estermonohydrate (ATEE)	$C_{13}H_{17}NO_4 \times H_2O$	99	Sigma-Aldrich
Tris(hydroxymethyl)amino methane (Tris base)	$C_4H_4N_3NaO_7S_2$	99.9	Sigma-Aldrich
Hydrochloric acid	$CH_3CH_2OH$	95	Acros Organics
Calcium chloride	$CaCl_2$	96	Sigma-Aldrich
$\alpha$ -Chymotrypsin from bovine pancreas (type II)	-	85	Sigma-Aldrich
Sodium hydroxide	$NaOH$	98	Sigma-Aldrich

## F.4. Immobilisation procedure

### F.4.1 Activation of Support

Table F.4 shows the chemicals used in Section 4.5.1.

**Table F.4. List of chemicals used in activation of support.**

Substance	Chemical formula	Purity (%)	Supplier
Silicon dioxide	SiO <sub>2</sub>	-	Daiso
Aluminium oxide	Al <sub>2</sub> O <sub>3</sub>	-	Sasol
Toluene	C <sub>6</sub> H <sub>5</sub> CH <sub>3</sub>	99.5	Acros Organics
3- Glycidoxypropyl- trimetoxysilane (GOPS)	C <sub>9</sub> H <sub>20</sub> O <sub>5</sub> Si	98	Sigma-Aldrich
Tetrahydrofuran (THF)	C <sub>4</sub> H <sub>8</sub> O	99	Fluka
Methanol	CH <sub>3</sub> OH	99.8	Sigma-Aldrich

## F.4.2 Covalent binding of the Enzyme

Table F.5 shows the chemicals used in Section 4.5.2.

**Table F.5. List of chemicals used in covalent binding of the enzyme.**

Substance	Chemical formula	Purity (%)	Supplier
Ammonium sulfate	$C_{13}H_{17}NO_4 \times H_2O$	99	Sigma-Aldrich
Sodium acetate	$CaCl_2$	96	Sigma-Aldrich
Sodium chloride	-	85	Sigma-Aldrich
Silica gel with moisture indicator (blue)	$SiO_2 (CoCl_2)$	97 ( $\leq 1$ )	Sigma-Aldrich

## F.5. Nuclear magnetic resonance

### F.5.1 Solution-state NMR

Table F.6 shows the chemicals used in Section 4.7.1 and Chapter 7.

**Table F.6. List of chemicals used in solution-state NMR.**

Substance	Chemical formula	Purity (%)	Supplier
Deuterium oxide	D <sub>2</sub> O	99.8	Sigma-Aldrich
Dimethyl sulfoxide-d <sub>6</sub>	(CD <sub>3</sub> ) <sub>2</sub> SO	99.9	Sigma-Aldrich
Potassium 4-fluorophenyltrifluoroborate	FC <sub>6</sub> H <sub>4</sub> BF <sub>3</sub> K	95	Sigma-Aldrich
R-1-acetamido-2-(4-fluorophenyl)ethane-1-boronic acid	C <sub>10</sub> H <sub>13</sub> BFNO <sub>3</sub>	-	Prof Gibson, University of Strathclyde
Tetramethylsilane	Si(CH <sub>3</sub> ) <sub>4</sub>	99.5	Sigma-Aldrich
Trichlorofluoromethane	CFCl <sub>3</sub>	99.5	Sigma-Aldrich

## F.5.2 Solid-state NMR

Table F.7 shows the chemicals used in Section 4.7.2, Chapter 5, Chapter 6 and Chapter 7.

**Table F.7. List of chemicals used in solid-state NMR.**

Substance	Chemical formula	Purity (%)	Supplier
$^{17}\text{O}$ enriched water	$\text{H}_2^{17}\text{O}$	99	Cambridge isotope laboratories
Adamantane	$\text{C}_{10}\text{H}_{16}$	96	Sigma-Aldrich
Polytetrafluoroethylene (PTFE)	$(\text{CF}_2\text{CF}_2)_n$	85	Sigma-Aldrich
Kaolinite	$\text{SiO}_2/\text{Al}_2\text{O}_3$	100	Sigma-Aldrich

## APPENDIX G

# Characterisation of inhibitors by solution-state NMR

### G.1. Potassium 4-fluorophenyl trifluoroborate

The characterisation and confirmation of the structure of a commercial PFPTB (Figure 3.11d) was conducted by solution-state NMR. The sample was dissolved in 90% DMSO/10% DMSO- $d_6$ . The concentration of inhibitor in the NMR tube was 5 M.

Figure G.1 shows the notation used for the proton and carbon assignment. Figure G.2 shows the  $^1\text{H}$  NMR spectrum of PFPTB where two triplets are present. The signal at 6.8 ppm is assigned to the pair of protons closer to the single fluorine atom (H2) and the signal at 7.3 ppm to the pair of protons closer to boron (H1). These assignments were confirmed with the two-dimensional  $\{^{19}\text{F}, ^1\text{H}\}$  HOESY spectrum (Figure G.3). The mixing time,  $\tau_m$ , for the free inhibitor was optimised by observing a maximum in signal intensity, with a  $\tau_m$  value of around 8 seconds being found. The two-dimensional  $\{^{19}\text{F}, ^1\text{H}\}$  HOESY spectrum of PFPTB (Figure G.3) provides a very clear interpretation of the intramolecular NOE between the fluorine atoms and protons of the inhibitor.

The  $^{19}\text{F}$  NMR spectrum of PFPTB is presented in Figure G.4. It can be seen from this spectrum that the NMR results confirm the two different fluorine atoms present in the inhibitor. The high frequency resonance (-118.3 ppm) is assigned to the fluorine

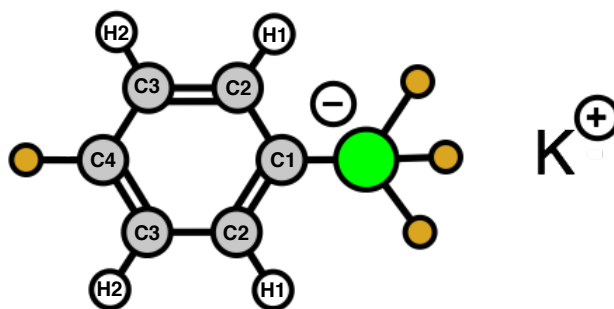


**Figure G.1. Structure of 4-fluorophenyl trifluoroborate (PFPTB).**

atom bonded to the phenyl group and the low frequency signal (-138.7 ppm) to the fluorines that are bonded to the boron atom.

The  $^{13}\text{C}$  NMR spectrum of the inhibitor is shown in 2.5. The high concentration (5 M) of sample allows a well resolved spectrum to be obtained. The doublet at high frequency with an isotropic chemical shift of 161 ppm is assigned to the carbon bonded to the single fluorine (C4) and the broad resonance at 146 ppm to the carbon bonded to the boron atom (C1). Carbon atoms from the phenyl ring arise at 133 and 113 ppm, with these signals corresponding to the pair of carbons closer to the single fluorine (C3) and to the boron atom (C2), respectively.

Figure G.6 provides the  $^{11}\text{B}$  NMR spectrum of PFPTB that agrees with the chemical shift expected for a boron atom bonded to a fluorine atom at 3 ppm.

## **G.2. (R)-1-acetamido-2-(4-fluorophenyl)ethane-1-boronic acid**

(R)-1-acetamido-2-(4-fluorophenyl)ethane-1-boronic acid (AFEB) (Figure 3.11b) is presently not commercially available. Professor Colin Gibson and one of his students, James Campbell, from University of Strathclyde collaborated in the synthesis of AFEB. Basically, the synthetic path followed was the one reported by Martichonok and Jones [340]. The characterisation by solution-state NMR confirms the structure and a purity of around 50 mol % from the  $^{11}\text{B}$  NMR spectrum (Figure G.7). The low purity of the inhibitor synthesised did not affect our experiments.

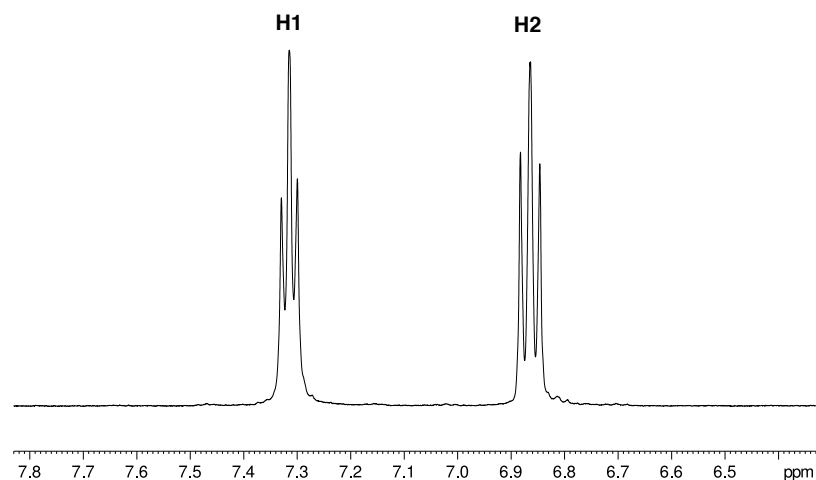


Figure G.2.  $^1\text{H}$  NMR spectrum of potassium 4-trifluorophenyltrifluoroborate (5 M in 90% DMSO/10% DMSO- $\text{d}_6$ ) at  $B_0 = 11.75$  T ( $90^\circ$  pulse length of 11  $\mu\text{s}$ , relaxation interval of 0.5 s, averaging 16 transients).

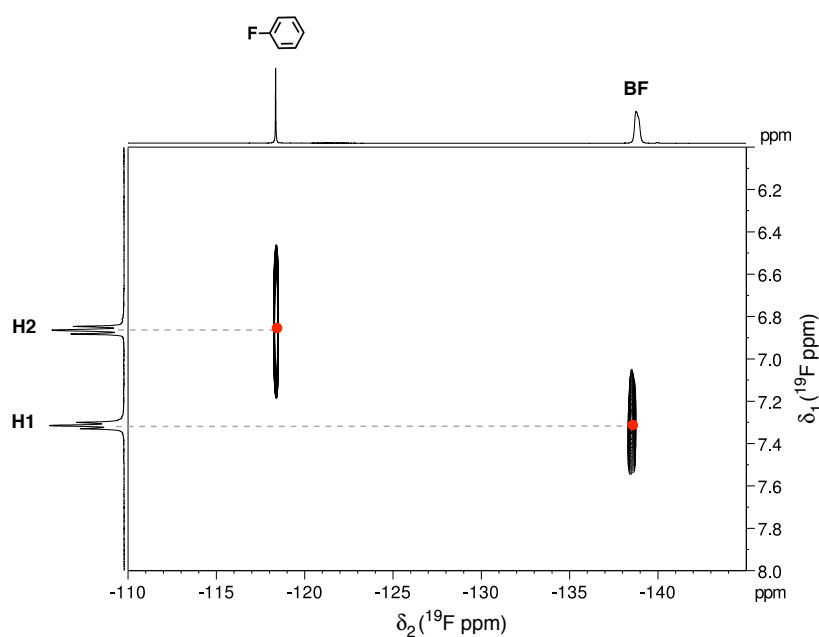
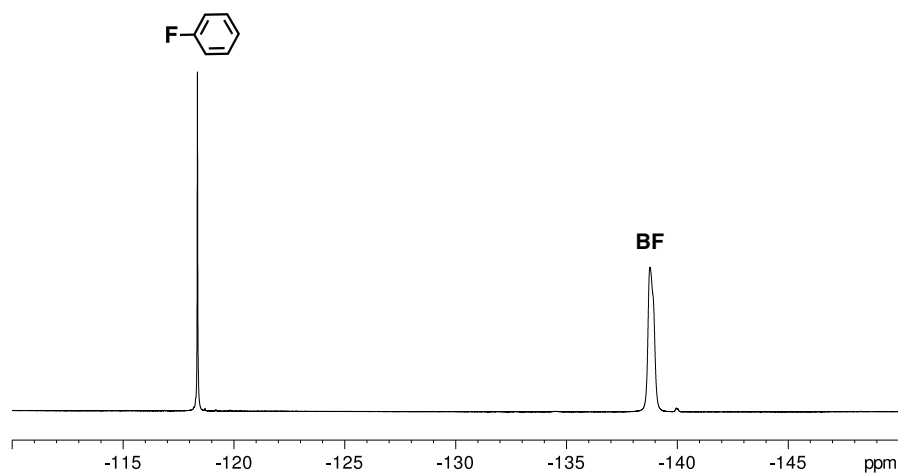


Figure G.3.  $\{^{19}\text{F}, ^1\text{H}\}$  HOESY NMR spectrum of potassium 4-trifluorophenyltrifluoroborate (5 M in 90% DMSO/10% DMSO- $\text{d}_6$ ) at  $B_0 = 9.4$  T. Spectra were recorded by averaging 1024 transients for each of the 16  $t_1$  increments of 310  $\mu\text{s}$  ( $90^\circ$  pulse length of 10  $\mu\text{s}$ , relaxation interval of 8.5 s). WALTZ-16 was used for proton decoupling. The  $^{19}\text{F}$  NMR spectrum along the  $F_2$  dimension corresponds to the spectrum shown in Figure G.4 and the  $^1\text{H}$  NMR spectrum along  $F_1$  dimension to the spectrum shown in Figure G.2.



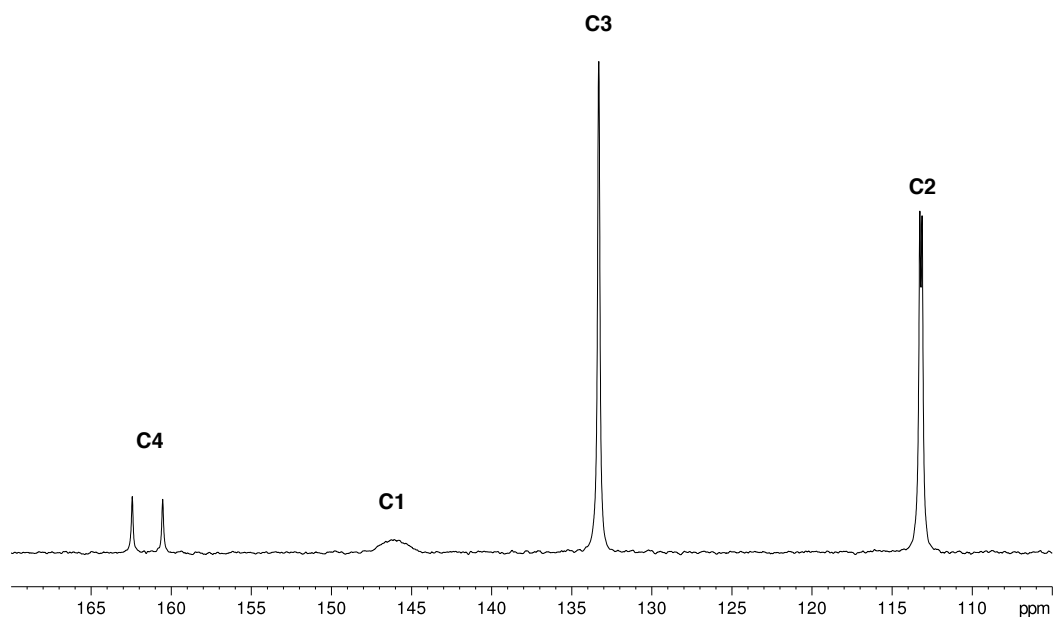
**Figure G.4.**  $^{19}\text{F}$  NMR spectrum of potassium 4-trifluorophenyltrifluoroborate (5 M in 90% DMSO/10% DMSO- $d_6$ ) at  $B_0 = 11.75$  T ( $90^\circ$  pulse length of  $10\ \mu\text{s}$ , relaxation interval of 12 s, averaging 16 transients). WALTZ-16 was used for proton decoupling.

Because of the restrictive amount of AFEB synthesised (only 25 mg), the characterisation by solution-state NMR was performed using a relatively low concentration (3 mM).

Figure G.8 shows the notation used here for the proton and carbon assignment. The  $^1\text{H}$  NMR spectrum is provided in Figure G.10. The signal at 2.0 ppm is assigned to the H1 protons, 2.4 ppm to H3, 2.7 ppm to H4, 7.0 ppm to H6, 7.2 ppm to H5 and 9.0 ppm to H2.

The  $^{19}\text{F}$  NMR spectrum (Figure G.9) shows a single peak at -117 ppm as expected from the fluorine atom in the phenyl ring.

Figure G.7 presents the  $^{11}\text{B}$  spectrum of AFEB where it is possible to observe two signals. It was expected that only one resonance would be observed for this nucleus. In the last step of the synthesis  $\text{BCl}_3$  is used to hydrolyse and remove a protecting group. It seems not all  $\text{BCl}_3$  was removed. The presence of this compound does not affect the system of study, therefore no further purification was conducted. The resonance at 11 ppm is assigned to  $\text{BCl}_3$  and the high frequency signal (19 ppm) to AFEB.



**2.5.  $^{13}\text{C}$  NMR spectrum of potassium 4-trifluorophenyltrifluoroborate (5 M in 90% DMSO/10% DMSO- $d_6$ ) at  $B_0 = 11.75$  T ( $90^\circ$  pulse length of  $7.5 \mu\text{s}$ , relaxation interval of 15 s, averaging 1024 transients). WALTZ-16 was used for proton decoupling.**

The two-dimensional  $\{^{19}\text{F}, ^1\text{H}\}$  HOESY spectrum of AFEB shows only one cross-peak signal, corresponding to the intramolecular NOE between the H6 protons and the fluorine atom (Figure G.11).

The concentration used was not enough to record a one-dimensional  $^{13}\text{C}$  experiment with a decent signal-to-noise ratio therefore an indirect through-bond technique was applied. Figure G.12 shows the two-dimensional  $\{^1\text{H}, ^{13}\text{C}\}$  HSQC spectrum where  $F_2$  represents  $^1\text{H}$  dimension and  $F_1$   $^{13}\text{C}$ . The presence of a variety of cross-peaks is noticeable. The cross-peaks from left to right are assigned to H1-C1, H3-C3, H4-C4, H6-C7 and H5-C6.

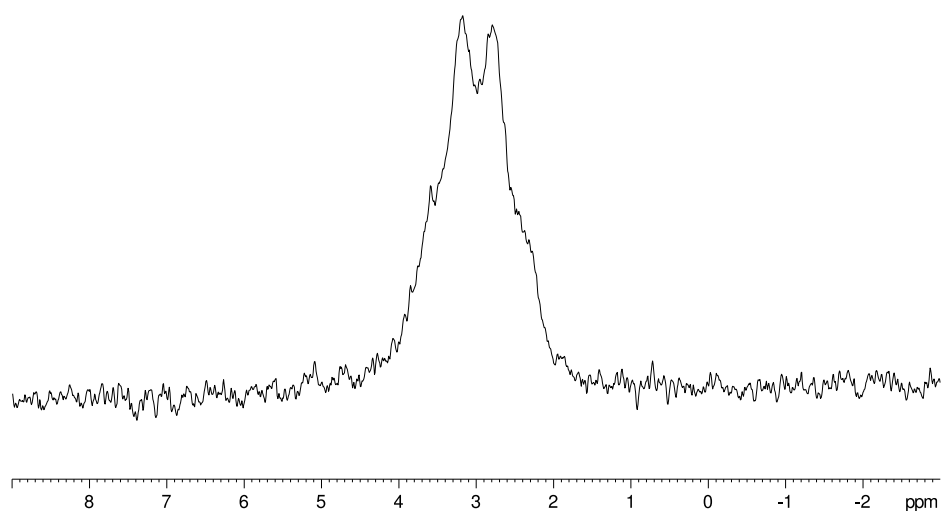


Figure G.6.  $^{11}\text{B}$  NMR spectrum of potassium 4-trifluorophenyltrifluoroborate (5 M in 90% DMSO/10% DMSO- $d_6$ ) at  $B_0 = 9.4$  T ( $90^\circ$  pulse length of  $10\ \mu\text{s}$ , relaxation interval of 2 s, averaging 4 transients).

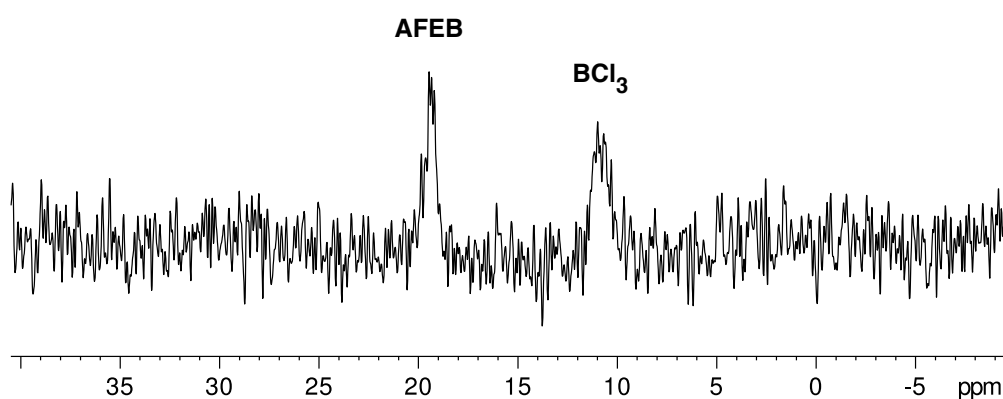


Figure G.7.  $^{11}\text{B}$  NMR spectrum of R-1-acetamido-2-(4-fluorophenyl)ethane-1-boronic acid (3 mM in 90%  $\text{H}_2\text{O}$ /10%  $\text{D}_2\text{O}$ ) at  $B_0 = 9.4$  T ( $90^\circ$  pulse length of  $12.2\ \mu\text{s}$ , relaxation interval of 0.5 s, averaging 4096 transients).

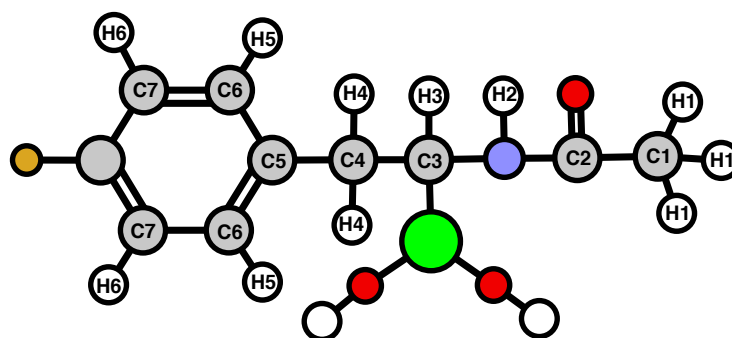


Figure G.8. Structure of (R)-1-acetamido-2-(4-fluorophenyl)ethane-1-boronic acid.

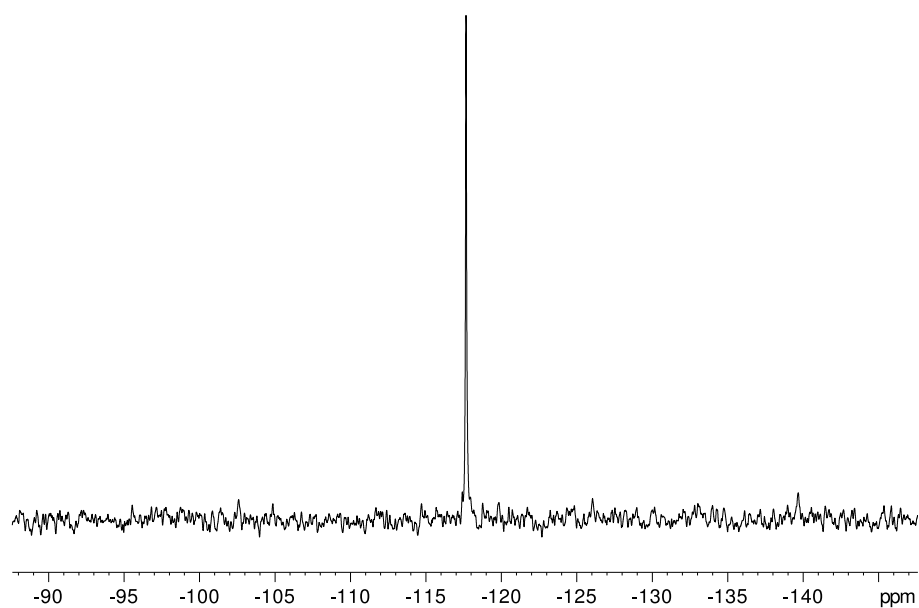


Figure G.9.  $^{19}\text{F}$  NMR spectrum of R-1-acetamido-2-(4-fluorophenyl)ethane-1-boronic acid (3 mM in 90%  $\text{H}_2\text{O}$ / 10%  $\text{D}_2\text{O}$ ) at  $B_0 = 9.4$  T ( $90^\circ$  pulse length of  $10\ \mu\text{s}$ , relaxation interval of 12 s, averaging 16 transients).

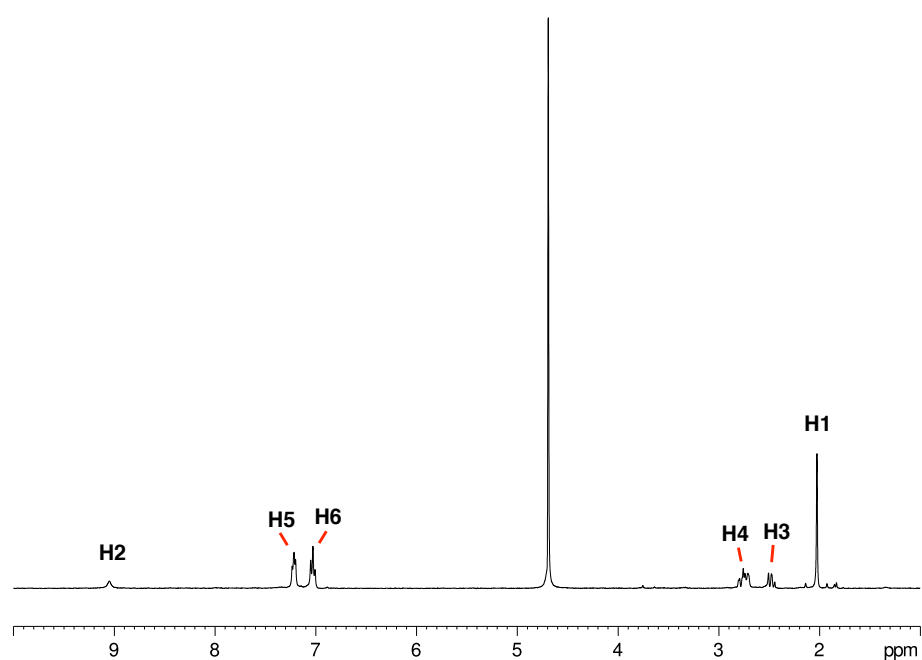


Figure G.10.  $^1\text{H}$  NMR spectrum of R-1-acetamido-2-(4-fluorophenyl)ethane-1-boronic acid (3 mM in 90%  $\text{H}_2\text{O}$ / 10%  $\text{D}_2\text{O}$ ) at  $B_0 = 9.4$  T ( $90^\circ$  pulse length of  $12\ \mu\text{s}$ , relaxation interval of 2 s, averaging 16 transients).

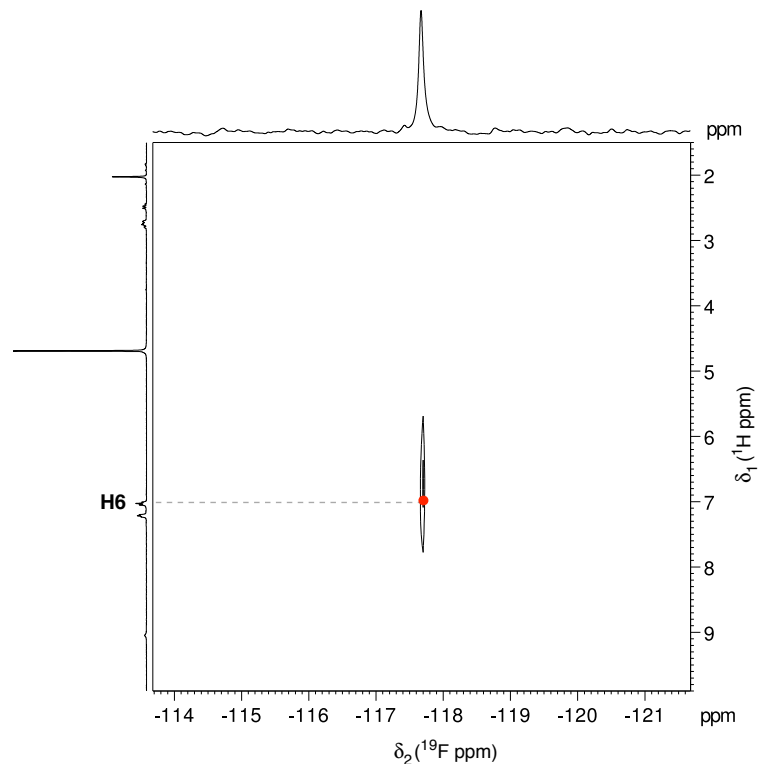


Figure G.11.  $\{^{19}\text{F}, ^1\text{H}\}$  HOESY NMR spectrum of R-1-acetamido-2-(4-fluorophenyl)ethane-1-boronic acid (3 mM in 90%  $\text{H}_2\text{O}/10\%$   $\text{D}_2\text{O}$ ) at  $B_0 = 9.4$  T. Spectra were recorded by averaging 128 transients for each of the 8  $t_1$  increments of  $57 \mu\text{s}$  ( $90^\circ$  pulse length of  $10 \mu\text{s}$ , relaxation interval of 8.5 s). WALTZ-16 was used for proton decoupling.

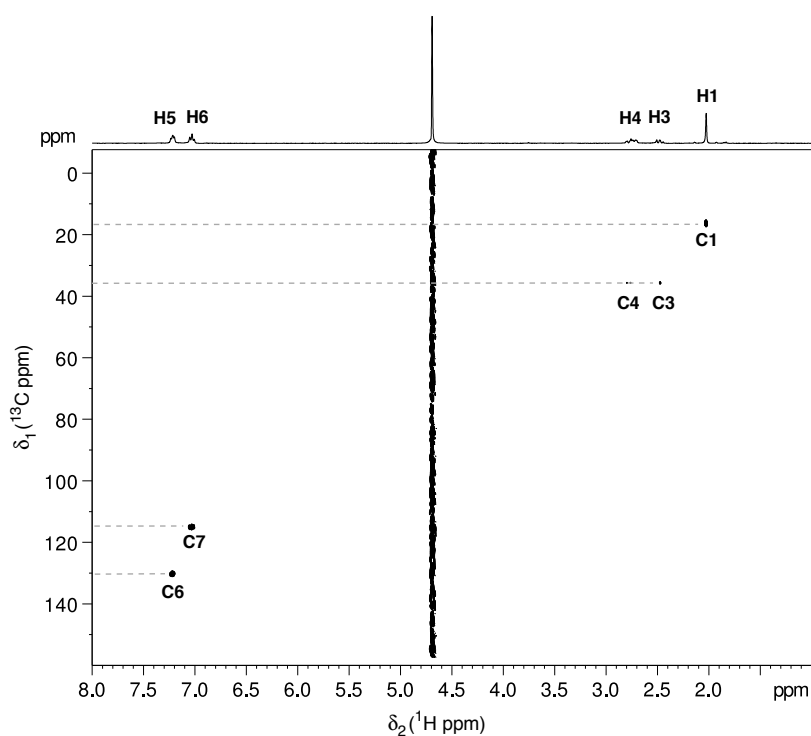


Figure G.12.  $\{^1\text{H}, ^{13}\text{C}\}$  HSQC NMR spectrum of AFEB (3 mM in 90%  $\text{H}_2\text{O}/10\%$   $\text{D}_2\text{O}$ ) at  $B_0 = 9.4$  T. Spectra were recorded by averaging 128 transients for each of the 128  $t_1$  increments of  $30 \mu\text{s}$  ( $90^\circ$  pulse length of  $12 \mu\text{s}$ , relaxation interval of 2 s).

# Bibliography

1. Fauré, N. E., P. J. Halling, and S. Wimperis. *J Phys Chem C* **118**, (2014).
2. Corey, R. B. and L. Pauling. *Rev Sci Instrum* **24**, (1953).
3. Koltun, W. L., *Space filling atomic units and connectors for molecular models*. 1965, United States Patent Office.
4. Wong, C. H. and G. M. Whitesides, "*Enzymes in synthetic organic chemistry*". (Pergamon, 1994).
5. Bickerstaff, G. F., "*Immobilization of enzymes and cells*". (Humana Press, 1997).
6. Katchalski-Katzir, E. and D. M. Kraemer. *J Mol Catal B: Enzym* **10**, (2000).
7. Guisan, J. M., "*Immobilization of enzymes and cells*". (Humana Press, 2006).
8. Boehr, D. D., H. J. Dyson, and P. E. Wright. *Chem Rev* **106**, (2006).
9. Franks, W. T., A. H. Linden, B. Kunert, B. J. van Rossum, and H. Oschkinat. *Eur J Cell Biol* **91**, (2012).
10. Apperley, D. C., R. K. Harris, and P. Hodgkinson, "*Solid-state NMR*". (Momentum Press, 2012).
11. McDermott, A. E. *Curr Opin Struct Biol* **14**, (2004).
12. Hore, P. J., "*Nuclear magnetic resonance*". (Oxford University Press, 1995).
13. Zheng, H. P., K. B. Handing, M. D. Zimmerman, I. G. Shabalin, S. C. Almo, *et al.* *Expert Opin Drug Dis* **10**, (2015).
14. Wang, R. Y. R., M. Kudryashev, X. M. Li, E. H. Egelman, M. Basler, *et al.* *Nat Methods* **12**, (2015).
15. Fischer, N., P. Neumann, A. L. Konevega, L. V. Bock, R. Ficner, *et al.* *Nature* **520**, (2015).
16. Zhu, G. P. and K. Chen, "*NMR of proteins and small biomolecules*". (Springer, 2012).
17. Frauenfelder, H., G. A. Petsko, and D. Tsernoglou. *Nature* **280**, (1979).
18. Johnas, S. K. J., B. Dittrich, A. Meents, M. Messerschmidt, and E. F. Weckert. *Acta Crystallogr D* **65**, (2009).
19. Torchia, D. A. *Prog Nucl Mag Res Sp* **84**, (2015).
20. Nesmelov, Y. E. *Protein Dynamics: Methods and Protocols* **1084**, (2014).

21. Levitt, M. H., "*Spin dynamics : basics of nuclear magnetic resonance*". (John Wiley & Sons, 2001).
22. Purcell, E. M., H. C. Torrey, and R. V. Pound. *Phys Rev* **69**, (1946).
23. Bloch, F., W. W. Hansen, and M. Packard. *Phys Rev* **70**, (1946).
24. Ernst, R. R., G. Bodenhausen, and A. Wokaun, "*Principles of nuclear magnetic resonance in one and two dimensions*". (Oxford University Press, 1987).
25. Zheng, G. and W. S. Price. *Prog Nucl Mag Res Sp* **56**, (2010).
26. Piotto, M., V. Saudek, and V. Sklenar. *J Biomol Nmr* **2**, (1992).
27. Sklenar, V. and A. Bax. *J Magn Reson* **74**, (1987).
28. Hwang, T. L. and A. J. Shaka. *J Magn Reson Ser A* **112**, (1995).
29. Keeler, J., "*Understanding NMR spectroscopy*". (John Wiley and Sons, 2010).
30. Overhauser, A. W. *Phys Rev* **92**, (1953).
31. Claridge, T. D. W., "*High-resolution NMR techniques in organic chemistry*". (Pergamon, 1999).
32. Andrew, E. R., A. Bradbury, and R. G. Eades. *Nature* **182**, (1958).
33. Hartmann, S. R. and E. L. Hahn. *Phys Rev* **128**, (1962).
34. Pines, A., J. S. Waugh, and M. G. Gibby. *J Chem Phys* **56**, (1972).
35. Schaefer, J. and E. O. Stejskal. *J Am Chem Soc* **98**, (1976).
36. Duer, M. J., "*Introduction to solid-state NMR spectroscopy*". (Blackwell, 2004).
37. Henzler-Wildman, K. and D. Kern. *Nature* **450**, (2007).
38. Kleckner, I. R. and M. P. Foster. *Biochim Biophys Acta* **1814**, (2011).
39. Zeeb, M. and J. Balbach. *Methods* **34**, (2004).
40. Bryant, R. G. *J Chem Educ* **60**, (1983).
41. Lewandowski, J. R. *Accounts Chem Res* **46**, (2013).
42. Palmer, A. G., C. D. Kroenke, and J. P. Loria. *Method Enzymol* **339**, (2001).
43. McConnell, H. M. *J Chem Phys* **28**, (1958).
44. Neudecker, P., P. Lundstrom, and L. E. Kay. *Biophys J* **96**, (2009).
45. Göbl, C. and N. Tjandra. *Entropy* **14**, (2012).
46. Jarymowycz, V. A. and M. J. Stone. *Chem Rev* **106**, (2006).
47. Case, D. A. *Accounts Chem Res* **35**, (2002).

48. Caballero-Manrique, E., J. K. Bray, W. A. Deutschman, F. W. Dahlquist, and M. G. Guenza. *Biophys J* **93**, (2007).
49. Chung, C. W. and S. Wimperis. *J Magn Reson* **88**, (1990).
50. Chung, C. W. and S. Wimperis. *Mol Phys* **76**, (1992).
51. Palmer, A. G. *Annu Rev Bioph Biom* **30**, (2001).
52. Parak, F. G. *Curr Opin Struct Biol* **13**, (2003).
53. Thomas, G. J. *Annu Rev Bioph Biom* **28**, (1999).
54. Zanni, M. T. and R. M. Hochstrasser. *Curr Opin Struct Biol* **11**, (2001).
55. Haustein, E. and P. Schwille. *Curr Opin Struct Biol* **14**, (2004).
56. Williams, M. A. and T. Daviter, "*Protein-ligand interactions : methods and applications*". (Humana Press ; Springer, 2013).
57. Pellecchia, M., I. Bertini, D. Cowburn, C. Dalvit, E. Giralt, *et al.* *Nat Rev Drug Discov* **7**, (2008).
58. Skinner, A. L. and J. S. Laurence. *J Pharm Sci* **97**, (2008).
59. Wyss, D. F., M. A. McCoy, and M. M. Senior. *Curr Opin Drug Disc* **5**, (2002).
60. Ludwig, C. and U. L. Guenther. *Front Biosci* **14**, (2009).
61. Aebersold, R. and M. Mann. *Nature* **422**, (2003).
62. Wingard, L. B., "*Enzyme engineering*". (Interscience Publishers, 1972).
63. Taylor, R. F., "*Protein immobilization : fundamentals and applications*". (M. Dekker, 1991).
64. Acevedo, F., J. C. Gentina, and A. Illanes, "*Fundamentos de Ingeniería Bioquímica*". (Eds. Universitarias PUCV, 2004).
65. Illanes, A., "*Enzyme biocatalysis : principles and applications*". (Springer, 2008).
66. Cao, L., "*Carrier-bound immobilized enzymes : principles, applications and design*". (Wiley-VCH, 2005).
67. Porath, J. *Method Enzymol* **34**, (1974).
68. Artyomova, A. A., O. I. Voroshilova, Y. S. Nikitin, and T. D. Khokhlova. *Adv Colloid Interfac* **25**, (1986).
69. Clark, D. S. and J. E. Bailey. *Biotechnol Bioeng* **25**, (1983).
70. Mozhaev, V. V., I. V. Berezin, and K. Martinek. *Crc Critical Reviews in Biochemistry* **23**, (1988).
71. Germain, P., T. Slagmolen, and R. R. Crichton. *Biotechnol Bioeng* **33**, (1989).
72. Baslé, E., N. Joubert, and M. Pucheault. *Chem Biol* **17**, (2010).

73. Schlick, T. L., Z. B. Ding, E. W. Kovacs, and M. B. Francis. *J Am Chem Soc* **127**, (2005).
74. Hooker, J. M., E. W. Kovacs, and M. B. Francis. *J Am Chem Soc* **126**, (2004).
75. Trinquier, G. and Y. H. Sanejouand. *Protein Eng* **11**, (1998).
76. Giovannozzi, A. M., C. Renacco, M. Derosas, E. Enrico, A. Farano, *et al.* *Phys Status Solidi C* **8**, (2011).
77. Malvi, B. and S. Sen Gupta. *Chem Commun* **48**, (2012).
78. Thorn, C., H. Gustafsson, and L. Olsson. *Micropor Mesopor Mat* **176**, (2013).
79. Miyahara, M., A. Vinu, and K. Ariga. *Mat Sci Eng C-Bio S* **27**, (2007).
80. Itoh, T., R. Ishii, T. Ebina, T. Hanaoka, Y. Fukushima, *et al.* *Bioconjugate Chem* **17**, (2006).
81. Matsuura, S., R. Ishii, T. Itoh, T. Hanaoka, S. Hamakawa, *et al.* *Micropor Mesopor Mat* **127**, (2010).
82. Piras, M., A. Salis, M. Piludu, D. Steri, and M. Monduzzi. *Chem Commun* **47**, (2011).
83. Secundo, F. *Chem Soc Rev* **42**, (2013).
84. Nordén, B., A. Rodger, and T. Dafforn, "*Linear dichroism and circular dichroism : a textbook on polarized-light spectroscopy*". (Royal Society of Chemistry, 2010).
85. Halling, P. J. *Anal Biochem* **387**, (2009).
86. Koutsopoulos, S., J. van der Oost, and W. Norde. *Biophys J* **88**, (2005).
87. Kranz, B., J. Burck, M. Franzreb, R. Koster, and A. S. Ulrich. *J Colloid Interf Sci* **316**, (2007).
88. Sharma, S., P. Kaur, A. Jain, M. R. Rajeswari, and M. N. Gupta. *Biomacromolecules* **4**, (2003).
89. Jackson, M. and H. H. Mantsch. *Crit Rev Biochem Mol* **30**, (1995).
90. Kong, J. and S. Yu. *Acta Bioch Bioph Sin* **39**, (2007).
91. Lei, C. H., Y. Shin, J. K. Magnuson, G. Fryxell, L. L. Lasure, *et al.* *Nanotechnology* **17**, (2006).
92. Vinu, A., V. Murugesan, and M. Hartmann. *J Phys Chem B* **108**, (2004).
93. Reategui, E. and A. Aksan. *J Biomech Eng-T Asme* **131**, (2009).
94. Vivian, J. T. and P. R. Callis. *Biophys J* **80**, (2001).
95. Chen, B. W., C. H. Lei, Y. S. Shin, and J. Liu. *Biochem Bioph Res Co* **390**, (2009).

96. Falahati, M., A. A. Saboury, A. Shafiee, S. M. R. Sorkhabadi, E. Kachooei, *et al.* *Biophys Chem* **165**, (2012).
97. Jing, H., X. F. Li, D. G. Evans, X. Duan, and C. Y. Li. *J Mol Catal B:Enzym* **11**, (2000).
98. Prakasham, R. S., P. R. Likhar, K. Rajyalaxmi, C. S. Rao, and B. Sreedhar. *J Mol Catal B:Enzym* **55**, (2008).
99. Kao, K. C., C. H. Lee, T. S. Lin, and C. Y. Mou. *J Mater Chem* **20**, (2010).
100. Zou, B., Y. Hu, L. Jiang, R. Jia, and H. Huang. *Ind Eng Chem Res* **52**, (2013).
101. Hudson, S., E. Magner, J. Cooney, and B. K. Hodnett. *J Phys Chem B* **109**, (2005).
102. Sang, L. C. and M. O. Coppens. *Phys Chem Chem Phys* **13**, (2011).
103. Thorn, C., D. B. R. K. G. Udatha, H. Zhou, P. Christakopoulos, E. Topakas, *et al.* *J Mol Catal B:Enzym* **93**, (2013).
104. Sorin, E. J. and V. S. Pande. *J Am Chem Soc* **128**, (2006).
105. Tian, J. H. and A. E. Garcia. *J Chem Phys* **134**, (2011).
106. Tosaka, R., H. Yamamoto, I. Ohdomari, and T. Watanabe. *Langmuir* **26**, (2010).
107. Rodriguez, J., M. D. Elola, and D. Laria. *J Phys Chem B* **114**, (2010).
108. Solveyra, E. G., E. de la Llave, V. Molinero, G. J. A. A. Soler-Illia, and D. A. Scherlis. *J Phys Chem C* **117**, (2013).
109. Nouredini, H. and X. J. Gao. *J Sol-Gel Sci Techn* **41**, (2007).
110. Lan, J. N., W. Na, Q. Wei, Q. Y. Li, W. Wang, *et al.* *Chem J Chinese U* **31**, (2010).
111. Jung, D., C. Streb, and M. Hartmann. *Int J Mol Sci* **11**, (2010).
112. Brown, L. S. and V. Ladizhansky. *Protein Sci* **24**, (2015).
113. Shaw, W. J. *Solid State Nucl Magn Reson* **70**, (2015).
114. Goobes, G., P. S. Stayton, and G. P. Drobny. *Prog Nucl Mag Res Sp* **50**, (2007).
115. Noske, R., F. Cornelius, and R. J. Clarke. *Bba-Bioenergetics* **1797**, (2010).
116. Olsen, S. N. *Thermochim Acta* **448**, (2006).
117. Henzler, K., B. Haupt, and M. Ballauff. *Anal Biochem* **378**, (2008).
118. Henao-Escobar, W., O. Dominguez-Renedo, M. A. Alonso-Lomillo, J. F. Cascalheira, A. C. Dias-Cabral, *et al.* *Electroanal* **27**, (2015).
119. Kasai, K. and S. Ishii. *J Biochem* **77**, (1975).
120. Hu, Y., J. Qian, H. Guo, S. Jiang, and Z. Zhang. *J Chromatogr Sci* **53**, (2015).

121. Zech, S. G., E. Olejniczak, P. Hajduk, J. Mack, and A. E. McDermot. *J Am Chem Soc* **126**, (2004).
122. Lange, A., K. Giller, S. Hornig, M. F. Martin-Eauclaire, O. Pongs, *et al.* *Nature* **440**, (2006).
123. Weingarth, M. and M. Baldus. *Accounts Chem Res* **46**, (2013).
124. Magner, E. *Chem Soc Rev* **42**, (2013).
125. Kotha, A., R. C. Raman, S. Ponrathnam, K. K. Kumar, and J. G. Shewale. *Appl Biochem Biotech* **74**, (1998).
126. Brunauer, S., P. H. Emmett, and E. Teller. *J Am Chem Soc* **60**, (1938).
127. Barrett, E. P., L. G. Joyner, and P. P. Halenda. *J Am Chem Soc* **73**, (1951).
128. Brun, M., A. Lallemand, J.-F. Quinson, and C. Eyraud. *Thermochim Acta* **21**, (1977).
129. Ritter, H. L. and L. C. Drake. *Ind Eng Chem* **17**, (1945).
130. Strange, J. H., M. Rahman, and E. G. Smith. *Phys Rev Lett* **71**, (1993).
131. Mitchell, J., J. B. W. Webber, and J. H. Strange. *Phys Rep* **461**, (2008).
132. Sing, K. S. W., D. H. Everett, R. A. W. Haul, L. Moscou, R. A. Pierotti, *et al.* *Pure Appl Chem* **57**, (1985).
133. Sing, K. S. W. *Adv Colloid Interfac* **76**, (1998).
134. Nelson, J. M. and E. G. Griffin. *J Am Chem Soc* **38**, (1916).
135. Weetall, H. H. *Trends Biotechnol* **3**, (1985).
136. Vansant, E. F., P. v. d. Voort, and K. C. Vrancken, "Characterization and chemical modification of the silica surface". (Elsevier, 1995).
137. Kallrath, G. and H. Biegler, *Process for producing silica in the form of hollow spheres*. 1968, United States Patent Office.
138. Beau, R., J. Duchene, and M. Le Page, *Porous silica particles containing a crystallized phase and method*. 1970, United States Patent Office.
139. Chiola, V., J. E. Ritsko, and C. D. Vanderpool, *Process for producing low-bulk density silica*. 1971, United States Patent Office.
140. Yanagisawa, T., T. Shimizu, K. Kuroda, and C. Kato. *B Chem Soc Jpn* **63**, (1990).
141. Kresge, C. T., M. E. Leonowicz, W. J. Roth, J. C. Vartuli, and J. S. Beck. *Nature* **359**, (1992).
142. Meynen, V., P. Cool, and E. F. Vansant. *Micropor Mesopor Mat* **125**, (2009).
143. Xu, R., W. Pang, J. Yu, Q. Huo, and J. Chen, "Chemistry of zeolites and related porous materials : synthesis and structure". (Wiley, 2007).

144. Zucca, P. and E. Sanjust. *Molecules* **19**, (2014).
145. Cardarelli, F., "*Materials handbook: A concise desktop reference*". (Springer, 2008).
146. Downs, A. J., "*Chemistry of aluminium, gallium, indium, and thallium*". (Blackie Academic & Professional, 1993).
147. John, C. S., N. C. M. Alma, and G. R. Hays. *Appl Catal* **6**, (1983).
148. Pecharroman, C., I. Sobrados, J. E. Iglesias, T. Gonzalez-Carreno, and J. Sanz. *J Phys Chem B* **103**, (1999).
149. Wyckoff, R. W. G., "*Crystal structures*". (Interscience Publishers, 1963).
150. Zhang, Z. R. and T. J. Pinnavaia. *J Am Chem Soc* **124**, (2002).
151. Gu, D. and F. Schuth. *Chem Soc Rev* **43**, (2014).
152. Knözinger, H. and P. Ratnasamy. *Catal Rev* **17**, (1978).
153. Sundberg, L. and J. Porath. *J Chromatogr* **90**, (1974).
154. Kraemer, D. M., K. Lehmann, H. Pennewiss, and H. Plainer. *Enzyme Eng* **4**, (1978).
155. Katchalski-Katzir, E. and D. M. Kraemer. *J Mol Catal B:Enzym* **10**, (2000).
156. Asai, T., G. Tena, J. Plotnikova, M. R. Willmann, W. L. Chiu, *et al.* *Nature* **415**, (2002).
157. Mateo, C., O. Abian, G. Fernandez-Lorente, J. Pedroche, R. Fernandez-Lafuente, *et al.* *Biotechnol Progr* **18**, (2002).
158. Kallenberg, A. I., F. van Rantwijk, and R. A. Sheldon. *Adv Synth Catal* **347**, (2005).
159. Boller, T., C. Meier, and S. Menzler. *Org Process Res Dev* **6**, (2002).
160. Sigler, P. B., B. A. Jeffery, B. W. Matthews, and D. M. Blow. *J Mol Biol* **15**, (1966).
161. Robillard, G. and R. G. Shulman. *J Mol Biol* **71**, (1972).
162. Blow, D. M., J. J. Birktoft, and B. S. Hartley. *Nature* **221**, (1969).
163. Blow, D. M., "*The Structure of Chymotrypsin*". (Academic Press, 1971).
164. Kraut, J. *Annu Rev Biochem* **46**, (1977).
165. Stryer, L., "*Biochemistry*". (W.H. Freeman, 1988).
166. Madala, P. K., J. D. A. Tyndall, T. Nall, and D. P. Fairlie. *Chem Rev* **110**, (2010).
167. Blow, D. M. *Trends Biochem Sci* **22**, (1997).
168. Freer, S. T., J. Kraut, J. D. Robertus, H. T. Wright, and N. H. Xuong. *Biochemistry* **9**, (1970).

169. Nelson, D. L., M. M. Cox, and A. L. Lehninger, "*Lehninger Principles of Biochemistry*". (Freeman, 2005).
170. Henderson, R. *J Mol Biol* **54**, (1970).
171. Ruhlmann, A., D. Kukla, P. Schwager, K. Bartels, and R. Huber. *J Mol Biol* **77**, (1973).
172. Krieger, M., L. M. Kay, and R. M. Stroud. *J Mol Biol* **83**, (1974).
173. Brady, K., A. Z. Wei, D. Ringe, and R. H. Abeles. *Biochemistry* **29**, (1990).
174. Bone, R., N. S. Sampson, P. A. Bartlett, and D. A. Agard. *Biochemistry* **30**, (1991).
175. Perona, J. J. and C. S. Craik. *Protein Sci* **4**, (1995).
176. Czapinska, H. and J. Otlewski. *Eur J Biochem* **260**, (1999).
177. Knowles, J. R. *J Theor Biol* **9**, (1965).
178. Hedstrom, L. *Chem Rev* **102**, (2002).
179. Hess, G. P., J. Mcconn, E. Ku, and G. Mcconkey. *Philos T Roy Soc B* **257**, (1970).
180. Fersht, A. R. *J Mol Biol* **64**, (1972).
181. Hunkapiller, M. W., S. H. Smallcombe, D. R. Whitaker, and J. H. Richards. *Biochemistry* **12**, (1973).
182. Hunkapiller, M. W., S. H. Smallcombe, D. R. Whitaker, and J. H. Richards. *J Biol Chem* **248**, (1973).
183. Bachovchin, W. W. *P Natl Acad Sci USA* **82**, (1985).
184. Robillar, G and R. G. Shulman. *J Mol Biol* **86**, (1974).
185. Robillar, G. and R. G. Shulman. *J Mol Biol* **86**, (1974).
186. Bachovchin, W. W. *Magn Reson Chem* **39**, (2001).
187. Markley, J. L. and W. M. Westler. *Biochemistry* **35**, (1996).
188. Glasstone, S. *T Faraday Soc* **33**, (1937).
189. Dulmage, W. J. and W. N. Lipscomb. *Acta Crystallogr* **4**, (1951).
190. Sutor, D. J. *Nature* **195**, (1962).
191. Grabowski, S. J., "*Hydrogen bonding : new insights*". (Springer, 2006).
192. Horowitz, S. and R. C. Trievel. *J Biol Chem* **287**, (2012).
193. Derewenda, Z. S., U. Derewenda, and P. M. Kobos. *J Mol Biol* **241**, (1994).
194. Ash, E. L., J. L. Sudmeier, R. M. Day, M. Vincent, E. V. Torchilin, *et al.* *Proc Natl Acad Sci USA* **97**, (2000).

195. Zaks, A. and A. M. Klibanov. *J Biol Chem* **263**, (1988).
196. Halling, P. J. *Philos T Roy Soc B* **359**, (2004).
197. Gregory, R. B., "Protein-solvent interactions". (Marcel Dekker, 1995).
198. Tarek, M. and D. J. Tobias. *Biophys J* **79**, (2000).
199. Bizzarri, A. R. and S. Cannistraro. *J Phys Chem B* **106**, (2002).
200. Raschke, T. M. *Curr Opin Struct Biol* **16**, (2006).
201. Pal, S. K., J. Peon, B. Bagchi, and A. H. Zewail. *J Phys Chem B* **106**, (2002).
202. Pal, S. K. and A. H. Zewail. *Chem Rev* **104**, (2004).
203. Russo, D., R. K. Murarka, J. R. Copley, and T. Head-Gordon. *J Phys Chem B* **109**, (2005).
204. Martini, S., C. Bonechi, A. Foletti, and C. Rossi. *ScientificWorldJournal* **2013**, (2013).
205. Grieve, S. M., B. Wickstead, A. M. Torres, P. Styles, S. Wimperis, et al. *Biophys Chem* **73**, (1998).
206. Baguet, E., B. E. Chapman, A. M. Torres, and P. W. Kuchel. *J Magn Reson Ser B* **111**, (1996).
207. Baguet, E., N. Hennebert, B. E. Chapman, A. M. Torres, and P. W. Kuchel. *Magn Reson Chem* **35**, (1997).
208. Baguet, E. and N. Hennebert. *Biophys Chem* **77**, (1999).
209. Halle, B. and V. P. Denisov, "Magnetic Relaxation Dispersion Studies of Biomolecular Solutions". (Academic Press, 2002).
210. Otting, G. *Prog Nucl Mag Res Sp* **31**, (1997).
211. Green, N. M., J. A. Gladner, L. W. Cunningham, and H. Neurath. *J Am Chem Soc* **74**, (1952).
212. Wu, F. C. and M. Laskowski. *Biochim. Biophys. Acta* **19**, (1956).
213. Kezdy, F. J. and M. L. Bender. *Biochemistry* **4**, (1965).
214. Shearwin, K. E. and D. J. Winzor. *Biochim. Biophys. Acta* **1038**, (1990).
215. Laszlo, P. *Angewandte Chemie* **17**, (1978).
216. Page, M. J. and E. Di Cera. *Physiol Rev* **86**, (2006).
217. Dang, Q. D. and E. Di Cera. *Proc Natl Acad Sci USA* **93**, (1996).
218. Guinto, E. R., S. Caccia, T. Rose, K. Futterer, G. Waksman, et al. *Proc Natl Acad Sci USA* **96**, (1999).
219. Krem, M. M. and E. Di Cera. *Embo J* **20**, (2001).

220. Di Cera, E., E. R. Guinto, A. Vindigni, Q. D. Dang, Y. M. Ayala, *et al.* *J Biol Chem* **270**, (1995).
221. Turk, B. *Nat Rev Drug Discov* **5**, (2006).
222. Smyth, T. P. *Bioorgan Med Chem* **12**, (2004).
223. Fu, H., H. Fang, J. Sun, H. Wang, A. Liu, *et al.* *Curr Med Chem* **21**, (2014).
224. Koehler, K. A. and G. E. Lienhard. *Biochemistry* **10**, (1971).
225. Philipp, M. and M. L. Bender. *Proc Natl Acad Sci USA* **68**, (1971).
226. Rawn, J. D. and G. E. Lienhard. *Biochemistry* **13**, (1974).
227. Matthews, D. A., R. A. Alden, J. J. Birktoft, S. T. Freer, and J. Kraut. *J Biol Chem* **250**, (1975).
228. Hall, D. G., "Structure, Properties, and Preparation Of Boronic Acid Derivatives. Overview of Their Reactions and Applications". (Wiley-VCH, 2005).
229. Antonov, V. K., T. V. Ivanina, I. V. Berezin, and K. Martinek. *Febs Lett* **7**, (1970).
230. Antonov, V. K., I. V. Berezin, K. Martinek, A. V. Levashov, T. V. Ivanina, *et al.* *Febs Lett* **20**, (1972).
231. Lindquis.Rn and C. Terry. *Arch Biochem Biophys* **160**, (1974).
232. Lindquist, R. N. and A. C. Nguyen. *J Am Chem Soc* **99**, (1977).
233. Matteson, D. S., K. M. Sadhu, and G. E. Lienhard. *J Am Chem Soc* **103**, (1981).
234. Bachovchin, W. W., W. Y. L. Wong, S. Farrjones, A. B. Shenvi, and C. A. Kettner. *Biochemistry* **27**, (1988).
235. Zhong, S., K. Haghjoo, C. Kettner, and F. Jordan. *J Am Chem Soc* **117**, (1995).
236. Bao, D. H., J. T. Cheng, C. Kettner, and F. Jordan. *J Am Chem Soc* **120**, (1998).
237. Gerig, J. T. *Magn Reson Chem* **37**, (1999).
238. Gerig, J. T. *Prog Nucl Mag Res Sp* **26**, (1994).
239. Sylvia, L. A. and J. T. Gerig. *Biochim. Biophys. Acta* **1163**, (1993).
240. Sylvia, L. A. and J. T. Gerig. *Bba-Protein Struct M* **1252**, (1995).
241. Gerig, J. T. *J Am Chem Soc* **102**, (1980).
242. Hammond, S. J. *J Chem Soc Chem Comm* (1984).
243. Darses, S., G. Michaud, and J. P. Genet. *Eur J Org Chem* (1999).
244. Darses, S. and J. P. Genet. *Chem Rev* **108**, (2008).

245. Oliveira, R. A., L. Savegnago, C. R. Jesse, P. H. Menezes, G. A. Molander, *et al.* *Basic Clin Pharmacol* **104**, (2009).
246. Lecat-Guillet, N. and Y. Ambroise. *Chemmedchem* **3**, (2008).
247. Smoum, R., A. Rubinstein, and M. Srebnik. *Org Biomol Chem* **3**, (2005).
248. Molander, G. A., L. N. Cavalcanti, B. Canturk, P. S. Pan, and L. E. Kennedy. *J Org Chem* **74**, (2009).
249. Kabalka, G. W. and V. Coltuclu. *Tetrahedron Lett* **50**, (2009).
250. Weetall, H. H. *Appl Biochem Biotech* **41**, (1993).
251. Pasternack, R. M., S. R. Amy, and Y. J. Chabal. *Langmuir* **24**, (2008).
252. Acres, R. G., A. V. Ellis, J. Alvino, C. E. Lenahan, D. A. Khodakov, *et al.* *J Phys Chem C* **116**, (2012).
253. Nawrocki, J., C. J. Dunlap, P. W. Carr, and J. A. Blackwell. *Biotechnol Progr* **10**, (1994).
254. Wheatley, J. B. and D. E. Schmidt. *J Chromatogr* **644**, (1993).
255. Wheatley, J. B. and D. E. Schmidt. *J Chromatogr A* **849**, (1999).
256. Felix, G. and V. Descorps. *Chromatographia* **49**, (1999).
257. Melander, W. R., D. Corradini, and C. Horvath. *J Chromatogr* **317**, (1984).
258. Smalla, K., J. Turkova, J. Coupek, and P. Hermann. *Biotechnol Appl Bioc* **10**, (1988).
259. Srere, P. A. and K. Uyeda. *Methods Enzymol* **44**, (1976).
260. Herman, D. P., L. R. Field, and S. Abbott. *J Chromatogr Sci* **19**, (1981).
261. Durbetaki, A. J. *Anal Chem* **28**, (1956).
262. Dijkstra, R. and E. A. M. Dahmen. *Anal Chim Acta* **31**, (1964).
263. Jay, R. R. *Anal Chem* **36**, (1964).
264. Bradford, M. M. *Anal Biochem* **72**, (1976).
265. Vandermeers, A., H. Lelotte, and J. Christophe. *Anal Biochem* **42**, (1971).
266. Maciel, G. E. and D. W. Sindorf. *J Am Chem Soc* **102**, (1980).
267. Maciel, G. E. *Nuclear Magnetic Resonance in Modern Technology* **447**, (1994).
268. Slade, R. C. T., J. C. Southern, and I. M. Thompson. *J Mater Chem* **1**, (1991).
269. Wang, J. A., X. Bokhimi, A. Morales, O. Novaro, T. Lopez, *et al.* *J Phys Chem B* **103**, (1999).
270. Tsyganenko, A. A. and P. P. Mardilovich. *J Chem Soc Faraday T* **92**, (1996).

271. Schwarz, J. A., C. Contescu, and A. Contescu. *Chem Rev* **95**, (1995).
272. Sohlberg, K., S. J. Pennycook, and S. T. Pantelides. *J Am Chem Soc* **121**, (1999).
273. Paglia, G., C. E. Buckley, T. J. Udovic, A. L. Rohl, F. Jones, *et al.* *Chem Mater* **16**, (2004).
274. Pearson, R. M. *J Catal* **23**, (1971).
275. Bell, A. T. and A. Pines, "NMR techniques in catalysis". (M. Dekker, 1994).
276. Morris, H. D. and P. D. Ellis. *J Am Chem Soc* **111**, (1989).
277. O'Reilly, D. E. *Adv Catal* **12**, (1960).
278. Digne, M., P. Sautet, P. Raybaud, P. Euzen, and H. Toulhoat. *J Catal* **226**, (2004).
279. Paglia, G., A. L. Rohl, C. E. Buckley, and J. D. Gale. *Phys Rev B* **71**, (2005).
280. Jackson, S. D. and J. S. J. Hargreaves, "Metal oxide catalysis". (Wiley-VCH, 2009).
281. Gaigneaux, E., D. E. De Vos, P. Grange, P. Ruiz, and G. Poncelet, "Scientific Bases for the Preparation of Heterogeneous Catalysts". (Elsevier, 2002).
282. Pecharromán, C., I. Sobrados, J. E. Iglesias, T. Gonzalez-Carreno, and J. Sanz. *J Phys Chem B* **103**, (1999).
283. Kwak, J. H., J. Z. Hu, D. H. Kim, J. Szanyi, and C. H. F. Peden. *J Catal* **251**, (2007).
284. Lee, D., N. T. Duong, O. Lafon, and G. De Paepe. *J Phys Chem C* **118**, (2014).
285. Bayer, E., K. Albert, J. Reiners, M. Nieder, and D. Muller. *J Chromatogr* **264**, (1983).
286. Bogart, G. R., D. E. Leyden, T. M. Wade, W. Schafer, and P. W. Carr. *J Chromatogr* **483**, (1989).
287. Osterholtz, F. D. and E. R. Pohl. *J Adhes Sci Technol* **6**, (1992).
288. Templin, M., U. Wiesner, and H. W. Spiess. *Adv Mater* **9**, (1997).
289. Wells, C. M. and E. Dicera. *Biochemistry* **31**, (1992).
290. Nayal, M. and E. Dicera. *P Natl Acad Sci USA* **91**, (1994).
291. Fioretti, E., M. Angeletti, G. Lupidi, and M. Coletta. *Eur J Biochem* **225**, (1994).
292. Angeletti, M., G. Lupidi, A. M. Eleuteri, R. Tacconi, E. Fioretti, *et al.* *J Biol Inorg Chem* **2**, (1997).
293. Venkataraman, S., T. A. Horbett, and A. S. Hoffman. *Abstr Pap Am Chem S* **170**, (1975).

294. Koch-Schmidt, A. C. and K. Mosbach. *Biochemistry* **16**, (1977).
295. Mateo, C., O. Abian, R. Fernandez-Lafuente, and J. M. Guisan. *Enzyme Microb Tech* **26**, (2000).
296. Ando, I. and T. Asakura, "*Solid state NMR of polymers*". (Elsevier, 1998).
297. Lowry, O. H., N. J. Rosebrough, A. L. Farr, and R. J. Randall. *J Biol Chem* **193**, (1951).
298. Smith, P. K., R. I. Krohn, G. T. Hermanson, A. K. Mallia, F. H. Gartner, *et al.* *Anal Biochem* **150**, (1985).
299. Gupta, R. K. and P. Gupta. *J Magn Reson* **47**, (1982).
300. Hubbard, P. S. *J Chem Phys* **53**, (1970).
301. Jaccard, G., S. Wimperis, and G. Bodenhausen. *J Chem Phys* **85**, (1986).
302. Pekar, J. and J. S. Leigh. *J Magn Reson* **69**, (1986).
303. Goodey, N. M. and S. J. Benkovic. *Nat Chem Biol* **4**, (2008).
304. Navon, G. *Magnet Reson Med* **30**, (1993).
305. Kemp-Harper, R., B. Wickstead, and S. Wimperis. *J Magn Reson* **140**, (1999).
306. Mason, J. J., "*Multinuclear NMR*". (Plenum, 1987).
307. Persson, E. and B. Halle. *J Am Chem Soc* **130**, (2008).
308. Halle, B. *Nato Adv Sci I a-Lif* **305**, (1999).
309. Werbelow, L. and G. Pouzard. *J Phys Chem* **85**, (1981).
310. Bull, T. E. *J Magn Reson* **8**, (1972).
311. Bull, T. E., S. Forsen, and D. L. Turner. *J Chem Phys* **70**, (1979).
312. Garrett, B. B., A. B. Denison, and S. W. Rabideau. *J Phys Chem* **71**, (1967).
313. Jang, H. M., Fuerstenau, D. W. *Langmuir* **3**, (1987).
314. Serdyuk, I. N., N. R. Zaccai, and G. Zaccai, "*Methods in molecular biophysics : structure, dynamics, function*". (Cambridge University Press, 2007).
315. Shimshick, E. and H. M. McConnel. *Biochem Bioph Res Co* **46**, (1972).
316. Steinbach, P. J. and B. R. Brooks. *P Natl Acad Sci USA* **90**, (1993).
317. Fogarty, A. C. and D. Laage. *J Phys Chem B* **118**, (2014).
318. Bruylants, G., C. Redfield, and K. Bartik. *Chembiochem* **8**, (2007).
319. Knotter, D. M. *J Am Chem Soc* **122**, (2000).
320. Liu, Y. and H. Nekvasil. *Am Mineral* **87**, (2002).

321. Jaeger, C. and F. Hemmann. *Solid State Nucl Mag* **57-58**, (2014).
322. Bockmann, A., F. Penin, and E. Guittet. *Febs Lett* **383**, (1996).
323. Gamcsik, M. P., J. T. Gerig, and R. B. Swenson. *Biochim Biophys Acta* **874**, (1986).
324. Tsukada, H. and D. M. Blow. *J Mol Biol* **184**, (1985).
325. Birktoft, J. J. and D. M. Blow. *J Mol Biol* **68**, (1972).
326. Wishart, D. S. and A. M. Nip. *Biochem Cell Biol* **76**, (1998).
327. Ulrich, E. L., H. Akutsu, J. F. Doreleijers, Y. Harano, Y. E. Ioannidis, *et al.* *Nucleic Acids Res* **36**, (2008).
328. Duggleby, R. G. *Enzyme Kinetics and Mechanism, Pt D* **249**, (1995).
329. Fielding, L. *Prog Nucl Mag Res Sp* **51**, (2007).
330. Scheuring, J., M. Fischer, M. Cushman, J. Lee, A. Bacher, *et al.* *Biochemistry* **35**, (1996).
331. Cao, L. Q. *Curr Opin Chem Biol* **9**, (2005).
332. Salis, A., E. Sanjust, V. Solinas, and M. Monduzzi. *J Mol Catal B:Enzym* **24-5**, (2003).
333. Li, Y. J., G. W. Zhou, C. J. Li, D. W. Qin, W. T. Qiao, *et al.* *Colloid Surface A* **341**, (2009).
334. Ison, A. P., A. R. Macrae, C. G. Smith, and J. Bosley. *Biotechnol Bioeng* **43**, (1994).
335. Brownstein, K. R. and C. E. Tarr. *Phys Rev A* **19**, (1979).
336. D'Orazio, F., J. C. Tarczoz, W. P. Halperin, K. Eguchi, and T. Mizusaki. *J Appl Phys* **65**, (1989).
337. Valckenborg, R. M. E., L. Pel, and K. Kopinga. *J Phys D Appl Phys* **35**, (2002).
338. Ball, V. and C. Maechling. *Int J Mol Sci* **10**, (2009).
339. Rijniens, L. A., P. C. M. M. Magusin, H. P. Huinink, L. Pel, and K. Kopinga. *J Magn Reson* **167**, (2004).
340. Martichonok, V. and J. B. Jones. *J Am Chem Soc* **118**, (1996).